Titre: Title:	A Study of In-Plane Charge Carrier Diffusion and Photon Recycling in Hybrid Organic-Inorganic Perovskites
Auteur: Author:	Aravindan Sridharan
Date:	2021
Type:	Mémoire ou thèse / Dissertation or Thesis
Référence: Citation:	Sridharan, A. (2021). A Study of In-Plane Charge Carrier Diffusion and Photon Recycling in Hybrid Organic-Inorganic Perovskites [Thèse de doctorat, Polytechnique Montréal]. PolyPublie. https://publications.polymtl.ca/9100/

URL de PolyPublie: PolyPublie URL:	https://publications.polymtl.ca/9100/
Directeurs de recherche: Advisors:	Stéphane Kéna-Cohen
Programme: Program:	Génie physique

POLYTECHNIQUE MONTRÉAL
affiliée à l'Université de Montréal

A study of in-plane charge carrier diffusion and photon recycling in hybrid organic-inorganic perovskites

ARAVINDAN SRIDHARAN
Département de génie physique

Thèse présentée en vue de l'obtention du diplôme de *Philosophiæ Doctor*
Génie physique

Juillet 2021

POLYTECHNIQUE MONTRÉAL
affiliée à l'Université de Montréal

Cette thèse intitulée :

A study of in-plane charge carrier diffusion and photon recycling in hybrid organic-inorganic perovskites

présentée par **Aravindan SRIDHARAN**
en vue de l'obtention du diplôme de *Philosophiæ Doctor*
a été dûment acceptée par le jury d'examen constitué de :

Oussama MOUTANABBIR, président
Stéphane KÉNA-COHEN, membre et directeur de recherche
David MÉNARD, membre
Libai HUANG, membre externe

DEDICATION

To my parents, who have been a fountain
of endless support and inspiration

இவ்வாராய்ச்சிக்கட்டுரையை சமர்ப்பிக்கிறேன்
ஊக்கத்தின் ஊற்றாக திகழ்ந்தயென் பெற்றொர்க்கு

ACKNOWLEDGEMENTS

I would like to express the first and foremost gratitude to my supervisor, Prof. Stéphane Kéna-Cohen whose time, patience, generosity, and continued guidance have been valuable beyond measure in the completion of this project.

I would like to thank alumni Fábio Barachati and Soroush Hafezian for making this lab a great place to join. Fábio was always generous in his technical counsel, while Soroush's wit and humour sailed us through some tough days at the glovebox workstation. Julien Brodeur and Elad Eizner deserve a special mention for the companionship and camaraderie, especially during conferences. I wish to acknowledge fellow colleagues John Ibrahim, Mohammad Zia Ullah Khan, Ashutosh Patri, Louis Haeberlé, Jian Mao, Afshin Shahalizad, David Myers, Grégorie Laflamme, Alex Malinge, Orlando Ortiz, Pierre-Luc Thériault and Félix Thouin for their constructive feedback and pleasant company making my stay in this group a more enjoyable experience.

As for the support in the completion of my Ph.D. project, our technical staff Jean-Paul and Francis deserve a special mention for their hard work in setting up the equipment. I also thank Hyeon Hwang, who as an intern under my guidance, performed critical diffusion measurements and calculations for the completion of my first paper.

I would like to formally thank Sifu Darrell Carreon and my VTMTL martials arts family for providing a vital sanctuary in stressful times to re-energize myself through the continued learning and practice of the magnificent Ving Tsun Kung Fu system.

Lastly, I thank my parents, my sister, Ashvitha, and especially my wife, Hema, for their tremendous support and encouragement in the past years. Thanks to their unconditional love and confidence in my abilities, which was a key enabler, I was able to chase my dreams and persevere in this daunting task.

RÉSUMÉ

Plusieurs études récentes prévoient une augmentation de près de 50% de la consommation énergétique mondiale avant 2050. Une chute de la production risque d'avoir des conséquences négatives à la fois sociales et économiques. De plus, les polluants issus des combustibles fossiles, les principales sources d'énergie à l'échelle mondiale, sont à la source de problèmes tels que le réchauffement planétaire, le smog et les pluies acides. Toute réponse à ce défi énergétique doit donc se faire par le moyen d'une alternative propre et renouvelable. En ce sens, l'énergie solaire est un excellent choix. Néanmoins, les panneaux solaires conventionnels restent dispendieux et relativement inefficaces par rapport aux combustibles fossiles. Récemment, la découverte des cellules solaires à base de pérovskites hybrides organique-inorganique a fait l'objet d'un intérêt considérable à travers le monde. Ces dispositifs ont surpassé leurs prédécesseurs organiques à base de colorants parce qu'ils sont plus efficaces, plus simples à fabriquer et moins coûteux. La croissance rapide de l'efficacité des cellules fabriquées à base de ces matériaux, présentement à 25.5%, est inégalée dans l'histoire des cellules solaires. Ceci représente une opportunité unique de créer une nouvelle génération de cellules solaires hautement efficaces pouvant stimuler l'industrie solaire.

Un panneau solaire est composé de plusieurs cellules photovoltaïques qui sont typiquement reliées en série. Chaque cellule, à son tour, est composée de plusieurs couches; soit une anode, un matériau transporteur d'électrons, un absorbeur, un matériau transporteur de trous et finalement une cathode. Le matériau absorbeur, dans notre cas la pérovskite, sert à la conversion de la lumière entrante en porteurs de charges libres, soit électrons et trous. Le transport des porteurs de charge aux électrodes résulte en une génération d'une différence de potentiel aux bornes de la cellule photovoltaïque. Les pérovskites hybrides, grâce à leur bande interdite (~1.5 eV) approchant la valeur idéale (~1.34 eV) pour l'efficacité de conversion maximale, sont d'excellents absorbeurs. Cependant, il reste beaucoup à découvrir en ce qui concerne la physique fondamentale des porteurs de charges permettant ces valeurs d'efficacité aussi élevées. Plus spécifiquement, comprendre l'influence des processus de recombinaison et de diffusion de porteurs de charges sur les efficacités de conversion énergétique continue à poser un défi à la communauté de recherche en pérovskites. La grande majorité des expériences initiales telles que la photoluminescence résolue en temps (TRPL) ignorent les propriétés latérales du matériau et assument des valeurs idéales pour les conditions de frontières. De plus, les études effectuées jusqu'à présent sur la forme/structure/frontières des grains demeurent inconclusives. Plus récemment, avec l'utilisation grandissante des techniques de

microscopie/spectroscopie, il est évident que les propriétés morphologiques du matériau ont un impact considérable sur l'efficacité énergétique de la cellule. Bref, notre première problématique de recherche peut être formulée ainsi : «Comment pouvons-nous déterminer de manière précise la diffusion des porteurs de charges dans les couches minces de pérovskite et comment ce phénomène est-il corrélé avec la morphologie?»

Notre deuxième problématique est la suivante : «Quel est l'ampleur de la contribution du processus de recyclage de photons au transport de porteurs de charges au sein des pérovskites hybrides?» Au-delà de la recombinaison et de la diffusion, certains effets tels que la réabsorption et le recyclage de photons ont été mesurés dans les pérovskites hybrides. Ces phénomènes sont bien connus pour leurs contributions bénéfiques aux paramètres de performance photovoltaïques dans d'autre matériaux tel que le GaAs. Cependant, dans le contexte des pérovskites hybrides, un grand nombre d'études sur le transport de charges sont effectuées sous des conditions microscopiques où l'excitation lumineuse pour injecter des porteurs de charges dans le matériau est fortement focalisée. De plus, les conclusions sont généralisées pour les dispositifs réels où le faisceau lumineux n'est pas focussé et où la densité de porteurs de charges est beaucoup plus faible. Nous devons donc examiner l'interdépendance entre les phénomènes de diffusion (latérale) et recyclage de photons dans les conditions d'excitation lumineuse focalisée par des méthodes expérimentales et analytiques.

Concernant la première problématique de recherche, afin de mesurer la diffusion latérale, nous présentons une méthode de microscopie spatio-temporelle basée sur la caméra à balayage de fente. Les résultats expérimentaux sont complétés par une procédure statistique d'ajustement de courbes permettant d'extraire les coefficients de recombinaison et de diffusion. La combinaison de méthodes expérimentales et analytiques est appliquée aux films de triiodure de plomb au méthylammonium ($\mathrm{MAPbI_3}$), obtenus par deux procédés de fabrications différentes, de tribromure de plomb au méthylammonium ($\mathrm{MAPbBr_3}$) et en dernier lieu un film composé de mélange de cations FA-MA et d'anions Br-I avec composition $\mathrm{FA_{0.85}MA_{0.15}Pb(I_{0.85}Br_{0.15})_3}$. Nous observons que les valeurs des coefficients de diffusion dans les films produisant les dispositifs les plus performants, soit $\mathrm{FA_{0.85}MA_{0.15}Pb(I_{0.85}Br_{0.15})_3}$ et $\mathrm{MAPbI_3}$ obtenu par traitement acétonitrile, sont inférieures aux autres films par plusieurs ordres de grandeur. Une étude détaillée de la dépendance temporelle démontre une présence minimale du processus de diffusion dans le transport électrique. En particulier, dans le $\mathrm{MAPbI_3}$ produit par acétonitrile, on aperçoit deux régimes distincts, soit un long et l'autre court en échelles temporelles, avec un coefficient de diffusion effectif constant et variant sur deux ordres de grandeur. Nous résultats soulignent qu'une augmentation en temps de vie n'est pas nécessairement corrélée avec des plus grandes longueurs de diffusion. De plus, nous constatons que l'efficacité quan-

tique est un meilleur indicateur de qualité et de performance dans les dispositifs réels.

Pour la deuxième problématique, nous modifions le montage précédant afin de mesurer l'évolution spectrale en fonction du temps et de la distance radiale partant du centre d'excitation. Il est reconnu que la présence du phénomène de recyclage de photons produit un décalage dans la signature spectrale avec la distance radiale. En anticipant ce décalage, nous présentons un modèle analytique incorporant les effets de diffusion latérale, de recombinaisons de porteurs de charges, et de recyclage de photons afin de mesurer la contribution exacte de chaque processus. Nos résultats démontrent que malgré certaines ressemblances avec d'autres études sur le recyclage de photons, le décalage spectral est principalement causé par un autre phénomène, le remplissage de bandes. Finalement, nous réalisons une étude purement numérique sur l'interaction entre la taille du profil d'excitation, du coefficient de diffusion et fluence sous l'influence du recyclage de photons. Nos données révèlent que le recyclage de photons élargit de manière négligeable la diffusion des porteurs de charge sous des conditions de faible injection dans les expériences de type micro-PL.

ABSTRACT

Over the next few decades, global energy consumption has been predicted to increase by nearly 50%. The possibility of a shortfall in production or availability could have severe socioeconomic repercussions. In addition, fossil fuels are the primary source of pollutants leading to climate change, smog, acid rain along with various health problems. Hence, any response to this challenge must include a plan to replace fossil fuels with clean and renewable energy sources. Solar energy, which draws upon our nearly infinite supply of solar irradiation, is widely considered to be our most important resource for a sustainable energy future. At present, however, conventional solar panels remain expensive and relatively inefficient, when compared to their fossil fuel alternatives. Despite making headlines internationally, hybrid organic-inorganic perovskite (HOIP) solar cells, are a very recent development in solar science. These new devices largely surpass their organic and dye-sensitized predecessors in terms of conversion efficiency, fabrication simplicity and materials cost. The rapid growth in perovskite solar cell power conversion efficiencies, which is currently at 25.5% has been unparalleled. Hence, this is a unique opportunity to create a new generation of highly efficient solar cells which could reinvigorate the energy industry.

A solar panel is composed of multiple cells which are typically configured in series. Each solar cell is composed of several layers, such as an anode, an electron transporting layer (ETL), an absorber, a hole transporting layer (HTL), and a cathode. The absorber material, i.e. the hybrid perovskite in our case, converts incident irradiation into free charge carriers, i.e. electrons and holes. The transport of charge carriers to their respective electrodes results in power across a load. Hybrid perovskites, thanks to a bandgap (~1.5 eV) approaching the ideal value (~1.34 eV) for maximum power conversion efficiency, are phenomenal absorbers. However, much remains to be discovered with respect to the underlying carrier physics producing such high efficiencies. Specifically, understanding the influence of recombination kinetics and diffusion on energy conversion efficiencies poses a challenge for the perovskite research community. Most of the initial measurements such as time-resolved photoluminescence (TRPL) ignores lateral material properties and assume ideal boundary conditions when fitting coefficients. Also, studies on the effect of grain shape/structure/boundaries on carrier diffusion remain inconclusive. With the recent surge in microscopic/spectroscopic methods for carrier transport characterization, we observe a greater emphasis on the importance of morphological aspects in shaping device performance. Our first research question is as follows: “How can we accurately measure carrier diffusion in perovskite thin films and how does it correlate

with morphology?”

Our second research question is “What is the extent to which photon recycling contributes to carrier transport within hybrid perovskites?” Besides recombination and diffusion, effects such as photon re-absorption and photon recycling have also been reported in hybrid perovskites. Both phenomena have been known to be beneficial in improving efficiencies in high efficiency materials such as GaAs. However, in the perovskite case, transport studies of the materials are often conducted using microscopic measurements where photogeneration is induced using a tightly focussed light beam. The results and interpretations of such measurements are also then generalized for real devices where light is not focussed and the carrier densities are much lower. Therefore, we must also explore the interplay between lateral diffusion and photon recycling under focussed conditions through both experimental and analytical methods.

To answer the first question, we developed a streak camera-based technique to measure lateral diffusion in halide perovskite materials and present a fitting procedure to extract the diffusion coefficients. The technique is applied to thin films of methylammonium lead tri-iodide ($MAPbI_3$) obtained with two different fabrication routes, to methylammonium lead tribromide ($MAPbBr_3$), and to an alloy of formamidinium lead tri-iodide ($FAPbI_3$) with $MAPbBr_3$, i.e. $FA_{0.85}MA_{0.15}Pb(I_{0.85}Br_{0.15})_3$. Average diffusion coefficients in the films leading to the highest device efficiencies and longest lifetimes, i.e., in $FA_{0.85}MA_{0.15}Pb(I_{0.85}Br_{0.15})_3$ and acetonitrile-processed $MAPbI_3$, are found to be several orders of magnitude lower than in the other films. Further examination of the time-dependence shows strong evidence for non-diffusive transport. In particular, acetonitrile-processed $MAPbI_3$ shows distinct diffusion regimes on short and long timescales with an effective diffusion constant varying over 2 orders of magnitude. Our results also highlight the fact that increases in carrier lifetime in this class of materials are not necessarily concomitant with increased diffusion lengths and that the PL quantum efficiency under solar cell operating conditions is a greater indication of material, and ultimately device, quality.

As for the second question, on top of temporal and spatial, we also study the spectral evolution of charge carriers in hybrid perovskite thin films after optical excitation with a small laser spot to probe the dynamics between diffusion and photon recycling. These are conditions typical of microscopy-based studies. After excitation, the spreading of charge carriers in space occurs due to a combination of diffusion, recombination, and photon recycling. To quantitatively understand their relative importance, a numerical model is used to simulate the anticipated photoluminescence (PL), while accounting for these processes.

We also experimentally study the evolution of the PL spectrum at different radial positions from the center of the excitation spot. This allows us to extend our previous work on carrier diffusion performed using time-resolved PL microscopy. Our numerical model predicts a position-dependent spectral shift of the waveguided photon energy in agreement with previous reports. However, we show that the spectral shift under our experimental conditions is dominated by band filling. Finally, we study the interplay between pump spot size, diffusion constant and fluence on carrier transport in the presence of photon recycling. Our results show that in typical micro-PL experiments and modest carrier densities, photon recycling plays a negligible role in enhancing the lateral spreading of carriers.

TABLE OF CONTENTS

LIST OF TABLES

LIST OF FIGURES

LIST OF SYMBOLS AND ACRONYMS

Abbreviations

1D	One dimension
2D	Two dimensions
3D	Three dimensions
BG	Bandgap
BL	Beer-Lambert
BP	British Petroleum
CB	Conduction band
CCD	Charge-coupled device
CI	Coulomb interaction
CW	Continuous wave
CZ	Czochralski method
DOS	Density of states
DS	Directional solidification
DSSC	Dye-sensitized solar cells
ETL	Electron transport layer
FZ	Float zone
HOIP	Hybrid organic-inorganic perovskite
IEA	International Energy Agency
IR	Infrared
IRENA	International Renewable Energy Agency
LED	Light emitting diode
LLC	Limited liability company
LP	Long pass (optical filter)
LT	Light trapping
MCDE	Minority carrier diffusion equations
MCP	Micro-channel plate
MSD	Mean squared distance
NREL	National Renewable Energy Laboratory
OHP	Organometal(lic) halide perovskites
OPV	Organic photovoltaics
R&D	Research and development

PL	Photoluminescence
PSC	Perovskite solar cell
PSF	Point spread function
PV	Photovoltaic(s)
RPM	Rotations per minute
SQ	Shockley-Queiesser
SRH	Shockley-Read-Hall
SRM	Square root model
TAS	Transient absorption spectroscopy
TGA	Thermal gravimetric analysis
TRPL	Time-resolved photoluminescence
TR-PEEM	Time-resolved photoelectron emission microscopy
TSC	Thermally stimulated currents
UV	Ultraviolet
vR-S	Van Roosbroeck-Shockley
VB	Valence band
XRD	X-Ray diffraction (spectroscopy)

Materials

a-Si	Amorphous silicon
Ag	Silver
Al_2O_3	Aluminium oxide
Au	Gold
BCP	Bathocuproine
CdTe	Cadmium telluride
CIGS	Copper indium gallium selenide
CO_2	Carbon dioxide
CZTS (Cu_2ZnSnS_4)	Copper zinc tin sulfide
CZTSSe (Cu_2ZnSnS_4Se)	Copper zinc tin sulfide/selenide
DM	Fluorene-terminated Spiro-OMeTAD
DMF ($(CH_3)_2NCH$)	Dimethylformamide
DMSO (C_2H_6OS)	Dimethyl sulfoxide
FA^+ ($CH(NH_2)_2^+$)	Formamidinium cation
FAI	Formamidinium iodide

$FA_{0.85}MA_{0.15}Pb(I_{0.85}Br_{0.15})_3$	Mixed cation (FA/MA) mixed halide (I/Br) perovskite
$FAPbI_3$	Formamidinium lead iodide
FTO	Fluorine-doped tin oxide
GaAs	Gallium arsenide
ITO	Indium-doped tin oxide
MA^+ ($CH_3NH_3^+$)	Methylammonium cation
MACl	Methylammonium chloride
MAI	Methylammonium iodide
$MAPbBr_3$	Methylammonium lead bromide
$MAPbCl_3$	Methylammonium lead chloride
$MAPbCl_xI_{3-x}$	Methylammonium lead iodide of lead chloride precursor
$MAPbI_3$	Methylammonium lead iodide
mc-Si	Monocrystalline silicon
N_2	Dinitrogen
$PbAc_2$ ($Pb(CHCOO)_2$)	Lead acetate
$PbBr_2$	Lead bromide
PbI_2	Lead iodide
pc-Si	Polycrystalline silicon
PCBM	Phenyl-C61-butyric acid methyl ester
PEDOT:PSS	Poly(3,4-ethylenedioxythiophene) polystyrene sulfonate
PEIE	Poly-ethyleneimine ethoxylate
PMMA	Polymethyl methacrylate
Pt	Platinum
Ru	Ruthenium
Si	Silicon
Spiro-OMeTAD	2,2’,7,7’-Tetrakis[N,N-di(4-methoxyphenyl)amino]-9,9’-spirobifluorene
TiO_2	Titanium dioxide

Universal constants

ϵ_0	Vacuum permittivity (8.854×10^{-14} F·cm^{-1})

μ_0	Vacuum permeability (1.257×10^{-8} H·cm^{-1})
c_0	Speed of light in vacuum (2.998×10^{10} cm·s^{-1})
h	Planck constant (6.626×10^{-30} cm^2·kg·s^{-1})
$\hbar$	Reduced Planck constant (1.055×10^{-30} cm^2·kg·s^{-1})
k_B	Boltzmann constant (1.381×10^{-19} cm^2·kg·s^{-2}·K^{-1})
m_0	Electron rest mass (9.109×10^{-31} kg)
q	Elementary charge (1.602×10^{-19} kg)

Symbols common to all chapters

α	Absorption coefficient [cm^{-1}]
$\widetilde{\varepsilon}$	Dielectric function [-]
η	Device related efficiency [-]
θ	Polar angular coordinate [rad]
κ	Imaginary component of refractive index [cm^{-1}]
λ	Wavelength [cm]
μ	Carrier mobility [cm^{2}V^{-1}s^{-1}]
υ	Frequency [Hz]
σ	Gaussian standard deviation [cm]
τ	Lifetime [s]
ϕ_{bb}	Blackbody spectrum [photons·cm^{-2}s^{-1}eV^{-1}]
a	Absorptance [-]
d	Sample thickness [cm]
D, D_n, D_p	Carrier diffusion coefficient [cm^{2}s^{-1}]
D_λ	Photon diffusion coefficient [cm^{2}s^{-1}]
E	Energy [eV]
E_b	Exciton binding energy [eV]
E_C	Conduction band energy [eV]
E_F	Fermi level energy [eV]
E_g	Bandgap energy [eV]
E_{ph}	Photon energy [eV]
E_V	Valence band energy [eV]
EFL	Effective focal length [cm]

EQE	External quantum efficiency [-]
FF	Fill factor [-]
G	Carrier generation rate [$\mathrm{s}^{-1}\mathrm{cm}^{-3}$]
I	Optical intensity [$\mathrm{W{\cdot}m}^{-2}$]
I_0	Reverse saturation current [A]
I_{SC}	Short-circuit current [A]
$J_0^{rad,int}$	Internal saturation current density [$\mathrm{A{\cdot}cm}^{-2}$]
$J_0^{rad,ext}$	External saturation current density [$\mathrm{A{\cdot}cm}^{-2}$]
k	Wavevector [cm^{-1}]
k_1	Monomolecular recombination rate [s^{-1}]
k_2	Bimolecular recombination rate [$\mathrm{s}^{-1}\mathrm{cm}^{3}$]
k_3	Auger recombination rate [$\mathrm{s}^{-1}\mathrm{cm}^{6}$]
L_D	Diffusion length [cm]
L_{D_λ}	Photon diffusion length [cm]
m_C	Effective electron mass [kg]
m_r	Reduced mass [kg]
m_V	Effective hole mass [kg]
n	Electron density [cm^{-3}]
n_r	Real component of refractive index [-]
N_C	Equilibrium electron density [cm^{-3}]
N_V	Equilibrium hole density [cm^{-3}]
NA	Numerical aperture [-]
p	Hole density [cm^{-3}]
P_E	Laser pulse energy [eV]
P_{escape}	Probability of photon escaping the film [-]
P_{stay}	Probability of photon remaining in film [-]
$PLQE$	Photoluminescence quantum efficiency [-]
r	Radial coordinate [cm]
R	Carrier recombination rate [$\mathrm{s}^{-1}\mathrm{cm}^{-3}$]
R_s	Photovoltaic series resistance [Ω]
R_{sh}	Carrier recombination rate [Ω]
t	Time [s]
T	Temperature [K]
V	Electric potential [V]
V_{OC}	Open-circuit voltage [V]
x, y, z	Cartesian spatial coordinates [cm]

LIST OF APPENDICES

CHAPTER 1 INTRODUCTION

Despite making headlines internationally, hybrid organic-inorganic perovskite (HOIP) solar cells are a very recent development in semiconductor research. Consequently, the rise of these materials creates an opening for a disruption of the solar market, and potentially the overall energy industry. Here, we detail the evolution of the solar market leading up to perovskites and conclude with an outline of the thesis focussing on research goals and methodology.

1.1 Background on Solar Energy

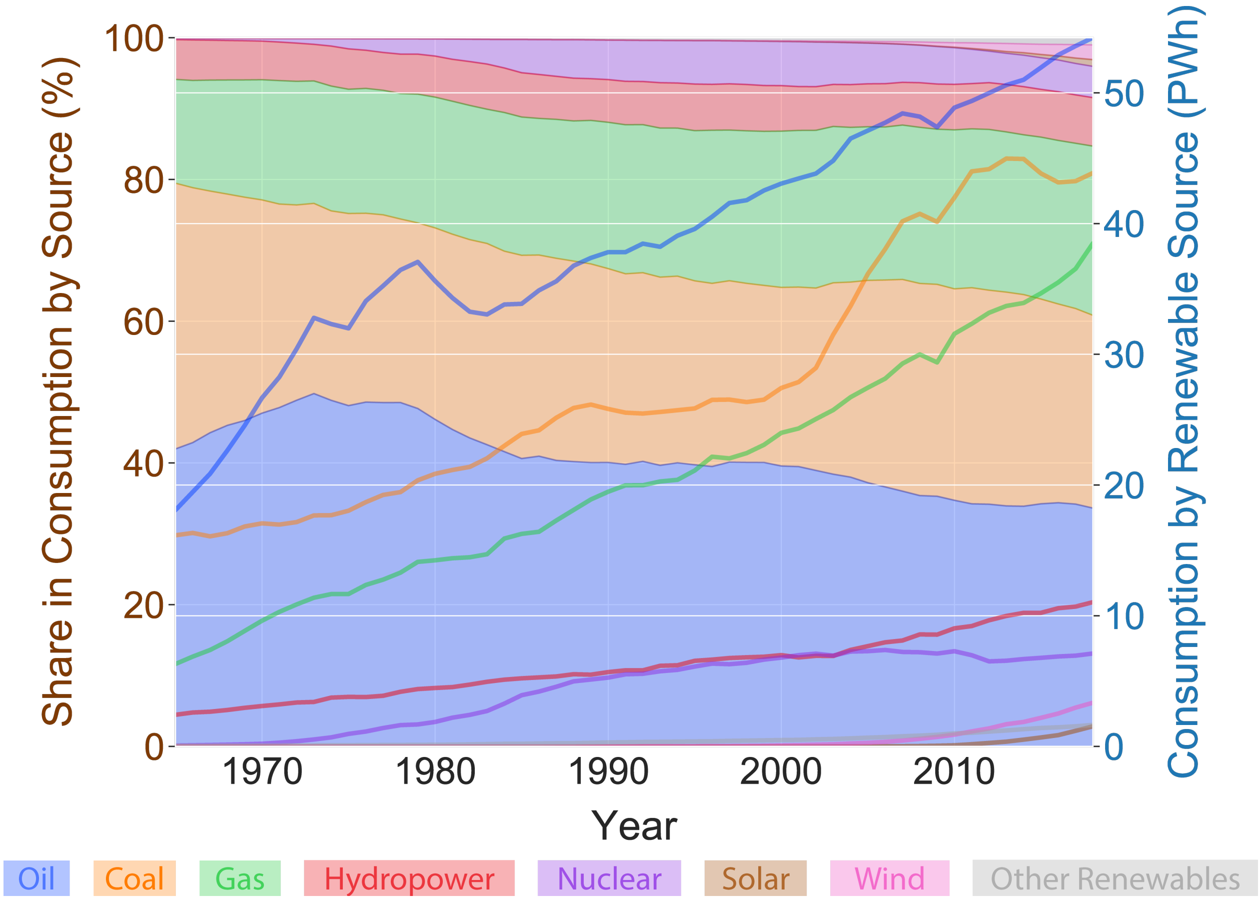

Figure 1.1 Evolution of world energy consumption by fuel source. Data Source: BP [1].

To better understand how perovskite solar cells could potentially shape our future, we first explore the evolution of the energy market over the past two centuries. A historical snapshot of energy consumption as a function of the energy source reveals an interesting picture from today's perspective in terms of sheer technological evolution. In 1850, over 90% of energy consumption came from three sources, which are: fuelwood, human muscle, and animal muscle. Fuelwood and coal, as newer technologies gaining ground at the time, helped to propel humanity through the remaining half of the nineteenth century and the industrial revolution. Subsequently, in the first half of the 20th century, the development of petroleum technologies combined with discoveries of vast fuel reserves across the globe led to the rise of oil as a major shareholder post world war II. This now brings us to Figure 1.1, which shows a snapshot of how the energy industry has since evolved. A careful scan of the figure reveals two important trends: first, the absolute values show an increase in demand across fuel sources and second, the share of fossil fuels demand is steadily decreasing. Consequently, we see a rapidly growing renewable energy market.

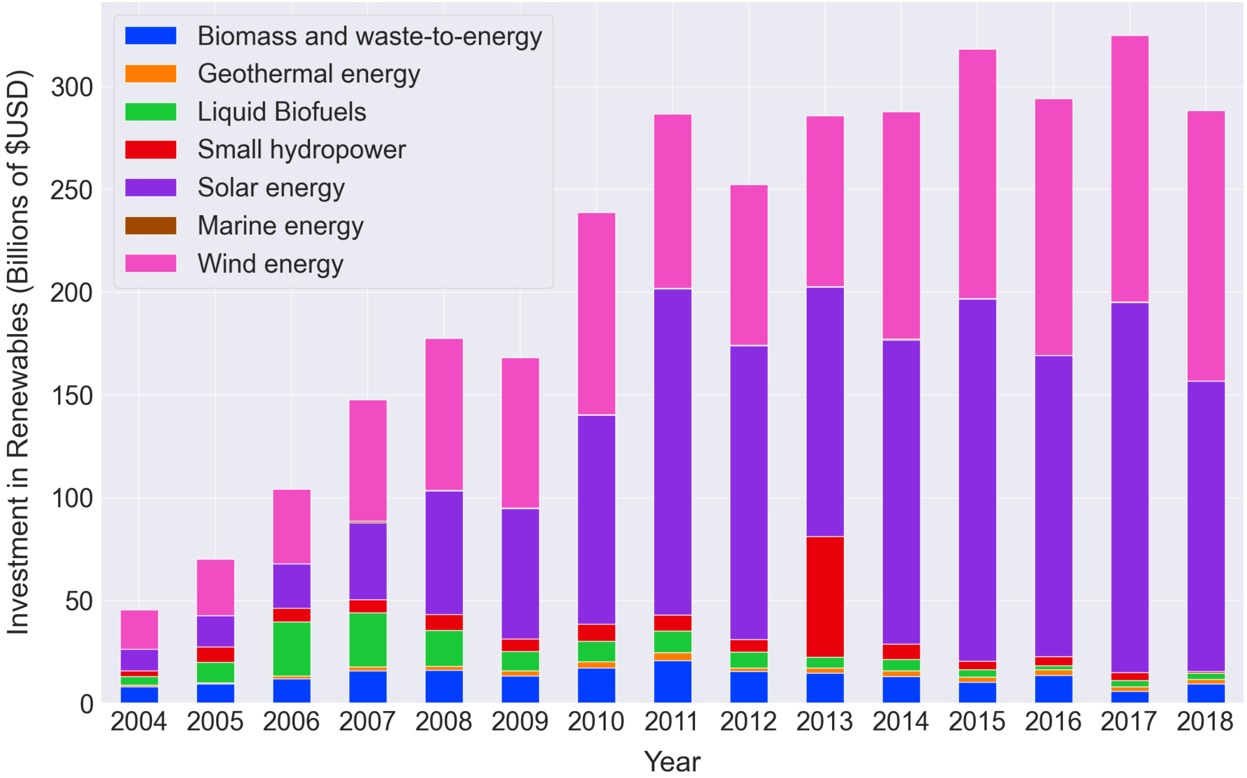

Figure 1.2 Worldwide investments in renewable energy by source. Data Source: IRENA [2].

Although economic reasons might have initially sparked the decline in demand for fossil fuels, there are two main compelling reasons as to why the current transition from fossil fuels to renewables should be forcibly accelerated: paucity and climate change. As per the BP Statistical Review of World Energy 2019 report, we only have 132 years of coal, 51 years of gas and 50 years of oil, respectively left at the current production rate [1]. We must also address the issue of climate which is fraught with many challenges. The observed repercussions globally include warming oceans, shrinking ice sheets, glacial retraction, rising sea levels and ocean acidification. Climate change can occur naturally due to phenomena such as oceanic current variations, increased volcanic activity, changes in solar output or even orbital changes in the planet's motion. Most of the listed consequences, however, are mainly attributed to global warming resulting from increased emission of greenhouse gases emitted via human activity. Despite significant division and lethargy among political entities and governments worldwide to enact on policies, most scientists agree on the need for a response to climate change. Hence, a planned transition towards renewable energy is paramount to ensure sustained activity and growth for all lives on the planet.

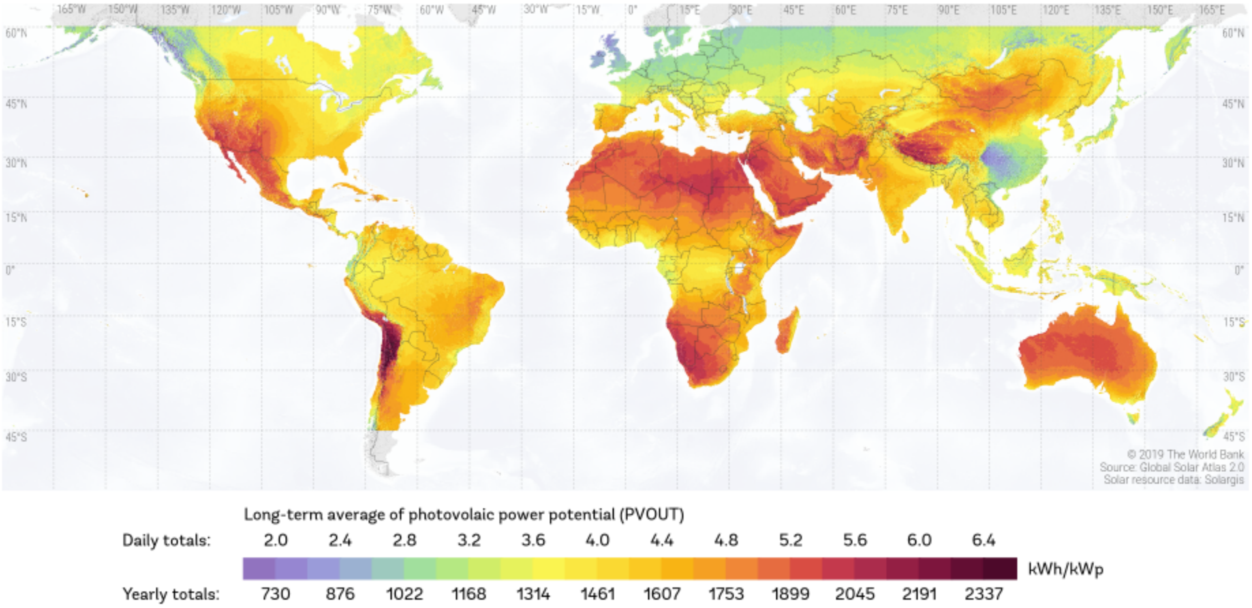

Figure 1.3 Worldwide investments in renewable energy by source. Data Source: Global Solar Atlas 2.0 [3].

Currently, the total share of renewables, excluding hydroelectricity is at a small value of ~4%. The World Energy Investment 2019 report by the International Energy Agency (IEA) does present a silver lining [4]. The power sector accounted for about 40% of total energy investments in 2019, of which more than 80% was directed towards three areas: renewable energy, battery storage/networks and lastly towards improving energy efficiencies in aspects such as grid, transport, and industrial processes, etc. Consequently, we can expect an overall increase of efficiency in generation, conservation, and transport of electricity to significantly contribute towards economic as well as climate goals. Furthermore, the potential for disruption by upcoming unicorn technologies is still unknown. Two examples include the new nuclear reactor which can convert depleted uranium into plutonium (TerraPower LLC), and the artificial intelligence based solar thermal mirror array concentrator (Helios Technologies Inc.). Outliers aside, as shown in Figure 1.2, the largest share of investments in renewable energies are mostly directed towards solar energy in recent years.

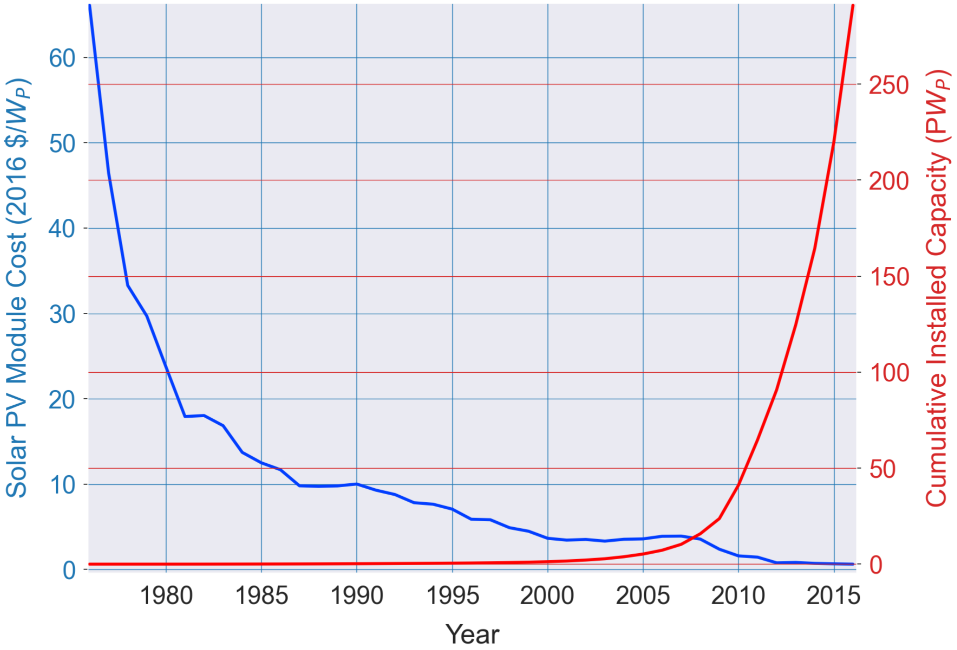

Figure 1.4 Annual trends for photovoltaic module costs versus cumulative installed capacity. Data Source: IRENA [2].

Solar energy is easily accessible to most places on the planet with varying levels of output power potential as shown by Figure 1.3. Countries especially near the tropics receive higher levels of irradiation. Besides, we have seen sizeable investments in places such as in the Kingdom of Saudi Arabia, United Arab Emirates, and India in recent years. Surprisingly, the photovoltaics are also highly attractive for non-equatorial countries like Japan and Germany, which are ranked 3rd and 4th globally in terms of cumulative installed capacity. China is currently ranked 1st while most of the densely populated areas within the country receives significantly lower levels of sunlight. The above indicates that absolute irradiation levels do not necessarily determine the demand for solar energy. What makes solar energy attractive in expanding energy markets is a trend akin to “Moore’s Law” seen in the case of memory chips. The average chip area is seen to shrink by half every year which leads to substantial reduction in costs. In the case of solar panels, similarly, the module cost is seen to drop inversely with the increasing cumulative installed capacity as shown in Figure 1.4. This is economically viable for both large scale investors as well as microgrid communities. Here, the costs savings is largely attributed to continued innovation in three areas: financing, photovoltaic technology, and power grid/storage. In sequence, better financing strategies attract investors towards large scale power projects as well as R&D in both private and public sectors. This drives advancements in photovoltaic design, resulting in panels with high efficiency to installed cost ratios, which combined with improvements in new transport and storage technologies generates profitable returns for investors. This ensures the continued expansion of the solar market.

1.2 Evolution of Photovoltaic Technology

An efficient photovoltaic cell fundamentally has three functions: to generate pairs of positive and negative charge carriers (holes and electrons) from incoming light (photons), then transport these carriers to the electrodes and lastly perform these operations at maximum voltage. Hence most research and development in this field is geared towards optimizing these functions. The first solar cell was a simple *p*-*n* junction demonstrated by Russell Ohl at AT&T-Bell labs in 1939 [5]. Ohl through his experiments, realized that variation in germanium doping in a silicon sample creates an electrical junction allowing the immediate transport of charge carriers to the electrodes. After 14 years, the first functional silicon solar cell of roughly 6% efficiency came into existence at AT&T Bell Labs through the work of Gerald Pearson, Daryl Chapin, and Calvin Fuller.

Solar cells can be categorized into fours generations based on their evolution as depicted in Figure 1.5. Beyond being the first technology to market, silicon also possesses the largest market share at about ~95% of which 66% is occupied by the only first generation technology, i.e. monocrystalline silicon (mc-Si). Monocrystalline silicon remains the most efficient form of silicon technology and is grown in single crystal pillars at 99.9999% purity through float zone (FZ) [6] and Czochralski (CZ) [7] methods. The crystal structure is extremely favorable for stability and carrier transport, allowing peak lab and commercial efficiencies of about 26.7%, and 20.8%, respectively [8, 9].

Moving on to second generation wafer technologies, polycrystalline silicon (pc-Si) is typically made through a process known as directional solidification (DS) in which silicon ingots, obtained through casting, are sliced into wafers. Polycrystalline silicon, unlike mc-Si, possesses a heterogeneous morphology with arbitrarily oriented grains which reduce the overall efficiency through recombination at grain boundaries. Current p-Si cell and module efficiencies crest at 20.8% and 18.5%, respectively [10]. Non-crystalline silicon, also second generation films, come under amorphous (a-Si) or micro-crystalline categories. In terms of thickness, amorphous silicon thin films measure about 200-300 nm, whereas the microcrystalline films fall in the range of several microns (~2 µm). The necessity for extra light trapping/enhancement schemes to compensate for the indirect bandgap of the material is a major drawback of silicon-based technologies. However, six decades of expertise and established technology still plays a significant role in directing consumer choice. Furthermore, conversion of raw silica to usable silicon is a highly pollutive process [11]. In the case of mc-Si, around 93.7% of CO_2 emission, equalling a staggering amount of ~2186 kg eq/kWp [12], is found to occur during the manufacturing process.

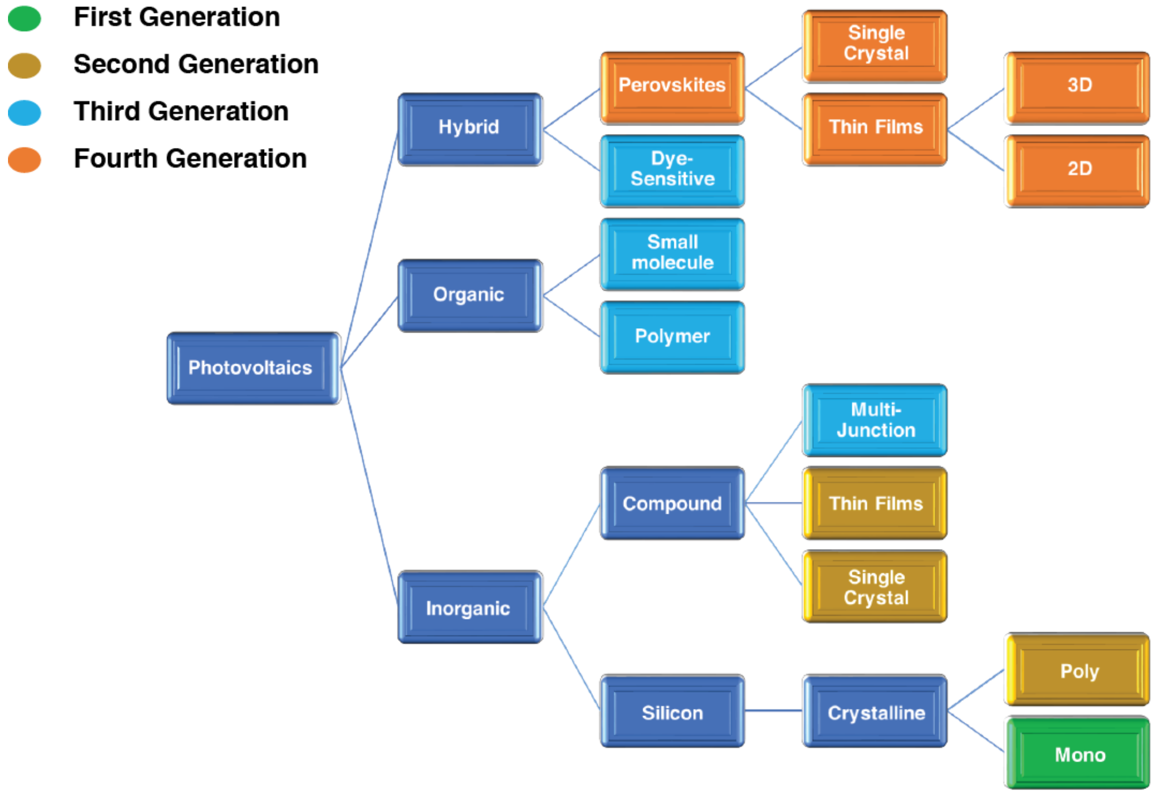

Figure 1.5 Sub-classification of photovoltaics by generation, composition and architecture. Adapted from [13].

Last amongst second generation photovoltaics, we have wafer based technologies such as GaAs followed by thin film compounds such as CdTe, CuInxGa$_{1-x}$Se$_2$ (CIGS) and Cu_2ZnSnS_4 (CZTS). GaAs is the best semiconductor for photovoltaic applications as demonstrated by the highest achieved single-junction efficiency of 29.1% [9]. If it were not for the excessive costs involved in fabrication, GaAs would reign supreme in the solar market due to its direct bandgap and inherently low non-radiative recombination rates that allow for robust light conversion and carrier extraction. Although new techniques such as epitaxial lift-off are being explored at a laboratory level for reducing costs, industrial volume production remains a challenge [14]. Thin films are great alternative to conventional wafer based technologies because of simple fabrication. CdTe, CIGS and CZTS lab efficiencies have been recorded at 21%, 23.4% and 11.0%, respectively [9]. CdTe currently dominates the total photovoltaic market share at 5.7% with CIGS and a-Si lagging behind at 1.6% and 0.2%. With the exception of CZTS, a significant issue hindering the long term potential of these thin films is the alarming scarcity of quintessential elements such as tellurium and indium. Furthermore, in the case of CdTe, toxicity of cadmium is a major concern in terms of legislation. Although CZTS is abundant, charge extraction in these materials remains a challenge due to cation disorder defects. This is also true for the Se based variant of CZTS, i.e. CZTSSe, for which the maximum efficiency is currently 12.6% [9].

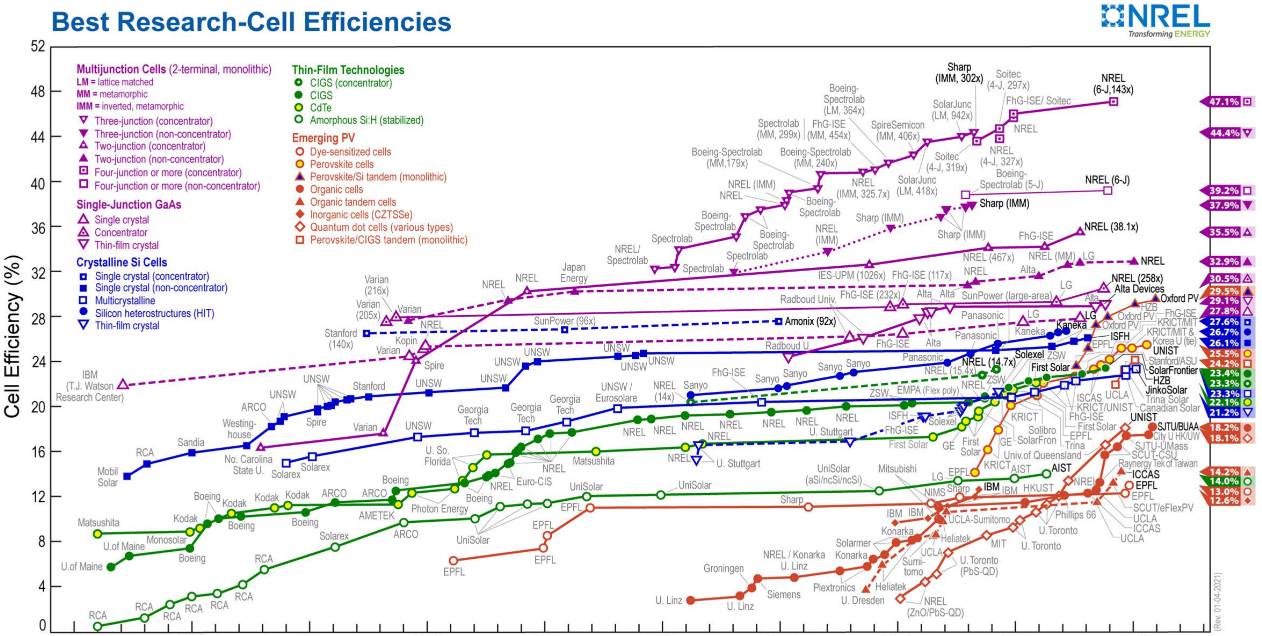

Figure 1.6 NREL photovoltaic efficiency chart [15].

Third generation photovoltaics include organic photovoltaic (OPV) and dye-sensitized solar cells (DSSC) as shown in Figure 1.5. Organic solar cells come under two main formats: single molecules and polymers. Unlike solid-state materials, organic molecules rely on incoherent electron transfer between nearby molecules for charge transport. Furthermore, excitons, or bound electron-hole pairs are initially generated by light, as opposed to free carriers in a crystal structure making OPVs less efficient overall due to the additional driving force needed for exciton dissociation. In the case of DSSCs, the core of the architecture is a mesoporous scaffold (TiO_2) containing absorber dye molecules such as Ruthenium (Ru) or porphyrins embedded in an electrolyte for ionic transportation. DSSC efficiencies currently cap at 12.25% [9]. This concludes our overview of existing PV architectures and we now direct our attention to an important emerging photovoltaic technology that is also the central focus of this thesis: hybrid organic-inorganic perovskites.

1.3 Hybrid Halide Perovskites

Lead halide perovskites have risen rapidly in terms of photovoltaics efficiencies in the past two decades leading to power conversion efficiencies of 25.5% [16]. Continually improving fabrication processes and material engineering have allowed these materials to surpass older generations of solar cells in terms of cost as well as operation [17–21] due to their superior optoelectronic properties [22]. Unique features of the perovskite crystal structure include long diffusion lengths (~1 µm), long lifetimes (low recombination rate), low exciton binding, and lastly a tunable bandgap (~1.5-1.6 eV) close to the Shockley-Queisser maximum efficiency value. Further, due to low recombination, hybrid perovskites exhibit higher short-circuit currents on top of having a photon recycling enhanced open-circuit voltage [23]. These superior I-V characteristics compare well with other highly performing materials such as GaAs [24].

Despite the phenomenal success of lead halide perovskite, little is understood about the physicochemical processes that make them so outstanding. The nature of the photogenerated species, binding energies, as well as recombination pathways are being continuously re-examined [25–41]. An important phenomenon to address, which can guide scientists towards the ideal architecture, is that of charge transport; specifically, diffusion, relates to material structure and composition. Long lifetimes combined with large diffusion lengths lead to easier extraction of the charge carriers in a perovskite solar cell (PSC). The reported values for carrier diffusion in these materials are either calculated or measured through indirect methods [42, 43]. In single crystals, diffusion lengths over 175 microns have been recorded, and the veracity of such claims is still a matter of debate [44]. These large values are attributed to a supposedly low density of trap states measured using hole-only or electron-only device schemes. Beyond diffusion, processes such as photon re-absorption and photon recycling have also been observed in these materials leading to longer lifetimes and increased efficiencies [45]. Hybrid perovskites are a trove for yet to be answered questions about the origin of their outstanding photovoltaic performance. Answering these will require the development of experimental techniques and mathematical models to accurately probe the relevant physical processes.

1.4 Thesis Objectives and Outline

The goals of this thesis revolve around the study of carrier transport in hybrid perovskite solar cells. Our objective therefore is to elucidate the nature of processes such as recombination, diffusion and photon recycling in a select number of hybrid perovskite films using direct innovative experimental techniques combined with analytical methods. Our mission, specifically, is rooted in the two following research questions:

- Research Question 1: What is the in-plane diffusion constant in hybrid perovskites and how does it potentially affect device efficiencies?
  - Sub-objective 1: Build an experimental setup for imaging lateral diffusion.
  - Sub-objective 2: Develop an analytical/statistical model for extracting diffusion constants from experimental data.
  - Sub-objective 3: Interpret the results across varying perovskite compositions.
- Research Question 2: What is the role of photon recycling in hybrid perovskites and how do focussed conditions, as in the case of microscopy measurements, influence apparent diffusion?
  - Sub-objective 1: Design an experimental technique to characterize the spectro-temporal behaviour of luminescence as a function of radial coordinates.
  - Sub-objective 2: Conceive an analytical/numerical model for lateral diffusion while simultaneously accounting for photon recycling.
  - Sub-objective 3: Reconcile observed spatio-spectro-temporal behaviour with modelling results to understand the nature and extent to which photon recycling plays a role in lateral carrier diffusion.

This thesis comprises six chapters, or rather four if one excludes the introduction and the conclusion. Each one builds upon the previous one with the aim to clearly demonstrate the progression of our research in line with the above questions and underlying objectives.

In Chapter 2, we review semiconductor theory with a focus on the basic functions of a solar cell to familiarize the reader to concepts relevant to subsequent chapters and provide context. We review semiconductor notions such as band theory and its relevance to a solar cell. We also go over theoretical derivations of recombination rates, via a semi-classical treatment, as well as transport parameters such as diffusion and mobility. Lastly, we look at the governing equations for solar cells with attention to how transport properties affect device performance.

Chapter 3 focuses on the opto-electronic characteristics of hybrid halide perovskite materials. The purpose of this chapter is to present perovskite specific theory from literature with an aim of acquainting the reader with recent advancements and progression in the field. We also connect concepts presented in Chapter 2 such as energy levels, devices parameters, recombination mechanisms and transport properties to observed results in hybrid perovskites. Lastly, we present a preliminary spatio-temporal study of perovskite photophysics using a streak camera measurement. The results of these measurements form the foundation for the fundamental questions underlying our subsequent in-depth studies.

In Chapter 4, we develop further on the experimental technique introduced in Chapter 3 and specifically address the sub-objectives stated under Research Question 1. Although diffusion along the perpendicular direction is well studied, much yet remains unknown in terms of how in-plane diffusion affects opto-electronic properties. Here, we study lateral diffusion in five perovskite films. In order, they are $\mathrm{MAPbI_3}$, $\mathrm{MAPbI_3}$ (acetonitrile processed), $\mathrm{FAPbI_3}$, $\mathrm{MAPbBr_3}$ and $\mathrm{FA_{0.85}MA_{0.15}Pb(I_{0.85}Br_{0.15})_3}$. The entirety of this chapter is devoted to the extraction of diffusion coefficients from these perovskite films using a combination of streak camera measurement and analytical fitting procedure. Our measurements show unique film morphology dependent spatiotemporal characteristics and diffusion regimes.

Lastly, in Chapter 5, we address the second research question which concerns the role of photon recycling with regards to carrier diffusion. Photon recycling is known to enhance diffusion, and therefore efficiencies as well in other direct bandgap semiconductors such as GaAs. This phenomenon has been reported in perovskites recently although spectral behaviour and impact on in-plane diffusion has not been quantitatively studied. In this chapter, we present a modified streak camera experimental setup for the study of photon recycling and also present a new model encompassing diffusion, carrier dynamics, photon recycling as well as band filling using the absorptive and emissive properties of the perovskite material.

CHAPTER 2 SEMICONDUCTOR THEORY

In this chapter, we review the basics of semiconductor physics and highlight the important aspects needed to understand the thesis and the relevance to hybrid perovskites. The emphasis is on light-matter interaction in semiconductors in the context of photovoltaic applications. The microscopic origins of parameters related to carrier dynamics/transport such as recombination, diffusion and mobility coefficients is discussed. The last section of the chapter details theory pertaining to photon re-absorption and photon recycling.

2.1 Electromagnetic Wave in Thin Film Sample

The wave equation for the electric field in a dielectric medium, obtained via Maxwell's Laws, is described as follows:

$$\nabla^2 \vec{E}(z,t) - \mu_0 \widetilde{\varepsilon} \frac{\partial \vec{E}(z,t)}{\partial t^2} = 0 \tag{2.1}$$

Where μ_0 is the magnetic susceptibility of vacuum. The plane wave solution to the wave equation in Equation 2.1 is given by:

$$\vec{E}(z,t) = Re\{\widetilde{E}(z,E)e^{i\omega t}\} \tag{2.2}$$

Where we write the phasor $\widetilde{E}(z,E)$ for a monochromatic wave of energy E as:

$$\widetilde{E}(z,E) = Ae^{-ik(E)z} \tag{2.3}$$

Where $k = 2\pi/\lambda$ is the wavenumber for wavelength λ and A is the amplitude of the electromagnetic wave. Also, $\widetilde{\varepsilon}$ is the complex dielectric function describing the response of a material to an external electric field $\vec{E}$ with photon energy ($E = h\nu$):

$$\widetilde{\varepsilon}(E) = \varepsilon'(E) + i\varepsilon''(E) \tag{2.4}$$

The real part describes polarization whereas the imaginary component describes gain ($\varepsilon'' > 0$) and absorption ($\varepsilon'' < 0$). The dielectric function is related to the refractive index via $\widetilde{n}^2 = \widetilde{\varepsilon}$. The complex refractive index of the material can be expressed as:

$$\widetilde{n}(E) = n_r(E) + i\kappa(E) \tag{2.5}$$

n_r, the real component is referred to as *refractive index* and κ imaginary part is known as the *extinction coefficient*. We can now establish the following relations: first, the speed of light in free space, c_0, is reduced by n_r to give a phase velocity in the medium $c = c_0/n_r$. Second, the free-space wavelength λ_0 is similarly reduced, i.e. $\lambda = \lambda_0/n_r$. Lastly, the extinction coefficient is related to the absorption coefficient α_0 via $\kappa = \lambda\alpha_0/4\pi$. From the above definitions, the phasor can be re-written as:

$$\widetilde{E}\left(z, E\right) = Ae^{-i2\pi v\widetilde{n}(E)z/c_0} = Ae^{\alpha_0(E)z/2}e^{-i2\pi n_r(E)z/\lambda_0} \tag{2.6}$$

From the definition of the Poynting power, the optical intensity for this plane wave is given by:

$$I\left(z, E\right) = \frac{n_r c_0 A^2}{2} e^{-\alpha_0(E)z} = I_0 e^{-\alpha_0(E)z} \tag{2.7}$$

The above equation describing the exponential decrease of intensity with distance is known as the Beer-Lambert law. For a monochromatic wave incident on a semi-infinite medium, the ratio of the reflected optical power to the incident one, or *Reflectance*, is given by:

$$R(E) = \frac{\left(n_r(E) - 1\right)^2 + \kappa(E)^2}{\left(n_r(E) + 1\right)^2 + \kappa(E)^2} \tag{2.8}$$

In the case of a sample of thickness $z = d$, we can express, the ratio of the transmitted optical power, or *transmittance*, as:

$$T(E) = \left[1 - R(E)\right] e^{-\alpha_0(E)d} \tag{2.9}$$

Consequentially, the ratio of the absorbed to the incident power, or *absorptance*, can also be expressed as $a(E) = 1 - R(E) - T(E)$. Note, that in the case of a fully reflecting backside, we substitute d for $2d$ in the above equation and the resulting absorptance is given by:

$$a(E) = 1 - e^{-2\alpha_0(E)d} \tag{2.10}$$

The dependence of $a(E)$ on α varies with the chosen optical model [45]. In a thin film, we could use the Beer-lambert model ($MAPbI_3$/Reflecting layer), which translates to $a_{BL}(E) = 1 - exp(-2\alpha(E)d)$ as derived in Equation (2.10). Lastly, in the case of a light trapping scheme [46], i.e. (Scattering Layer/$MAPbI_3$/Reflecting layer), we have $a_{LT}(E) = (1 + (4\alpha(E)n_r^2 d)^{-1})^{-1}$ for a sample of thickness d.

2.2 Carrier Dispersion Relations

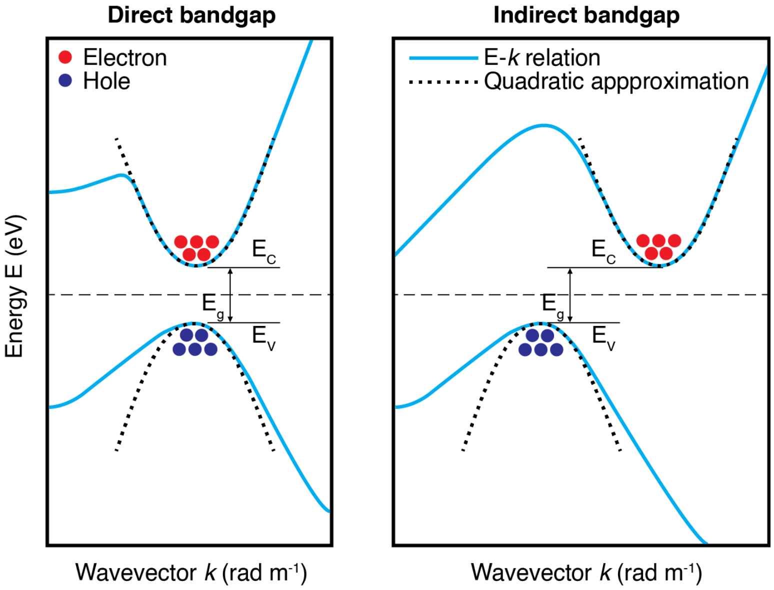

Figure 2.1 a) Direct bandgap semiconductor and b) Indirect bandgap semiconductor. Adapted from [47].

For a given crystal structure, the allowed electronic states are derived from the Schrödinger equation [48]:

$$\left[\frac{-\hbar^2}{2m_0}\nabla^2 + V(r)\right]\psi(r) = E\psi(r) \tag{2.11}$$

Where m_0 is the electron rest mass, $V(r)$ is periodic crystal-lattice potential and E is the energy. As per Bloch's theorem, the solution to this equation is of the form $\psi(r) = u_{nk}(r)e^{ik\cdot r}$, where the quantum numbers n and k identify the energy eigenstate. By solving the above equation, we find the existence of bands, corresponding to each value of n and parametrized by the wavevector k. In a semiconductor, the highest occupied band is called the valence band. Beyond this band, an energy gap exists before the first unoccupied band. Quantitatively, this bandgap is situated between the upper limit of the "valence" ($E > E_V$) and the lower limit of the "conduction" ($E < E_C$) bands. The wavefunctions at the band edges determine fundamental opto-electronic properties of a semiconductor such as transition dipole moment giving rise to absorption and emission. From wave mechanics, the quadratic approximation $E = \hbar^2k^2/2m^*$, where m^* is the effective mass, can be used near the edge of the bands to express the dispersion relation. A material in which the minima of the conduction and valence bands coincide at a k value is known as direct bandgap semi-conductor; else, it is an indirect bandgap semiconductor. The E-k diagram for an arbitrary semiconductor is shown in Figure

2.1 for the both cases. Based on Figure 2.1, we can re-express the quadratic approximation as:

$$E = E_C + \hbar^2 k^2/2m_C \tag{2.12}$$

$$E = E_V - \hbar^2 k^2/2m_V \tag{2.13}$$

Where $E_C = E_V + E_g$. Also, m_C and m_V are the negative and positive carrier effective masses, which, unlike the free electron mass m_0, account for the lattice potential contribution. The general definition of the effective carrier mass follows a tensorial form and is given by $m_{ij}^{-1} = (1/\hbar^2)\partial^2 E(k)/\partial k_i \partial k_j$. This definition for the effective mass provides one perspective to the source of differing properties between the negative and positive charge carriers, also known as "electrons" and "holes", found in the conduction and valence bands.

2.3 Carrier Concentrations

To determine the concentration of electrons and holes in a semiconductor, we need to know the density of states (DOS). Given an infinite three-dimensional rectangular potential, the density of states ϱ is defined as [47]:

$$\varrho\,(k) = \frac{k^2}{\pi^2} \tag{2.14}$$

Using $\varrho\,(k) = \varrho(E)dE/dk$, we then write $\varrho\,(k)$ as a function of E instead of k. dE/dk is derived from Equations (2.12) and (2.13) for carriers and holes separately and after substituition in (2.14) we obtain:

$$\varrho_C(E) = \frac{(2m_C)^{3/2}}{2\pi^2\hbar^3}\sqrt{E - E_C}\ , \qquad E \geq E_C \tag{2.15}$$

$$\varrho_V(E) = \frac{(2m_V)^{3/2}}{2\pi^2\hbar^3}\sqrt{E_V - E}\ , \qquad E \leq E_V \tag{2.16}$$

Here, the square root dependence is a consequence of the quadratic band-edge approximation. We now find the energy level probability of occupancy.

In thermal equilibrium, the probability for an electron to occupy a given energy level is given by the Fermi-Dirac distribution (Figure 2.2b):

$$f(E) = \frac{1}{e^{\frac{E-E_F}{k_B T}} + 1} \tag{2.17}$$

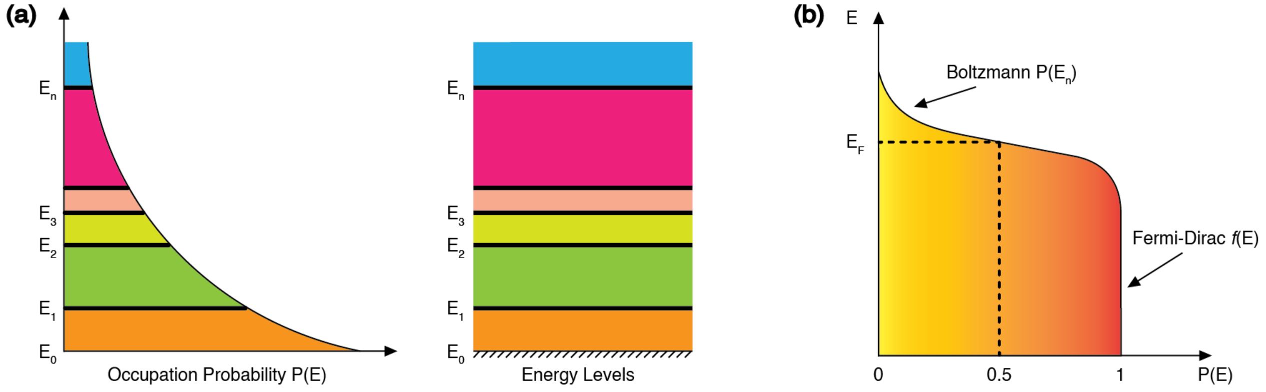

Figure 2.2 a) Direct bandgap semiconductor and b) Indirect bandgap semiconductor. Adapted from [47].

Here, E_F is the Fermi energy. Conversely, given $f(E)$, $1 - f(E)$ is then given by:

$$1 - f(E) = \frac{e^{\frac{E-E_F}{k_B T}}}{e^{\frac{E-E_F}{k_B T}} + 1} \tag{2.18}$$

These distributions are shown in Figure 2.2. It is well noticeable in panel b that the Fermi-Dirac distribution can be modelled as a Boltzmann distribution when $E \gg E_F + 3k_BT$. We can use the above relation to calculate either n, the electron density, or p, the hole density, based on the knowledge of the other. Using the DOS and Fermi-Dirac distribution, we can finally compute the carrier concentrations using the following integrals:

$$n = \int_{E_C}^{\infty} n(E)dE = \int_{E_C}^{\infty} \varrho_C(E) f_C(E)dE = N_C F_{1/2}\left(\frac{E_{F,C} - E_C}{k_B T}\right) \tag{2.19}$$

$$p = \int_{-\infty}^{E_V} p(E)dE = \int_{-\infty}^{E_V} \varrho_V(E) f_V(E)dE = N_V F_{1/2}\left(\frac{E_V - E_{F,V}}{k_B T}\right) \tag{2.20}$$

Here, $F_{1/2}(x)$ is the Fermi-Dirac integral of order ½, $N_{C/V} = 2(2\pi m_{C/V} k_B T/h^2)^{3/2}$ and $E_{F,C/V}$ is the electron/hole quasi-Fermi energy level used to account for non-equilibrium conditions. Here, n_i is the intrinsic carrier concentration. A semiconductor's initial lattice structure can be "doped" to have higher concentrations for either holes (p-type) or electrons (n-type). In n-type extrinsic semiconductors, we have $E_{F,C} - E_C > E_V - E_{F,V}$, as opposed to $E_{F,C} - E_C < E_V - E_{F,V}$ in p-types. A semiconductor is nondegenerate when the quasi-Fermi levels lie within $E_V + 3k_BT$ and $E_C - 3k_BT$ region. In such a case, we can use an approximation for the Fermi-Dirac function, i.e. $f(E) \approx e^{-(E-E_F)/k_BT}$, in Equations (2.19) and (2.20) and obtain:

$$n \approx N_C e^{(E_F - E_C)/k_B T} \tag{2.21}$$

$$p \approx N_V e^{-(E_F - E_V)/k_B T} \tag{2.22}$$

Where E_F is given by:

$$E_F = \frac{1}{2}\left(E_{F,C} + E_{F,V}\right) + \frac{1}{2} k_B T ln \left(\frac{N_V}{N_C}\right) \tag{2.23}$$

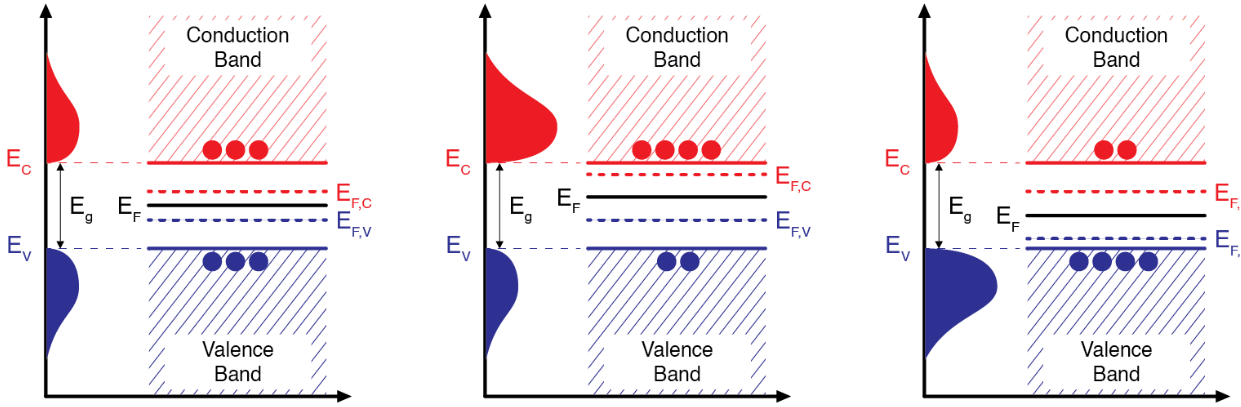

Figure 2.3 a) Direct bandgap semiconductor and b) Indirect bandgap semiconductor. Adapted from [47].

The law of mass action states that the product of the hole and electron concentrations remains constant as follows:

$$np = n_i^2 = N_C N_V e^{-E_g k_B T} \tag{2.24}$$

However, when the semiconductor is degenerate, we must use the full integral definitions shown in Equations (2.19) and (2.20) to find the carrier concentrations and the law of mass action no longer holds good. Figure 2.3 shows carrier concentrations for different values of the Fermi energy. We can see that the n and p concentrations are equal for the intrinsic condition in panel a. In panels b and c, when the Fermi energy is increased/lowered, the conduction/valence band becomes more populated.

The doping process alterates the Fermi level by introducing interstitial or substitutional impurities to the crystal lattice. The former involves in inserting an impurity atom between existing atoms while the latter replaces a host atom resulting in extra electrons from N_D^+ ionized donors concentration or extra holes from N_A^- ionized acceptors concentration. Table 2.1

Table 2.1 Carrier density approximations and Fermi levels for extrinsic semiconductors

n-type	p-type
Density Equations: $n = N_C F_{1/2}\left(\frac{E_{F,C}-E_C}{k_B T}\right)$ $p - n + N_D^+ = 0$	Density Equations: $n = N_C F_{1/2}\left(\frac{E_{F,C}-E_C}{k_B T}\right)$ $p - n + N_D^+ = 0$
Approximations considering $n \gg p$: $N_D^+ \approx N_D$ $n \approx N_D$ $p \approx \frac{n_i^2}{N_D} \ll n$	Approximations considering $p \gg n$: $N_A^- \approx N_A$ $p \approx N_A$ $n \approx \frac{n_i^2}{N_A} \ll p$
Fermi Level: $E_{F,C} = E_C + k_B T ln\left(\frac{N_D}{N_C}\right)$	Fermi Level: $E_{F,V} = E_V - k_B T ln\left(\frac{N_A}{N_V}\right)$

shows the commonly used approximations for carrier densities as well as Fermi levels in extrinsic or doped semiconductors. In the density equations, we have also included conservation of charge through Poisson's equation:

$$\vec{\nabla}_x \cdot \tilde{\varepsilon}(-\vec{\nabla}_x V) = q(p - n \ + N_D^+ - N_A^-) \tag{2.25}$$

Where V is the potential in the junction and $\tilde{\varepsilon}$ is the dielectric function. $N_D^+ \approx N_D$ and $N_A^- \approx N_A$ specify that not all donors (N_D) and acceptors (N_A) get ionized, but most do. The table and approximations are well suited to model non-degenerate conditions, as found in actual devices. However, these approximations are no longer valid for high injection regimes where the ambipolar model, presented in subsequent sections, is better suited.

2.4 Absorption and Emission

In this section, we look at the different electronic transitions that lead to absorption and emission of light. Particularly, we derive expressions for the transition rates which play an important role in determining semiconducting properties of a given material.

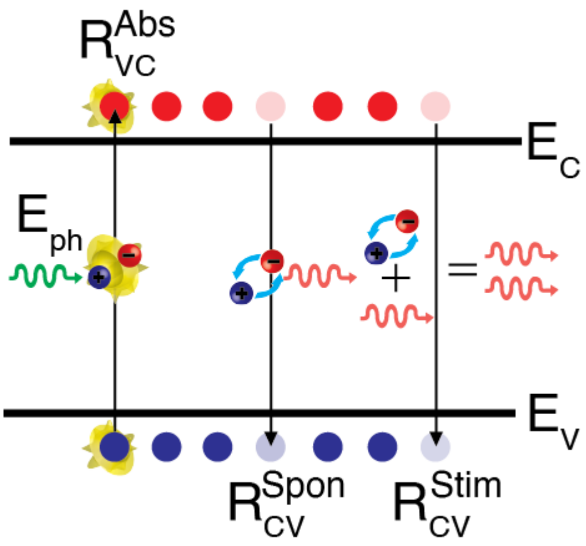

Figure 2.4 The three main transitions occurring in a semiconductor: absorption, spontaneous emission and stimulated emission.

To understand the interaction of semiconductors with light, let us consider two energy levels E_1 (valence band) and E_2 (conduction band) as well as a photon of energy $E = h\upsilon$. The following rules govern interactions occurring between the photon and carrier transitioning between the two energy levels:

- Conservation of energy: $E_2 = E_1 + E$
- Conservation of momentum (k selection rule): $p_2 = p_1 + h/\lambda$ or $k_2 = k_1 + 2\pi/\lambda$
- Carriers and photons interact only under specific energy-momentum conditions. From Equations (2.12) and (2.13) we can establish:

  $$E_2 - E_1 = \left(E_C + \frac{\hbar^2 k^2}{2m_C}\right) - \left(E_V - \frac{\hbar^2 k^2}{2m_V}\right) = E_g + \frac{\hbar^2 k^2}{2}\left(\frac{1}{m_C} + \frac{1}{m_V}\right) = E_g + \frac{\hbar^2 k^2}{2m_r} = h\upsilon \tag{2.26}$$

  Where we use the reduced mass, defined as:

  $$m_r = \left(\frac{1}{m_C} + \frac{1}{m_V}\right)^{-1} \tag{2.27}$$

The absorption at thermal equilibrium is then given by [48]:

$$\alpha_0(E) = K\left|\hat{e} \cdot \boldsymbol{p}_{CV}\right|^2 \int \frac{2d^3k}{(2\pi)^3} \delta\left(E_g + \frac{\hbar^2 k^2}{2m_r} - E\right) \tag{2.28}$$

Solving analytically and expressing in terms of dipole moment $\boldsymbol{p}_{CV} = \boldsymbol{\mu}_{CV}(im_0E_{CV}/\hbar e)$, we can now write the above equation as:

$$\alpha_0(E) = \left(\frac{\pi E}{n_r c \varepsilon_0 \hbar}\right) |\hat{e} \cdot \boldsymbol{\mu}_{CV}|^2 \varrho(E) \tag{2.29}$$

Where $\varrho(E)$ is the joint density of states expressed as:

$$\varrho(E) = \frac{(2m_r)^{3/2}}{2\pi^2\hbar^3}\sqrt{E - E_g}\ , \qquad E \geq E_g \tag{2.30}$$

For non-equilibrium conditions, we include the Fermi inversion factor $(f_V - f_C)$ as shown below to obtain the complete expression for optical absorption in semi-conductors:

$$\alpha(E) = \alpha_0(E)(f_V - f_C) \tag{2.31}$$

An electron in the conduction band (E_2) can transition downwards towards to valence band (E_1), leading to emission of a photon of energy $E = E_2 - E_1 = h\upsilon$. We can establish the following relation between the total transition rates of the three processes depicted in Figure 2.4:

$$R_{VC}^{abs} = R_{CV}^{spon} + R_{CV}^{stim} \tag{2.32}$$

Emission can occur in two ways: spontaneous or stimulated. Stimulated emission is the process in which an incoming photon instigates the downward transition of an excited carrier, resulting in an additional photon. Stimulated emission, therefore, depends on the incoming photon density unlike the case of spontaneous emission, where a downward transition occurs naturally independent of external photons. The resulting spectral rate equations are shown below [49].

$$r_{CV}^{spon} = \left(\frac{8\pi n_r^2 E^2}{h^3 c_0^2}\right) \frac{\alpha(E)}{\left(e^{\frac{E_{21}-E_{F,21}}{k_B T}} - 1\right)} = \left(\frac{8\pi n_r^2 E^2}{h^3 c_0^2}\right) \frac{\alpha(E) f_C (1 - f_V)}{(f_V - f_C)} \tag{2.33}$$

$$r_{VC}^{abs} = \left(\frac{8\pi n_r^3 E^2}{h^3 c_0^3}\right) \alpha(E) \tag{2.34}$$

$$r_{CV}^{stim} = \left(\frac{8\pi n_r^3 E^2}{h^3 c_0^3}\right) g(E) \tag{2.35}$$

Under high excitation, i.e. $f_C > f_V$, $\alpha(E)$ becomes negative and leads to gain, i.e. $g(E) = -\alpha(E)$, and emission is the dominant mechanism. Consequently, the stimulated emission spectrum is simply by the additive inverse of the absorption spectrum. The total rates shown in Equation (2.32) are obtained by integrating the equations above over the whole energy spectrum E, i.e.:

$$R_{CV}^{spon} = \int r_{CV}^{spon} dE \tag{2.36}$$

$$R_{VC}^{abs} = \int r_{VC}^{abs} dE \tag{2.37}$$

$$R_{CV}^{stim} = \int r_{CV}^{stim} dE \tag{2.38}$$

The above terms form the base of carrier dynamics, which will be discussed in the subsequent sub-sections. We can get an expression for the relation between emission and absorption through the van Roosbroeck-Shockley equation [50]. Unlike the results above, which find their roots in a semiclassical treatment, here the rates are derived through the principle of detailed balance: under thermal equilibrium, the total rate of carrier recombination must equal the total rate of electron-hole pair generation due to thermal generation over a given energy range, and can be written as [45]:

$$R_{vR-S,\ eq.} = \ G_{thermal.\ eq.} = \frac{1}{n_i^2} \int_0^\infty 4\alpha(E) n_r^2(E) \phi_{bb}(E) dE \tag{2.39}$$

Where $\phi_{bb}(E)$ is the Planck black body spectrum for an emitter under equilibrium conditions:

$$\phi_{bb}(E) = \frac{2\pi E^2}{h^3 c^2} \frac{1}{e^{\frac{E}{k_B T}} - 1} \tag{2.40}$$

Adjusting for non-equilibrium conditions via $np/n_i^2 = e^{\Delta E_F / k_B T}$, the van Roosbroeck-Shockley relation becomes:

$$R_{vR-S} = R_{vR-S,\ eq.} np = R_{vR-S,\ eq.}\ e^{\frac{\Delta E_F}{k_B T}} = \int_0^\infty 4\alpha(E) n_r^2(E) \phi_{bb}(E) e^{\frac{\Delta E_F}{k_B T}} dE \tag{2.41}$$

This equation is useful when one needs to find the recombination rate using experimental information alone, i.e. the absorption spectrum for a given material. From the radiative recombination rate, we can also calculate the current density that is generated internally within a semiconductor. Assuming uniform generation along z, the internal dark saturation current density $J_0^{rad,int}$ at equilibrium can be found by integrating over the thickness d of a film as follows:

$$J_0^{rad,int} = q\int_0^d G_{thermal.\ eq.}dz = qdG_{thermal.\ eq.} = qd\int_0^\infty 4\alpha(E)n_r^2(E)\phi_{bb}(E)dE \tag{2.42}$$

The dark saturation current can then be obtained from the equation above by integrating over a given area.

$$I_0^{rad,int} = \iint J_0^{rad,int}dA \tag{2.43}$$

The above current term will be later used when explaining the photovoltaic properties of semiconductors. For non-equilibrium conditions, we include $e^{\Delta E_F/k_BT}$ term in the integral of Equation (2.42).

$$J^{rad,int} = qd\int_0^\infty 4\alpha(E)n_r^2(E)\phi_{bb}(E)e^{\frac{\Delta E_F}{k_BT}}dE \tag{2.44}$$

In this section, we have derived an expression for an ideal current based on the radiative recombination rate and material absorption ignoring non-radiative processes and other loss mechanisms. This will serve as reference for comparing currents from actual devices in future sections.

2.5 Generation of Charge Carriers

Under optical excitation, we can calculate the generation rate of charge carriers from the absorption coefficient α and the incident spectral irradiance $I(x, y, t, E)$. Assuming a constant intensity in x, y, and t, $I(x, y, t, E)$ can be reduced to $I = I_0(E)$ (W·cm^{-2}eV^{-1}). We have shown in Section 2.1 that incident light intensity decreases exponentially as $I_0(E)e^{-\alpha z}$ for Beer-Lambert absorption. Hence, the incident photon flux as a function of z can be written as:

$$\phi_{inc}(z, E) = \phi_0(E)e^{-\alpha z} = \frac{I_0(E)}{E}e^{-\alpha z} \tag{2.45}$$

Where $\phi_0(E)$ (photons $\cdot$ cm^{-2}s^{-1}eV^{-1}) is obtained by dividing I_0 (J $\cdot$ cm^{-2}s^{-1}eV^{-1}) with the photon energy $E = hc/\lambda$ (J/photon). We obtain an expression for the generation rate $G(z, E)$:

$$G(z, E) = -\frac{d\phi_{inc}(z, E)}{dz} = \alpha(E)e^{-\alpha(E)z}\phi_0(E) \tag{2.46}$$

The above equation tells us that $\alpha(E)$ is critical for efficient generation. For high $\alpha(E)$, most of the absorption and subsequent generation can occur at surface. Otherwise, a very thick device or a reflecting back surface is required to capture the entirety of the incident light.

We can also consider the case for a Gaussian laser pulse where we have dependence in x, y and t and independence along z (no Beer-Lambert absorption) as derived in Appendix A. For such a scenario, we get the following result:

$$G(r,t) = \frac{\alpha P_E}{E_{ph}(2\pi)^{3/2}\sigma_L^2\sigma_\tau} \cdot e^{-\frac{r^2}{2\sigma_L^2}} \cdot e^{-\frac{(t-t_0)^2}{2\sigma_\tau^2}} \cdot e^{-\alpha z} \tag{2.47}$$

Where P_E is the pulse energy, σ_L the laser spatial profile standard deviation and σ_τ the pulse standard deviation. The above equation is useful for modelling carrier dynamics in the 2D plane in conjunction with photoluminescence measurements.

2.6 Recombination Mechanisms

There are three main recombination mechanisms that occur in semiconductors [51]. The first recombination mechanism, i.e. Shockley-Read-Hall (SRH) or trap-assisted recombination, occurs due to defects and impurities, allowing for energy levels to exist within the forbidden bandgap. Such a forbidden level acts as an electron trap if:

- When empty, the probability for an electron to be captured from the conduction band is higher than the probability of being captured from the valence band.
- When occupied, the probability for an electron to be released into the conduction band is higher than the probability of a release into the valence band.

The same holds true for hole traps where the holes are more likely to be captured from or released into the valence band. However, there are special traps, usually situated in the middle of the bandgap, called recombination centers. In such a case, transitions for both holes and electrons in either direction is equiprobable. These transitions are demonstrated in panel a of Figure 2.5. The net transition rate for the trap assisted processes can be expressed as [51]:

$$U_{SRH} = \sigma\vartheta_{th}N_t \frac{(np - n_i^2)}{n + p + 2\cosh\left(\frac{E_T - E_{F,i}}{k_B T}\right)} \tag{2.48}$$

Where σ represents the capture cross section (in cm^2), ϑ_{th} the thermal velocity of carriers (in cm/sec), N_t the concentration of traps (in cm^{-3}/sec), E_T the trap energy (in eV) and $E_{F,i}$ the intrinsic Fermi energy (in eV). In Equation (2.48), n and p can be expressed as $n = n_0 + \delta n$ and $p = p_0 + \delta p$; where n_0 and p_0 are the initial carrier densities while δn and δp the excess injected densities. For non-degenerate semiconductors, the mass-action law stipulates that $np = n_0p_0 = n_i^2$ in thermal equilibrium, wherein n_i is the intrinsic concentration of holes and electrons in the semiconductor. In an n-type semiconductor, $(np - n_i^2)$ can be simplified to $(n_0 + \delta n)(p_0 + \delta p) - n_i^2 \approx n_0\delta p$ considering $n_0 \gg \delta n$. The denominator of Equation (2.48) would similarly reduce to $n+p+2\cosh((E_T-E_{F,i})/k_BT) \approx n_0$ as $n \gg p$ and $n \gg 2\cosh((E_T-E_{F,i})/k_BT)$. Hence for an n-type, Equation (2.48) can be approximated as:

$$U_{SRH,n-type} = \sigma_h\vartheta_{th}N_t\delta p = \tau_{n-type}^{-1}\delta p = k_{1,n}\delta p \tag{2.49}$$

The rate is clearly dependent on the increase in minority carriers and the concentration of traps in the material. Repeating the same procedure for p-type semiconductors, we obtain:

$$U_{SRH,p-type} = \sigma_e\vartheta_{th}N_t\delta n = \tau_{p-type}^{-1}\delta n = k_{1,p}\delta n \tag{2.50}$$

The second recombination mechanism shown in panel b of Figure 2.5, i.e., band-to-band, is the decay process in which an electron in the conduction band directly recombines with a hole in the valence band. The energy is released from this process through radiation as a photon. The recombination rate can be expressed as [51]:

$$R_{b-b} = k_2np \tag{2.51}$$

Where R_{b-b} is the recombination rate (or R_{CV}^{spon} found in previous section), k_2 is the band-to-band recombination coefficient (in cm^3/sec), n is the total concentration of electrons (in cm^{-3}/sec) and p is the total concentration of holes (in cm^{-3}/sec). The net recombination rate in non-equilibrium conditions, i.e. the difference between recombination and generation rates $U_{b-b} = R - G_{thermal\ eq.}$ can be expressed as [51, 52]:

$$U_{b-b} = k_2(np - n_i^2) \tag{2.52}$$

Where n_i is the intrinsic charge carrier concentration. Band-to-band recombination can be monomolecular or bimolecular depending on the injection levels δn and δp. This is demonstrated below:

$$U_{b-b} = k_2\left((n_0 + \delta n)(p_0 + \delta p) - n_i^2\right) \tag{2.53}$$

$$U_{b-b} = k_2\left(\delta n\delta p + \delta n p_0 + \delta p n_0 + n_0p_0 - n_i^2\right) \tag{2.54}$$

For $\delta n = \delta p$, that is equal injection of electrons and holes, and $n_0 p_0 = n_i^2$:

$$U_{b-b} = k_2 \delta n^2 + k_2 \delta n (p_0 + n_0) \tag{2.55}$$

We can see for low injection (LI), the term on the left will be negligible, and a monomolecular recombination with linear dependence on injection ensues.

$$U_{b-b,LI} = k_2 \delta n (p_0 + n_0) = k_{2,low} \delta n \tag{2.56}$$

Whereas at high injection (HI), the term on the right can be ignored and instead a quadratic dependence on injection is obtained. This is the bimolecular recombination regime, i.e.:

$$U_{b-b,HI} = k_2 \delta n^2 \tag{2.57}$$

The third and final recombination mechanism, i.e. Auger recombination, is a third order non-radiative process known to occur at higher levels of pumping. An electron and a hole undergo normal band-to-band transition and give the excess energy off to a third particle, another hole or electron. The excited third particle subsequently relaxes through thermalisation [52].

$$U_{Aug} = (K_p p + K_n n) \left(np - n_i^2 \right) = K_p p \left(np - n_i^2 \right) + K_n n \left(np - n_i^2 \right) \tag{2.58}$$

Where K_p and K_n are the Auger recombination coefficients for holes and electrons, respectively. This recombination mechanism is illustrated in panel c of Figure 2.5. This equation is quite similar to the band-to-band transition Equation (2.52) with exception to the terms on the left corresponding to the third particle receiving the released energy. At high injection, where $n_0, n_i \ll \delta n$ and $\delta n = \delta p$, we can simplify Equation (2.58) to:

$$U_{Aug,HI} = k_3 \delta n^3 \tag{2.59}$$

We can now re-unify all three mechanisms under a single net recombination rate at high injection as follows:

$$R_{Total,HI} = U_{SRH} + U_{b-b,HI} + U_{Aug,HI} = k_1 \delta n + k_2 \delta n^2 + k_3 \delta n^3 \tag{2.60}$$

The usage of this equation in an applied context will be discussed further in subsequent sections. Lastly, we define the photoluminescent quantum efficiency ($PLQE$) of a material

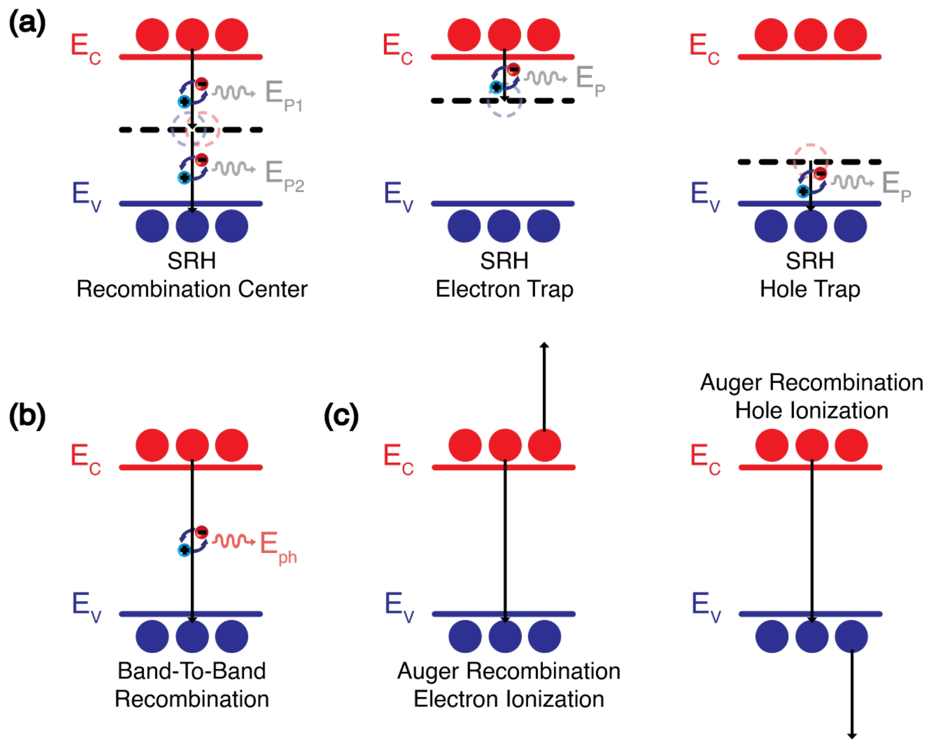

Figure 2.5 Diagram of semiconductor recombination mechanisms showing in (a) SRH recombination where energy is emitted through phonons (E_P), (b) Band-To-Band recombination where energy is emitted as a photon (E_{ph}) and (c) Auger recombination. Adapted from [53, 54].

as follows:

$$PLQE = \frac{k_{rad}}{k_{rad} + k_{non-rad}} = \frac{k_2 \delta n}{k_1 + k_2 \delta n + k_3 \delta n^2} \tag{2.61}$$

The $PLQE$ of a material provides a ratio which allows us to measure the strength of the bimolecular recombination within a material. A high $PLQE$ is an indicator of a high level of photoluminescence and this parameter is particularly critical for efficiencies of light-emitting diodes. For solar cells, carrier diffusion and mobility are paramount, although $PLQE$ can boost performance by contributing to processes such as photon recycling. More on this will follow in subsequent sections.

2.7 Diffusion of Charge Carriers

Free carriers in a solid behave similarly to molecules in the gas phase. Boltzmann studied the statistical mechanics of gases and the equation he found, applied to the case of charge carriers, can be expressed as [55]:

$$\frac{\partial f}{\partial t}+\frac{\vec{F}_{ext}}{\hbar}\cdot\vec{\nabla}_k f+\vec{v}\cdot\vec{\nabla}_x f=-\frac{(f-f_0)}{\tau} \tag{2.62}$$

$\vec{v}$ is the carrier velocity and $f(k,x,t)$ is a probability distribution function for a carrier under non-equilibrium conditions for momentum k, position x and time t. Similarly, f_0 corresponds to the equilibrium case. The main components of this equation are an external force ($\vec{F}_{ext}$) term, a diffusion term ($\vec{\nabla}_x f$) and a collision term, shown on the right side with collision time τ. Using the method of moments, which consists of multiplying each term in Equation (2.62) by a moment generating function $\Theta^l(k)$ of order l and subsequently integrating over k as follows:

$$\int\Theta^n(k)\frac{\partial f}{\partial t}dk+\int\Theta^n(k)\frac{\vec{F}_{ext}}{\hbar}\cdot\vec{\nabla}_k f dk+\int\Theta^n(k)\,\vec{v}\cdot\vec{\nabla}_x f dk=-\int\Theta^n(k)\frac{(f-f_0)}{\tau}dk \tag{2.63}$$

The complete derivation of the continuity equations as well as the drift-diffusion equation can be found in literature [55]. Some of the main assumptions are:

- Parabolic band-structure, i.e. $E=\hbar^2k^2/2m$
- Isotropic material for energy and temperature, i.e. $\vec{\nabla}_x T=0$ and $\vec{\nabla}_x E=0$
- Isotropic and constant mass m, i.e. $m=m_x=m_y=m_z$

Using $\Theta=\vec{v}$ and $l=1$, the equation below is obtained:

$$\frac{\partial(n\vec{v})}{\partial t}-\frac{\vec{F}_{ext}}{m}n+\frac{k_BT}{m}\vec{\nabla}_x n=\frac{-n}{\tau} \tag{2.64}$$

In the above equation, n the carrier concentration, while q is the electronic charge. We multiply the above equation by $-q$, substitute the force term $\vec{F}_{ext}$ by a field term ($-q\vec{F}$) and reshuffle the terms to obtain [55]:

$$\frac{\partial(-\tau qn\vec{v})}{\partial t}-qn\vec{v}=\frac{\tau q^2\vec{F}}{m}n+\frac{q\tau k_BT}{m}\vec{\nabla}_x n \tag{2.65}$$

We now have the drift-diffusion equation for the n-type carrier where the current density vector is given by $J_n=-qn\vec{v}$. We also find two important material properties: first, the electron mobility given by $\mu=q\tau/m$ and second, the diffusion constant given by $D=\tau k_BT/m$. In the latter, we can notice that mobility and diffusion are linked through the

Einstein relation [55]:

$$D = \frac{\mu k_B T}{q} \tag{2.66}$$

The terms drift and diffusion are respectively related to concepts of field-induced versus concentration gradient-induced motion. Diffusion will be addressed in detail in the next section. Equation (2.65) can be rewritten as follows based on the above definitions [55]:

$$\tau \frac{\partial J_n}{\partial t} + J_n = \mu q \vec{F} n + q D \vec{\nabla}_x n \tag{2.67}$$

For zeroth order of the moment, the current derivative term disappears, i.e. $\partial J_n / \partial t = 0$, and we finally obtain the better-known version of the drift-diffusion equations for electrons and holes:

$$J_n = \mu_n q n \vec{F} + q D_n \vec{\nabla}_x n \tag{2.68}$$

$$J_p = \mu_p q p \vec{F} - q D_p \vec{\nabla}_x p \tag{2.69}$$

The sign of the first term in the p-type equation becomes positive due to the existence of a q within the definition of the carrier mobility $\mu = q\tau/m$. When the external field $\vec{F}$ is absent, the generated current is purely a diffusion based current, i.e.:

$$J_n = q D_n \vec{\nabla}_x n \tag{2.70}$$

$$J_p = -q D_p \vec{\nabla}_x p \tag{2.71}$$

The above equations apply to the quasi-neutral region of a p-n junction as well as in other cases such as excitation of thin film absorber samples where no external field $\vec{F}$ exists. The method of moments can be repeated using $\Theta = 1$ and $l = 1$ to obtain the following continuity equation:

$$\frac{\partial n}{\partial t} + \vec{\nabla}_x \cdot (n\vec{v}) = 0 \tag{2.72}$$

Multiplying by $-q$, the above equation can be re-expressed for both electrons and holes as:

$$\frac{\partial n}{\partial t} - \frac{1}{q} \vec{\nabla}_x \cdot J_n = 0 \tag{2.73}$$

$$\frac{\partial p}{\partial t} + \frac{1}{q} \vec{\nabla}_x \cdot J_p = 0 \tag{2.74}$$

An addition to above equations would be the inclusion of recombination and generation terms mentioned in preceding sections.

$$\frac{\partial n}{\partial t} - \frac{1}{q}\vec{\nabla}_x \cdot J_n = G_n - R_n \tag{2.75}$$

$$\frac{\partial p}{\partial t} + \frac{1}{q}\vec{\nabla}_x \cdot J_p = G_p - R_p \tag{2.76}$$

The last equation of interest is the one pertaining to conservation of charge presented in Equation (2.26). The drift-diffusion equations can be combined with the continuity equation via the $(1/q)\vec{\nabla}_x\cdot$ operator applied to Equations (2.68) and (2.69) as follows:

$$\frac{1}{q}\vec{\nabla}_x \cdot J_n = \mu_n \vec{\nabla}_x \cdot n\vec{F} + D_n \vec{\nabla}_x \cdot \vec{\nabla}_x n \tag{2.77}$$

$$\frac{1}{q}\vec{\nabla}_x \cdot J_p = \mu_p \vec{\nabla}_x \cdot p\vec{F} - D_p \vec{\nabla}_x \cdot \vec{\nabla}_x p \tag{2.78}$$

Substituting and re-arranging the above in Equations (2.75) and (2.76), we obtain:

$$\frac{\partial n}{\partial t} = D_n \vec{\nabla}_x^2 n + \mu_n \vec{\nabla}_x \cdot n\vec{F} + G_n - R_n \tag{2.79}$$

$$\frac{\partial p}{\partial t} = D_p \vec{\nabla}_x^2 p - \mu_p \vec{\nabla}_x \cdot p\vec{F} + G_p - R_p \tag{2.80}$$

The above equations can be simplified in special circumstances of ambipolar transport where a large perturbation in $\delta n/\delta p$ overshadows the initial thermal equilibrium carrier densities $n = n_0$ and $p = p_0$. We can re-write the total carrier densities as $n = n_0 + \delta n$ and $p = p_0 + \delta p$, then substitute the terms in Equations (2.79) and (2.80) and simplify to get:

$$\frac{\partial \delta n}{\partial t} = D_n \vec{\nabla}_x^2 \delta n + \mu_n (\delta n \vec{\nabla}_x \cdot \vec{F} + \vec{F}\vec{\nabla}_x \cdot \delta n) + G_n - R_n \tag{2.81}$$

$$\frac{\partial \delta p}{\partial t} = D_p \vec{\nabla}_x^2 \delta p - \mu_p (\delta p \vec{\nabla}_x \cdot \vec{F} + \vec{F}\vec{\nabla}_x \cdot \delta p) + G_p - R_p \tag{2.82}$$

Accounting the above changes in Equation (2.25) for $\delta p, \delta n \gg N_D^+, N_A^-$, we have the following Poisson's equation implying a constant electric field as function of space:

$$\vec{\nabla}_x \cdot \tilde{\varepsilon}\vec{\nabla}_x V = -\tilde{\varepsilon}\vec{\nabla}_x \cdot \vec{F} = -(\delta p - \delta n) = 0 \tag{2.83}$$

We can then eliminate the $\vec{\nabla}_x \cdot \vec{F}$ term in Equations (2.81) and (2.82). Lastly, for ambipolar transport at excess carrier conditions, we can assume charge neutrality, i.e. $\delta p = \delta n$, $G_n = G_p$

and $R_p = R_n$. Equations (2.81) and (2.82) and therefore be unified and simplified into one equation as follows:

$$\frac{\partial \delta n}{\partial t} = D\vec{\nabla}_x^2 \delta n + \mu \vec{F}\vec{\nabla}_x \cdot \delta n + G - R \tag{2.84}$$

Where the ambipolar D and μ are defined as follows [56]:

$$D = \frac{D_n D_p (n+p)}{D_n n + D_p p} \tag{2.85}$$

$$\mu = \frac{\mu_n \mu_p (n+p)}{\mu_n n + \mu_p p} \tag{2.86}$$

Lastly, we generalize the $\vec{\nabla}_x$ operator for more than one dimension as $\vec{\nabla}$ and include the recombination term R as shown in Equation (2.60) for the excess carrier condition in Equation (2.81):

$$\frac{\partial \delta n}{\partial t} = D\vec{\nabla}^2 \delta n + \mu \vec{F}\vec{\nabla} \cdot \delta n + G - k_1 \delta n - k_2 \delta n^2 - k_3 \delta n^3 \tag{2.87}$$

In the case of excess carriers, n and δn can be used interchangeably as $n \approx \delta n$ considering $\delta n \gg n_0$. Therefore, the above equation can also be written as:

$$\frac{\partial n}{\partial t} = D\vec{\nabla}^2 n + \mu \vec{F}\vec{\nabla} \cdot n + G - k_1 n - k_2 n^2 - k_3 n^3 \tag{2.88}$$

This completes our derivation of the ambipolar transport equation for charge carriers in semiconductors films and devices. A key point presented here is the Einstein relation which states that we only need to find the diffusion coefficient D of a material to know its mobility μ and vice-versa. Both coefficients are important to assess the performance of a device as will be shown in subsequent sections. The main approach in this thesis will be to assess the performance of devices from a diffusion perspective.

Diffusion occurs in any scenario involving a concentration gradient as a function of space. A well-known example is the introduction of a new liquid/gas B in an environment already having a liquid/gas A. The liquid/gas B will initially have a high concentration at the spatial coordinates where it is released. Subsequently, it will spread towards areas where it is least present until an equilibrium is reached throughout the control environment. Charge carriers within semiconductor films also follow the same laws under the effect of a concentration gradient. For an arbitrary function $W(x, y, z, t)$ representing the concentration of a diffusing substance, we consider the case of isotropic diffusion. The time-dependent differential equation for this scenario was first formulated by Fick as follows [57]:

$$\frac{\partial W}{\partial t} = D\nabla^2 W = D\left(\frac{\partial^2 W}{\partial x^2} + \frac{\partial^2 W}{\partial y^2} + \frac{\partial^2 W}{\partial z^2}\right) \tag{2.89}$$

In the case of anisotropic diffusion, instead of a single D, we would have D_x, D_y and D_z in front of each respective derivative term. Here diffusion is considered to be isotropic and reasons for this in the case of hybrid perovskites will be presented in subsequent chapters. Now, let us consider only one variable, say x, Equation (2.60) becomes:

$$\frac{\partial W}{\partial t} = D\frac{\partial^2 W}{\partial x^2} \tag{2.90}$$

Two main types of solutions exist for equations such as one above: a series-based and another based on Gaussian formalism, which is most suitable for our later application in hybrid perovskites. The Gaussian solution for the above equation is given by:

$$W(x,t) = \frac{M}{\sqrt{t}}e^{-\frac{x^2}{4Dt}} \tag{2.91}$$

Here, M is an arbitrary constant. The derivation of the solution above is given in Appendix B, Section B.1. We can also consider the case of adding recombination terms to the diffusion equation as in the case of Equations (2.79) and (2.80). The equations reduce to:

$$\frac{\partial n}{\partial t} = D_n\vec{\nabla}_x^2 n + G_n - R_n \tag{2.92}$$

$$\frac{\partial p}{\partial t} = D_p\vec{\nabla}_x^2 p + G_p - R_p \tag{2.93}$$

In a standard solar cell, the excess minority carriers δn and δp primarily contribute to the net diffusion. Here, δp is assumed as the excess hole density in the n-region and δn, the excess electron density in the p-region. For $R_n = -\delta n/\tau_{n-type}^{-1}$ and $R_p = -\delta p/\tau_{p-type}^{-1}$, the equations above can be re-written as the Minority Carrier Diffusion Equations (MCDE) [58]:

$$\frac{d\delta n}{dt} = D_n\frac{d^2\delta n}{dx^2} + \frac{\delta n}{\tau_n} + G_{\delta n} \tag{2.94}$$

$$\frac{d\delta p}{dt} = D_p\frac{d^2\delta p}{dx^2} + \frac{\delta p}{\tau_p} + G_{\delta p} \tag{2.95}$$

The homogeneous steady-state solution, i.e. $G_{\delta n/\delta p} = 0$, for both equations is given by:

$$\delta n\left(x\right) = Ae^{-x/\sqrt{D_n\tau_n}} + Be^{+x/\sqrt{D_n\tau_n}} \tag{2.96}$$

$$\delta p\left(x\right) = Ge^{-x/\sqrt{D_p\tau_p}} + He^{+x/\sqrt{D_p\tau_p}} \tag{2.97}$$

Where we define the hole diffusion length $L_p = \sqrt{D_p\tau_p}$ and electron diffusion length $L_n = \sqrt{D_n\tau_n}$. The diffusion length is defined as the expectation of the carrier trajectory. For example, taking $\delta n\left(x\right) = Ae^{-x/\sqrt{D_n\tau_n}}$, we obtain the same result using $\langle x\rangle$.

$$\langle x\rangle = \frac{\int_0^\infty x\delta n(x,t)dx}{\int_0^\infty \delta n(x,t)dx} = \sqrt{D_n\tau_n} \tag{2.98}$$

Although, the above result is widely used in scientific literature, a proper definition of diffusion length is based on the mean squared distance (MSD) of a random particle in Brownian motion:

$$L_{MSD} = \sqrt{2ZD\tau} \tag{2.99}$$

In the equation above, Z corresponds to the number of dimensions and we see that there is also a factor of 2, which is dropped from the commonly used definition shown in (2.98). In this work, we use the popular definition, while keeping the Z constant for multiple dimensions when we refer to diffusion length, i.e. $L_D = \sqrt{ZD\tau}$.

Let us now consider the simple case of a thin film in absence of a junction for the two-dimensional diffusion of carriers. We start by extracting the x and y terms from Equation (2.60).

$$\frac{\partial W}{\partial t} = D\left(\frac{\partial^2 W}{\partial x^2} + \frac{\partial^2 W}{\partial y^2}\right) \tag{2.100}$$

As we are still in the case of isotropic diffusion, it is easier to solve the above equation in polar coordinates. We do a coordinate transformation from (x, y) to (r, θ) using relations $x = rcos(\theta)$ and $y = rsin(\theta)$ and obtain:

$$\frac{\partial W}{\partial t} = D\left(\frac{\partial^2 W}{\partial r^2} + \frac{1}{r}\frac{\partial W}{\partial r} + \frac{1}{r^2}\frac{\partial^2 W}{\partial \theta^2}\right) \tag{2.101}$$

We can get rid of the θ term as there is no angular dependence and therefore, we get:

$$\frac{\partial W}{\partial t} = D\left(\frac{\partial^2 W}{\partial r^2} + \frac{1}{r}\frac{\partial W}{\partial r}\right) \tag{2.102}$$

For the above 2D diffusion equation, the complete derivation of the solution presented below is given in Section B.2 of Appendix B.

$$W\left(r,t\right)=\frac{M}{t}e^{-\frac{r^2}{4Dt}} \tag{2.103}$$

The 2D solution is very similar to the 1D solution with exception to the t variable in the denominator which is no more a square root.

2.8 Ideal Current-Voltage Relations

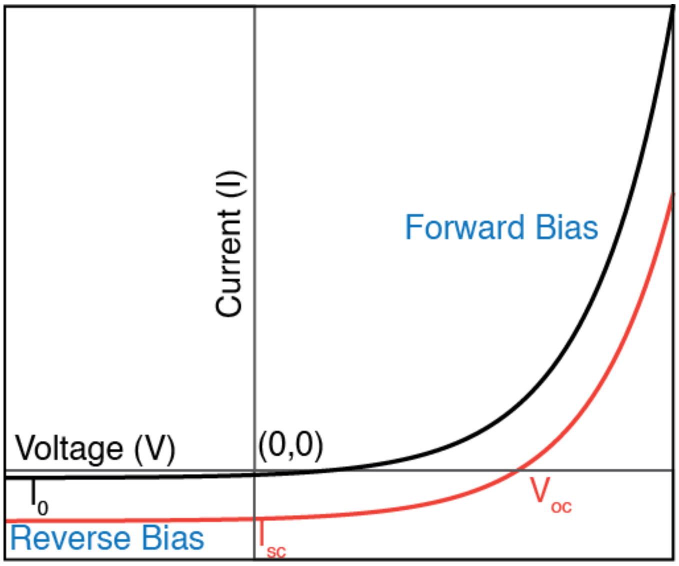

Figure 2.6 Dark (Shockley's Diode Equation) and light, i.e. under illumination, current-voltage (I-V) lines in a simple p-n photovoltaic cell.

The current-voltage (I-V) properties of the p-n junction was analyzed by William Shockley in 1949. In his paper [59], he presented the well-known Shockley diode equation:

$$I_D=I_0\left(e^{\frac{qV}{n_I k_B T}}-1\right) \tag{2.104}$$

Where I_0 is the reverse saturation current, q is the charge of the carrier, V is the applied external voltage and n_I is an ideality constant which varies from one material to another. This equation describes the variation of the current as a function of voltage for a p-n junction and the typical is shape is shown in the black line of Figure 2.6. We have used the "D" subscript to classify this current as the dark current. We can also look at the case under illumination based on our understanding of carrier generation. The total current in the diode is then written as:

$$I = I_L - I_D = I_L - I_0 \left(e^{\frac{qV}{n_I k_B T}} - 1 \right) \tag{2.105}$$

The shape of the above current is also plotted in red in Figure 2.6. The short-circuit current I_{SC}, i.e. for $V = 0$, is given by $I_{SC} = I_L$. Equation (2.105) is a simple and practical model based on some important assumptions. For a given illumination power spectrum, we can find I_{SC} for a device from the expression of carrier generation presented in Equation (2.46). It is useful to define the external quantum efficiency (EQE) based on spatial collection efficiency $\xi(z)$ to know the exact ratio of generated carriers to incident photons:

$$EQE\left(E\right) = \int_0^d G_{normalized}\left(z, E\right) \xi\left(z\right) dz = \int_0^d \frac{1}{\phi_0(E)} G\left(z, E\right) \xi\left(z\right) \tag{2.106}$$

The EQE of a device can be measured experimentally using single-wavelength excitation. The dark J_0 and short-circuit densities J_{SC} as a function of EQE are then given by:

$$J_0 = \int J_0(E) dE = q \int EQE\left(E\right) \phi_{BB}\left(E\right) dE \tag{2.107}$$

$$J_{SC} = \int J_{SC}(E) dE = q \int EQE\left(E\right) \phi_0\left(E\right) dE \tag{2.108}$$

We have used $\phi_0(E)$ as defined in Equation (2.45). For a photovoltaic cell, this corresponds to the photon flux of the solar spectrum $\phi_{sun}(E)$ shown in Figure 2.10. However, we are leaving it open-ended here for any type of incident spectrum. From Equation (2.105), we now express the voltage V as a function of the current I as follows:

$$V = \frac{n_I k_B T}{q} ln\left(\frac{I_L - I}{I_0} + 1\right) = \frac{n_I k_B T}{q} ln\left(\frac{I_{SC} - I}{I_0} + 1\right) \tag{2.109}$$

The open-circuit voltage, i.e. for $I = 0$, is given by:

$$V_{OC} = \frac{n_I k_B T}{q} ln\left(\frac{I_L}{I_0} + 1\right) = \frac{n_I k_B T}{q} ln\left(\frac{I_{SC}}{I_0} + 1\right) \tag{2.110}$$

Both I_{SC} and V_{OC} are important as parameters, as they have significant bearing on the performance of a device. When both have high values, a greater amount of electric power can be extracted. The short-circuit current is mainly impacted by the absorption efficiency of the device, i.e. the capability of the device to convert the incident photons into usable carriers. This is equally true for V_{OC}, for which, the logarithmic term is maximized when

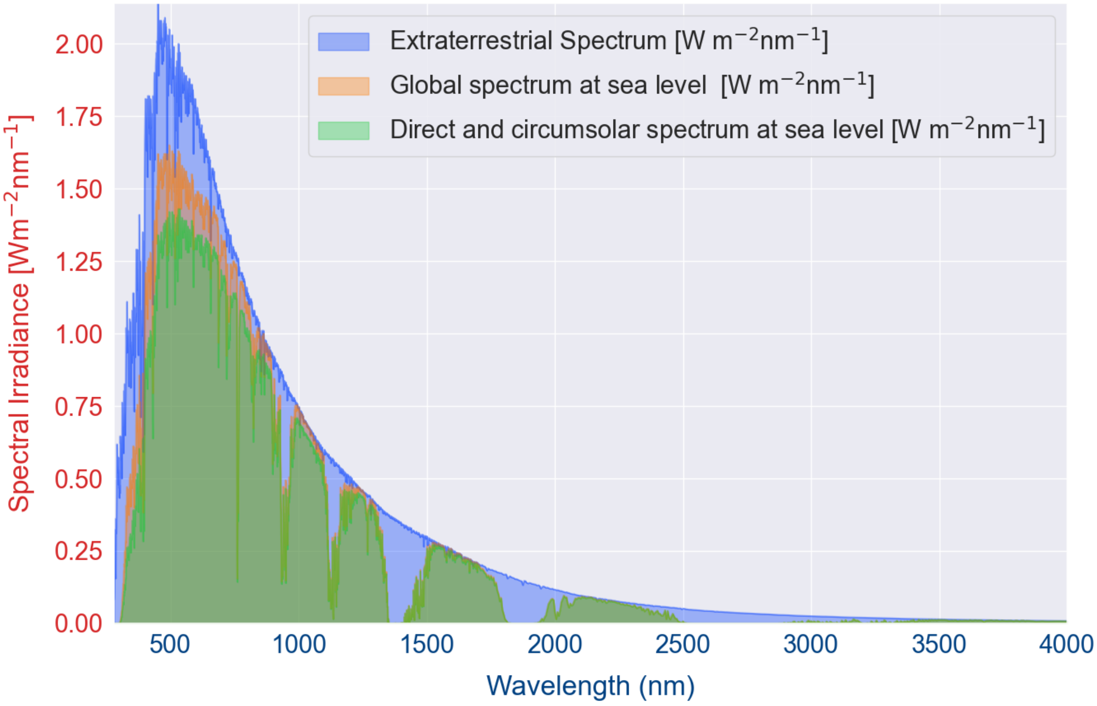

Figure 2.7 ASTM G-173 solar spectral irradiance. Data from NREL [60].

$I_L \gg I_0$. The voltage V_M and current I_M at which the extracted photovoltaic power is maximized, can be determined by optimizing the derivative of the electric power $P = IV$. We know the voltage is maximum when:

$$\frac{dP}{dV} = \frac{d(IV)}{dV} = \frac{d\left(\left[I_L - I_0\left(e^{\frac{qV}{n_I k_B T}} - 1\right)\right]V\right)}{dV} = 0 \tag{2.111}$$

Through algebraic manipulation, we find the following transcendental equation for V_M which can be solved numerically:

$$V_M = V_{OC} - \frac{n_I k_B T}{q} ln\left(\frac{n_I k_B T V_M}{q} + 1\right) \tag{2.112}$$

I_M is found by substituting the resulting V_M into Equation (2.105). The fill factor (FF), a parameter quantifying device performance, is a ratio defined as:

$$FF = \frac{I_M V_M}{I_{SC} V_{OC}} \tag{2.113}$$

The efficiency η of a device is then calculated as follows:

$$\eta = \frac{P_M}{P_{inc}} = \frac{I_M V_M}{P_{inc}} = \frac{I_{SC} V_{OC} FF}{P_{inc}} \tag{2.114}$$

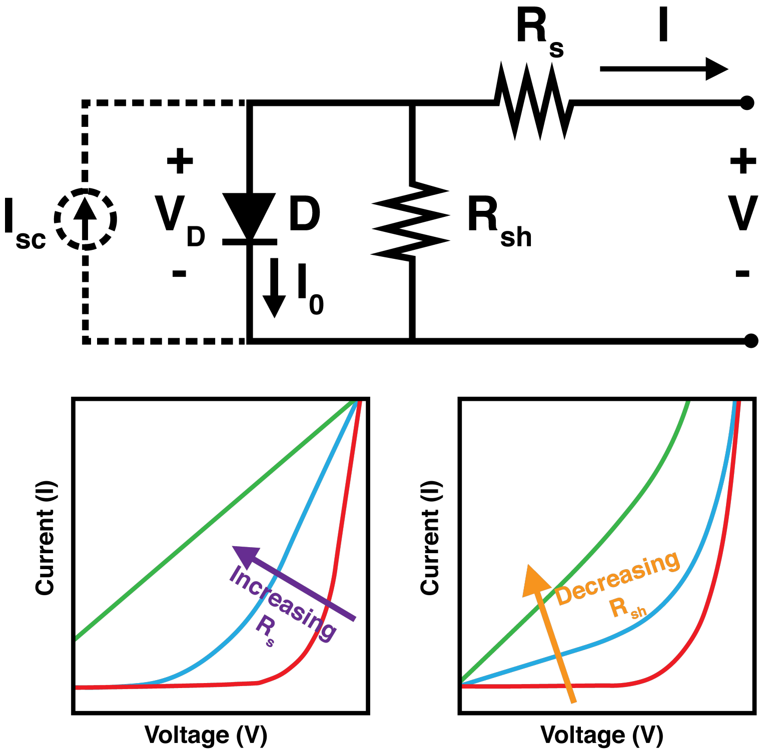

Figure 2.8 Top - Equivalent circuit model of a photovoltaic cell. Bottom – Effects of series resistance R_s and shunt resistance R_{sh} on the shape of I-V curves. Adapted from [61].

The efficiency of a device depends on many factors ranging from microscopic elements such as transition lifetimes to macroscopic ones such as morphology. Other factors are the low absorptance $a(E)$, non-radiative recombination mechanisms and inefficient device architecture, etc. The latter is a broad topic which encompasses the selection of correct materials with optimum parameters to obtain maximum efficiency. The diode equation for a real device is closer to the one shown below:

$$I = I_{SC} - I_0 \left(e^{\frac{q(V+IR_s)}{n_I k_B T}} - 1 \right) - \frac{V + IR_s}{R_{sh}} \tag{2.115}$$

Where R_s is termed as the series sentence and R_{sh}, the shunt resistance. The equivalent circuit model described in Equation (2.115) is depicted in Figure 2.8. If external illumination is absent, the path on the left in dotted lines is neglected in Equation (2.115), i.e. $I_{SC} = 0$.

The series resistance in a solar cell is generally attributed to losses at interfaces between layers forming a solar cell whereas the shunt resistance is attributable to the leaking currents between electrodes. From Figure 2.8, we can deduce that R_s needs to approach 0 where as R_{sh} should be as high as possible to approach an ideal diode curve.

2.9 Maximum Efficiency Bandgap

Previously, we used the principle of detailed balance to derive an expression for the bimolecular recombination rate at thermal equilibrium (Section 2.4). Here, we consider the application of this principle for a solar cell. William Shockley and Hans Queisser devised a way to determine the maximum efficiency of a single junction solar cell by optimizing the bandgap energy E_g dependence through the principle of detailed balance. The principle of detailed balance derives its origins on the idea of maintaining perfect thermodynamical equilibrium. This can be viewed as a result of the 2nd law of thermodynamics where equilibrium is maintained in a body via counter-balancing processes with respective in/out-flowing energy. For solar cells, the fundamental assumptions underlying the detailed balance principle are first, an infinite mobility and second, the complete absorption of photons of energy $E_{ph} > E_g$. For detailed balance, the net generated current within a solar cell is obtained by tallying currents from incident photon fluxes and outgoing photogenerated charge carriers. Photons can be emitted out as well via radiative recombination in the absence of a charge collection mechanism, in which case, the body is also assumed to be a perfect light-emitter. Based on Planck's and Kirchhoff's laws, the emission spectrum for non-equilibrium conditions is as follows:

$$\phi_D\left(V,E\right) = \frac{2\pi E^2}{h^3 c^2}\frac{a(E)}{e^{\frac{E-qV}{k_B T}}-1} \tag{2.116}$$

Here, $a(E)$ is the absorptance, presented in Section 2.1. In the original Shockley-Queiesser model, $a(E)$ was a simple Heaviside function $\Theta(x)$, i.e. $a(E) = \Theta(E - E_g)$. In other words, $a(E) = 1$ for $E > E_g$. The generated current density J_{gen} for a "black box" solar cell under a bias voltage is given by:

$$J_{gen} = q\int_{E_g}^{\infty} a(E)\phi_D\left(V,E\right)dE = q\int_{E_g}^{\infty} a(E)\phi_{bb}\left(E\right)e^{\frac{qV}{k_B T}}dE \tag{2.117}$$

$\phi_{bb}(E)$ is the black-body spectrum given in Equation (2.40). Here, $\phi(V,E)$ is approximated using a Boltzmann distribution assuming $E - qV \gg k_B T$. Similarly, the recombination current J_0^{rec} is given by:

$$J_{rec} = q \int_{E_g}^{\infty} a(E)\phi_{bb}(E)dE \tag{2.118}$$

The total current is therefore $J_{net} = J_{gen} - J_{rec}$ given by:

$$J_{0,net}^{SQ} = \left(e^{\frac{qV}{k_BT}} - 1\right) \int_{E_g}^{\infty} a(E)\phi_{bb}(E)dE = \left(e^{\frac{qV}{k_BT}} - 1\right) J_0^{SQ} \tag{2.119}$$

Note, that for $V = 0$, the net current is zero. We have now defined the dark saturation current density for this solar cell as:

$$J_0^{SQ} = q \int_{E_g}^{\infty} a(E)\phi_{bb}(E)dE = q \int_{E_g}^{\infty} \phi_{bb}(E)dE \tag{2.120}$$

Similarly, we can define the short-circuit current density under illumination as:

$$J_{SC}^{SQ} = q \int_{E_g}^{\infty} a(E)\phi_0(E)dE = q \int_{E_g}^{\infty} \phi_0(E)dE \tag{2.121}$$

From the equations above, $EQE(E) = a(E)$ is a natural relation and its origin is based on the derivation in the previous section. Therefore, the Shockley-Queiesser open-circuit voltage can now be written as:

$$cV_{OC}^{SQ} = \frac{n_I k_B T}{q} ln\left(\frac{AJ_{SC}^{SQ}}{AJ_0^{SQ}} + 1\right) = \frac{n_I k_B T}{q} ln\left(\frac{I_{SC}^{SQ}}{I_0^{SQ}} + 1\right) \tag{2.122}$$

For an ideal diode, the net current is then given by:

$$J(V) = J_{0,net}^{SQ} - J_{SC}^{SQ} = \left(e^{\frac{qV}{k_BT}} - 1\right) J_0^{SQ} - J_{SC}^{SQ} \tag{2.123}$$

The incident power introduced in Equation (2.114) is calculated by integrating the incident spectral irradiance defined in Equation (2.45) over E and multiplying by the Area A.

$$P_{inc} = qA \int_{E_g}^{\infty} I_0(E)dE = qA \int_{E_g}^{\infty} E\phi_0(E)dE \tag{2.124}$$

The electrical power from the Shockley-Queiesser model is given by $P_{SQ} = VI(V) = AVJ(V)$. Once again by following the approach in the previous section, we find the I and V values, i.e. I_M^{SQ} and V_M^{SQ}, which maximize the power output by solving $dP_{SQ}(V)/dV = 0$.

Holding all parameters constant except for E_g, a plot of the device efficiency (Shockley-

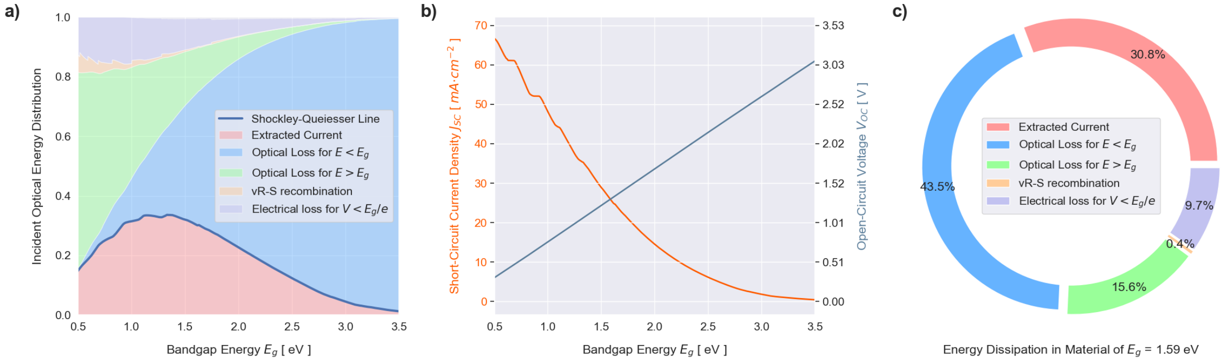

Figure 2.9 a) Optical energy loss distribution b) Short-circuit current density J_{SC}^{SQ} and open-circuit voltage V_{OC}^{SQ} as a function of bandgap energy E_g. c) Optical energy dissipation in a material of bandgap energy $E_g = 1.59$ eV.

Queiesser line) defined in Equation (2.114) using variables I_M^{SQ}, V_M^{SQ}, I_{SC}^{SQ} and V_{OC}^{SQ} is shown in panel a of Figure 2.9 as a function of E_g. The short-circuit current density J_{SC}^{SQ} and open-circuit voltage V_{OC}^{SQ} presented in Equations (2.121) and (2.122) are plotted as a function of bandgap energy E_g in panel b. The Shockley-Queiesser line shows that the maximum achievable efficiency for an ideal device is 33% at a E_g value of 1.42 eV. This also means that for any given material of bandgap energy E_g, the maximum achievable efficiency is determined by the Shockley-Queiesser line as shown in panel c for a hybrid perovskite (MAPbI$_3$) of $E_g = 1.59$ eV. We can measure the EQE profile of a material experimentally and then determine the maximum theoretical efficiency using the approach shown above.

2.10 Photon Reabsorption and Recycling

In the previous section, we mentioned that parameters such as short-circuit current and open-circuit voltage are critical for maximizing the efficiency of a device. In particular, bimolecular recombination, plays a significant role in increasing the value of the open-circuit voltage. The relation between them from an energy level approach is best described by the following equation [62–64]:

$$V_{OC} = \frac{E_g}{q} - \frac{k_B T}{q} ln\left(\frac{k_2^{app} N_C N_V}{G}\right) \tag{2.125}$$

In the above equation, we notice that V_{OC} depends on both, an apparent bimolecular recombination rate k_2^{app} as well as the generation rate G. The parameter k_2^{app} here actually refers to a bimolecular recombination which is lower than the intrinsic bimolecular recombination rate k_2^{int}. This, we derived in Section 2.4, as a consequence of two processes which occur in materials with high internal quantum efficiency: photon re-absorption and photon recycling. Photon re-absorption is a process in which emitted photons are re-absorbed by the material, thereby contributing to the generation of new carriers. Whereas photon recycling refers to the subsequent chained re-absorption and re-emission of photons within the film. The degree by which the internal and apparent rates differ depends on the optical architecture. For example, a light trapping or layered scheme will increase absorptance and conserve light within to promote re-absorption and recycling of photons. To quantify the trapping of photons, we refer to the definition of the generated current density J_{gen} in Equation (2.117). The latter be described as a current density corresponding to photon flux leaving the film and therefore also referred to as the external radiative saturation current $J_0^{rad,ext}$. We also defined an internal saturation current density $J_0^{rad,int}$ in Section 2.4 based on radiative recombination through the Van Roosbroeck-Shockley relation. From the ratio of these two currents, we obtain the probability P_{escape} of an emitted photon escaping the film.

$$P_{escape} = \frac{J_0^{rad,ext}}{J_0^{rad,int}} = \frac{k_2^{app}}{k_2^{int}} \tag{2.126}$$

Conversely, the probability that a photon will remain within the film P_{stay} can be expressed as follows [45, 65]:

$$P_{stay} = 1 - P_{escape} - P_{absorption} \tag{2.127}$$

We have also included the probability of the photon undergoing parasitic absorption $P_{absorption}$. Equation (2.125) can now be re-written also as:

$$V_{OC} = V_{OC}^{Rad} + \Delta V_{OC}^{PR} = \frac{n_I k_B T}{q} ln\left(\frac{J_{SC}}{J_0^{rad,int}} + 1\right) + \frac{n_I k_B T}{q} ln\left(\frac{J_0^{rad,int}}{J_0^{rad,ext}} + 1\right) \tag{2.128}$$

$$V_{OC} \approx \frac{n_I k_B T}{q}\left[ln\left(\frac{J_{SC}}{J_0^{rad,int}}\right) + ln\left(\frac{J_0^{rad,int}}{J_0^{rad,ext}}\right)\right] \tag{2.129}$$

$$V_{OC} \approx \frac{n_I k_B T}{q} ln\left(\frac{J_{SC}}{J_0^{rad,ext}}\right) \tag{2.130}$$

$$V_{OC} \approx \frac{n_I k_B T}{q} ln\left(\frac{J_{SC}}{P_{escape}\ J_0^{rad,int}}\right) \tag{2.131}$$

V_{OC}^{Rad} is the normal open-circuit voltage defined in Equation (2.110) whereas ΔV_{OC}^{PR} is the change because of photon recycling. From the above equations, it is quite clear that by decreasing the probability of photons escaping, we also reduce the apparent bimolecular recombination rate, which in turn maximizes the device performance through Equation (2.125). It is important to note that J_{SC} remains unchanged as it is only a function of absorptance and incoming photon flux. We also look at photon recycling from a quantum efficiency perspective. The $PLQE$ and EQE are linked as follows based on P_{Stay} [66]:

$$EQE = \frac{PLQE \cdot (1 - P_{Stay})}{1 - PLQE + PLQE \cdot (1 - P_{Stay})} \tag{2.132}$$

And lastly, ΔV_{OC}^{PR} is can also be expressed as:

$$\Delta V_{OC}^{PR} = \frac{n_I k_B T}{q} ln\left(EQE\right) = \frac{n_I k_B T}{q} ln\left(\frac{PLQE \cdot (1 - P_{Stay})}{1 - PLQE + PLQE \cdot (1 - P_{Stay})}\right) \tag{2.133}$$

From the above equation, it is clear that V_{OC} is maximized for both high $PLQE$ and P_{Stay} values. Overall, photon recycling is enhanced when $PLQE$ and light confinement are high. Now another question that we might ask is how far the photons travel due to recycling. A complete stochastic model taking the optical architecture of the device into account is quite complex. However, we can start by looking at the Gaussian spreading due to a single photon recycling event. Photons can be treated as particles undergoing Brownian motion with a diffusion coefficient like charge carriers:

$$D_\lambda = \frac{c}{3 n_r \alpha_\lambda} \tag{2.134}$$

Where c is speed of light, n_r is the refractive index of the perovskite film and α_λ the absorption at wavelength λ. The average photon lifetime is given by:

$$\tau_\lambda = \frac{n_r}{c \alpha_\lambda} \tag{2.135}$$

The average diffusion length of a re-emitted photon prior to reabsorption can then be obtained as:

$$L_{D_\lambda} = \sqrt{D_\lambda \tau_\lambda} = \sqrt{\frac{c}{3 n_r \alpha_\lambda} \frac{n_r}{c \alpha_\lambda}} = \sqrt{\frac{1}{3} \frac{1}{\alpha_\lambda}} \tag{2.136}$$

Using a similar series-based calculation, it is possible to determine the photon recycling induced effective displacement for a carrier [67]. In this method, the total displacement of the carrier is written as:

$$\vec{L} = \vec{L}_D + \Upsilon \vec{L}_{D_\lambda} + \Upsilon \vec{L}'_D + \Upsilon^2 \vec{L}'_{D_\lambda} + \Upsilon^2 \vec{L}''_D + \ldots \tag{2.137}$$

Where we have $\Upsilon = PLQE{\cdot}P_{Stay}$, carrier diffusion length $\vec{L}_D = \sqrt{D\tau}$ and photon diffusion length $L_{D_\lambda} \sim \alpha_\lambda^{-1}$. Through statistical averaging, i.e. the evaluation of $\langle \vec{L}^2 \rangle$, we find the effective diffusion length for a carrier under the influence of photon recycling.

$$L_{eff} = \sqrt{\langle \vec{L}^2 \rangle} = \sqrt{\frac{D\tau + \Upsilon^2 \alpha_\lambda^{-2}}{1 - \Upsilon^2}} \tag{2.138}$$

The above equations provide rough estimates for characteristic lengths when photon recycling is involved. A better way of quantifying these parameters is to develop numerical spatio-temporal modelling of the ambipolar diffusion equation with extra components pertaining to photon recycling. This type of calculation will be discussed in Chapter 5.

CHAPTER 3 ORGANIC-INORGANIC HALIDE PEROVSKITES

In this chapter, we explore the chemical composition as well as the fundamental physical aspects which form lead halide perovskites from a materials point-of-view. This entails a detailed study of crystalline structure, phase transitions and the role of ions to see how they determine fundamental semiconducting properties. We look at the progress made until now in device architecture, fabrication, and interfacial engineering. We also provide insights on the current understanding of the fundamental photophysical processes such as charge carrier recombination kinetics, diffusion, and photon recycling. Lastly, we present preliminary spatiotemporal measurement results forming the foundation for subsequent studies on diffusion and photon recycling in Chapters 4 and 5.

3.1 Crystal Structure

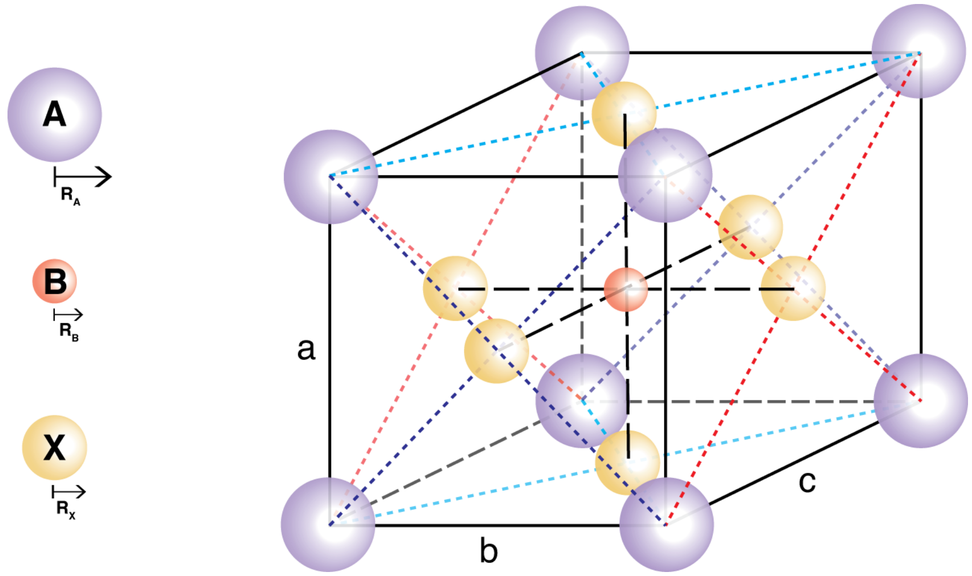

Figure 3.1 Perovskite ABX_3 crystal structure.

Perovskites are defined by their ABX_3 crystal structure and were first discovered by Gustav Rose in 1839 in a $CaTiO_3$ mineral [68]. The compound was later named after Count Lev Aleksevich von Perovski, a well-known Russian nobleman and mineralogist. In 1926, Victor Goldschmidt first characterized and reported the crystalline lattice structure, shown in Figure (3.1), as well as the tolerance factors of perovskites [69]. The purple spheres (A) in the eight corners and the red sphere (B) at the center of the cubic lattice (O_h symmetry) represent cations, whereas the yellow spheres (X) represent the anions. Besides $CaTiO_3$, other examples include $KMgF_3$, $SrZrO_3$, $MgSiO_3$, $SrFeO_3$, $BaTiO_3$ and $LiNbO_3$. Starting from their first appearance, the most widely studied perovskites are metal-oxide based (i.e. $X = O$), mainly thanks to their interesting ferroelectric and magnetic properties, and to the possible application as superconductive materials. The interest in hybrid metal-halide perovskite gained momentum ever since the first hybrid metal-halide perovskite structure was developed using gold and chloride in 1884 [70]. In the year 1978, Weber explored the possibility of using methylammonium at the A atomic site and discovered new light absorbing properties for $CH_3NH_3SnBr_xI_{3-x}$ PSCs [71]. Subsequently, Kojima et al. have demonstrated the PCEs of ~3.81% and ~3.13% for $CH_3NH_3PbI_3$ and $CH_3NH_3PbBr_3$ PSCs, respectively in mesoporous dye-sensitized solar cells [72]. Interestingly, Pb^{2+} in B can be swapped with other divalent metal atoms such as Sn^{2+}, Bi^{2+} and Cu^{2+}. Similarly, I^- in X can also be replaced with another single (or combination) of halide anion(s) such as Cl^- and Br^-.

3.2 Compositional Properties

Hybrid perovskites offer a unique structural flexibility due to multiple phases which can be accessed in a reversible manner by tuning parameters such as temperature, pressure and electric/magnetic fields. These phases are cubic ($a = b = c$), tetragonal ($a = b \neq c$), orthorhombic ($a \neq b \neq c$), trigonal and lastly monoclinic polymorphous states that vary with the orientation of the BX_3 component in the crystal lattice [73]. The stability and distortion of the perovskite lattice can be evaluated using the Goldschmidt tolerance factor:

$$t_G = \frac{R_A + R_X}{\sqrt{2}\,(R_B + R_X)} \tag{3.1}$$

Where R_A, R_B and R_X are the ionic radii depicted in Figure 3.1. Tolerance factor ranges of $t_G < 8$, $0.8 < t_G < 1$ and $t_G > 1$ are each favorable for the orthorhombic, cubic and hexagonal phases, respectively [74]. To maintain the ideal cubic lattice, the value of the above-mentioned factor is unity, implying therefore the following relation:

$$\sqrt{2}R_B + (\sqrt{2} - 1)R_X = R_A \tag{3.2}$$

The above relation requires the cation radius R_A to be significantly larger than the other two for a stable cubic structure. In the case of hybrid perovskite, the tolerance factor values typically fall in the range of 0.8 to 0.95 as shown in Figure 3.2.

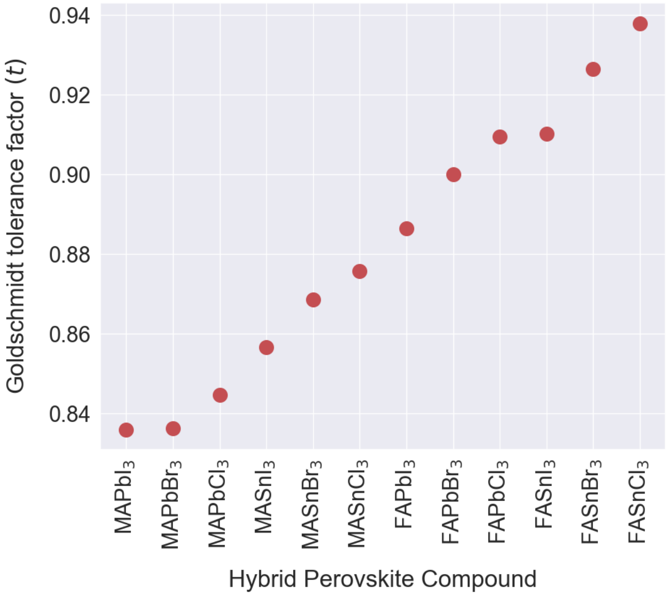

Figure 3.2 Goldschmidt tolerance factor t_G for different hybrid organic-inorganic compounds. Adapted from data in [75].

In Figure 3.2, we find that the tolerance factor increases with the cation and divalent metal replacements along the x-axis. Replacing MA^+, which has a 2.17 Å radius, with a larger organic cation of 2.53 Å radius, i.e. formamidinium (FA^+), leads to a higher fulfillment of the condition imposed in Equation (3.2). Similarly, substitution of Sn for Pb also exhibits the same effect. In the case of anions, decreasing the atom radius contributes to the higher t_G value. DFT calculations at $T = 0$ K reveal cubic (α) as an unstable phase due to the high difficulty of stabilizing t_G at unity [76–78]. The best opto-electronic transport properties are found in the cubic phase due to the high overlap of orbitals between the metal (B) and halide (X) atoms. More often, the perovskite is found in the tetragonal phase (β) if not a low temperature ($T \sim 100$ K), albeit highly stable, orthorhombic (γ) phase.

For $MAPbI_3$, the tetragonal-cubic transition happens around a temperature of 327 K (Table 3.1). Since solar cells typically operate at a temperature of ~85 ℃, there is an increasing interest in the usage of FA^+ as an alternative for a stable room temperature crystal structure. The transition temperature for this material is around 293 K for the α phase [76]. Beyond thermal stability, the use of FA^+ has also been shown to increase the absorption wavelength range as well [80]. This implies therefore a lowered bandgap range of 1.45-1.52 eV, which is much closer to the ideal Shockley-Queiesser value, as opposed to ~1.60 eV for $MAPbI_3$. A drawback of the FA^+ based perovskite is the simultaneous formation of a non-luminescent hexagonal lattice structure (δ-phase) at room temperature [81]. A major solution for this

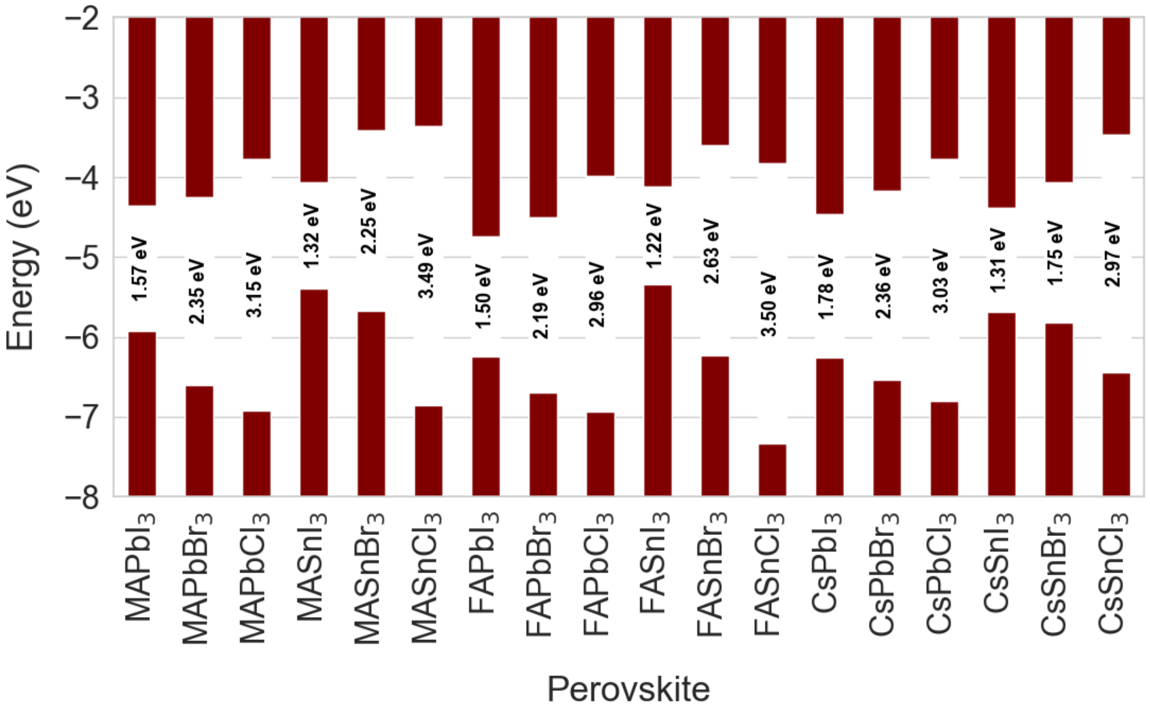

Figure 3.3 Energy level diagram for different perovskites. Adapted from data in [79].

issue is the addition of a smaller ratio of MA^+ alongside FA^+ to stabilize the perovskite structure [82]. The resulting compound $FA_{1-x}MA_xPbI_3$ is amenable for tunable bandgap via x. This imparts high efficiencies of ~19% [83]. An alternative route for achieving similar cation-based stabilization is the use of inorganic cations such as Cs^+, Li^+, K^+, Na^+. In pure inorganic ones, excluding Cs^+, none of the other cations provide a reasonable tolerance factor to achieve a stable α phase [84]. Even when using Cs^+ as the cation, the resulting film is unstable at room temperatures. However, the addition of small amounts of Cs^+ (up to 10%) in $FAPbI_3$ was discovered to be highly beneficial in terms of stabilization as with MA^+ previously resulting in a $FA_{1-x}Cs_xPbI_3$ chemical compound [74] with efficiencies reaching up to ~21.1% [84]. The films also displayed better morphology, enhanced absorption, and a tunable bandgap.

We now consider the halide/anion substitution and mixing hybrid perovskites. As shown in Table 3.1, in $MAPbI_3$, the halide atom I can be substituted but this alters the values of the transition temperatures. Both Cl^- and Br^- are structurally stable at room temperature as shown by the decrease tetragonal/cubic transition temperatures. This is also in consonance with what we observe in Figure 3.2, where the tolerance factor approaches unity as we replace I^- with anions of smaller radii. However, a major drawback of using smaller radii ions is the

Table 3.1 Structural data for the methylammonium lead halides. Adapted from [85].

X	Temperature	Crystal Structure	Space group	Lattice Parameters		
				a	b	c
Cl	>178.8	Cubic	*Pm3m*	5.675		
	172.9-178.8	Tetragonal	*P4/mmm*	5.656		5.630
	<172.9	Orthorhombic	$P222_1$	5.673	5.628	11.182
Br	>236.9	Cubic	*Pm3m*	5.901		
	155.1-236.9	Tetragonal	*I4/mcm*	8.322		11.832
	149.5-155.1	Tetragonal	*P4/mmm*	5.894		5.861
	<144.5	Orthorhombic	$Pna2_1$	7.979	8.580	11.849
I	>327.4	Cubic	*Pm3m*	6.329		
	162.2-327.4	Tetragonal	*I4/mcm*	8.855		12.659
	162.2	Orthorhombic	$Pna2_1$	8.861	8.581	12.620

resulting increase in bandgap energy. For example, the observed bandgap energies for single crystals of $MAPbCl_3$, $MAPbBr_3$ and $MAPbI_3$ are about 3.0, 2.2 and 1.5 eV, respectively. The large bandgap in bromide perovskites limits the absorption to 550 nm. An ideal solution requires a compromise between the optimal radius and the bandgap energy for single junction photovoltaic applications, each represented with Cl^- and I^- representing either ends of the spectrum, respectively. Therefore, mixing halides as in $MAPbI_{3-x}Cl_x$, rather than pure substitution, presents a potential opportunity.

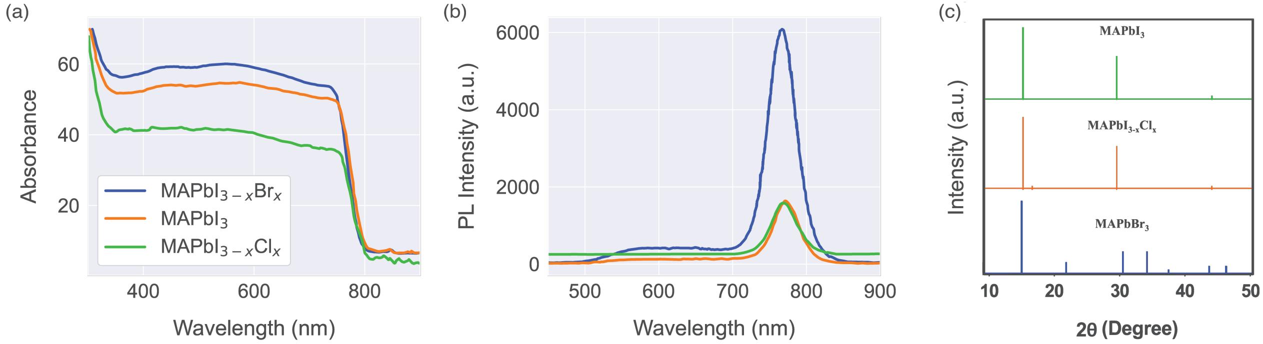

Figure 3.4 (a) Absorbance and (b) photoluminescence spectra of $MAPbI_{3-x}Z_x$ (Z = Cl, Br, I) perovskite films on glass for bandgap energies of 1.6, 1.56 and 1.56 eV, respectively. Digitized and adapted from [86]. (c) XRD data for $MAPbI_3$, $MAPbI_{3-x}Cl_x$ and $MAPbBr_3$ adapted from [87].

Some of the key points that make $MAPbI_{3-x}Cl_x$ ideal for photovoltaic applications are its optical and electronic properties. For example, incorporation of Cl^- was known to reduce bulk

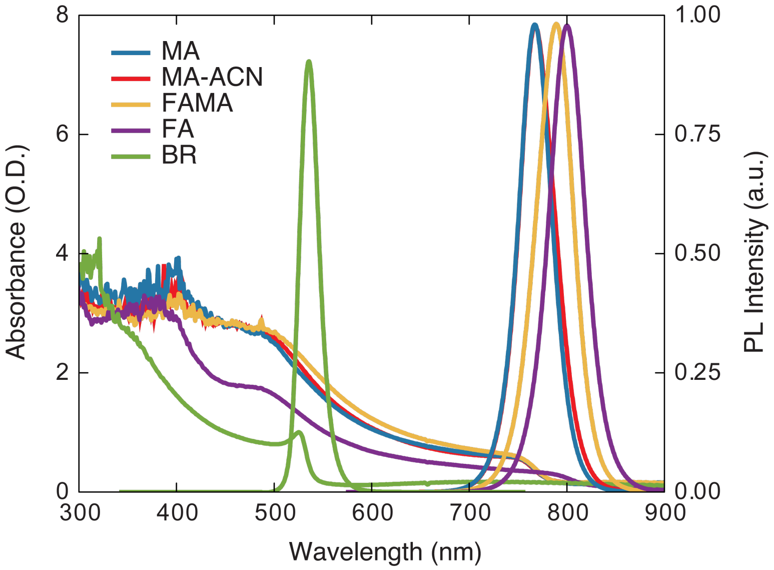

Figure 3.5 Absorption and emission profiles of perovskite thin film samples used in our experiments (Chapter 5). MA : $MAPbI_3$, MA-ACN : Acetonitrile processed $MAPBI_3$, FAMA : $FA_{0.85}MA_{0.15}Pb(I_{0.85}Br_{0.15})_3$, FA : $FAPbI_3$, BR : $MAPbBr_3$.

as well as surface defects while maximising grain formation [29, 88–91]. The absorption and emission spectra of $MAPbI_{3-x}Cl_x$ are shown in panels a and b of Figure 3.4. The absorption is extended up to ~800 nm; a wavelength corresponding to a bandgap of ~1.56 eV. Thus the ability to extend the absorbance widely in the visible range is ideal for sunlight harvesting ($\alpha \approx 1.5 \times 10^4$ cm^{-1} at 550 nm). Interestingly, $MAPbI_{3-x}Cl_x$ composition ultimately results in $MAPbI_3$ as it is quite hard to stabilize this mixed halide perovskite at temperatures below 625 K. The "x" is mainly used in the chemical formula to specify the usage of $PbCl_2$ as a precursor. Hence, the XRD data in Figure 3.4c for $MAPbI_3$ (PbI_2 source) is almost identical to $MAPbI_{3-x}Cl_x$ ($PbCl_2$ source). Unlike Cl^- which helped in terms of crystallinity, introduction of Br^- is found to be useful in raising the conduction band level to an ideal position with regards to an extraction material or transfer layer in a device scheme. Like I^--Cl^-, I^--Br^- combination fails to stabilize at room temperatures (whereas Br^--Cl^- is stable). Nevertheless, mixing Br^- with I^-, for ratios up to 29%, greatly increases the performance of devices. This band engineering minimizes geminate recombination and helps to augment carrier extraction efficiency. More importantly, the main benefit of $MAPbI_{3-x}Br_x$ perovskites, particularly for tandem applications, is the tunable bandgap over a large range of 0.6 eV from 1.6 to 2.2 eV [23]. A major drawback, however, is that too much Br leads to instability, caused by I rich domains, acting as recombination centers, because of halide phase segregation [92]. This is severe especially for the $MAPbI_{3-x}Br_x$ where a large part of the compositional range for x is compromised [93]. Going one step further in terms of mixing, the current materials with the highest efficiencies possess both mixed cations as well as mixed halides of the form $\mathrm{FA}_x\mathrm{MA}_{1-x}\mathrm{Pb}(\mathrm{I}_x\mathrm{BrA}_{1-x})_3$ [83]. The MA^+ here is used to stabilize FA^+ and prevent transition to the yellow phase, while Br^- is added in moderate amounts for band alignment and to provide stability as well. Here, the advantages of both cations and anions are leveraged to optimize optoelectronic properties and crystallinity.

Lastly, an important requirement for identifying a long-term lead-free alternative material, for toxicity reasons, is highly essential in line with safety protocols. Most efforts are directed towards Sn for metal-based perovskites. From a toxicological or chemical hazards perspective, Sn is still potentially harmful, although at a lower level health risks in comparison to Pb [94]. Literature on this subject is still growing as current studies are yet inconclusive. Above all, there are no obstacles currently from a legislation perspective. Presently, mixed cation compounds such as $\mathrm{FA}_x\mathrm{Cs}_{1-x}\mathrm{SnI}_3$ in particular show greater potential in terms of approaching the Shockley-Queiesser limit due to the low bandgap values (Figure 3.3). However, a major issue restricting the efficiency of these materials is the oxidation of Sn^{2+} into Sn^{4+} during all stages of fabrication. This leads to a high amount of vacancy defects/trap states which reduce the extraction efficiency in devices. Techniques such as acid treatment [95–97] and solvent engineering [98] are still being studied to mitigate this problem within an Sn framework. However, more efforts are deployed towards alloying techniques [99–101] with Pb and currently efficiencies for tandem applications have reached about 24.8% [102].

3.3 Device Architecture

Continuous experimentation by various research groups have led to substantial improvements in efficiency values reaching above ~20% in a span of ~7 years, as shown in the chronological development in Table 3.2. The development of perovskite solar cells was originally based on the pre-existing designs for dye sensitized solar cells. A typical perovskite solar cell (PSC) architecture is made up of five layers: an anode, an electron transport layer (ETL), a perovskite absorber layer, a hole transport layer (HTL) and lastly a cathode. These five layers together perform the three fundamental operations required for solar cell operation: charge carrier generation from incident light absorption, charge transport and lastly, charge extraction. In some cases, excitons, rather than charge carriers, are generated and conversion to charge carrier occurs only at the perovskite-transfer layer interface through a series of conversion mechanisms. In both cases, the ETL and HTL layers are crucial for both efficient charge carrier extraction from the perovskite layer as well as subsequent transfer to the anode

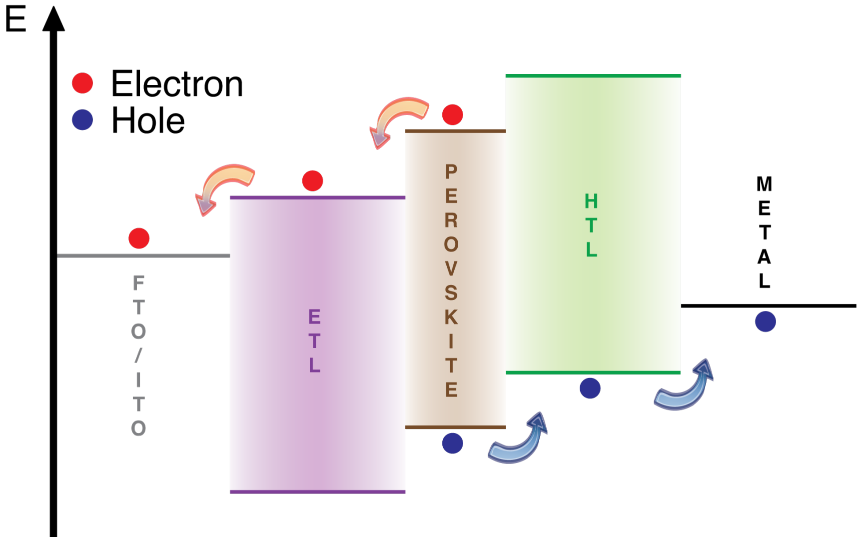

Figure 3.6 Energy model showing extraction pathway for photogenerated carriers in a standard five-layer perovskite solar cell. Adapted from [103].

and cathode, respectively. However, single transport layer or (ETL/HTL)-free devices tested in the past have also shown promising results. A schematic of the band diagram for a typical PSC architecture is shown in Figure 3.6. The choice of material in each architecture at a fundamental level is largely determined by the energy level as shown conceptually in Figure 3.6, where carriers and holes are energetically directed towards their respective electrodes. For example, electrons generated in the perovskite layer can only travel leftwards as the barrier on the right side requires extra energy to traverse.

Furthermore, the junction can be regular (n-i-p) or inverted (p-i-n) based on the transfer layer first in contact with incident light as shown in Figure 3.7. In panels a and c, we have a mesoporous structure using a TiO_2 (or Al_2O_3) scaffold for carrier transport from the perovskite layer to the transport layers. Further experimentation later revealed that perovskite in a planar architecture (panels b and d) had excellent transport properties. Above all, embedding within a mesoscopic design was found to be non-essential. The planar architecture, besides having a simpler fabrication process, supported even higher efficiencies with proper interfacial engineering [114]. Various combinations of materials beyond the example shown in Figure 3.7 are used to make perovskite solar cells in accordance with energy level constraints depicted in Figure 3.6. The energy levels and work functions of various perovskites, charge extraction layers as well as electrodes are shown in Figure 3.8.

In Chapter 2, we presented the J-V curves for a simple p-n junction for conceptual purposes.

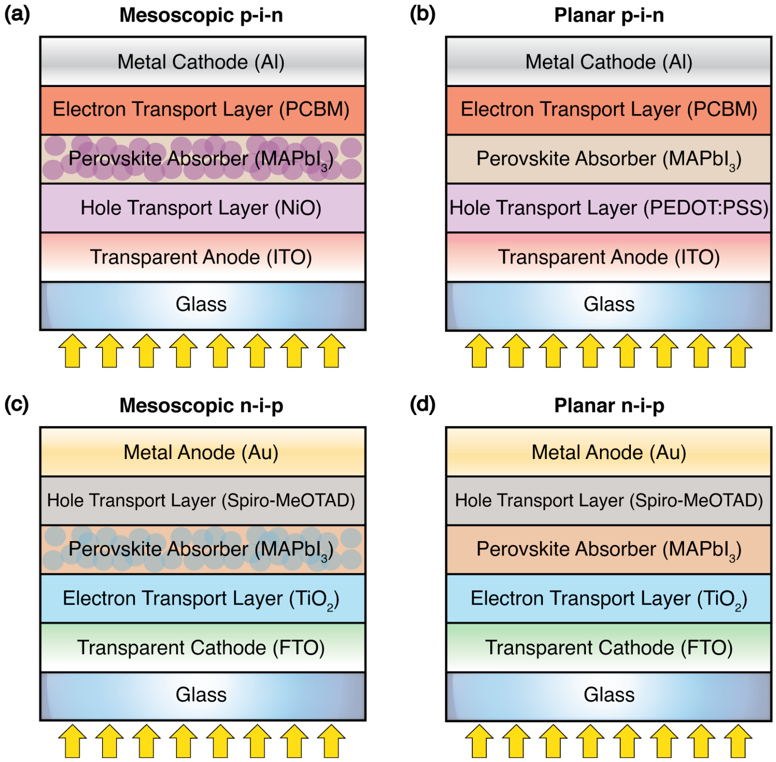

Figure 3.7 Diagram of common perovskite solar cell designs. Adapted from [104].

The energy diagram for the *p*-*i*-*n* differs from that of the *p*-*n* junction, and the profile within a PSC diverges even more as depicted in panels a-c of Figure 3.9. The experimental profiling of the carrier densities along the cross section was initially carried out by Edri et al. using electron beam-induced current (EBIC) measurements [39]. Since the PSC profile is akin to two *p*-*n* profiles placed adjacently, it is therefore natural for the photovoltaic circuit model to have a second diode as well. The added diode in a series scheme is shown in the circuit presented in the inset of Figure 3.9d. This diode modifies the *J*-*V* curves as depicted in the log plot of Figure 3.9d. These curves differ significantly from the ones of the single diode model presented earlier in Figure 2.8. Equation (2.115) is now modified as follows for the double diode model [106]:

$$I = I_{SC} - I_0 \left(e^{\frac{q(V+IR_s)}{(n_I+n_{II})k_B T}} - 1 \right) - \frac{V + IR_s}{R_{sh}} \tag{3.3}$$

Where we now have two ideality constants n_I and n_{II}, one for each diode, in the denominator of the exponential argument. Typical values for PSC ideality constants range from 2 to 4 [106]. For further accuracy in modelling the *J*-*V* curves, it is also customary to include a term for the recombination current besides the diffusion current. The recombination term

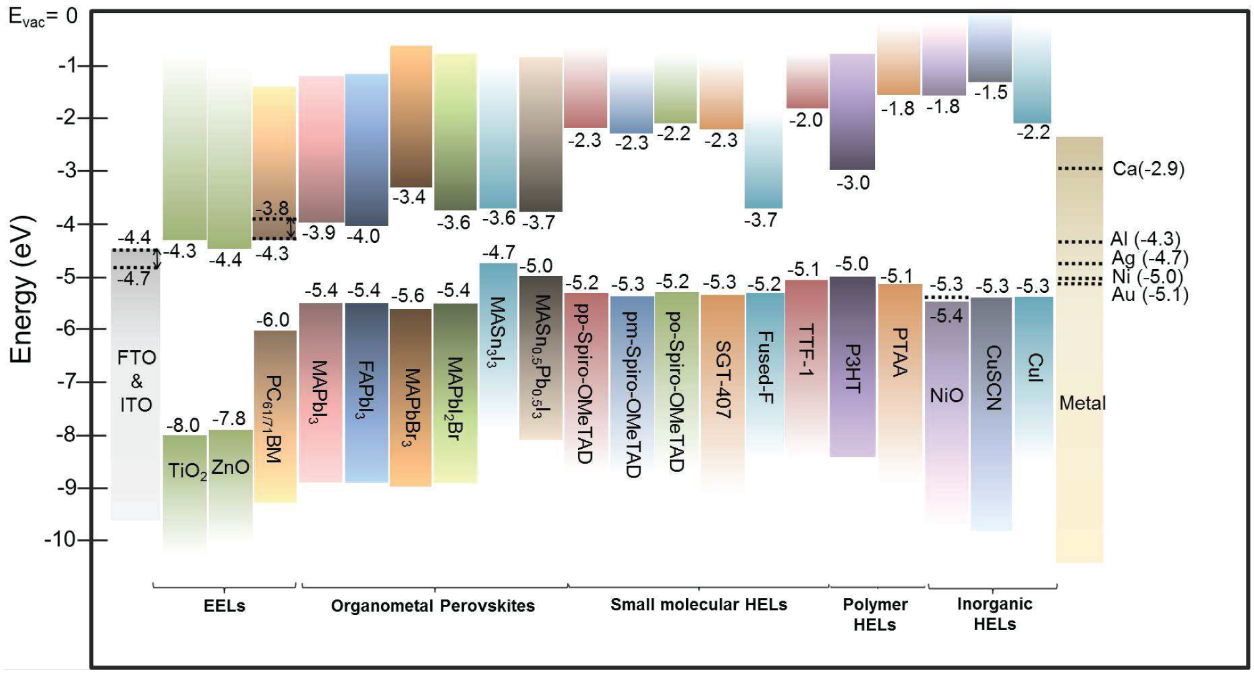

Figure 3.8 Energy diagram of perovskites, extraction layers and electrodes. Reproduced from Ref. [105] with permission from the Royal Society of Chemistry.

could be considered as two more diodes parallel to the first two in the circuit. The current is then expressed as [106]:

$$I = I_{SC} - I_R \left(e^{\frac{q(V+IR_s)}{n_R k_B T}} - 1 \right) - I_0 \left(e^{\frac{q(V+IR_s)}{n_{I,II} k_B T}} - 1 \right) - \frac{(V - IR_s)}{R_{sh}} \tag{3.4}$$

Where I_R is the recombination current, $n_R = n_{I,R} + n_{II,R}$, I_0 is the diffusion current and $n_{I,II} = n_I + n_{II}$. Typically, for a well-designed device with proper choice of materials and fabrication routes, I_R is minimal while I_0 is maximized. Hence, proper interfacial engineering and optimization is crucial for good solar cell parameters.

3.4 Film Fabrication and Morphology

Among the multitude of fabrication methods employed for perovskite solar cells, the most popular and widely used ones are the single-step and two-step spin-coating based deposition techniques. In the one-step deposition technique, a perovskite precursor solution is created via mixing of MAX and PbX_2 compounds (X = Br, Cl, I) in a solvent, i.e. dimethyl sulfoxide (DMSO), gamma-butyrolactone (GBL), or dimethylformamide (DMF). The solution is then dripped onto a spinning substrate as shown in Figure 3.10 followed by annealing at a tem-

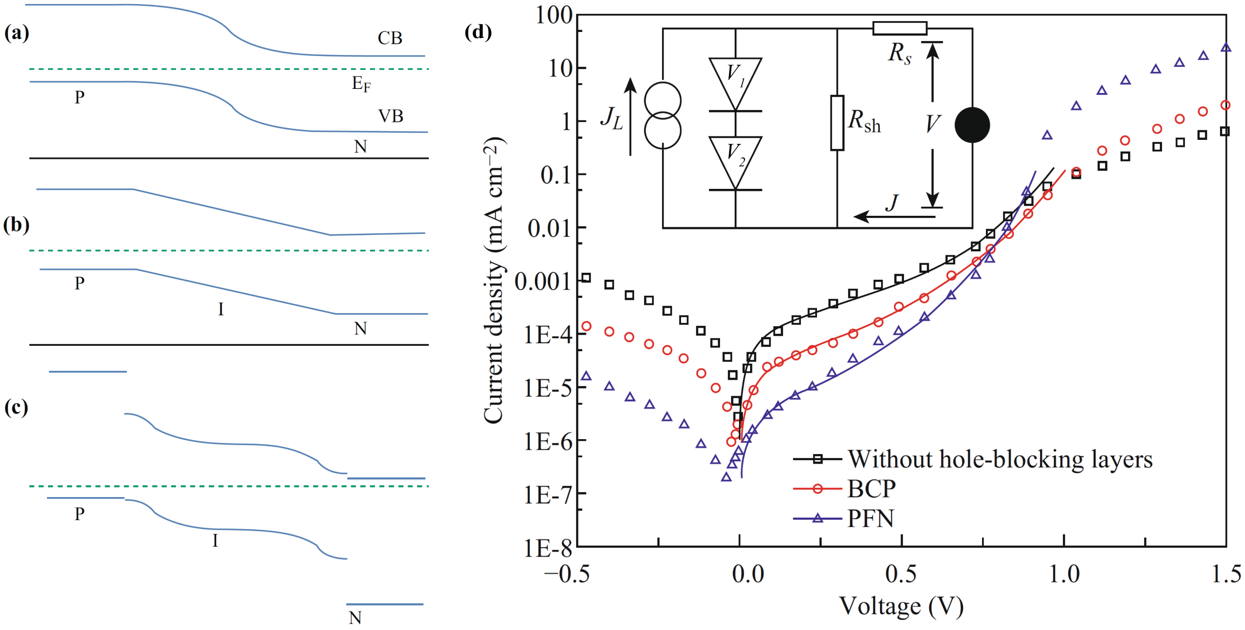

Figure 3.9 Energy band diagram for a) a *p*-*n* junction solar cell, b) a *p*-*i*-*n* solar cell with a homogeneous built-in electric field and c) MAPbI$_{3-x}$Cl$_x$ perovskite-based cell with an inhomogeneous built-in electric field. d) Dark *I*-*V* curves and double junction PV circuit model for PSCs. Adapted from [106].

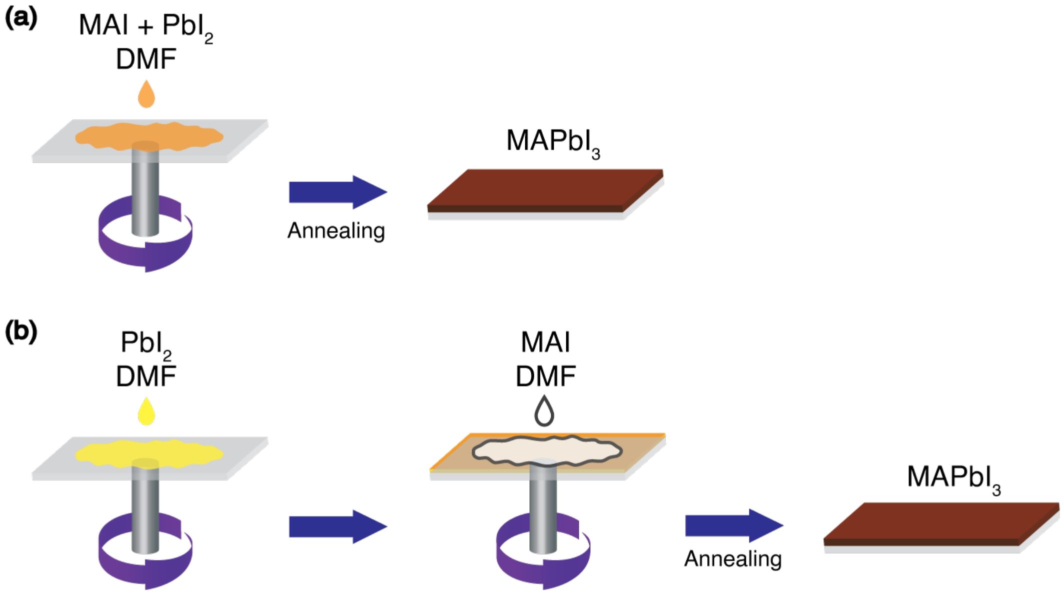

Figure 3.10 a) Single-step deposition method b) Two-step deposition technique

perature between 110 and 150 ℃, resulting in a dark brown crystallized film. Perovskites are surprisingly very tolerant in terms of stoichiometric proportions and allow high efficiencies

Table 3.2 Chronological development of heterojunction perovskite devices [107, 108].

Year	**Type**	**Layers**	**η (%)**	**Authors**	**Ref.**
2009	-	FTO/c-TiO_2/mp-TiO_2/$MAPbI_3$/LE/Pt-coated FTO	3.8	Kojima et al.	[72]
2011	-	FTO/c-TiO_2/mp-TiO_2/$MAPbI_3$ QD/LE/Pt-coated FTO	6.5	Im et al.	[109]
2012	mp	FTO/c-TiO_2/mp-TiO_2/$MAPbI_3$/Spiro-OMeOTAD/Au	9.7	Kim et al.	[110]
	mp	FTO/c-TiO_2/mp-Al_2O_3/$MAPbI_2Cl$/Spiro-OMeTAD/Ag	10.9	Lee et al.	[111]
2013	*n-i-p*	FTO/c-TiO_2/ mp-TiO_2/$MAPbI_{3-x}Cl_x$/Spiro-OMeTAD/Au	15.0	Burschka et al.	[112]
	mp	FTO/c-TiO_2/mp-Al_2O_3/$MAPbI_{3-x}Cl_x$/Spiro-OMeTAD/Ag	12.3	Ball et al.	[113]
2014	*n-i-p*	ITO-PEIE/Y-TiO_2/$MAPbI_{3-x}Cl_x$/Spiro-OMeTAD/Au	19.3	Zhou et al.	[114]
	n-i-p	ITO/ZnO-np/$MAPbI_3$/Spiro-OMeTAD/Ag	15.7	Liu et al.	[115]
2015	*p-i-n*	ITO/PEDOT:PSS/$MAPbI_3$/PCBM/Au	18.1	Heo et al.	[116]
	mp	FTO/c-TiO_2/mp-TiO_2/$(FAPbI_3)_{1-x}(MAPbBr_3)_x$/PTAA/Au	20.1	Yang et al.	[117]
2016	mp	c-TiO_2/mp-TiO_2/$FA_{0.81}MA_{0.15}PbI_{2.51}Br_{0.45}$/Spiro-OMeTAD/Au	19.6	Li et al.	[118]
	mp	FTO/c-TiO_2/mp-TiO_2/$Cs_x(MA_{0.17}FA_{0.83})_{1-x}Pb(I_{0.83}Br_{0.17})_3$/Spiro-OMeTAD/Au	21.1	Saliba et al.	[119]
2017	mp	FTO/c-TiO_2/mp-TiO_2/$(FAPbI_3)_{1-x}(MAPbBr_3)_x$/PTAA/Au	22.1	Yang et al.	[83]
	n-i-p	ITO/c-SnO_2/$(FAPbI_3)_{1-x}(MAPbBr_3)_x$/Spiro-OMeTAD/Au	21.6	Jiang et al.	[120]
2018	mp	FTO/c-TiO_2/mp-TiO_2/$(FAPbI_3)_{0.95}(MAPbBr3)_{0.05}$/DM/Au	22.1	Jeon et al.	[121]
2019	*n-i-p*	FTO/c-TiO_2/CHI-$CsPbI_3$/Spiro-OMeTAD/Ag	18.4	Wang et al.	[122]
	mp	FTO/c-TiO_2/mp-TiO_2/$FAPbI_3$ (MACl treated)/Spiro-OMeTAD/Au	23.5	Kim et al.	[123]
2020	*n-i-p*	FTO/c-TiO_2/CHI-$CsPbI_3$/Spiro-OMeTAD/Ag	25.5	Jeong et al.	[16]

Full form of table acronyms: c – compact or barrier layer, CHI – Chlorine Iodine Interfacial treatment, LE - Liquid Electrolyte, mp - mesoporous, np - nanoparticle, QD - Quantum Dot.

for MAI:PbI_2 ratios ranging from 1:2 to 3:1 [124]. Despite the compositional tolerance, perovskites require proper control of external factors such as ambient temperature, humidity, O_2 levels as well as deposition parameters such as spin-coating time, velocity, acceleration, and processing temperatures for optimal high efficiency films. Beyond the one, and two-step deposition techniques, there are many others such as vacuum deposition, hybrid vapor assisted solution processing, meniscus coating and doctor blading. The type of coating technique as well as management of parameters have extreme implications in terms of sample morphology. Morphological aspects such as coverage, grain size and defect concentration in grain boundaries play a key role in determining device quality.

Previously, we presented the usage of mixed halides as a stabilizing solution to achieve both an ideal bandgap as well as a tolerance factor close to unity. There are also morphological reasons to opt for this composition such as increased grain size and smoother films. Although the role of chloride in enhancing the film quality [125, 126] as well as electrical transport properties is still debated hotly, currently, the addition of Cl^- seems to inhibit the formation of both PbI defects [127] and interstitial defects [128]. The incorporation amount "x" has

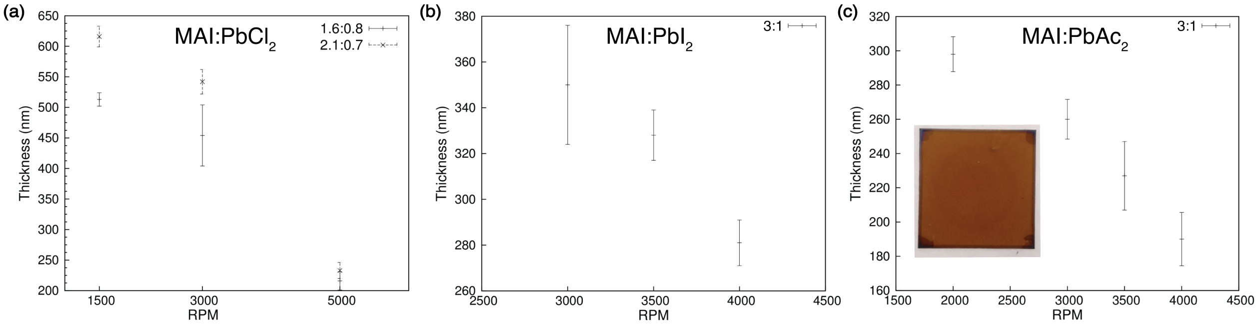

Figure 3.11 $MAPbI_3$ spin coating thickness calibration for a) $PbCl_2$, b) PbI_2 and c) $PbAc_2$ precursors. Data courtesy of Soroush Hafezian.

been confirmed to be less than 3-4 % [88]. Despite large amounts of chloride precursors in the initial solution, most of the Cl^- seems to evaporate during the annealing process when it is stuck in an intermediate phase of low sublimation enthalpy, i.e. a mixture of MACl and MAI. The loss of mass occurs either during an initial drying phase or the annealing process. This was confirmed using thermal gravimetric analysis (TGA) by Yantara et al. [89]. Interestingly, excess MACl and MAI act as critical agents in slowing down the crystallisation rate, thereby resulting in a very smooth film.

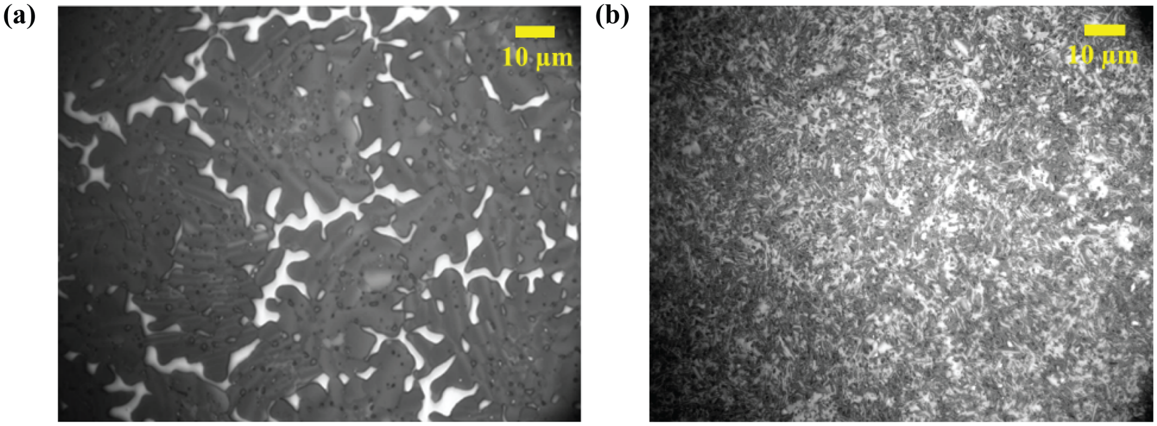

Figure 3.12 CCD camera image of a) toluene washed film versus b) untreated $MAPbI_3$ ($PbCl_2$ precursor) sample.

The application of above-mentioned single-step deposition method is demonstrated here for $MAPbI_3$ thin film samples in our experiments. Using a 99.9% purity PbX_2 (X = Cl, I, Ac) compound (Sigma-Aldrich) and MAI (Lumtec), we make a 3:1 MAI:PbX_2 ratio solution at 40 wt. % in DMF, which is subsequently left to stir for 24 hours. For deposition, we use $25 \times 25 \times 1$ mm^3 UV-ozone treated glass substrates which are initially cleaned using detergent, deionized water, acetone, and isopropanol. We then spin coat 250 µL of the $MAPbI_3$ solution at RPMs between 2000 to 4000 for a duration of 30 secs while toluene washing in the last 15 secs. The sample is annealed on a hot plate at a temperature of 100 ℃, after which, one final layer of PMMA is subsequently spin-coated for 5 minutes for moisture resistance. A calibration measurement indicates the average thickness for a sample to be around 300 to 400 nm for RPMs used above (Figure 3.11a).

Above all, for drastic morphological improvement, adding an extra step of anti-solvent treatment in the spin-coating process appears to be key. The films shown in Figure 3.12 show the effects of toluene washing on a $MAPbI_3$ ($MAI{:}PbCl_2$) sample. These samples are made via spin-coating of the perovskite solution directly onto UV-ozone (~15 mins) treated glass substrates. In panel a, the toluene anti-solvent washes away most of the DMF from the deposited solution and increases aggregation; thereby resulting in larger "islands" that are ideal for PL measurements. This is in stark contrast to the case without anti-solvent treatment in panel b where holes are evenly spread across the film. The toluene washed sample in panel a can still be improved to cover the bright boundary zones between islands, where a clear lack of coverage is observed.

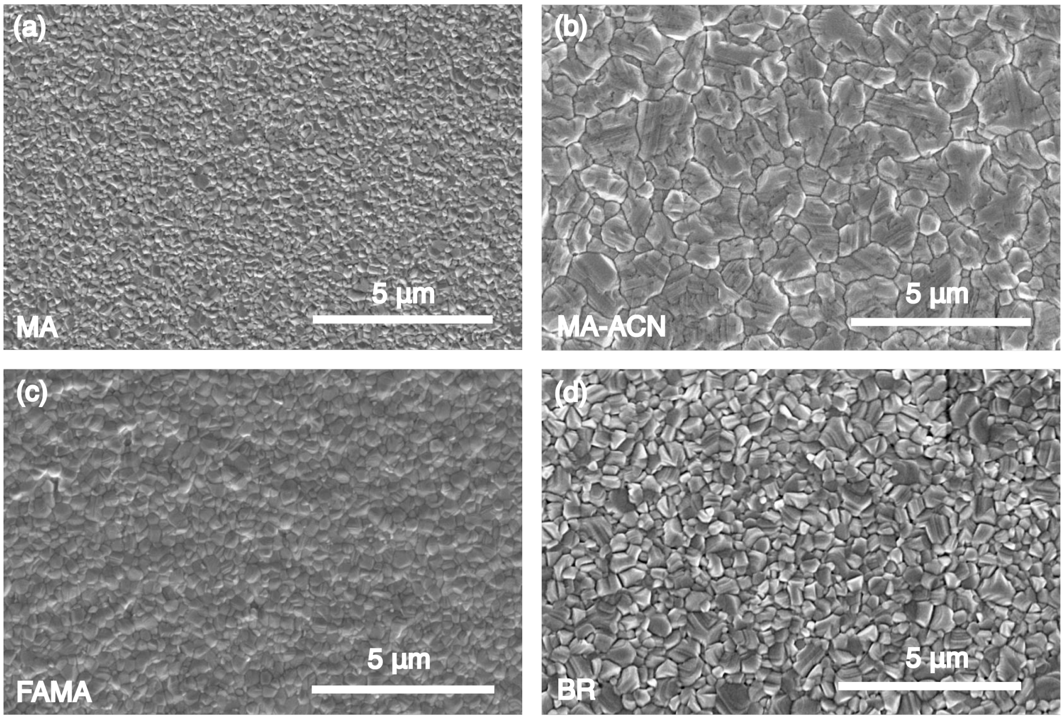

Figure 3.13 SEM images of the studied samples. a) Antisolvent-processed $MAPbI_3$, b) Acetonitrile-processed $MAPbI_3$, c) $FA_{0.85}MA_{0.15}Pb(I_{0.85}Br_{0.15})_3$ and d) $MAPbBr_3$. Fabricated by Nakita K. Noel.

Similarly, SEM images of some perovskite samples used in our experiments (Chapter 5), treated using a different anti-solvent, i.e. anisole, are shown in Figure 3.13. The images shown here are characteristic of films used in high efficiency devices [129, 130]. The most important factor determining the quality of the film is the coverage of the substrate surface. Once again, the addition of anisole, combined with proper spin-coating parameter control, results in films which have tightly packed crystals with no visible pinholes. The effects of composition and processing on the film formation is well illustrated in this figure. For example, the inclusion of acetonitrile processing in the $MAPbI_3$ leads to the formation of large crystals with well defined borders. $MAPbBr_3$ appears to be much grainier and rougher compared to the other films. In a device, this may translate to undesirable optoelectronic consequences in terms of carrier transport because of increased resistance from uneven contact between adjacent grains. Lastly, $FA_{0.85}MA_{0.15}Pb(I_{0.85}Br_{0.15})_3$ seems extremely smooth with barely visible boundary lines between crystals. This represents a conducive environment for good carrier transport.

3.5 Device Fabrication and Performance

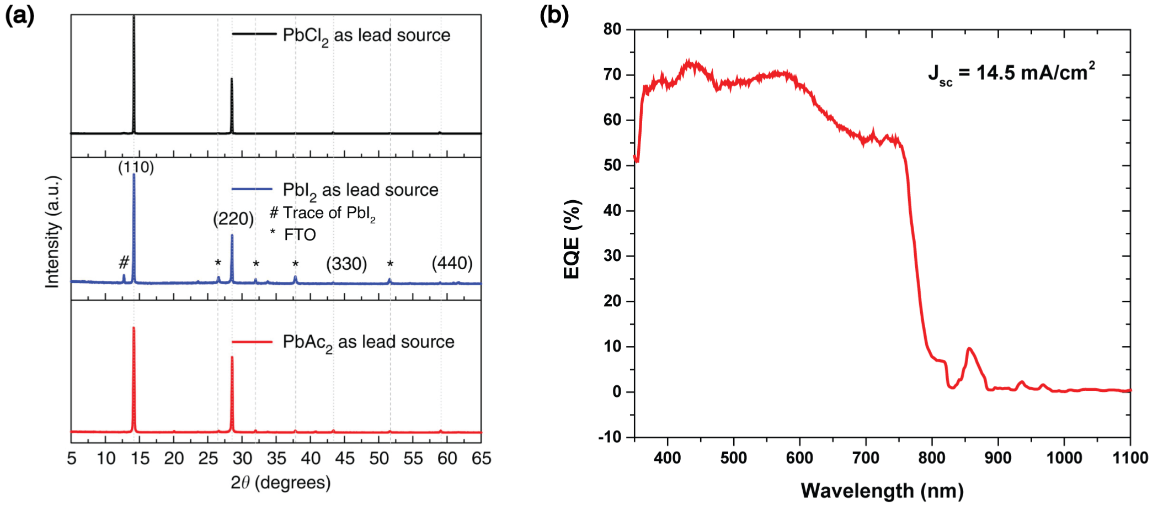

Figure 3.14 a) XRD of thin films deposited on FTO. b) EQE of $MAPbI_3$ fabricated through $PbAc_2$ precursor. The J_{sc} is calculated using Equation (2.108).

One way to see if our carrier transport measurement results are relevant is to verify whether the thin film sample fabrication process also results in working devices. Using the mixed halide composition described in the previous section, we also attempted to fabricate devices. Both the initial XRD and EQE results for our samples were promising in terms what can be expected for a functioning cell (Figure 3.14). As for the XRD data in panel a, samples made from the $PbCl_2$ and $PbAc_2$ precursors, in particular, show very clean crystallographic lines which are characteristic of the mixed halide perovskite introduced earlier in Figure 3.4. PbI_2 however, appeared to have traces of contamination based on the emergence of smaller peaks. Regarding the $PbAc_2$ EQE data shown in panel b, the percentages observed are quite high although not to the extent of other entries in literature. Using Equation (2.108), our theoretical short-circuit current density J_{sc} is found to be 14.5 mA/cm^2 in this particular thin film.

Let us look at the detailed fabrication process for the devices of ITO/PEDOT:PSS/MA-PbI_3/PCBM/Ag architecture. We decided to proceed with $PbCl_2$ and $PbAc_2$ precursors for devices and characterization measurements based on the superior XRD lines. For both precursors, we used a 3:1 MAI:$PbCl_2$ molar ratio (40% wt.). Patterned ITO substrates are initially cleaned and treated via UV-ozone as mentioned earlier. A PEDOT:PSS solution is sonicated for 30 minutes, processed through a 0.45-micron Nylon filter and spin-coated on to the substrate at 5000 rpm (60 nm thickness), after which, annealing is done at 120 ℃. The perovskite solution is applied on top of the PEDOT:PSS using the method described previously for thin films. This step is followed by the spin-coating of PCBM at 3000 RPM (60 nm thickness) and subsequent annealing at 110 ℃. In the final step, 150 nm of Ag is vacuum deposited inside a thermal vapor deposition system onto the sample.

Current-voltage curves for a $PbCl_2$ sample consisting of six devices are presented in Figure 3.15. The data is shown for both dark and AM1.5G illumination (Figure 2.7). Only three of the devices in this sample were working and so only these results are shown. Unfortunately, these devices were of low quality in terms of efficiencies as shown in Table 3.3 despite the anti-solvent treatment. The slope on the right side is almost steep enough to follow the ideal I-V curve as well, indicating a significant amount of series resistance present in the transport layers as well as electrode interfaces. Our perovskite devices, in panel b, and most cells of all architectures reported in literature exhibit hysteresis in the I-V curves [131]. Hysteresis refers to a situation where the current dependence on voltage is non-identical amongst the

Table 3.3 Device Parameters from J-V curves for ITO/PEDOT:PSS/$MAPbI_3$ (MAI:$PbCl_2$ - 3:1)/PCBM/Ag architecture sample of six devices.

Device	V_{oc} (V)	J_{sc} (mA/cm^2)	FF (-)	η (%)
1	0.28	12.4	0.31	1.11
2	0.4	17.8	0.31	2.22
6	0.46	19.8	0.33	3.01

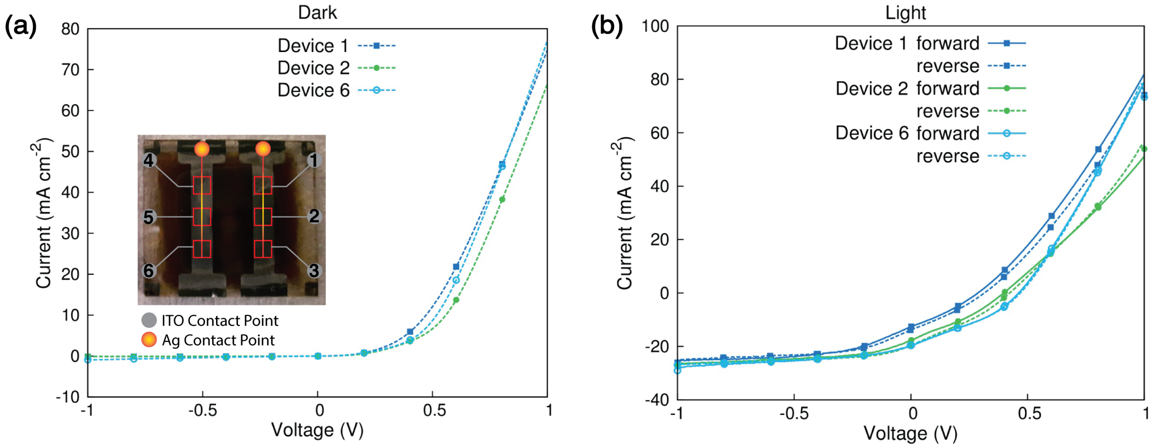

Figure 3.15 *J*-*V* curves for ITO/PEDOT:PSS/$MAPbI_3$ ($MAI:PbCl_2$ - 3:1)/PCBM/Ag architecture sample of 3 out of 6 working devices. a) Dark (forward scan only) and b) 1 Sun (1000 W/cm^2) illumination. Fabricated by Soroush Hafezian.

forward and reverse sweeping directions. The fundamental reasons behind this phenomenon are heavily debated. However, processes such as ionic migration, ferroelectric domains, charge trapping, and capacitive effects are proposed as probable causes [107]. Similarly, we have also measured the *J*-*V* curves for solar cells made from a $PbAc_2$ route (Figure 3.17). The devices parameters are shown in Table 3.4.

For this sample, all six devices were working, and their power conversion efficiencies span over 8.33% to 12.2%. These values compare well with many of the early papers published for this architecture. The kinks in the *J*-*V* curves are most likely a consequence of recombination currents presented previously in the double diode model. These results show that our $PbAc_2$ perovskite films are of quality comparable to those used to fabricate high-efficiency solar cells. As a result, it is highly expected that future diffusion measurements using these samples will

Table 3.4 Device Parameters from *J*-*V* curves for ITO/PEDOT:PSS/$MAPbI_3$ ($MAI:PbAc_2$ - 3:1)/PCBM/Ag architecture sample of six devices.

Device	V_{oc} (V)	J_{sc} (mA/cm^2)	FF (-)	η (%)
1	0.90	27.3	0.38	9.45
2	0.91	29.0	0.46	12.2
3	0.80	29.5	0.44	10.6
4	0.78	26.3	0.45	9.2
5	0.84	28.0	0.43	10.3
6	0.71	27.3	0.43	8.33

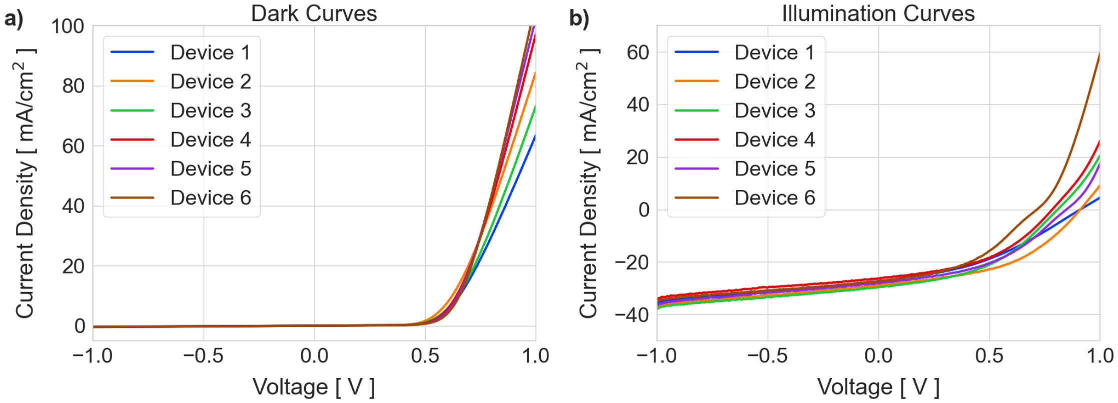

Figure 3.16 *J*-*V* curves for ITO/PEDOT:PSS/MAPbI$_3$ (MAI:PbAc$_2$ - 3:1)/PCBM/Ag architecture sample with 6 out of 6 working devices. Forward scans for a) Dark and b) Under 1 Sun (1000 W/cm^2) illumination. Fabricated by Soroush Hafezian.

provide new insight into the charge transport phenomena of these PSCs. Although the results shown here are in line with reported values for devices in literature, it is quite clear from panel b that the shunt resistance is not high enough. When the shunt resistance tends towards infinity (or a realistic large value), the bottom part of the light curve is perfectly flat, as explained previously in Figure 2.8. The decreased shunt resistance here is most likely due to pinholes that span across the device cross-section. The pinholes get filled with metal during the fabrication and this leads to current leaks between the electrodes, thereby lowering the shunt resistance. Although the PbAc$_2$ precursor is much better than PbCl$_2$, for our preliminary measurements, we will characterize both samples to get a base calibration for different perovskite films, independent of their performance efficiency.

3.6 Excitons or Free Carriers

An important question to be addressed is the nature of excitons generated or formed in MAPbI$_3$ perovskite films. Excitons are bound charge carriers which come to existence when Coulomb interaction between carriers in a material is significant. Based on whether carriers are separated by more than one lattice site, excitons can be categorized as either Frenkel exciton or a Wannier-Mott (delocalized). Carriers in Frenkel excitons are closely bound to a single site and have an effective Bohr radius on the order of the lattice parameter as opposed to Wannier-Mott excitons which span over multiple atoms. Wannier excitons are modelled in a similar fashion to the hydrogen atom in bulk semiconductors and are characterized by a total excitonic energy:

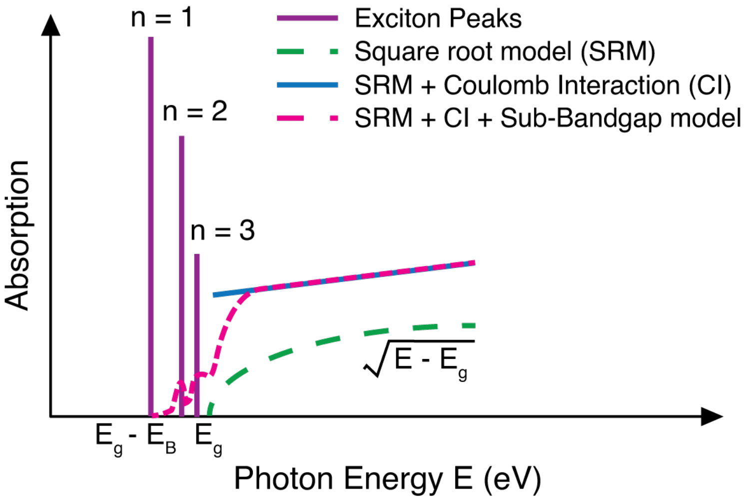

Figure 3.17 Schematic diagram of the absorption spectrum with inclusion of Coulomb Interaction, room temperature excitons and sub-bandgap absorption modelling. Adapted from [48].

$$E\left(n\right) = E_g - \frac{1}{n^2}\left(\frac{m^*}{m_0\epsilon_r^2}R_H\right) = E_g - \frac{R_X}{n^2} \tag{3.5}$$

Where R_H is the Rydberg constant, m^* is the reduced mass, and lastly R_X is the exciton Rydberg constant. We define the exciton binding energy $E_b = R_X$ for $n = 1$. When excitons are present, the square root model for the absorption spectrum presented in Equation (2.31) is strongly modified (Figure 3.17) by both Coulomb interaction and sharp peaks which decrease with n near the band edge for energy values derived from Equation (3.5). Mathematical modelling for absorption under these circumstances will be presented in Chapter 5 in detail. The relevance of excitonic effects depends critically on the exciton binding energy. For example, at room temperature, i.e. $T = 300K$, E_b should be higher than k_BT 25 meV for excitons to exist. Exciton dissociation and carrier production at the extraction layers of a solar cell is an energy consuming step which encompasses a multitude of transfer processes. Therefore, excitons in perovskite devices significantly lower both the short-circuit current and the fill factor, as demonstrated by Yang et al. [64]. Therefore, E_b is vital in determining whether a particular material is suitable for photovoltaic applications. As for perovskites, the first calculations on this subject were performed in 1994 by Hirasawa et al. on $MAPbI_3$ where estimations of 28 Å, ~37 meV and $0.12m_0$ were presented for the exciton Bohr radius, binding energy and reduced mass, respectively [132]. The relatively large radii of ~20-30 Å indicate that excitons in perovskite are of the Wannier-Mott type [133]. In 2013, the question of excitons versus free charge carriers was addressed by D'innocenzo et al. [35].

Through temperature-dependent absorption line width measurements, they estimated the exciton binding energy to be ~50 meV. However, Miyata et al. used a direct method, i.e. high field magnetic spectroscopy, to probe the exciton binding energy in $MAPbI_3$ thin films at low temperatures [134]. Their experiments reveal a much smaller binding energy value of ~16 meV which better supports the idea of a purely free charge carrier-based recombination at room temperature. In $MAPbBr_3$, the exciton binding energies were reported to be rather high (~150 meV). Excitons are quite visible in the absorption spectra of bromide perovskites and marked by a sharp exciton peak near the band edge as shown in Figure 3.5. Although later studies showed a reduced value of ~76 meV for E_b, this is still above the room temperature threshold of 25 meV, thus making these materials suboptimal for photovoltaic applications. As for mixed-cation mixed-halide perovskites, excitonic presence appears negligible based on the lack of sharp peaks in the absorption spectrum in Figure 3.5. In fact, recent temperature-dependent electro-reflectance spectroscopy measurements indicate these materials exhibit an even lower binding energy than $MAPbI_3$ at room temperature [135]. With the inclusion of Cs^+ alongside FA^+, a suppressed phase-transition is observed, leading to lowered binding energies between 24-32 meV, rather than 36-41 meV [135]. Excitons could be included in carrier dynamics through the exciton mass-action law for an electron gas combined with the Saha equation [28, 35]. The law of mass-action can be written as:

$$np = n_X n_{eq} \tag{3.6}$$

Where we can use the Saha equation to calculate equilibrium density n_{eq}:

$$n_{eq} = \left(\frac{\mu_X k_B T}{2\pi\hbar^2} \right)^{3/2} e^{-\frac{E_b}{k_B T}} \tag{3.7}$$

From the equation, we notice that exciton density is always a function of both electron and hole density in the system. The exciton binding energy E_b plays an important role in determining n_{eq} and therefore n_X. Throughout this work, although some theory will be detailed as in the case above, excitons will be assumed negligible for most circumstances. Only free carriers will be considered in our photophysical models based on the observed low binding energies at room temperature for the vast majority of materials in the 3D perovskite family [136].

3.7 Recombination Pathways

The photophysical model in halide perovskites is an important aspect that requires proper understanding. One question that comes to mind is how do processes such as generation, recombination, and diffusion fair quantitatively in perovskite films. A starting point to this question is the model for recombination kinetics detailed by Stranks et al. [31]. Using their model, one can better elucidate the nature of carrier dynamics and how this ultimately affects device parameters. A basic assumption of their photophysical model is that depopulation from trap states occurs at a constant rate. This is reasonable considering the much longer trap depopulation timescales (ms to second) in comparison with those of recombination processes (µs), which are several orders lower. Also, excitons and free charge carriers are assumed to be in thermal equilibrium. Saba et al. have also presented very similar results with some variation in the rate equations [37]. Their experimental data also indicate that exciton recombination is quite negligible with free charge carriers being the dominant species.

In $MAPbI_3$, as in any typical semiconductor, vacancies (MA, Pb, I) and interstitial (Pb, I) defects have been verified within the band structure [137–142]. The identification of the dominant trapping mechanism, i.e. hole versus electron traps, in perovskites is currently an unresolved issue. This question was studied by Wetzelaer et al. [32]. *J-V* curves for the double carrier, hole-only and electron-only devices reveal a drop in current values for the electron-only devices. They attribute this drop in current values principally to electron traps. However, thermally stimulated currents (TSC) measurements were done for hole-only devices by Qin et al. [143]. They compared the TSC spectrum of the degraded hole-only devices with the degraded PSC devices and found identical TSC peaks (trapping states) at temperatures of 161 K and 213 K for both samples, thereby suggesting holes to be the main trapped charge carriers. Further theoretical predictions and experimental studies also seem to indicate hole trapping as the dominant mechanism [142, 144]. The large density of hole traps is attributed to iodine rich areas, containing significant dangling bonds, which reduced the carrier lifetimes [145]. Considering the contradictory reports, the nature of the traps is still a mystery and more work in this direction is crucial to have an accurate understanding of carrier dynamics. In this work, we assume electron trapping as the dominant pathway in line with the two works on which our model is based [31, 37]. Therefore, we present an adaptation of both models as schematized in panel a of Figure 3.18. The corresponding rate equations for both excitons and charge carriers are as follows:

$$\frac{dn}{dt} = R_d n_X - R_f np - k_1 n - k_2 np - k_3 np^2 + P \tag{3.8}$$

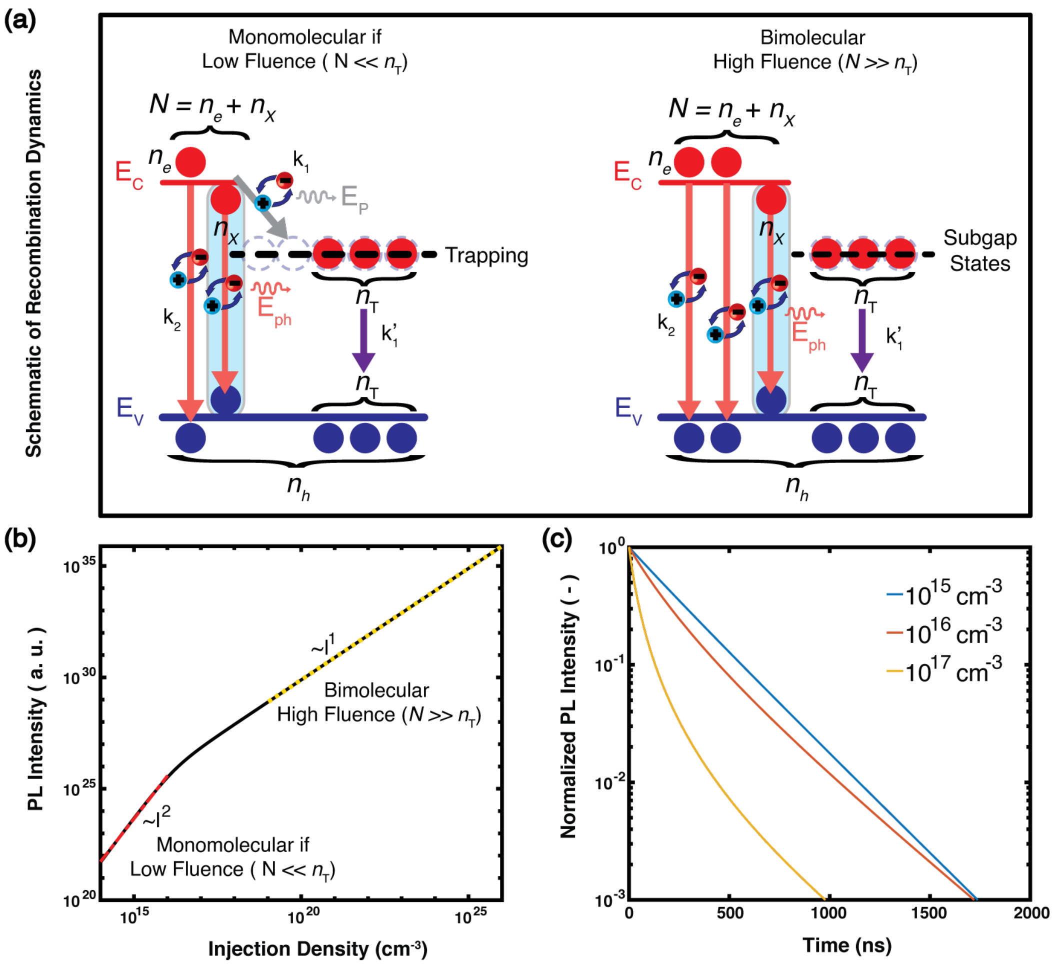

Figure 3.18 : a) Schematic of photophysical processes at low and high fluences. Modelling for b) Power dependence and c) PL lifetimes at different fluences. Adapted from [31].

$$\frac{dp}{dt} = -k_2np - k_3np^2 - k_1'pn_t + P \tag{3.9}$$

$$\frac{dn_t}{dt} = k_1n - k_1'pn_t \tag{3.10}$$

$$\frac{dn_X}{dt} = R_fnp - R_dn_X - k_Xn_X \tag{3.11}$$

$$PL = k_Xn_X + k_2np \tag{3.12}$$

Where R_f is the exciton formation rate, R_d is the exciton dissociation rate, $k_1 = \gamma_1(N_t - n_t)$ is the trapping rate for electrons, k_2 is the bimolecular recombination coefficient, k_3 is the Auger recombination coefficient, k_X is the monomolecular exciton recombination rate, k_1' is the trap depopulation coefficient, N_t is the density of available traps, n_t is the density of occupied traps, P is the carrier injection rate, n_X is the exciton density, n is the electron density, p

is the hole density, the bimolecular recombination rate and $R(N)$ is the rate of spontaneous emission. In line with assumptions regarding excitons, note that we have $R_f = 0$, $R_d = 0$ and $k_X = 0$ for our modelling, for which, the results are shown in Figure 3.18.

The coupled differential equations were solved in MATLAB for three different carrier densities, i.e. 10^{15}, 10^{16} and 10^{17} cm^{-3}. The parameters for the fitting, taken/inspired from literature [31, 37], are as follows: $N_t = 2.5 \times 10^{16}$ cm^{-3}, $\gamma_1 = 2 \times 10^{-10}$ cm^3s^{-1}, $k_1' = 8 \times 10^{-12}$ cm^3s^{-1}, $k_2 = 1.3 \times 10^{-10}$ cm^3s^{-1} and $k_3 = 4 \times 10^{-28}$ cm^3s^{-1}. For low fluences, the population n_t present in the subgap trap states N_t is higher than the population of photoexcited species N found in the conduction band. In this regime, SRH recombination is the dominating process, and a corresponding squared dependence is observed in panel b of Figure 3.18 at lower densities. A single exponential trend is observed in the PL decay curves at 10^{15} cm^{-3} (Figure 3.18c). However, at higher fluences, the trap states are saturated, and the conduction band has a greater population. As ΔN becomes higher with injection, bimolecular recombination starts to dominate. This regime is nascent around densities of 10^{16} cm^{-3} but becomes full-fledged at 10^{17} cm^{-3} (Figure 3.18b). The lifetimes plots show a corresponding fast decay component at higher densities in Figure 3.18c. The calculations shown here will later serve as reference for our preliminary characterization measurements detailed in Section 3.9.

3.8 Advances in Carrier Transport Imaging

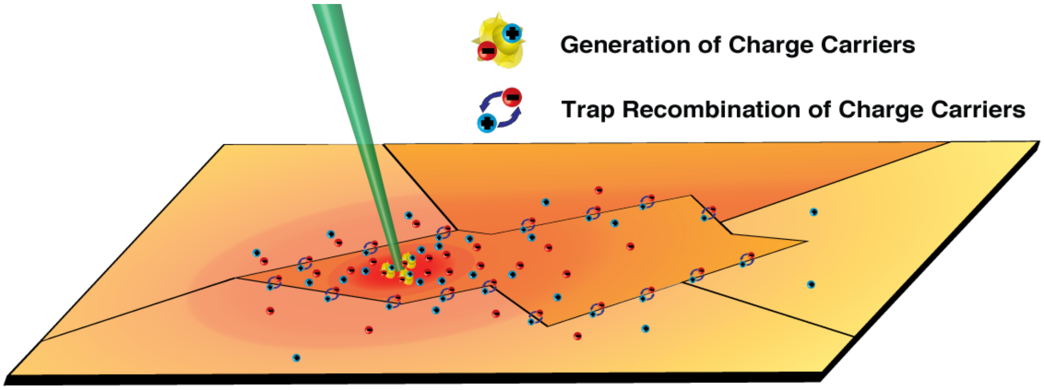

Figure 3.19 Schematic showing grain boundaries acting as carrier recombination centers under laser illumination. A depiction of anisotropic diffusion typically observed in microscopy measurements is also highlighted by the brighter grain at the top.

Long carrier diffusion lengths have been identified as an important aspect enabling high efficiencies in planar heterojunction architectures, but reports differ greatly with respect to reported values. In methylammonium lead iodide ($\mathrm{MAPbI_3}$) and $\mathrm{MAPbI_{3-\mathit{x}}Cl_\mathit{x}}$ thin films, i.e. $\mathrm{MAPbI_3}$ processed from a $\mathrm{PbCl_2}$ precursor to improve film quality, photoluminescence (PL) quenching and transient absorption measurements are used to extract respective diffusion lengths of ~100 nm and ~1 µm in the direction perpendicular to the substrate. This corresponds to diffusion coefficients D = 0.01–0.05 $\mathrm{cm^2s^{-1}}$ [42, 43]. In such measurements, the reduced lifetime in the presence of a (perfectly) quenching interface for one carrier type is fit to the diffusion equation. Alternatively, the diffusion coefficient can be obtained via Einstein's relation, using measurements of the carrier mobility, μ. In $\mathrm{MAPbI_3}$ single crystals, time-of-flight and transport measurements have been used to extract diffusion lengths exceeding 175 µm and up to 3 cm under low fluence excitation [146]. In other single crystal perovskites, mobilities ranging from μ = 105–2000 $\mathrm{cm^2V^{-1}s^{-1}}$ have been measured using the Hall effect, corresponding to D = 3-50 $\mathrm{cm^2s^{-1}}$ [76, 147]. In $\mathrm{MAPbI_3}$ thin films, time-resolved THz conductivity [148] and microwave conductivity measurements [149] have found mobilities of ~30 $\mathrm{cm^2V^{-1}s^{-1}}$ [150], corresponding to D = 0.8 $\mathrm{cm^2s^{-1}}$. Optical conductivity measurements tend to provide slightly higher values than the other techniques given that they yield the sum of both carrier mobilities and probe the motion of charge carriers on the few-nanometer length scale.

Although the direction of most importance to photovoltaic efficiencies is the perpendicular direction, lateral diffusion has been shown to be critical in perovskite films due to the impact of grain boundary recombination on device performance [151]. The study of lateral diffusion also lends itself well to spatially-resolved measurement techniques. For example, spatially-resolved photocurrent measurements have been employed to extract diffusion lengths of L_d = 10–28 µm (electrons) and 27–65 µm (holes) in $\mathrm{MAPbI_3}$ single crystals and to demonstrate unbalanced charge transport in $\mathrm{MAPbBr_3}$ [152]. All-optical methods such as four-wave mixing [153], the related light-induced transient grating technique [154] and transient absorption microscopy [155] are used to analyze in-plane carrier diffusion on thin films without the need for quenching layers. These measurements have yielded values of $L_D(D)$ of 1 µm (2 $\mathrm{cm^2s^{-1}}$), 0.1–0.3 µm (0.02–0.07 $\mathrm{cm^2s^{-1}}$), and 0.2 µm (0.05–0.08 $\mathrm{cm^2s^{-1}}$). These values of D correspond to the ambipolar diffusion coefficient described in Equation 2.85.

The usefulness of optical/spectroscopic techniques, as those mentioned above, is being established rapidly through recent advances in the field of charge carrier transport at both microscopic and macroscopic levels. As previously said, sample morphology and particularly grain properties such as orientation, size and boundary thickness play a significant role in devices performances. Although initial studies suggest that grain boundaries have no impact on carriers, subsequent theoretical calculations indicated to the contrary that grain boundaries indeed act as recombination centers as depicted in Figure 3.19 [156]. For one, the strength of the emitted PL varies from grain to grain depending on the film as reported by DeQuilettes et al. using a combination of confocal and scanning electron microscopy techniques [157]. In some situations, the PL appears confined to a single grain, whereas in others, connected grains are seen to brighten in an arbitrary fashion. Similarly, their non-radiative decay times seem to initially indicate that the darker grain boundaries are non-beneficial for device applications. However, Ciesielski et al. have contrary results to the others mentioned above with longer PL lifetimes at the boundaries as opposed to within [158]. Local compositional aspects and lattice strains have also been proposed as possible causes for the random variations in observed PL properties amongst different grains [159, 160]. This opens the possibility of different spatial diffusion coefficients based on the range that is being studied. For example, over multiple grains, the effective spreading could be lower than the spreading within the grain. Above all, microscopic studies are not typical circumstances of device operation and therefore generalization of results to all scenarios is not applicable. These focussed conditions, on their own, could significantly alter the optoelectronic landscape and therefore interpretation of our results. For example, transient grating measurements by Ščajev et al. reveal the existence of intensity dependent diffusion regimes in perovskites [154]. Last, but not least, effects such as light trapping, photon re-absorption and photon recycling may also contribute in unknown ways due to these focussed conditions. Therefore, development of further experimental and analytical methods to study these phenomena are the need of the hour.

3.9 Preliminary Spatiotemporal Measurements

In this work, we present a new take on carrier transport visualization based on microscopic/spectroscopic techniques through the usage of a streak camera technique for measuring the spatio-temporal carrier/PL spreading. Figure 3.20 presents a detailed schematic of the optical setup used to probe the diffusion of carriers in hybrid perovskite thin films. The streak camera is an instrument which can be used for capturing spatial or spectral data at high temporal resolution. The photoluminescence from the laser-excited sample is imaged using a microscope onto the entrance of the streak camera. For this imaging technique to be successful, a small laser spot, i.e. as close as possible to the diffraction limit, is required (~375 nm diameter at 532 nm). This is only possible if the incoming beam is Gaussian and completely fills the objective aperture. Moreover, the spatial profile of the incoming beam must be clean and devoid of aberrations.

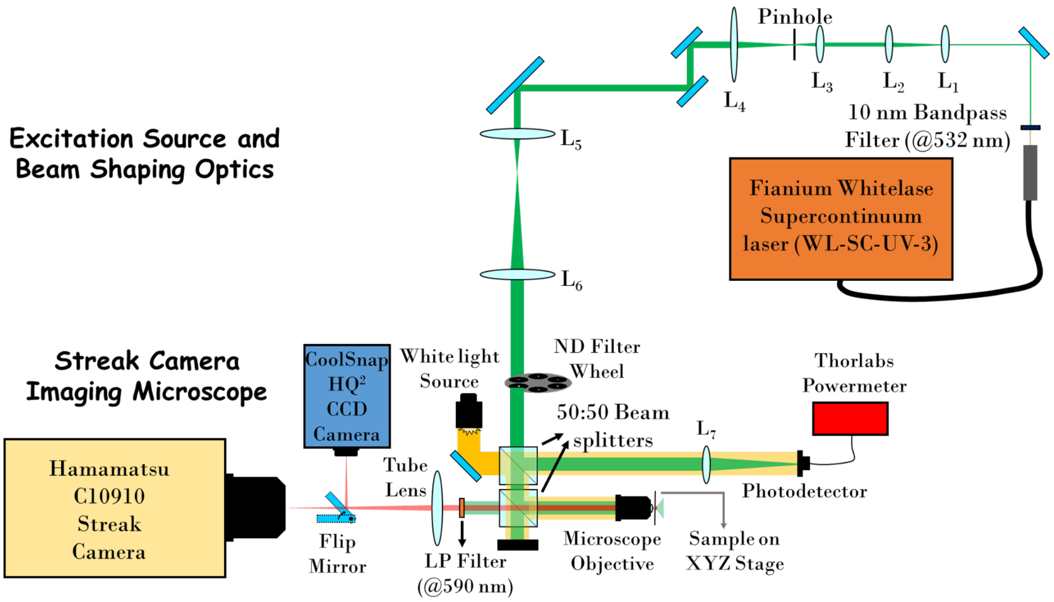

Figure 3.20 Schematic of experimental setup for spatio-temporal measurements.

Two elements are necessary: firstly, beam-shaping optics with a pinhole to clean up the initial laser beam and secondly, telescopes to magnify the beam diameter sufficiently. These components are shown on the top part of Figure 3.20. The optical components for beam shaping are the following: L_1 – 150 mm planoconvex lens, L_2 – -75 mm planoconcave lens, L_3 – 50 mm aspheric lens, L_4 – 200 mm biconvex lens, L_5 – 100 mm achromatic doublet lens, L_6 – 150 mm achromatic doublet lens. L_1 and L_2 first reduce the beam diameter to half of the original size. The beam is then sent to the L_3-L_4 telescope. A 25 µm high-intensity pinhole is used between L_3 and L_4 as a spatial filter to ensure a smooth beam profile. The beam is subsequently guided to the L_5-L_6 lens pair. Magnification values of 4 and 1.5 are induced by the lens pairs L_3-L_4 and L_5-L_6, resulting in a total magnification of 3 at the laser output. Lens L_7 is used to focus the light reflected from the first beam splitter onto the power meter.

The bottom half of Figure 3.20 shows the microscopy and detection part of the setup. The remaining laser power alongside white light is coupled into the microscopy setup for spatiotemporal imaging through the second beam splitter. An coverslip-corrected plan apochromatic Olympus 60X oil immersion objective of 1.42 *NA* and 0.15 mm working distance serves the dual purpose of focusing the beam on the sample and relaying back the collected image from the surface onto the streak/CCD camera through a 200 mm effective focal length (EFL) tube lens. The Fianium Whitelase Supercontinuum Laser (WL-SC-UV-3) was used as the excitation source for this experiment. The broadband picosecond pulses (~48 ps) are

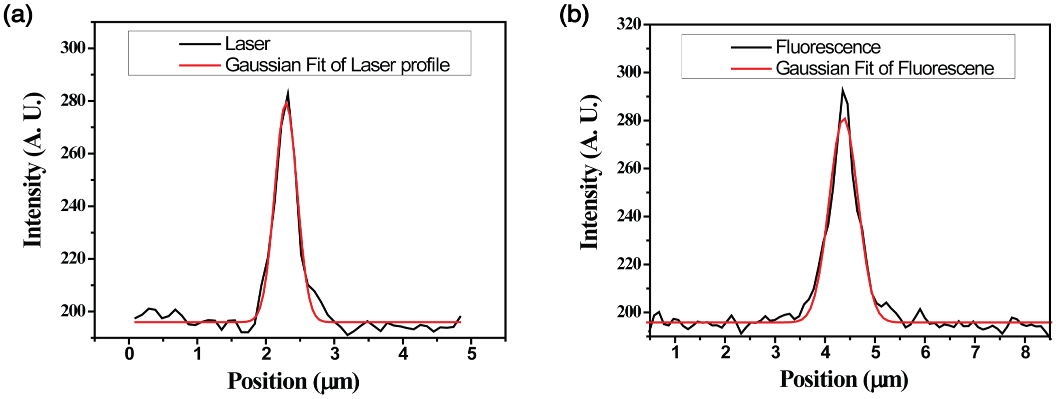

Figure 3.21 For $MAPbI_3$ ($MAI:PbCl_2$) toluene washed sample, we have in a) Laser profile (σ = 191 nm), in b) Fluorescence profile (σ = 338 nm)

first spectrally filtered with a 10 nm bandpass filter centered at 532 nm, which was chosen as the excitation wavelength. Depending on the experimental requirements, the repetition rate of can be varied between 200 kHz and 40MHz using a pulse picker. The measurement presented here was conducted at a rate of 2 MHz.

We started with toluene washed $MAPbI_3$ ($MAI:PbCl_2$) films for our preliminary spatiotemporal characterization of perovskite photophysics. Despite low performances, the toluene washed $MAPbI_3$ ($MAI:PbCl_2$) films are interesting candidates for this experiment due to the large smooth island formations seen earlier in Figure 3.12. An ideal optical alignment can be defined as a perfect overlap of the following focal planes on the sample surface: the image of the surface, the focused laser spot, and the fluorescence spot. This condition can be obtained by fine tuning the camera-tube lens and the objective-sample distances in conjunction. Figure 3.21 shows the laser and fluorescence profiles captured using the CCD camera at ideal alignment. At 532 nm, the standard deviation of the diffraction limited spot ($\lambda/2NA$) for a 1.42 NA objective is ~188 nm. The measured value of 191 nm is thus representative of a well-focused laser. However, the fluorescence will have a greater width due to spreading of the charge carriers as seen in panel b (~382 nm).

The results of our streak camera measurements are presented in Figure 3.22. In a streak camera measurement, the magnified image of the fluorescence spot is sent directly to the entrance slit of the streak camera. The photons, after passing through the slit, strike a photocathode, generating free electrons in the streak tube. A pair of electrodes is used to vertically sweep the electrons using a laser-synchronized electric potential, which is applied to spread the incoming electrons in time. The electrons then pass through an amplifying

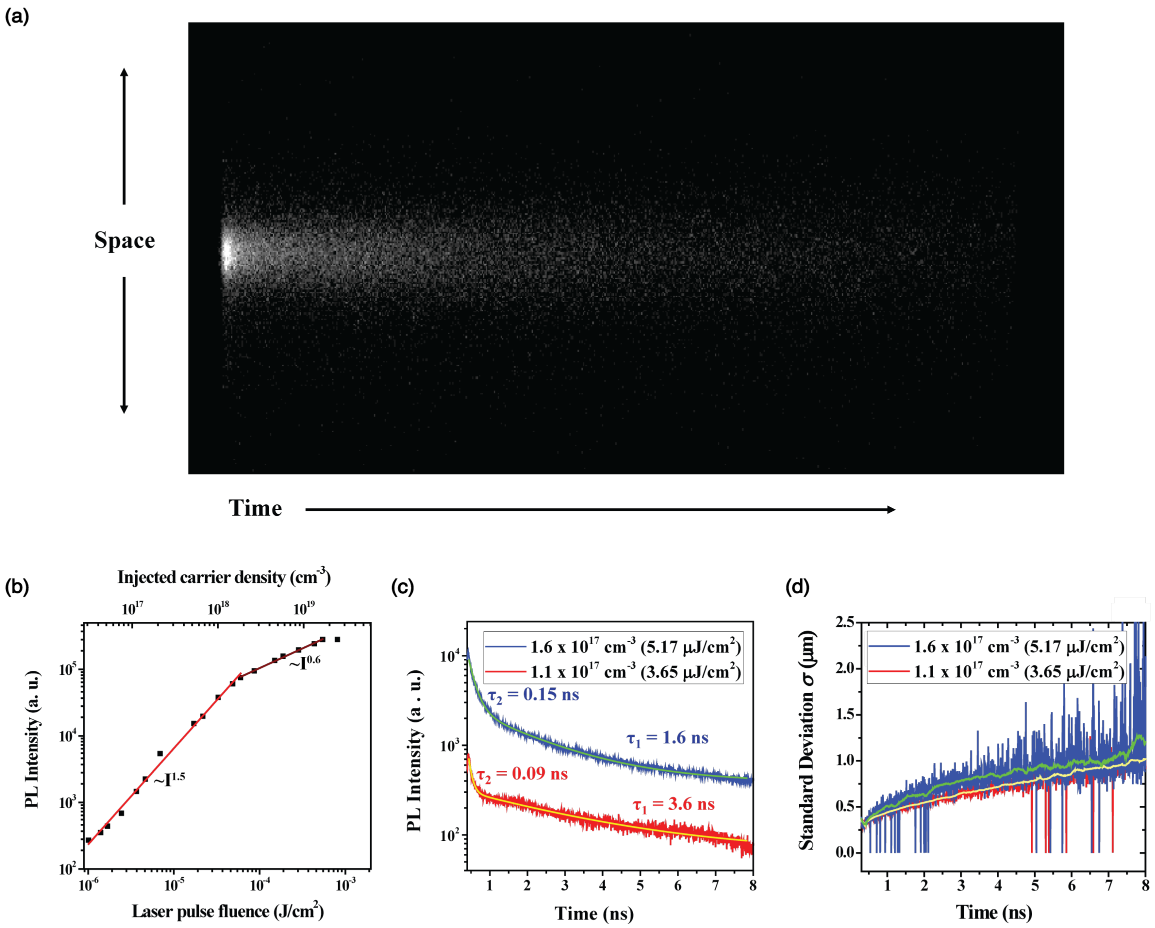

Figure 3.22 For $MAPbI_3$ ($MAI:PbCl_2$), in a) PL streak camera data for 1.1×10^{17} cm^{-3}, b) Power dependence measurement, c) Photoluminescence lifetime decay alongside biexponential fits (solid lines) and in d) Spreading, i.e. standard deviation of PL profile (µm), as a function of time (ns) alongside smooth lines (solid) for injection densities of 1.1×10^{17} cm^{-3} and 1.6×10^{17} cm^{-3}.

micro-channel plate (MCP) and hit a phosphor screen, thereby generating a physical imprint of the spatio temporal data that is captured by a CCD camera at back of the system. In the single sweep mode, the streak camera can resolve data from ~10 ps to ~ ms timescales. For the mixed lead halide perovskite thin film samples, the ideal capture time window was about 10 ns based on their observable lifetime. The spatial spreading with time as observed in the streak camera is depicted in panel a of Figure 3.22 for an injection density 1.1×10^{17} cm^{-3}.

Alongside streak camera measurements, we also studied the recombination pathways to experimentally validate literature data as well as calculations presented in the previous section. For this, we performed a power dependence measurement wherein the intensity of the PL spot, monitored using the CoolSnap HQ^2 CCD camera, is varied as a function of fluence. The measurement results are presented in panel b of Figure 3.22 in a logarithmic scale wherein we have performed linear regression fitting for the two observed recombination regimes. At low fluences, the PL varies to the power of ~1.45 ± 0.03 as a function of intensity, i.e. $PL \propto I^{3/2}$, whereas at higher fluences, the slope was found to be ~0.6 ± 0.02, otherwise $PL \propto I^{0.6}$. The final point on the right side indicates a regime of complete saturation as no more increase is observed. Although inconsistent with our calculation, this power law is in line with results presented by Saba et al. [28, 37]. Since the observed photoluminescence is a result of the band-to-band transition term $U_{b-b} = bnp$, it is quite likely that the density for one of the two carrier types scales to power of 1 with the other scaling to ½ as in $p \propto I^1$ and $n \propto I^{1/2}$ or $p \propto I^{1/2}$ and $n \propto I^1$. This corresponds to a situation where the traps capture a single carrier type, either electron or hole. Although authors assume electron traps to be the dominant recombination pathway, as previously explained, consensus on the subject is yet to be achieved. The focus of the Saba and co-scientists was on elucidating the underlying mechanism for a conducting plasma of Coulomb-correlated electron-hole pairs through photoluminescence and transmission spectroscopy [37]. According to their analysis, the plasma is beneficial for promoting efficient charge separation within the perovskite. Their results however slightly differ from those of Stranks et al. on some points. For one, lifetimes here are in the 10-100 ns scale as opposed to the >100 ns range. Moreover, the bimolecular regime starts at densities of 10^{18} cm^{-3} as opposed to the 10^{17} cm^{-3} value in the other paper. On top of the power law similarity, our threshold for the bimolecular regime, i.e. ~2×10^{18} cm^{-3} shown in Figure 3.21, is also consistent with the Saba et al. model [28, 37].

Time resolved PL curves, obtained via integration of raw streak camera data, are shown for two different injection densities, 1.1×10^{17} cm^{-3} and 1.6×10^{17} cm^{-3}, in panel c for the $MAPbI_3$ ($MAI{:}PbCl_2$) film. We have used a biexponential function to fit the curves and extract monomolecular and bimolecular lifetimes τ_1 and τ_2. Further, we attempted to get a pure monomolecular decay to accurately isolate τ_1, but lower injections did not yield PL data with a meaningful signal-to-noise ratio on the streak camera. For the low fluence curve, the monomolecular lifetime τ_1 is 3.6 ns as opposed to the higher fluence value of 1.6 ns, indicating that bimolecular recombination is influencing this value. Therefore, 3.6 ns is the lower bound for τ_1, corresponding to an upper limit for k_1 of $1/\tau_1 = 2.8 \times 10^8\ s^{-1}$. The order of this value is quite high and potentially indicative of significant quantity of trap state densities within the material. As for the bimolecular lifetime τ_2, we have 0.15 ns and 0.09 ns for the high and low fluence respectively. Intuitively, τ_2 should become smaller with higher densities as it is inversely proportional to n through the relation $\tau_2 = 1/k_2 n$. Since, in our case τ_2 is getting larger, it is highly likely that the biexponential fit is unable to properly account for the contributions of each process. However, the effective lifetime $\tau_{eff} = \left(\tau_1^{-1} + \tau_2^{-1}\right)^{-1}$ of the higher fluence measurement is definitely greater at a value of 0.137 ns, as opposed to the smaller fluence value of 0.088 ns. This indicates that there are more effects at play which need to be explored. The model and values obtained here fail to capture the observed nuances. Nevertheless, both the power dependence and lifetime measurements clearly indicate a strong necessity to account for recombination kinetics and fluence dependence while modelling diffusion in perovskite films. In panel c, we calculated the spreading of the photoluminescence as a function of time. The spreading is quantified through the standard deviation σ of a Gaussian fit to the raw spatial data at every time slice. Looking at this preliminary spreading result, we observe that at time $t = 0$, we have $\sigma = 300$ nm. At 1.1×10^{17} cm^{-3}, by the end of the time window the spreading extends by ~700 nm up to a value of ~1 µm, whereas at 1.6×10^{17} cm^{-3}, we observe an increase of 1 µm from 300 nm to 1.2 µm. The increase in spreading with fluence is quite interesting and requires thorough quantitative modelling on top of experiments for deeper understanding. We will revisit this aspect in Chapter 5.

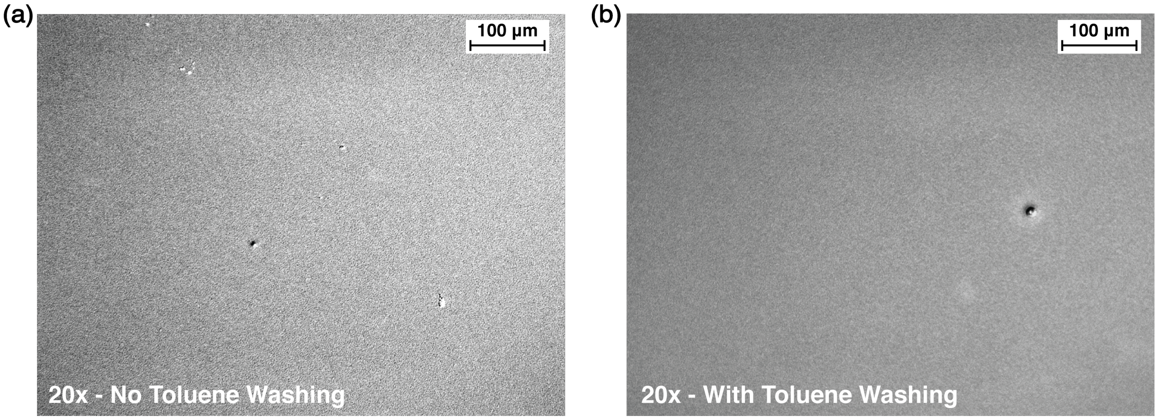

Figure 3.23 Microscope images of $PbAc_2$ precursor based films a) without and b) with toluene washing. The toluene washed film has reduced pinholes.

Besides higher efficiencies, the $PbAc_2$ precursor films also displayed excellent morphological properties, making them ideal for microscopic streak camera measurements. Here, we look at both cases, with and without toluene anti-solvent washing. This was not possible for $MAPbI_3$ ($MAI:PbCl_2$) as the untreated (no toluene washing) sample morphology was too rough for microscopic measurements. This is not the case when using $PbAc_2$ as evinced by the smoothness of both films depicted in Figure 3.23. The lifetime and spatial spreading results obtained using the streak camera are shown in Figure 3.24. Looking at these results, there are many features that stand out. The fluences for the two samples, albeit different,

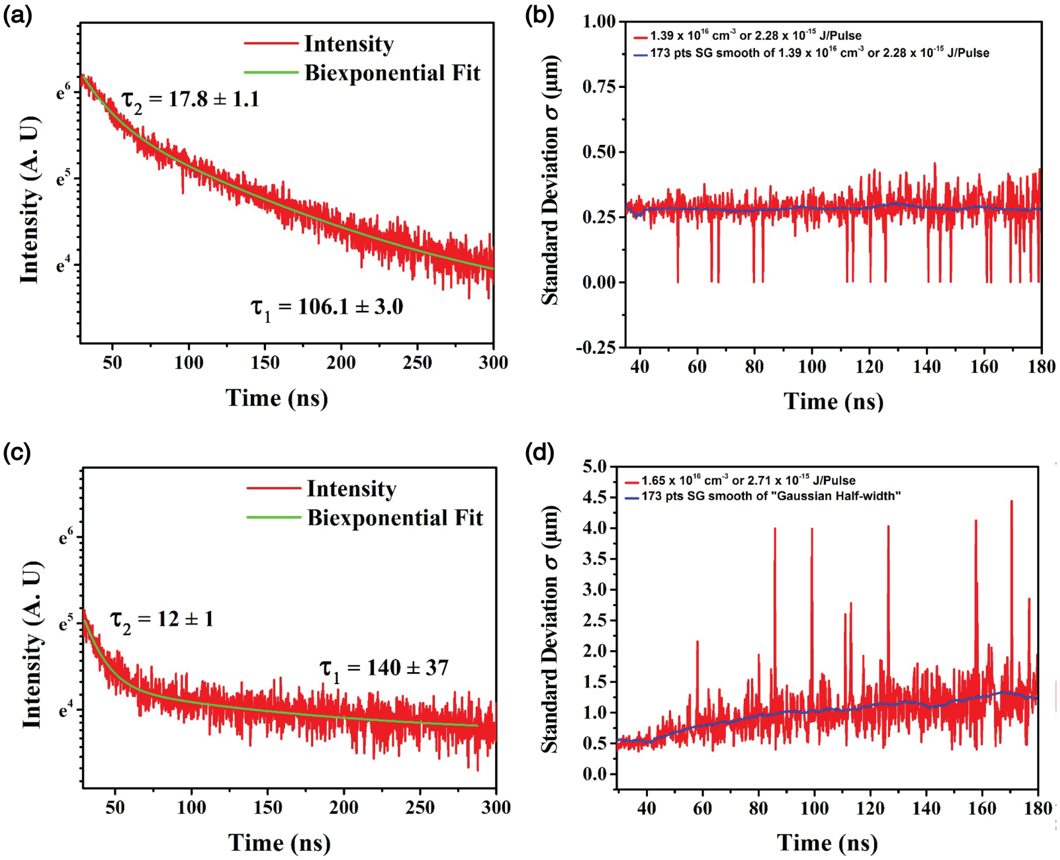

Figure 3.24 a) Lifetime and b) Spatial spreading for a sample without toluene washing and with toluene washing in c) and d). The injected carrier densities for the two samples are 1.39 × 10^{16} cm^{-3} and 1.65 × 10^{16} cm^{-3}.

are still very close in terms of absolute value. We would therefore expect the lifetime curves to look very similar. However, it is easily noticed that monomolecular recombination is now more suppressed when toluene is used, i.e. 140 ns (panel a) as opposed to 106.1 ns (panel c). This indicates that the anti-solvent treatment has most likely led to the passivation of many traps within the perovskite. Furthermore, the bimolecular component is more dominant despite similar fluences from the shorter lifetime of 12 ns (panel c). This may indicate a rapid saturation of the trap states as the overall density is now reduced. The spreading data shown in panels b and d illustrate an interesting story. To begin, the σ value for the toluene washed case is around 500 nm, which is roughly twice the value of the unwashed case, i.e. 250 nm. Moreover, the trend in the unwashed case shows no variation, indicating a complete lack of spreading. This contrasts with the washed condition where σ increases by another ~700 nm, reaching a value close to 1.2 µm.

For the exact same material with identical fabrication procedure, a simple anti-solvent treatment has a dramatic impact on both lifetimes and spreading of charge carriers. The reasons as to how the carriers spread in one case and not the other could be likely due to quenching at grain boundaries. Similarly, effects such as photon recycling could also be subdued to absorption or loss of recycled light in constricted geometries. We will attempt to answer some of these questions in the subsequent chapters. In general, both lifetimes as well as diffusion lengths seen in our results are consistent with values reported by others [42, 43]. Albeit the encouraging results, the picture is far from complete as an accurate interpretation is only possible through a complete spatio-temporal fit of the experimental data. In the following chapter, we present a more rounded spatio-temporal model of diffusion; based on results obtained on a refined understanding of the experimental setup applied to a variety of stable device certified perovskite thin film samples.

CHAPTER 4 TIME-RESOLVED IMAGING OF CARRIER DIFFUSION

Copyright notice: parts of the discussion presented in this chapter were adapted with permission from

> A. Sridharan, N. K. Noel, H. Hwang, S. Hafezian, B. P. Rand, and S. Kéna-Cohen, “Time-resolved imaging of carrier transport in halide perovskite thin films and evidence for nondiffusive transport,” *Physical Review Materials*, vol. 3, no. 12, pp. 1–10, 2019. Copyright © 2019 by the American Physical Society. DOI: 10.1103/PhysRevMaterials.3.125403.

4.1 Introduction

As elucidated in the previous chapter, the broad spread of values suggests both a need for further study, and for techniques which can unambiguously identify diffusion coefficients under a limited number of assumptions. In this work, we directly image the spreading of charge carriers in both time and space. Subsequently, we extract the diffusion length from a fit to the 3-dimensional (3D) diffusion equation. We present results for $MAPbI_3$ (MA) processed via antisolvent quenching, $MAPbI_3$ processed using an acetonitrile/methylamine compound solvent (MA-ACN), the mixed-cation, mixed-halide perovskite $FA_{0.85}MA_{0.15}Pb(I_{0.85}Br_{0.15})_3$ (FAMA) and $MAPbBr_3$ (BR). Surprisingly, we find that samples with long, monomolecular lifetimes tend to be characterized by small diffusion coefficients, resulting in negligible increases in the diffusion length as compared to the prototypical $MAPbI_3$. Further examination of MA-ACN shows strong evidence for non-diffusive transport. In this case, we observe a very large effective diffusion coefficient during the first few nanoseconds, while on a timescale comparable to the µs lifetime, the diffusion coefficient drops by more than 2 orders of magnitude. Fitting of the studied samples in different time windows suggest that this effect is present in most of the films to a varying extent. We also emphasize various effects and assumptions that can lead to artifacts in diffusion length measurements. A notable example is the apparent spatial spreading of charge carriers that can occur in the complete absence of diffusion when both monomolecular and bimolecular recombination are present. This effect is analogous to one recently observed in a study of exciton diffusion in monolayer transition metal dichalcogenides in the presence of exciton-exciton annihilation [161].

4.2 Methods

4.2.1 Diffusion Measurement

To probe carrier diffusion, we record the spreading of luminescence in both space and time, after excitation with a diffraction-limited pump spot, which generated the initial carrier distribution. The technique is depicted schematically in panel a of Figure 4.1. This approach was originally introduced to examine exciton diffusion in tetracene single crystals [162]. Here, we implement a slight variant that uses a streak camera to avoid the need for any moving parts [161]. By fitting the time and space-dependent luminescence to the diffusion equation, we are able to directly obtain the recombination and ambipolar diffusion coefficients of free carriers for a range of hybrid organic-inorganic perovskite thin films. When linear recombination is present alone, in-plane diffusion leads to a time-dependent spreading of the Gaussian luminescence width $\sigma(t)$, such that $\sigma^2(t) = \sigma^2(0) + 2Dt$. However, a full solution to the diffusion equation becomes necessary when bimolecular recombination occurs. In this case, the spreading is no longer determined by this simple relationship and apparent spreading occurs even in the case $D = 0$ [161]. This is the regime typical of free carrier materials and that is where our measurements and all previous in-plane measurements of perovskite thin films have been performed.

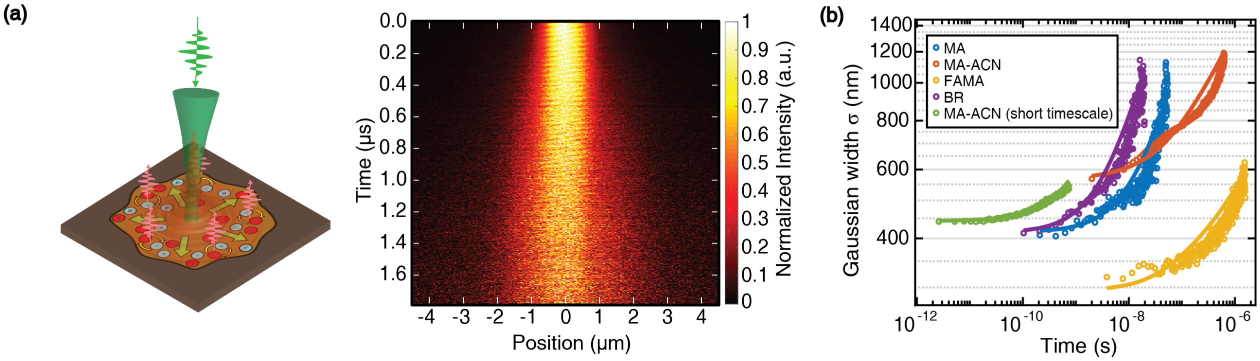

Figure 4.1 a) Left: Schematic of the experiment showing the incoming laser pulse generating electron-hole pairs which diffuse and subsequently recombine, emitting photons that contain information on the spatial distribution of carriers. Right: A streak camera measurement showing spreading of charge carriers in time and space for a film of $MAPbI_3$ processed using an acetonitrile/methylamine (MA-ACN) compound solvent. Data are normalized at each time step to highlight the spreading. b) Log-log plot showing spreading of the standard deviation obtained from a Gaussian fit to the spatial profiles as a function of time for samples MA ($MAPbI_3$), MA-ACN on both long and short timescales, FAMA ($FA_{0.85}MA_{0.15}Pb(I_{0.85}Br_{0.15})_3$), and BR ($MAPbBr_3$). The circles and solid lines correspond to raw streak camera data and modelled results respectively.

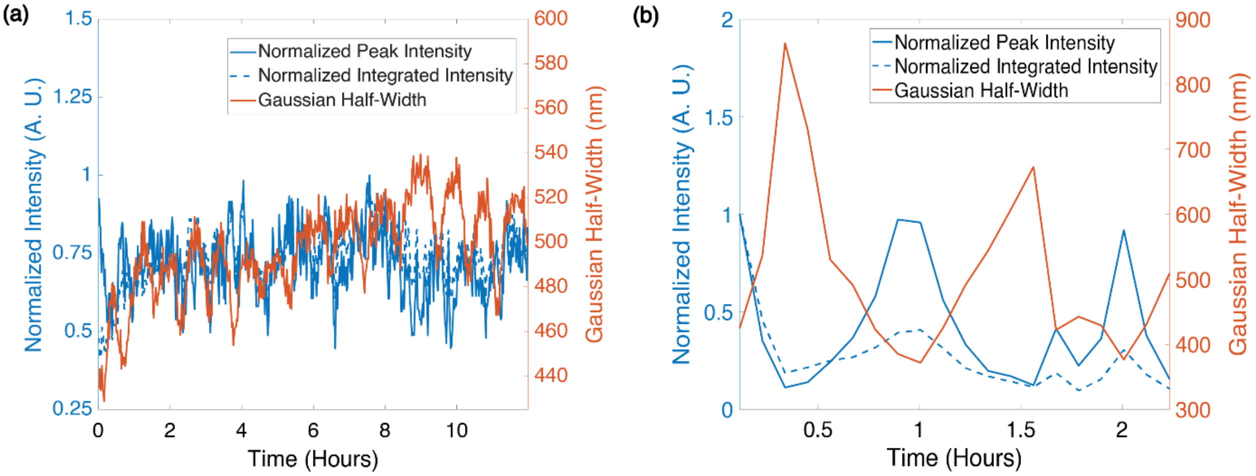

Figure 4.2 Normalized peak intensity, integrated intensity and Gaussian half-width calculated for each data frame in time from streak camera measurement shown for samples a) BR and b) MA-ACN. Slow fluctuations in time occur due to defocussing, but no long-time degradation is observed. For the data analysis, we only keep the frames where the focus is good.

Prior to performing measurements with a tightly focused pump, we first estimate the linear and bimolecular recombination coefficients by performing time-resolved measurements with a large excitation spot. Under these conditions, diffusion plays a reduced role which allows us to decouple diffusion from the apparent lifetime observed when measuring photoluminescence with a diffraction-limited pump. We then perform diffusion measurements by focusing the $\lambda = 532$ nm pump laser on the sample surface, through the glass coverslip substrates using an oil-immersion objective to a nearly diffraction-limited spot of width $\sigma = 120$ nm. In this configuration, a slice through the center of the pump spot is imaged through the same objective onto the streak camera entrance slit. This allows us to obtain the spreading of the PL in both space and time as shown schematically on the right-hand side of panel a in Figure 4.1. The use of immersion oil also prevents any artificial spreading of the spatial profile due to the re-absorption of photons that are totally internally reflected in the glass. A schematic of the optical setup and additional details are given in the previous chapter in Figure 3.20. The single-sweep unit (M10913-11) in the Hamamatsu C10910 streak camera provides a temporal resolution of < 20 ps resolution for the smallest time window of 1 ns. All experiments were carried out in photon counting mode at 10 ms exposure time and maximum MCP gain. Detailed measurement conditions are described in Table 4.1.

The PL spot intensity and waist were found to be unstable with time as shown by the calibration measurements depicted in Figure 4.2 for samples BR and MA-ACN. The mean reverting cyclical trend is likely caused by external thermal and mechanical perturbances affecting the optical stability. In our measurements, we conserve data for only those time where the standard deviation of the PL spot is minimal. Panel b of Figure 4.1 shows the Gaussian half-width (standard deviation σ) obtained by fitting the photoluminescence (PL) spatial profile to a Gaussian profile at each time step. For all samples, we find a clear increase in the PL spot size as a function of time. This increase, however, is due to an interplay between bimolecular recombination and diffusion as will be shown below. The difference between the initial PL spot size and the pump size is ascribed to photon recycling which can occur on the picosecond timescale [163]. Note that the degree of time-dependent spreading varies significantly amongst the various films. One strength of the streak-camera based technique as compared to pump-probe, which is noticeable in panel b of Figure 4.1, is its adaptability to a wide range of lifetimes, ranging from sub-ns up to ~10 µs.

Table 4.1 Experimental conditions and calculated initial parameters for fitting procedure described in experimental section shown for the perovskite thin film samples.

Sample	**Laser wavelength λ_L [nm]**	**Sample thickness t_s [nm]**	**Absorption Length t_α [nm]**	**Electron density n_0 [10^{16} cm^{-3}]**	**Laser Repetition Rate (60× Objective) [MHz]**
MA	532	398	172	2.49	2
MA-ACN	532	353	161	4.29	0.5
FAMA	532	486	192	1.25	0.1
BR	450	290	251	0.76	20

4.2.2 Film Fabrication

For the mixed-cation, mixed halide perovskite FAMA, a 1.25 M solution of $FA_{0.85}MA_{0.15}Pb(I_{0.85}Br_{0.15})_3$ was prepared using a 4:1 v:v ratio of DMF:DMSO. The solution was spin-coated onto the desired substrate at 1000 rpm for 10 s, followed by 6000 rpm for 35 s. 100 µL of anisole was dropped onto the substrate 35 s after the beginning of the spin-coating. The films were then annealed at 100 °C for 60 min. The same protocol was repeated for the $MAPbI_3$ and $MAPbBr_3$ samples, where the concentration of the precursor solutions was 1 M. In the case of the acetonitrile processed $MAPbI_3$, a solution of methylamine in ethanol (Sigma Aldrich, 33 wt%) was placed into an aerator which was kept in an ice bath. A carrier gas, N_2, was then bubbled into the solution, thus degassing the solution of methylamine. The produced methylamine gas was then passed through a drying tube filled with a desiccant (Drierite and CaO) before being bubbled directly into the acetonitrile (Sigma Aldrich) which contained the perovskite precursors (MAI:PbI_2 ratio of 1:1.06 M) at a concentration of 0.5

M. The gas was bubbled into the black dispersion until the perovskite particles were wholly dissolved resulting in a clear light yellow solution. Scanning electron micrographs of the studied samples are shown in Figure 3.13. We note that the different processing routes and compositions lead to drastically different surface morphology and apparent grain sizes. For the samples showing clear grain boundaries, the excitation laser was centered within individual domains to minimize scattering of the Gaussian pump beam. All of the films were fabricated by our collaborators.

4.2.3 Fitting

From the data, the diffusion and recombination coefficients can be extracted by simultaneously fitting the entire data set (space and time) to the three-dimensional diffusion equation:

$$\frac{\partial n(r,z,t)}{\partial t} = G(r,z,t) - D\left[\frac{\partial^2 n(r,z,t)}{\partial r^2} + \frac{1}{r}\frac{\partial n(r,z,t)}{\partial r} + \frac{\partial^2 n(r,z,t)}{\partial z^2}\right] - k_1 n(r,z,t) - k_2 n(r,z,t)^2 \tag{4.1}$$

Here, $G(r,z,t)$ is the carrier generation rate determined from the pump, D is the (isotropic) diffusion constant; and k_1 and k_2 are the monomolecular (Shockley-Read-Hall) and bimolecular (band-to-band) recombination coefficients, respectively. Auger recombination can be safely ignored given the low initial carrier densities in our experiments ($< 5 \times 10^{17}$ cm^{-3}). We assume high-level injection and ambipolar conditions, i.e. $n = n_0 + \Delta n \approx \Delta n = \Delta p$, where Δn and Δp correspond to the excess minority carrier density. This assumption is justified when Δn exceeds the majority carrier density n_0 (or p_0). At the carrier densities relevant for most of our experiments, this is a reasonable assumption. Previously reported values are $p_0 \sim 10^{15}$ cm^{-3} in MAPbI$_3$ and MAPbI$_{3-x}$Cl$_x$ thin films, and values ranging from $p_0 = 10^9$–10^{12} cm^{-3} in MAPbI$_3$ single crystals [146, 147, 164]. Samples from synthetic routes and compositions which yield longer monomolecular lifetimes (fewer traps), such as MA-ACN and FAMA, are expected to possess even lower majority carrier densities. Alternatively, a quadratic dependence of the PL on the pump power, such as that observed BR, can also be used to demonstrate the validity of the high-level injection assumption [165]. Because of the low exciton binding energy (<16 meV) in the materials under study, any excitonic contribution to the photoluminescence at the excitation densities utilised is considered negligible [134]. The reported diffusion coefficients correspond to the ambipolar D in Equation (2.85), which is dominated by the least diffusing species. With the assumption of high-level injection, the PL can be calculated from the simulated carrier density using PL $\propto \Delta n^2$. The dependence of the initial carrier density on the pump profile depends on the relative contributions of monomolecular vs bimolecular recombination. In all samples except BR, bimolecular recombination dominates at initial times, i.e. $k_2 \Delta n(t=0) > k_1$. Given that the samples are fabricated on glass and capped with PMMA thin films, we assume corresponding reflecting boundary conditions at the top and bottom interfaces in our modelling.

The initial carrier density profile can be obtained from the measured pump laser profile and the $t = 0$ PL streak camera data. The peak density of excess photogenerated charge carriers Δn_0 is derived from:

$$\Delta n_{total} = \int\limits_V \Delta n(r, z, t=0) dV = \Delta n_0 \int\limits_0^{t_s} \int\limits_0^{2\pi} \int\limits_0^{\infty} f(r) g(z) d^2 r dz \tag{4.2}$$

Where $f(r)$ and $g(z)$ correspond to the normalized initial density profiles in-plane and in the z-direction, respectively, $\Delta n_{total} = P_E/E_{ph}$ is the total number of excess charge carriers obtained via the pulse energy P_E and the photon energy $E_{ph} = hc_0/\lambda_L$, while t_s is the sample thickness. In high-level injection. i.e. PL $\propto \Delta n^2$ and a $t = 0$ recombination rate that exceeds the pump pulse length, the initial density profiles are obtained from the square root of the $t = 0$ measured PL, i.e. $f(r) = e^{-r^2/4\sigma^2_{PL,t=0}}$, where $\sigma^2_{PL,t=0}$ is the PL Gaussian width. Since in all measurements, the Gaussian width of the PL is much larger than that of the imaging system PSF at the emission wavelength, we can safely ignore the PSF contribution. Similarly, $g(z) = e^{-z/2t_\alpha}$ is given by the square root of the Beer-Lambert equation. Here, t_α is the absorption length at laser wavelength λ_L. After further operations, we obtain the following expression for Δn_0:

$$\Delta n_0 = \frac{\Delta n_{total}}{8\pi \sigma^2_{PL,t=0} t_\alpha \left(1 - e^{-t_s/2t_\alpha}\right)} \tag{4.3}$$

Parameters λ_L, t_α, t_s, and Δn_0 are shown in Table 4.1 for each sample. The obtained initial carrier density is then used as the initial condition to evaluate subsequent time steps of the diffusion equation using the forward Euler discretization scheme, i.e. Equation (4.1). The resulting 3D array from the simulation, integrated along the z-axis, produces a 2D (r, t) intensity matrix for the same spatiotemporal coordinates as the streak camera data. Fit coefficients are then found by a least squares minimization of the error between the simulation result and the experimental data as depicted in Figure 4.3.

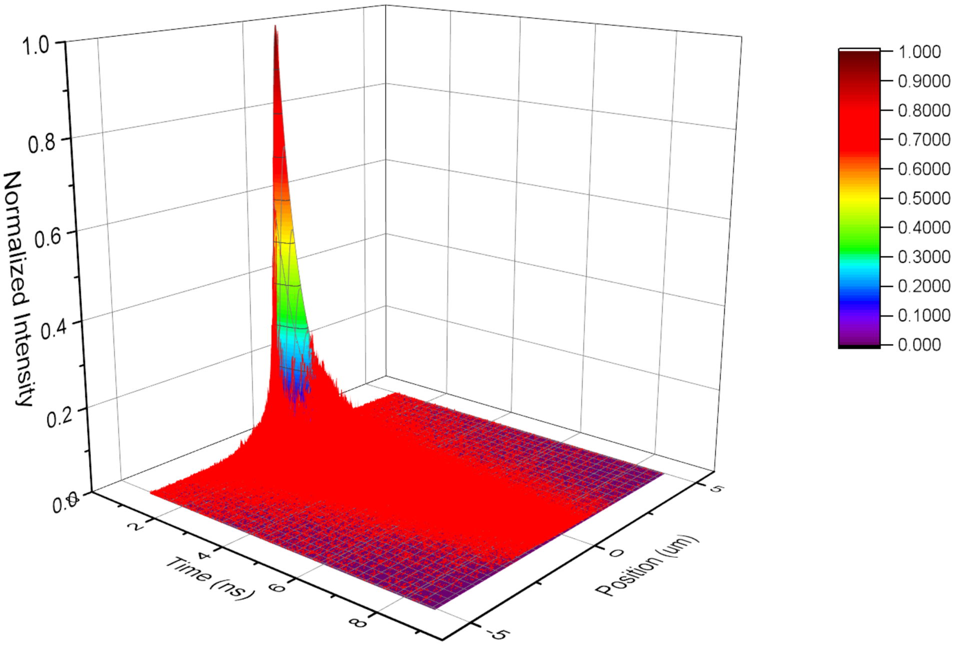

Figure 4.3 Demonstration of the least squares minimization process. The colorful mesh is a fit whereas the red spikes correspond to the experimental data.

4.3 Experimental Results

The measurement and fit results are shown in Figure 4.4 for all samples for peak excitation densities given in Table 4.1. The panels on left show a cross-sectional fit to the time-resolved data taken from the center of the spot, while the ones on the right show spatially-resolved fits taken at various times. The time dependence and spatial spreading are both well-reproduced by the calculation. The fits show excellent agreement with the model, which confirms that invoking the explicit presence of an exciton population or trap states is unnecessary for explaining the results under our measurement conditions (although they may be present). Some minor discrepancies arise in the tails at longer times that appear to be due to deviations between the Gaussian initial condition ($t = 0$) for the simulation and the real experimental profile (see Methods Section 4.2). A summary of the diffusion and recombination coefficients obtained for the different samples is given in Table 4.2. The 1D monomolecular diffusion length, defined as $L_D = \sqrt{D/k_1}$, is also indicated. For MA, we obtain a value of $D = (1.25 \pm 0.01) \times 10^{-1}$ cm^{2}s^{-1} and a monomolecular diffusion length of $L_D = (1.68 \pm 0.03)$ µm. Processing perovskite films using an acetonitrile/methylamine compound solvent system leads to solar cell efficiencies of up to 19% [129]. Our calculations indicate that the diffusion coefficient in the MA-ACN sample is $D = (6.9 \pm 0.1) \times 10^{-3}$ cm^{2}s^{-1}, which is two orders of magnitude lower than that of MA. The much smaller value k_1, however, leads to a comparable

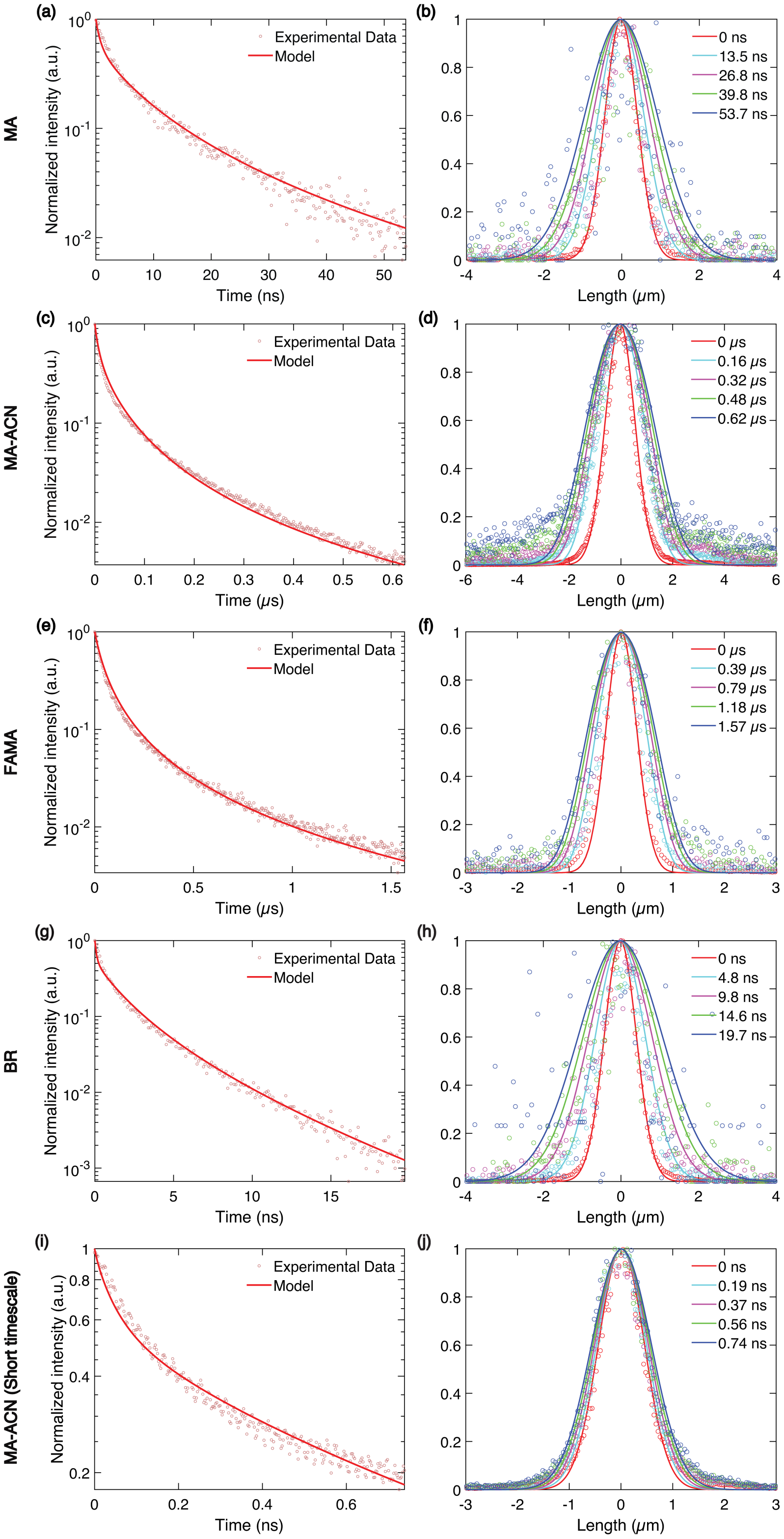

Figure 4.4 Photoluminescence transient measured in the center of the spatial profile, i.e. spatial position of 0 µm, on the left and spatial profiles (horizontal slices) for different times extracted from 3D diffusion model-based fitting and experimental data on the right for all samples.

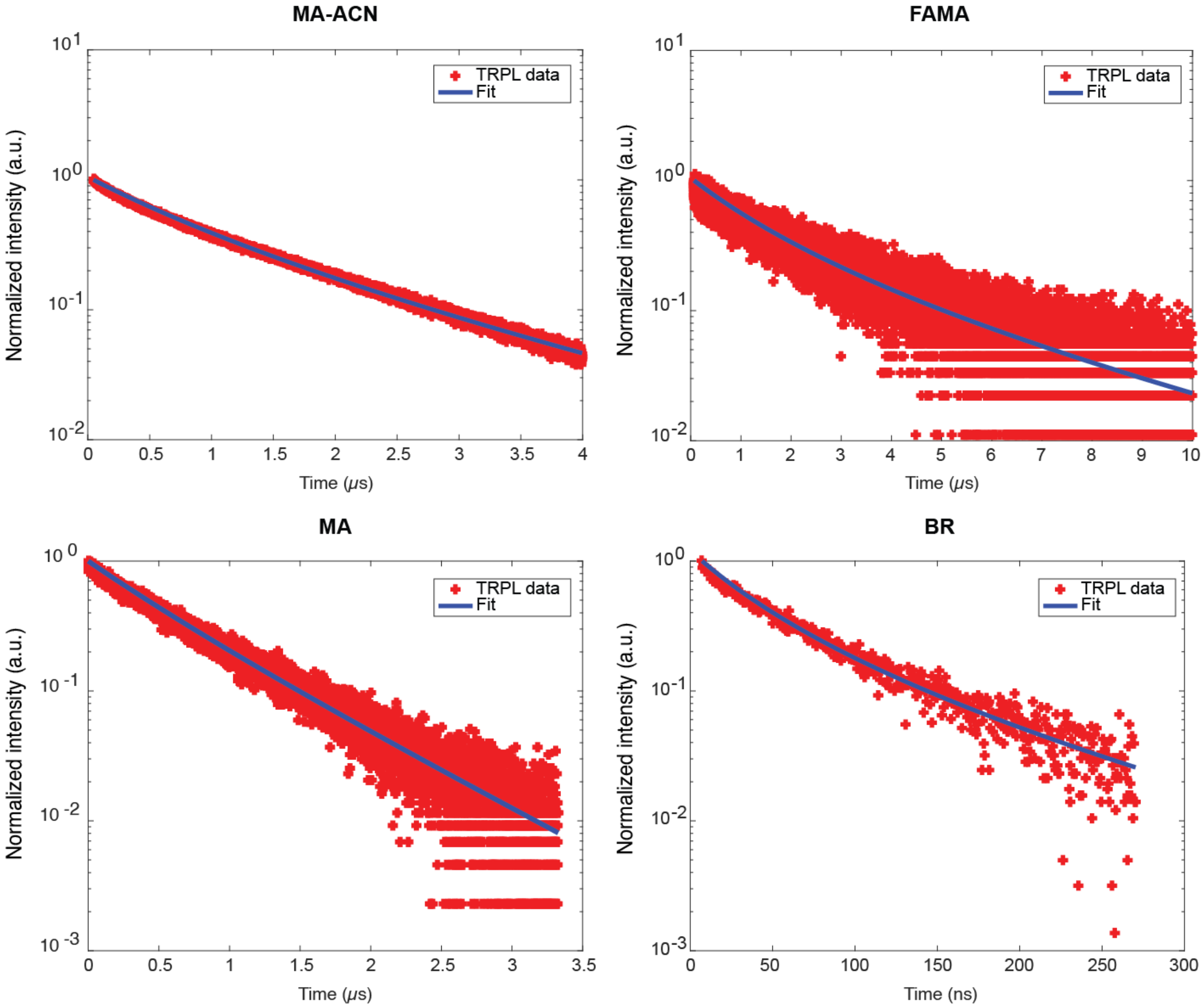

Figure 4.5 Time resolved photoluminescence data measured at low power with a 110 µm pump spot and least squared fits used to obtain the monomolecular recombination coefficient k_1. The obtained values are $(2.331 \pm 0.003) \times 10^5$, $(9.25 \pm 0.08) \times 10^4$, $(6.47 \pm 0.02) \times 10^5$ and $(3.2 \pm 0.1) \times 10^6$ for MA-ACN, FAMA, MA and BR, respectively.

monomolecular diffusion length $L_D = (1.73 \pm 0.04)$ µm.

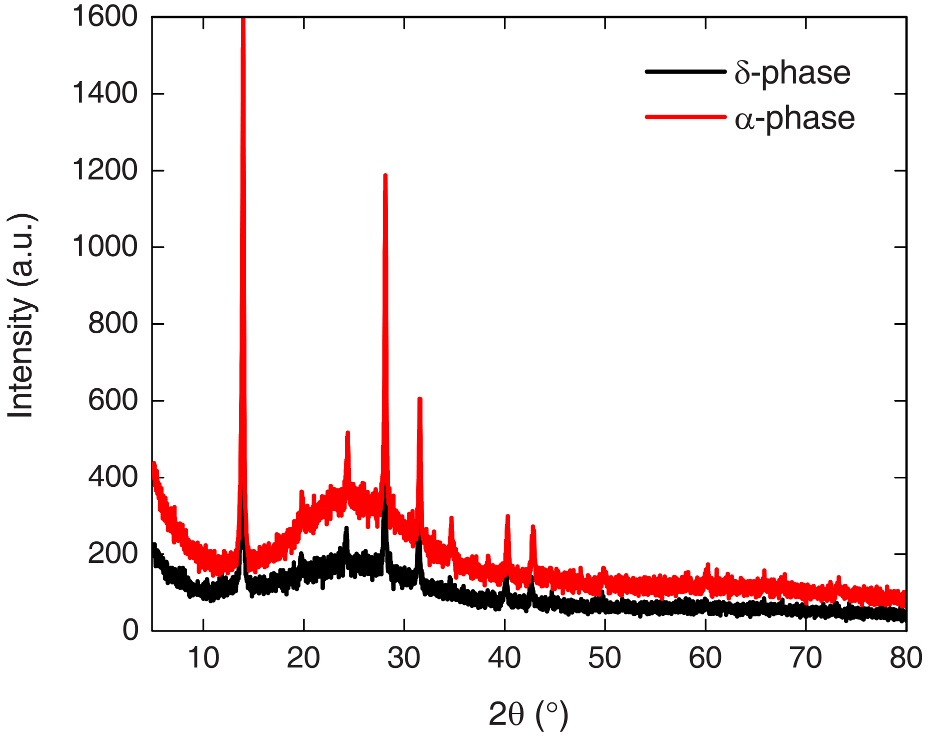

Figure 4.6 XRD data showing $FAPbI_3$ in pure α-phase (experimental condition), and with appearance of δ-phase peaks (near ~12°).

The FAMA composition was engineered as a thermodynamically stable substitute to the $FAPbI_3$ α-phase perovskite, which was found to undergo a transition into a non-perovskite δ-phase at room temperature (Figure 4.6) [80]. For FAMA, which is the composition of the highest-reported device efficiencies (~22%) [83], the extracted diffusion coefficient is even smaller, $D = (5.6 \pm 0.1) \times 10^{-4}$ cm^{2}s^{-1} with a corresponding diffusion length of $L_D = (0.78 \pm 0.04)$ µm. We have also performed measurements on BR ($MAPbBr_3$) and our results show a large diffusion coefficient of $D = (5.08 \pm 0.05) \times 10^{-1}$ cm^{2}s^{-1}. Despite the high value of D, the short diffusion length $L_D = (0.96 \pm 0.04)$ µm obtained for BR is a consequence of its very short lifetime.

For MA, which is the most studied film, the recombination coefficients agree with previously reported values [150], with the caveat that we ignore photon recycling in the transverse direction, but implicitly account for it in the lateral direction. The diffusion coefficient we observe for MA is comparable to that obtained in several previous reports (~0.04 cm^{2}s^{-1}) [42,

Table 4.2 Diffusion and recombination coefficients obtained through iterative fitting of streak camera data for various perovskite films. Error values correspond to 95% confidence intervals obtained from the fits. In this context, D is an “effective” diffusion coefficient which does not account for photon recycling. The value of k_2 is not corrected for photon recycling along the n of the film and depends on the approach used to determine the initial carrier density (see text). For MA, MA-ACN and FAMA, the values of k_1 were obtained using separate measurements with larger spot sizes (Figure 4.5).

Sample	D [$\mathrm{cm^2 s^{-1}}$]	k_1 [$\mathrm{s^{-1}}$]	k_2 [$\mathrm{cm^3 s^{-1}}$]	L_D [µm]
MA	$(1.25 \pm 0.01) \times 10^{-1}$	$(4.4 \pm 0.1) \times 10^{6}$	$(7.38 \pm 0.06) \times 10^{-10}$	(1.68 ± 0.03)
MA-ACN	$(6.9 \pm 0.1) \times 10^{-3}$	$(2.331 \pm 0.003) \times 10^{5}$	$(8.58 \pm 0.08) \times 10^{-10}$	(1.73 ± 0.04)
MA-ACN[a)]	(1.56 ± 0.01)	—	—	—
FAMA	$(5.6 \pm 0.1) \times 10^{-4}$	$(9.25 \pm 0.08) \times 10^{4}$	$(1.23 \pm 0.06) \times 10^{-9}$	(0.78 ± 0.01)
BR[b)]	$(5.08 \pm 0.05) \times 10^{-1}$	$(5.55 \pm 0.05) \times 10^{7}$	—	(0.96 ± 0.01)

a) Measured in the short 1 ns time window; b) In BR, k_2 could not be obtained due to the dominance of the monomolecular regime $k_1 >> k_2 n$ under the experimental conditions.

43, 155]. Our results point to an inverse relation between long lifetimes and D for both MA-ACN and FAMA which suggests weakly mobile, localized minority carriers as the source of the PL in long-lifetime films. When $\mathrm{MAPbI_3}$ is processed from the acetonitrile/methylamine solvent, we observe a much longer monomolecular lifetime, suggesting a reduced trap density, but at the same time, a diffusion coefficient that is reduced by one order of magnitude compared to MA. The same trend is observed in FAMA, but with an even longer lifetime and smaller diffusion coefficient.

4.4 Discussion

4.4.1 Potential Artifacts in Time-Resolved PL Measurements

Two potential artifacts need to be considered when analyzing the kinetics. First, we note that diffusion can strongly modify the time-dependent luminescence, particularly in geometries with a tightly focused pump such as in confocal fluorescence lifetime measurements [166]. Panel a of Figure 4.7 shows a series of linear (monomolecular) PL transients calculated for increasing values of the diffusion coefficient. Diffusion outside of the excitation spot leads to apparent non-linear behavior, which is simply an artifact due to the spatial dynamics. For this reason, initial conditions for our fits were obtained by first measuring k_1 and k_2 using measurements performed with a large pump spot (with $D = 0$). These values were then refined using the tightly focused data.

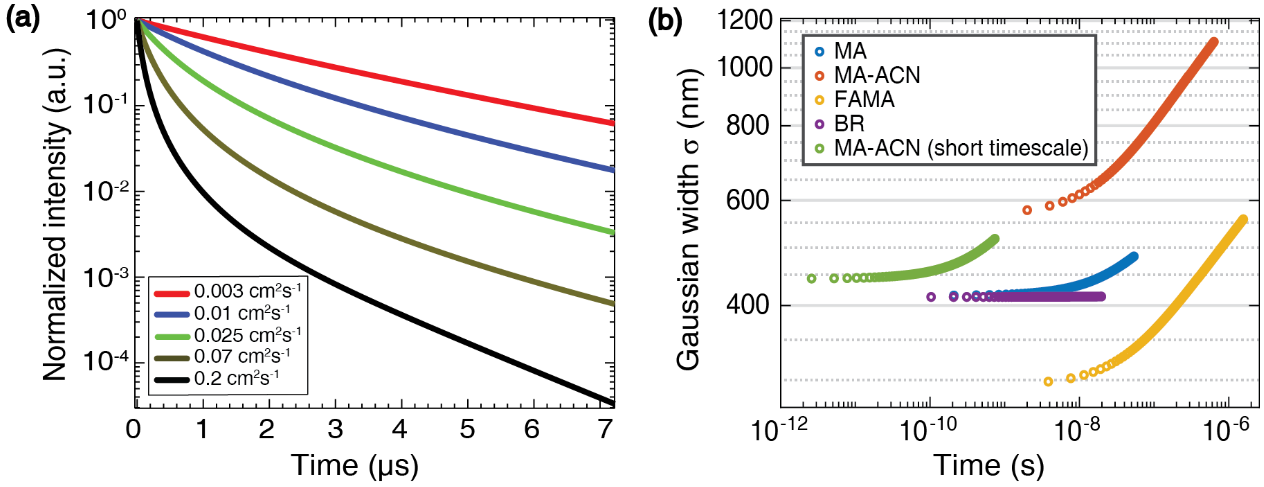

Figure 4.7 a) Impact of the diffusion coefficient on the linear lifetime i.e. with monomolecular recombination only ($k_1 = 1.02 \times 10^5$ s^{-1}), in the tightly-focused regime. The rates for bimolecular and Auger recombination are neglected to highlight the significant impact of diffusion alone on the initial part of the lifetime curve. b) Modelled spreading of the Gaussian width due to bimolecular recombination coefficient k_2 in the absence of diffusion ($D = 0$).

Second, bimolecular recombination leads to an artificial spreading of the PL spatial profile in time. To illustrate this, panel b shows the calculated spreading of the Gaussian width of the spatial profile for our samples using recombination coefficients from Table 4.2, but in the absence of diffusion ($D = 0$). The figure shows a large increase of the Gaussian width that is purely due to k_2. This is analogous to a recent demonstration that exciton-exciton annihilation leads to increases in the apparent D for excitonic materials [161]. This effect becomes more important for increasing carrier densities. At the densities relevant for our measurements (10^{16}–10^{17} cm^{-3}), both D and k_2 play important roles in dictating the time-dependent spreading. This is always the case under high-level injection for D and k_2 values typical of perovskite thin films. As a result, one cannot directly use the Gaussian width as a function of time to extract the diffusion constant. Note also that the traditional transient grating decay formula, which has previously been used for measuring in-plane diffusion in perovskite films, has not been properly modified to account for bimolecular recombination [153, 167, 168].

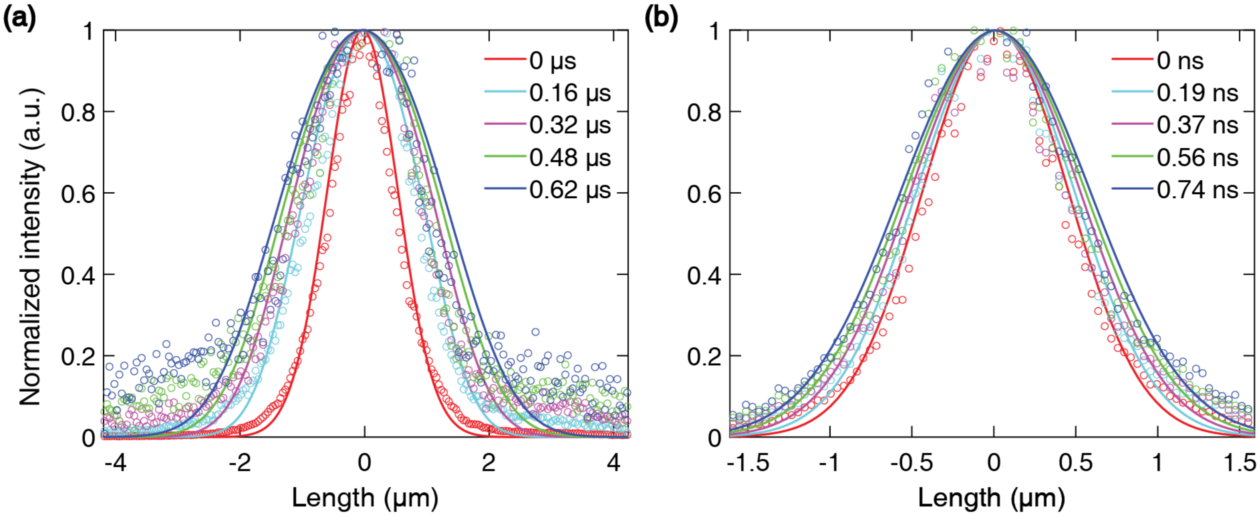

Figure 4.8 Spatial profiles of the PL for the MA-ACN sample at the times indicated in the legend. These are shown a) over a timescale comparable to the monomolecular lifetime and b) at very short times.

4.4.2 Photon Recycling

Finally, photon recycling also plays an important role in dictating the time-dependent behavior in the directions perpendicular and parallel to the substrate. Recent studies show that in films thicker than the absorption length, the measured k_2 can differ from the intrinsic k_2 by up to one order of magnitude due to photon recycling in the direction perpendicular to the substrate [163, 164]. In the simplest picture, emission and re-absorption, redistribute the initial carrier density over the entire thickness of the film on a sub-nanosecond time scale. Here, we have only reported the apparent k_2, without correcting for this effect. In principle, under high-level injection and when bimolecular recombination dominates, the initial carrier density in-plane should agree with that obtained from the laser profile using $\Delta n(0) \propto \sqrt{P(r,0)}$, where $P(r,t)$ is the laser pump profile. However, the mismatch between the laser ($\sigma_L \approx 120$ nm) and the photoluminescence ($\sigma_{PL,t=0} \approx 300 - 580$ nm) Gaussian widths is evident from panel c of Figure 4.1.

To understand the difference in initial widths, we have measured the spreading of the spatial profile of MA-ACN at the highest resolution possible in our system (~50 ps) (Figure 4.4 - panels i and j). The spreading of the spatial profiles is also shown side by side for the short and long timescales in Figure 4.8. Even for this time resolution, there is a large mismatch between $\sigma_L = 120$ nm and $\sigma_{PL,t=0} = 444$ nm. This is indicative of very fast spreading on a < 50 ps timescale. One can show that this agrees well with a single photon recycling event.

Table 4.3 Simulation results for Sample MA showing fitted coefficient D for varying initial excess carrier densities Δn_0. These changes in the initial charge carrier densities simulate photon recycling conditions.

$\boldsymbol{\Delta n_0}$ [$\mathbf{10^{17}\ cm^{-3}}$]	$\boldsymbol{D}$ [$\mathbf{10^{-1}\ cm^2s^{-1}}$]
1.5	(1.29 ± 0.01)
2.0	(1.27 ± 0.01)
2.5	(1.25 ± 0.01)
3.0	(1.23 ± 0.01)
3.5	(1.21 ± 0.01)

Taking $\alpha_\lambda = 2.24 \times 10^4$ cm^{-1} for MA-ACN at the peak emission wavelength, i.e. $\lambda = 754.2$ nm (Figure 3.5) and Equation (2.136), we obtain $L_{D_\lambda} = 2.58 \times 10^{-5}$ cm. We can estimate the temporal spreading of the Gaussian width via $\sigma^2(t) = \sigma^2(0) = 2D\tau_\lambda + \sigma^2(0) + 2L^2_{D_\lambda}$, or:

$$\Delta\sigma_{ph.\ \ recycling} = \sqrt{\sigma^2(t) - \sigma^2(0)} = \sqrt{2}L_{D_\lambda} \tag{4.4}$$

Thus, we obtain $\Delta\sigma_{ph.\ recycling} = 3.65 \times 10^{-5}$ cm or 365 nm, a value which roughly corresponds to the observed mismatch between excitation σ_L and $\sigma_{PL,t=0}$. When exciting at energies high above the bandgap, Guo et al. have recently observed fast spreading of carriers over ~100 nm in only 1.2 ps in MA [155]. Although this effect may contribute to the spreading, the spectral redshift that we observe towards the edge of the PL spot (not shown) and the absence of a strong dependence on the pump wavelength is more indicative of photon recycling. In any case, we implicitly account for the initial in-plane spreading by using the $t = 0$ PL width to determine the initial carrier density. This leads to much lower initial carrier densities than those that would be obtained directly from the pump size. One could appropriately include photon recycling in the theoretical model or modify the initial transverse density to account for redistribution. However, we have verified that although such changes can affect k_2 by up to an order of magnitude, the effect on D is negligible (Table 4.3). The values for MA in Table 4.2 coincide well with *apparent* values of k_2 measured for films of similar thickness although one should be wary of the various assumptions made when comparing different values [163, 164]. Note, for example, the importance of correctly calculating the carrier density from the pump profile when measuring the bimolecular recombination coefficient. Under high-level injection and at carrier densities where bimolecular recombination dominates, $\Delta n(0)$ is given by the square root of the pump profile in space (or of the $t = 0$ PL profile). The spatial width of $\Delta n(0)$ thus differs by a factor $\sqrt{2}$ from that of the pump (or PL).

4.4.3 Non-Diffusive Transport

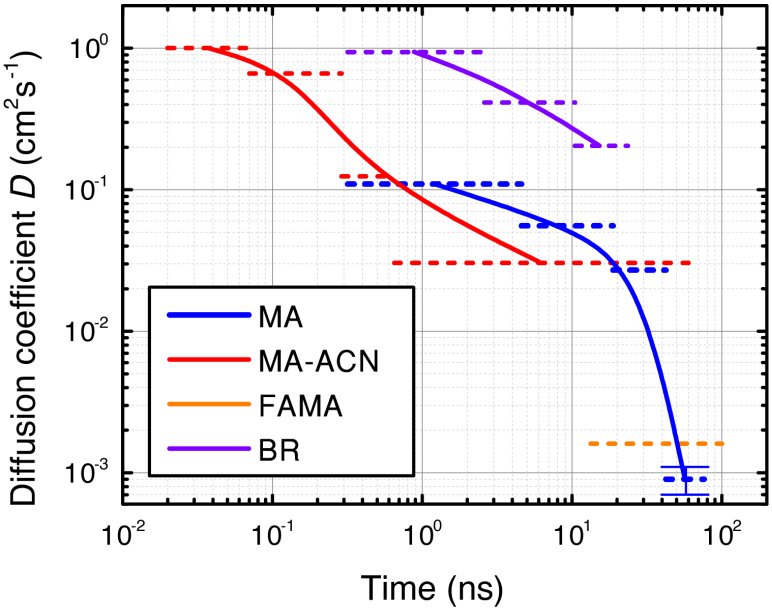

Figure 4.9 Diffusion coefficient, D, as a function of time obtained by fitting the data over different time sections, whose ranges are shown as horizontal dashed lines. The sections are chosen to ensure a single global minimum with a good confidence interval on the value of D. The solid lines are guides to the eye. For MA-ACN the result of the short-time data has been combined with that of the longer time data set. Only one data point is shown for FAMA since $D \approx 0$ cm^{2}s^{-1} reproduces the data very well for all later time sections.

For the shorter time window in Figure 4.8, our modelling gives a diffusion coefficient of $D = (1.559 \pm 0.006)$ cm^{2}s^{-1} for MA-ACN. This high value of D, which corresponds to a mobility of ~60 cm^{2}V^{-1}s^{-1} is more characteristic of intrinsic values measured on single crystals or over short distances using THz conductivity measurements. Our results thus point to two distinct diffusive regimes in the longer lifetime film. Very fast initial diffusion over a time window nearly 1000 times shorter than the monomolecular lifetime, followed by very slow diffusion on longer timescales. One can systematically study this effect for all of the film compositions.

Figure 4.9 shows best fits to the diffusion coefficient over distinct time slices from the data (dashed lines), with k_1 and k_2 fixed to the values in Table 4.2. Although the weighted diffusion coefficients are like those obtained using the global fit (Table 4.2), we observe a clear time-dependent decrease of the diffusion coefficient for all of the films except FAMA. The latter is characterized by a very small diffusion constant (undistinguishable from $D \sim 0$ cm^{2}s^{-1}) for all times other than the one shown in the figure. We suspect that these trends are due to very efficient trapping of the initial rapidly diffusing carriers on defects and at grain boundaries, followed by slower de-trapping/re-trapping. This hypothesis is supported by recent measurements of the microscopic surface potential that have found very large potential fluctuations for MA-ACN (~40–80 meV) as compared to antisolvent-quenched MA (~20 meV) [130]. Ščajev et al. have also observed a strong dependence of D on the initial carrier density and suggested the presence of band-like and localized diffusion mechanisms. The latter was found to be dominant in mixed-halide films and was attributed to a diffusion mechanism that is dominated by carrier hopping and delocalization in localized states due to alloy disorder [154]. Localization due to alloy disorder in the mixed-halide, mixed-cation FAMA film might thus be another source of the reduced D. Similarly, multi-hour absolute intensity photoluminescence combined with lateral photoconductivity measurements also show regimes where diffusion is seen to decrease due to carrier localization in smaller domains [169].

4.4.4 Relevance to Photovoltaic Efficiencies

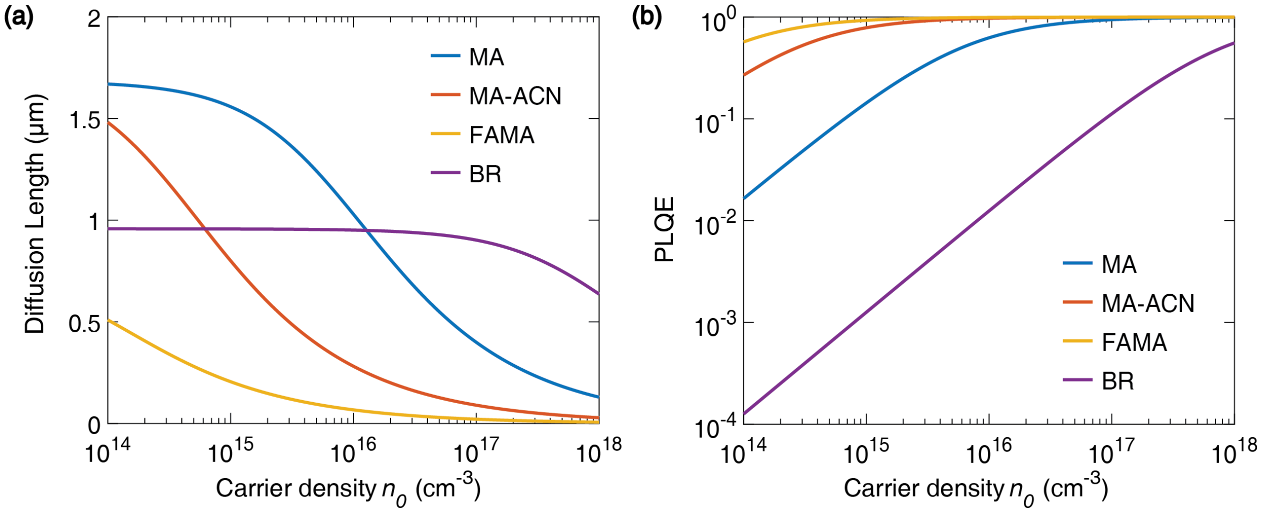

Figure 4.10 Calculated a) diffusion length and b) internal $PLQE$ as a function of carrier density using the coefficients in Table 4.2 for various metal-halide perovskite films. In both graphs, the lines for BR were calculated using the previously reported value $k_2 = 7 \times 10^{-11}$ cm^{3}s^{-1} [170].

The diffusion length and the photoluminescence quantum efficiency ($PLQE$) as a function of the photogenerated carrier density, can also be calculated from the recombination coefficients shown in Table 4.2. In panel a of Figure 4.10, the diffusion length is calculated as a function of the photogenerated carriers via $L_{D,eff} = \sqrt{D/k_{eff}}$, where $k_{eff} = k_1 + k_2\Delta n$, and as in Table 4.2, MA, MA-ACN and BR show the highest diffusion lengths. By performing

$PLQE$ measurements in an integrating sphere at low carrier density (~10 µW/cm^2), we have confirmed that the radiative (low-level injection) component of k_1 is negligible ($\lesssim$1%), which further validates the assumption of high-level injection. We thus estimate the $PLQE$ as the ratio of bimolecular recombination to total recombination rate, i.e. $k_2\Delta n/(k_1 + k_2\Delta n)$. The result shown in panel b ignores Auger recombination and any possible change in the coefficients themselves that can occur due to phase-space filling at high carrier densities [154]. We note that MA-ACN and FAMA show the highest $PLQE$ values at carrier densities typical of solar cell operating conditions (~10^{15} cm^{-3}). Given that these film compositions show the best device performance, the low non-radiative loss appears to be the key factor to attaining high-performance optoelectronic devices [171]. A similar anti-correlation between diffusion lengths and $PLQE$ has been observed in the presentation of a novel screening technique for highly efficient perovskite thin films devices [172] wherein high $PLQE$ values are seen to translate into high V_{OC} for devices.

4.5 Summary

In summary, we have directly imaged the diffusion of charge carriers in a range of perovskite thin films. Our 3D diffusion model shows excellent agreement with experimental data and is used to extract the diffusion and recombination coefficients. Surprisingly, the application of this technique to film compositions that show the best device performance such as $FA_{0.85}MA_{0.15}Pb(I_{0.85}Br_{0.15})_3$ and ACN processed $MAPbI_3$ reveal the smallest diffusion coefficients. Furthermore, we have observed that in the latter, very efficient diffusion does occur, but only on a scale much shorter than the lifetime. Time-resolved fitting of the diffusion coefficient provides strong evidence for non-diffusive transport. In all of the films, except for FAMA, we observe a notable decline of D as a function of time, on a scale shorter than the carrier lifetime. In general, we find an inverse relationship between carrier lifetime and diffusion coefficient, which may be due to the presence of weakly localized minority carriers in the longest lifetime films. In contrast, we find a strong correlation between the $PLQE$ at carrier densities typical of solar cell operating conditions and reported device performances [83, 129]. This indicates that reduced non-radiative loss plays a much greater role than the diffusion length in determining solar cell efficiencies.

CHAPTER 5 PHOTON RECYCLING AND DIFFUSION INTERPLAY

Copyright notice: parts of the discussion presented in this chapter were adapted with permission from

> A. Sridharan, N. K. Noel, B. P. Rand, and S. Kéna-Cohen, “Role of photon recycling and band filling in halide perovskite photoluminescence under focussed excitation conditions,” *The Journal of Physical Chemistry C*, vol. 125, no. 4, pp. 2240–2249, Feb. 2021. Copyright © 2021 by the American Chemical Society. DOI: 10.1021/acs.jpcc.0c09103.

5.1 Introduction

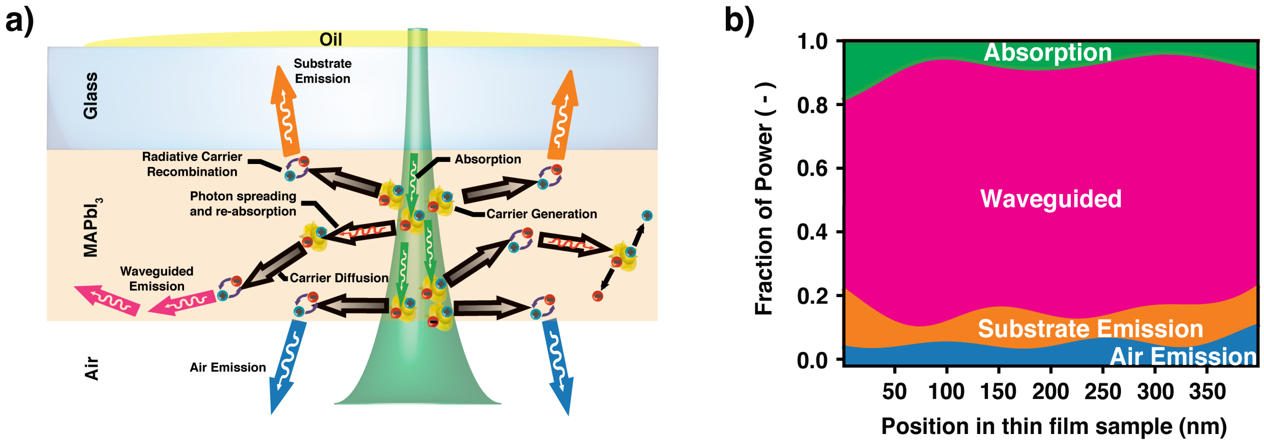

Figure 5.1 a) Schematic of the photophysical processes occurring after excitation of free carriers by the pump. The four main pathways which are initial absorption, waveguiding, substrate emission and air emission are represented via arrows of distinct colors. The blank arrow containing an oscillating red line corresponds to recycled photons whereas the grey arrows refer to diffusing carriers. b) Distribution of the total power, excluding re-absorption, dissipated by radiation in an $MAPbI_3$ thin film assuming isotropic dipole emission, as a function of the emission region position (0 nm corresponds to the substrate/perovskite interface). Oscillations in the power as a function of distance stem from the classical electromagnetic treatment of dipole emission within interfacial layers [173]. As detailed in the main text, this power distribution serves to estimate P_{stay}, a critical parameter for modelling re-absorption and photon recycling.

When a perovskite thin film is photoexcited, charge carriers are initially generated within the bulk. This can be followed by carrier diffusion, radiative and non-radiative bulk recombination [25–41, 174], surface recombination [151, 175–178] or trapping [143, 166, 179]. Radiatively emitted photons have several possible fates. They can be emitted into free space, waveguide or substrates modes, re-absorbed within the film, and if so, possibly re-emitted (recycled). These different possibilities are depicted in Figure 5.1a. In this chapter, we study the extent to which photon re-absorption and recycling contribute to carrier transport under local excitation conditions, as opposed to the more commonly studied homogeneous case. The probability of photon re-absorption depends on the degree of spectral overlap between the PL and absorption spectra. Re-absorption can occur anywhere in the film, but it is most likely for waveguided photons propagating within the plane of the film (as opposed to those within the radiation cone), due to the longer path lengths travelled by these photons. In cases where significant re-absorption occurs, a red-shifted spectrum can be observed when measured along the propagation direction due to the higher material absorption at shorter wavelengths. Efficient recycling, i.e. re-emission of these absorbed photons, requires a high PL quantum yield. When present in a device, photon recycling can contribute to increasing the photovoltaic efficiency [65].

In the homogeneous case, photon recycling has considerable impact on the apparent PL lifetimes measured in perovskites [164, 172]. Apparent lifetimes are lengthened due to the possibility that several recycling events occur before a photon can be extracted. The ratio of the apparent radiative recombination rate (k_2^{app}), to the intrinsic one (k_2^{int}), which is a material property, can be related to P_{stay}, the probability that emitted photons remain in the film, using $P_{escape} = k_2^{app}/k_2^{int}$. One approach to calculate P_{stay} is via the internal and external radiative saturation currents [45, 65]. Given the spatial inhomogeneity, typical of perovskite thin films, micro-spectroscopy techniques such as micro-PL, have been at the forefront of developing a better understanding of perovskite photophysics and for assessing material quality. Microscopy is used extensively to study transport, diffusion and recombination. In early work on photon recycling, signatures of photon recycling were observed in the spectrum of waveguided photons up to 50 µm away from the exciting laser spot [180]. In our previous work, we also highlighted the importance of bimolecular recombination in determining the shape of the PL spot after excitation [181]. Bimolecular recombination leads to an apparent spreading of carriers, which is not accounted for in the linear diffusion equation, due to faster recombination in the center of the laser spot [181, 182]. In this work, we study how photon recycling, in the presence of diffusion and bimolecular recombination also modifies the shape of the photogenerated charge carrier distribution in spectroscopic experiments. In addition, we study the spectrum of waveguided photons and find a red-shift of the perovskite PL by $\Delta\lambda \sim 20$ nm over a distance of a few µm. Our previous work attributed a similar experimental red-shift to photon recycling, but here a quantitative comparison will show that this experimental red-shift is due to the Burstein-Moss effect (band filling). In contrast to predictions for homogeneous excitation, our calculations show that for typical microscopy conditions (< few µm spot size and $< 10^{18}$ cm^{-3} carrier density), photon recycling does not play an important role in modifying the shape of PL and can be safely ignored. This is typical, for example, of experiments aiming to study carrier diffusion or kinetics.

5.2 Theory

5.2.1 Photon Recycling

An elegant approach to obtain the probability that an emitted photon remains in the film, P_{stay}, is through the ratio of the external and internal radiative saturation current densities [45, 65]. It can be expressed as follows:

$$P_{stay} = 1 - P_{escape} = 1 - \left(\frac{\int_0^\infty a(E)\phi_{bb}(E)\, dE}{\int_0^\infty 4n_r^2(E)\, d\alpha(E)\, \phi_{bb}(E)\, dE} \right) \tag{5.1}$$

where E is the photon energy, d is the sample thickness, α the absorption coefficient, n_r the refractive index, ϕ_{bb} is the Planck black body spectrum, and a is the absorptance. The term on the right hand side follows from detailed balance considering the Shockley and Queisser approach [183] for the numerator and the van Roosbroeck-Shockley [50] relation for the denominator. Applying these relations to a real structure leads to some complications. The use of the Shockley-Queisser relation requires one to link a to α, which will depend on the details of the layered structure [45]. Parasitic absorption is usually neglected. More importantly, the van Roosbroeck-Shockley relation also has some inherent limitations. Notably, $\alpha(E)$ depends on the carrier density and the $\alpha(E)$ satisfying detailed balance is not the ground state absorption coefficient, but rather that at the relevant carrier density [184]. In addition, van Roosbroeck-Shockley assumes a free space photonic density of states. However, in a thin layered structure, the photonic density of states exhibits sharp maxima at wavevectors corresponding to critical angles or waveguide modes. For these reasons, we take a different approach and explicitly calculate the probability that a photon emitted within the perovskite layer will radiate into free space using classical electromagnetic theory [173, 185, 186]. This allows us to directly account for the layered structure and dipole orientation. The proportion of radiation within the different possible emission pathways for an isotropic dipole are shown in 5.1b, as a function of the position of the emitter within a 400 nm-thick film. For simplicity, this calculation is performed at the (undistorted by re-absorption) PL maximum of 760 nm reported by Crothers et al. [163] As in previous reports, we ignore the fact that in reality, the PL maximum itself is a function of carrier density, but describe how this could be accounted for below. We will consider the case where index-matching immersion oil is used so that substrate emission can be deemed to be fully radiative. Since our two-dimensional (2D) simulations will ignore variations along the film thickness, we take $P_{stay} = 0.85$, which is representative of emission occurring from the center of the film. The use of 2D simulations is justified for thin films, for which direct re-absorption within the ~23° radiation cone does not contribute significantly to the lateral spreading. Moreover, previous work has shown that photon recycling and carrier diffusion tend to homogenize the initial carrier density along the film thickness [163].

5.2.2 Continuity Equations

Drift, diffusion, generation and recombination are described by the following continuity equation, which includes photon recycling is described by the following equations [187]:

$$\frac{dn(r,t)}{dt} = D\nabla^2 n\left(r,t\right) + G\left(r,t\right) + \frac{c}{n_r}\sum_{\lambda} \alpha_\lambda \gamma_\lambda\left(r,t\right) - k_1 n\left(r,t\right) - k_2 n\left(r,t\right)^2 - k_3 n\left(r,t\right)^3 \tag{5.2}$$

$$\frac{d\gamma_\lambda\left(r,t\right)}{dt} = D_\lambda \nabla^2 \gamma_\lambda\left(r,t\right) - \frac{c}{n_r}\alpha_\lambda \gamma_\lambda\left(r,t\right) + \left(k_2 n\left(r,t\right)^2 P_{stay}\right) P_\lambda \tag{5.3}$$

Equation (5.2) describes the evolution of excess charge carriers, $n(r,t)$, under the assumption of ambipolar transport ($n = p$) and high-level injection ($n \gg n_0$), where n_0 is the equilibrium carrier density, D is the ambipolar diffusion constant, $G(r,t)$ is the carrier generation rate determined by the laser pump, and, k_1, k_2 and k_3 are the monomolecular, bimolecular and Auger recombination coefficients, respectively. The third term describes the generation of charge carriers by the re-absorption of waveguided photons. Here, α_λ is the absorption coefficient, c is the speed of light and n_r is the group refractive index. Equation (5.3) describes the propagation of the emitted photons, with flux γ_λ, within the perovskite film. The last term in Equation (5.3) describes the generation of photons from PL. Band-to-band recombination, $k_2 n(r,z,t)^2$, acts as a source term and is multiplied by the probability of a photon of wavelength λ being generated (P_λ), which depends on the PL spectrum of the thin film, and of that photon being emitted within the layer (P_{stay}), as opposed to free-space. The photon diffusion coefficient is taken to be $D_\lambda = c/(3n_r\alpha_\lambda)$. Additional details on the analytical and numerical treatment of the continuity equations are provided in Appendix C.

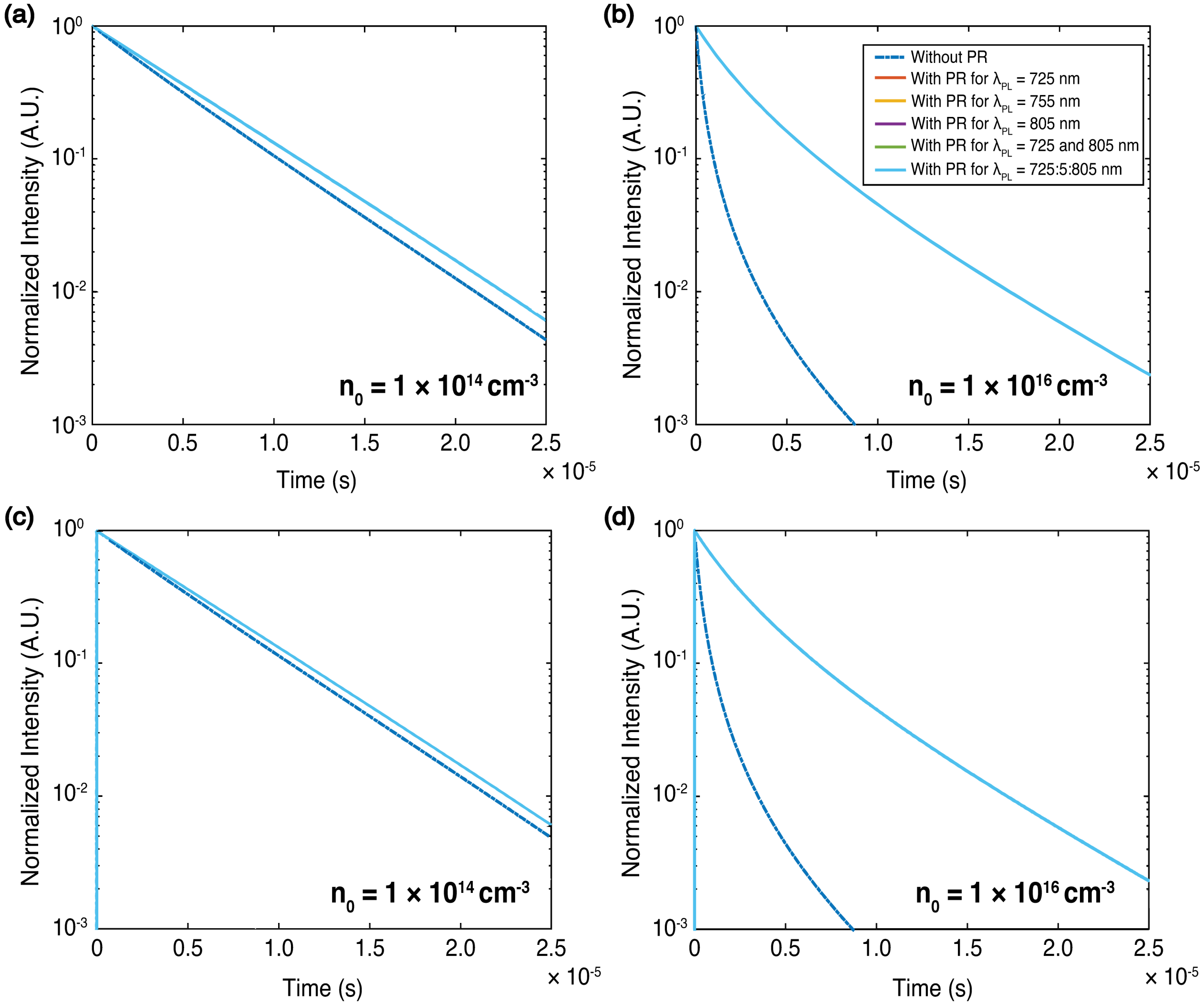

Figure 5.2 Reproduction of lifetime curves with and without photon recycling for the homogeneous case (only temporal component) using identical parameters from literature [174]. A generation term $G(t) = G_0 \cdot e^{-(t-t_0)^2/2\sigma_\tau^2}$, i.e. $n(t=0) \;=\; 0$, is used to reach the desired peak density value of n_0 in c) and d) as opposed to simply having $n(t=0) \;=\; n_0$ in insets a and b.

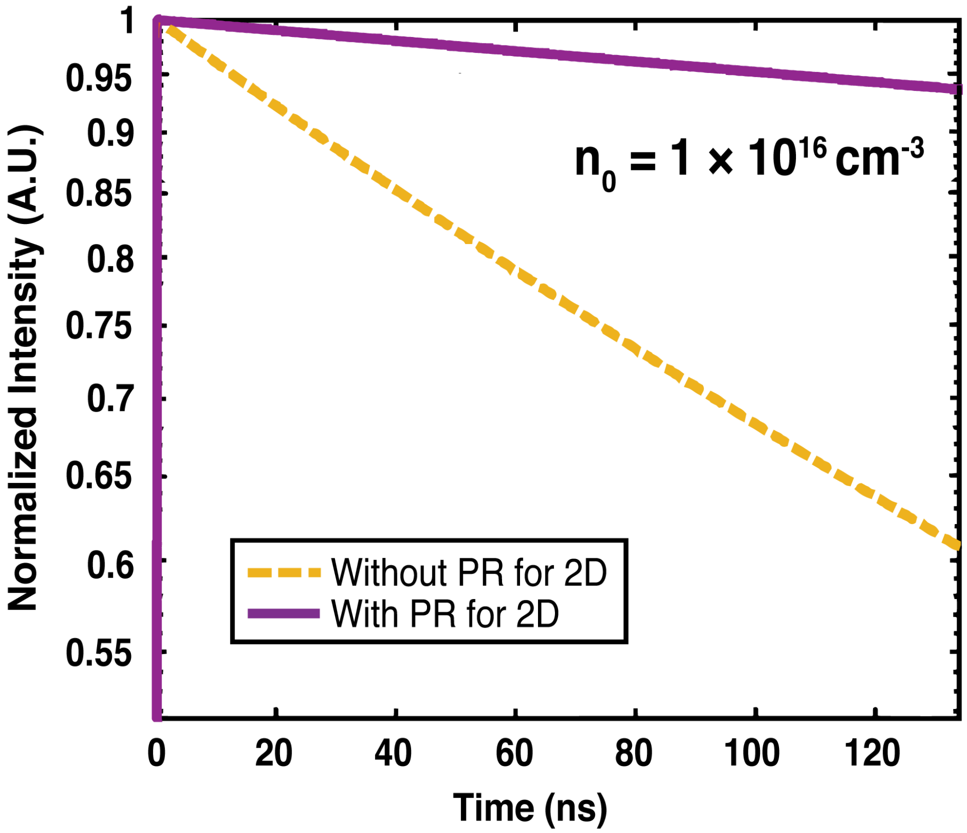

Figure 5.3 2D Modelling for a homogeneous radial profile with $D_\lambda = 0$ and $D_n = 0$ for input parameters from literature [174]. Our results demonstrate perfect overlap with the calculation from Figure 5.2 in the 135 ns timescale.

For all calculations, we use the following values, i.e. $k_1 = 2.3 \times 10^5$ s^{-1}, $k_2 = 8.6 \times 10^{-10}$ cm^{3}s^{-1} and $k_3 = 1.0\times 10^{-29}$ cm^{6}s^{-1}. These correspond to the values obtained for acetonitrile-processed methylammonium lead iodide ($\mathrm{MAPbI_3}$) films on which measurements were performed (Chapter 4). While they are representative of $\mathrm{MAPbI_3}$ films, the precise values do not affect the general conclusions of our work. To confirm the accuracy of our simulations, we first reproduced the literature [174] time-dependent results (no spatial component) as shown in Figure 5.2. Subsequently, we used those results to cross-validate the isotropic 2D $(r - \theta - t)$ simulation by forcing homogeneous conditions along the radial profile $(dn/dr = 0)$. As can be seen in Figure 5.3, our homogeneous 2D results (for $D_\lambda = 0$ and $D_n = 0$) perfectly match the time-dependent simulation in Figure 5.3. This benchmark allows further scaling of our model for non-homogeneous situations such as those encountered in our streak camera measurements, where, we use a tightly focused laser excitation of Gaussian spatio-temporal profile to generate charge carriers.

5.2.3 Band Filling

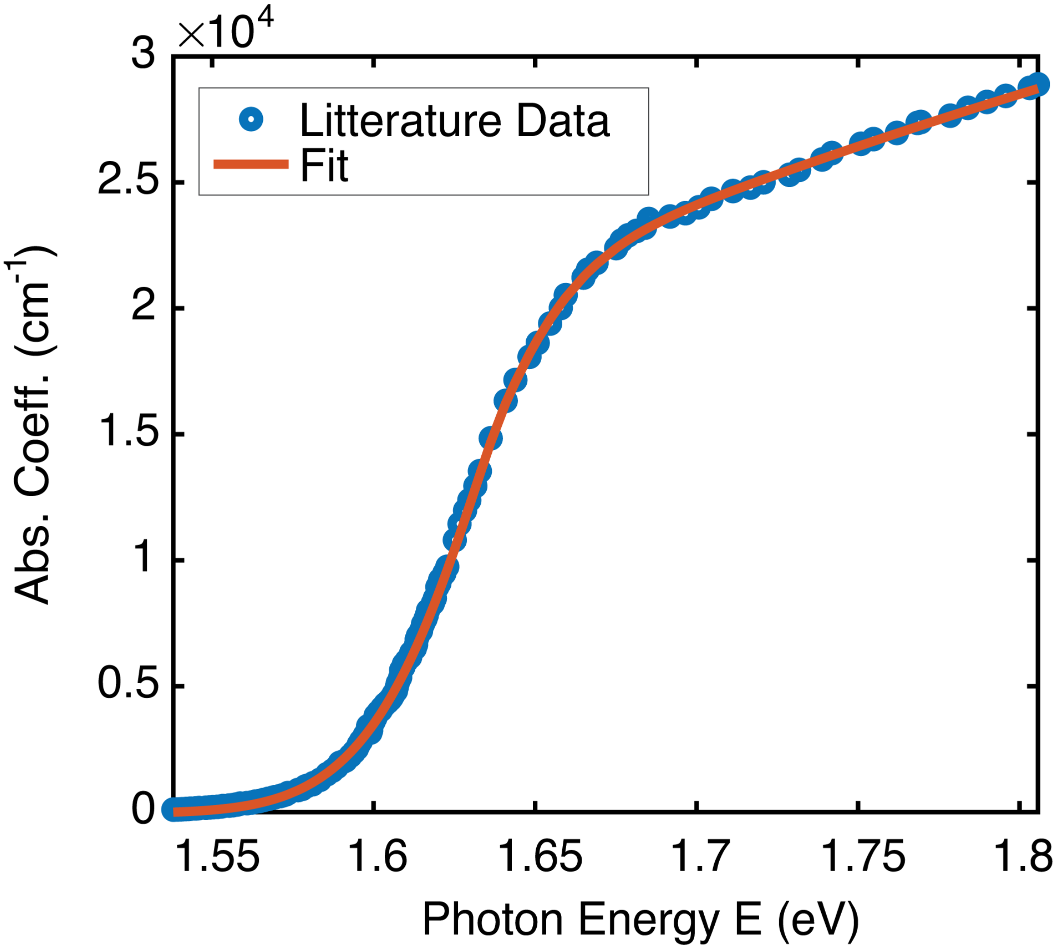

Figure 5.4 $MAPbI_3$ bandgap absorption data and fit using Katahara sub-bandgap and Elliott band-edge absorption models.

In addition to re-absorption, spectral shifts of the PL can occur due to bandgap renormalization and the Burstein-Moss effect (band filling). The first mechanism originates from the Coulomb interactions between carriers and leads to a reduction of the bandgap as a function of increasing carrier density. In contrast, band filling, which describes the filling of states near the band edges, leads to a larger apparent bandgap due to the Pauli exclusion principle. In $MAPbI_3$, the magnitude of the shifts anticipated from bandgap normalization can be estimated using the exciton binding energy and one finds that they are negligible compared to band filling. We should then expect a spectral measurement from the center to the edge of a Gaussian carrier distribution to show the bluest spectrum at center. Using detailed balance and the measured absorption spectrum, following the van Roosbroeck-Shockley approach, it is possible to calculate the magnitude of this spectral shift as a function of carrier density as described below.

Table 5.1 Absorptivity fitting

Fitting Coefficient	**Coefficient Value**	**Confidence Interval**
Bandgap Energy E_g [eV]	1.648	0.001
Sub-BG Energy Parameter ϵ [eV]	0.036	0.001
Sub-BG Exponent Parameter θ [-]	1.6	0.1
Exciton binding energy E_b [eV]	9.2×10^{-3}	0.1×10^{-3}
Scaling constant α_0 [cm^{-1}]	2.9×10^4	-

Although the exciton binding energy is small compared to room temperature in MAPbI$_3$, Coulomb correlations still play an important role in dictating the shape of the absorption spectrum. The absorption spectrum can thus be modelled using Elliot's equation [48, 188]:

$$\alpha_{BE}(E) \propto E_b \sum_{n=1}^{\infty} \frac{4\pi}{n^3}\delta(E - E_g - E_b/n^2) + \frac{\pi e^{\pi\sqrt{E_b/(E-E_g)}}}{\sinh(\pi\sqrt{E_b/(E-E_g)})}\Theta(E - E_g) \tag{5.4}$$

In the above equation, E_b is the exciton binding energy whereas $\delta(E)$ and $\Theta(E)$ are Dirac and Heaviside functions, respectively. To account for sub-bandgap absorption due to the Urbach tail, the Elliott expression can be convoluted with the phenomenological expression from Katahara et al. [189]:

$$\alpha_{Sub-BG}(E) = \frac{e^{-\left|\frac{E-E_g}{\epsilon}\right|^{\theta}}}{2\epsilon\Gamma(1+\theta^{-1})} \tag{5.5}$$

Here, θ and ϵ are fitting coefficients and $\Gamma(\theta)$ is the gamma function. The total absorption in MAPbI$_3$ can be very accurately reproduced by $\alpha(E) = \alpha_0 \cdot [\alpha_{BE}(E) * \alpha_{Sub-BG}(E)]$, where $*$ denotes a convolution. Table 5.1 shows parameters of the Katahara sub-bandgap and Elliott band-edge absorption models. Using these values, we can compare the fitted model to the literature absorption data [163]. The absolute PL intensity and its dependence on carrier density can be calculated from the absorption using the Lasher-Stern-Würfel relation [190, 191] which must be modified to account for non-equilibrium conditions. From Katahara et al. [189], the result can be approximated as:

$$I_{PL} = \frac{2\pi}{c^2h^3}E^2\left(\frac{1-e^{\left(1-\frac{2}{e^{\frac{E-\Delta\mu}{k_BT}}+1}\right)\alpha(E)d}}{e^{\frac{E-\Delta\mu}{k_BT}}+1}\right) \tag{5.6}$$

Where h and k_B are the Planck and Boltzmann constants, d is the effective absorption length, T is the temperature and $\Delta\mu$ is quasi-Fermi level splitting. From Equation (5.6) and $\alpha(E)$, we have calculated the absolute PL intensity spectrum I_{PL} for $\Delta\mu$ values ranging from 0 to 2 eV. Finally, under high-level injection conditions, the corresponding carrier density is extracted using $\sqrt{n^2} = \sqrt{np} = \sqrt{N_pN_cF_{1/2}(\Delta\mu/k_BT)}$, where $N_{c/v} = 2(2\pi m_{c/v}k_BT/h^2)^{3/2}$ and $F_{1/2}(x)$ is the Fermi-Dirac integral of order $1/2$ [192].

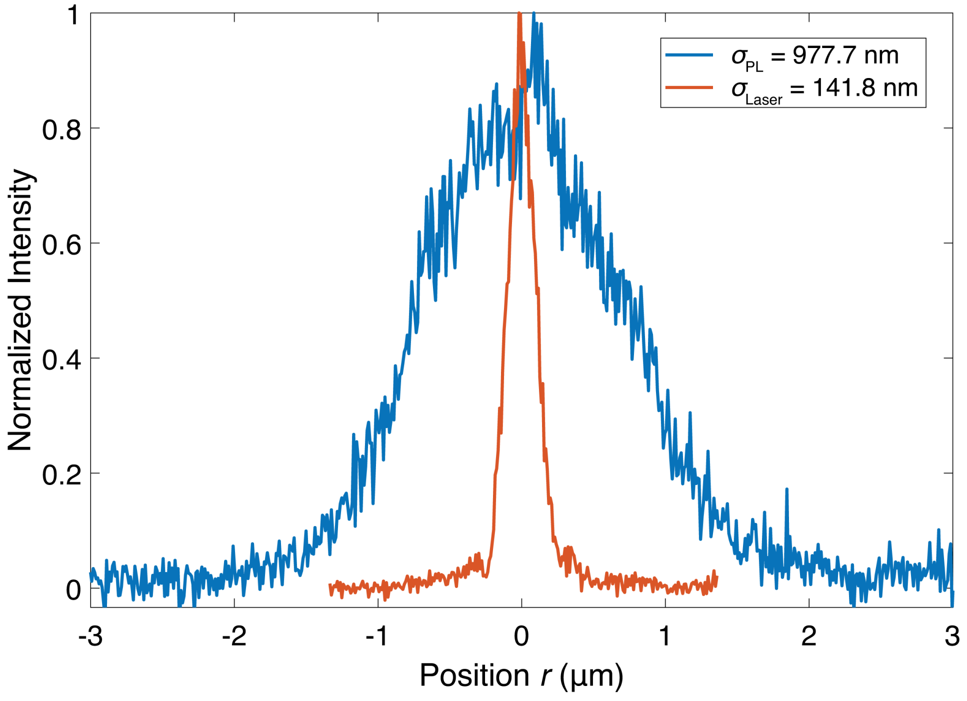

Figure 5.5 Experimental spatial profiles for laser and PL spots obtained using a CCD camera.

We previously measured the time-resolved spatial evolution of the PL for a variety of perovskite films after excitation with a diffraction-limited pump. Here, we measure the temporal evolution of the spectrum as a function of radial position along the radius of the PL spot (Figure 5.5). The experimental setup, which is based around the use of a streak camera, is shown in Figure 5.6. The excitation laser is a supercontinuum source of ~48 ps pulse width, operating at 500 kHz, spectrally filtered at 532 nm with a 10 nm bandpass filter. For spectral measurements, a 200 µm multimode optical fiber is translated along the horizontal axis in the image plane of a PL spot. Note that the spectral measurements were performed at a fluence higher than that in the previous chapter to obtain good signal-to-noise resolution. This will thus lead to larger spectral shifts. The pulse fluence of 0.15 mJ/cm^2 corresponds to a peak density of $n_0 = 4.9 \times 10^{18}$ cm^{-3}. Lower pump fluences are considered in Section 5.3.3.

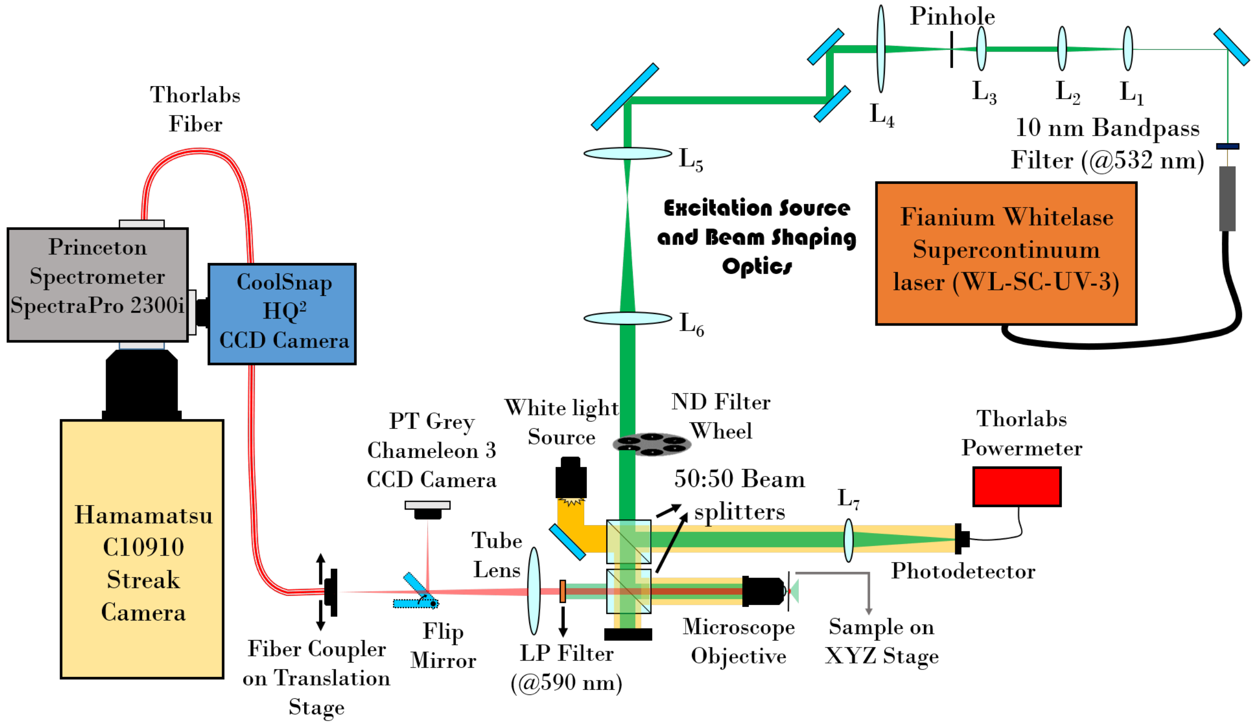

Figure 5.6 Modified version of setup presented in Figure 3.20. Here, we have rotated the streak camera anti-clockwise by 90° and linked it to a spectrometer. A 200-micron multimode fiber is used to scan the horizontal axis of the PL spot image to acquire the radial emission spectrum which is converted to time-resolved data in the streak camera.

5.3 Results and Discussion

5.3.1 Spatiotemporal Characterization

We use the parameters from Figure 5.7 for the simulation results presented in Figure 5.8 to Figure 5.11. In all cases, we use 161 wavelength points in the range of 725 nm to 805 nm. The value of $D = 0$ cm^{2}s^{-1} is used as well to clearly distinguish the effects of photon recycling.

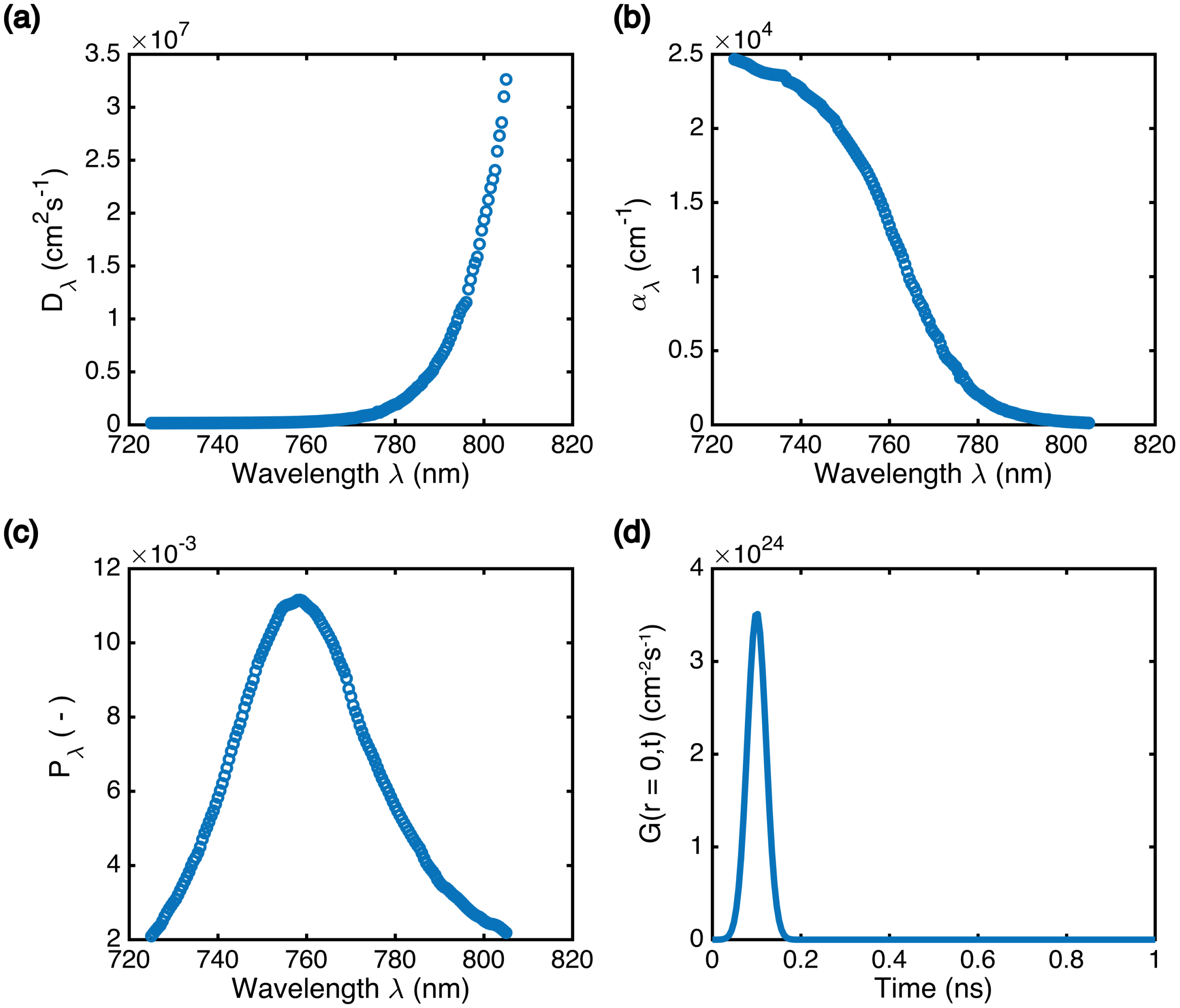

Figure 5.7 Input parameters matching streak camera experimental conditions for $n_{0-3\mathrm{D}} = 4.93 \times 10^{18}$ cm^{-3}. a) Photon diffusion constant D_λ, b) Absorption coefficient α_λ, c) Probability of emission at λ and d) Generation function $G(r,t)$ at $r = 0$ µm.

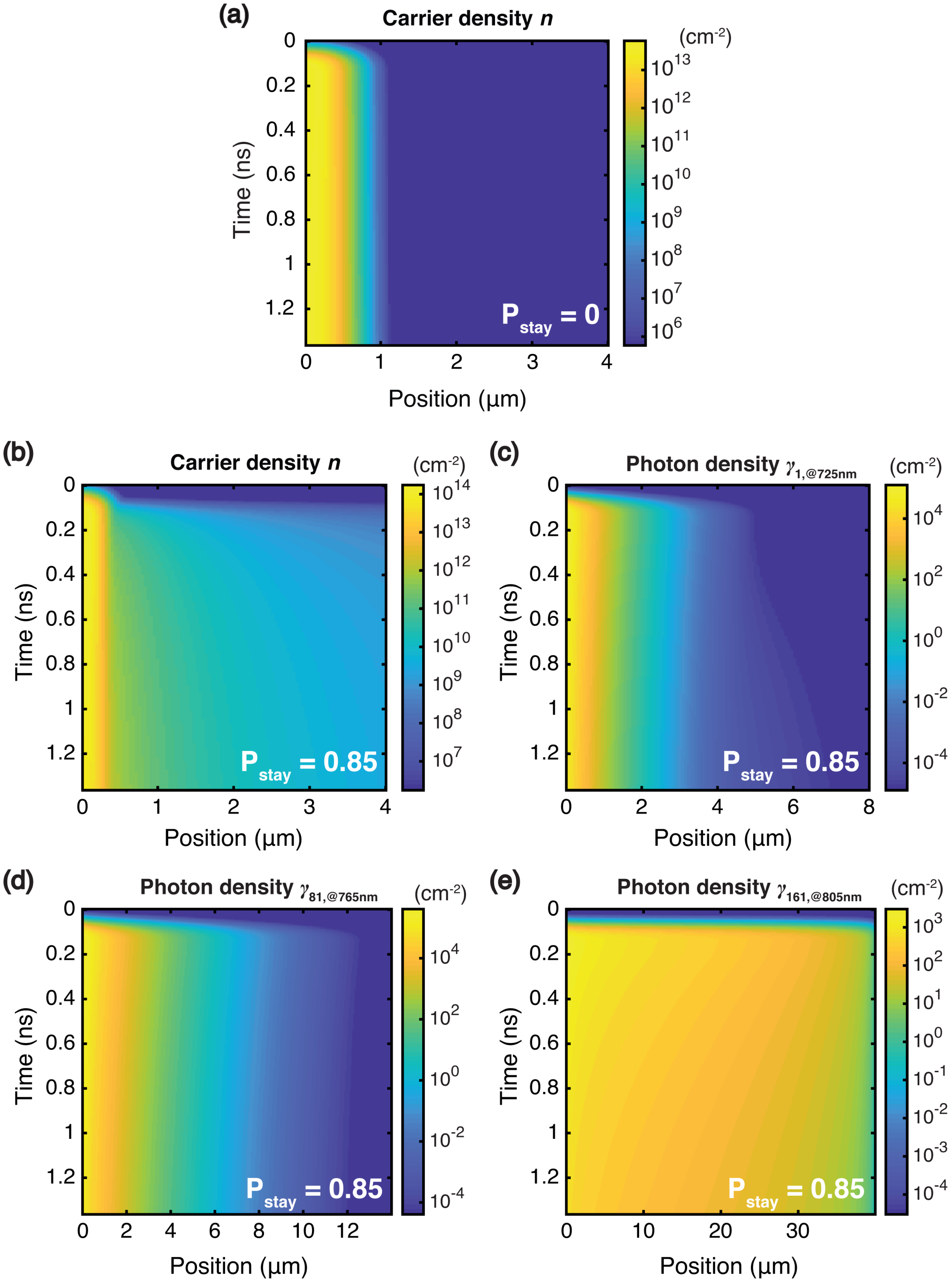

Figure 5.8 Simulated spatial and temporal evolution of a-b) carrier and c)-e) photon densities, under excitation conditions with a peak density, $n_{0-3\mathrm{D}} = 4.93 \times 10^{18}$ cm^{-3}, when photon recycling is absent for a) ($P_{stay} = 0$) and with photon recycling ($P_{stay} = 0.85$) for b-e). Photon densities are shown at wavelengths of 705, 765 and 805 nm.

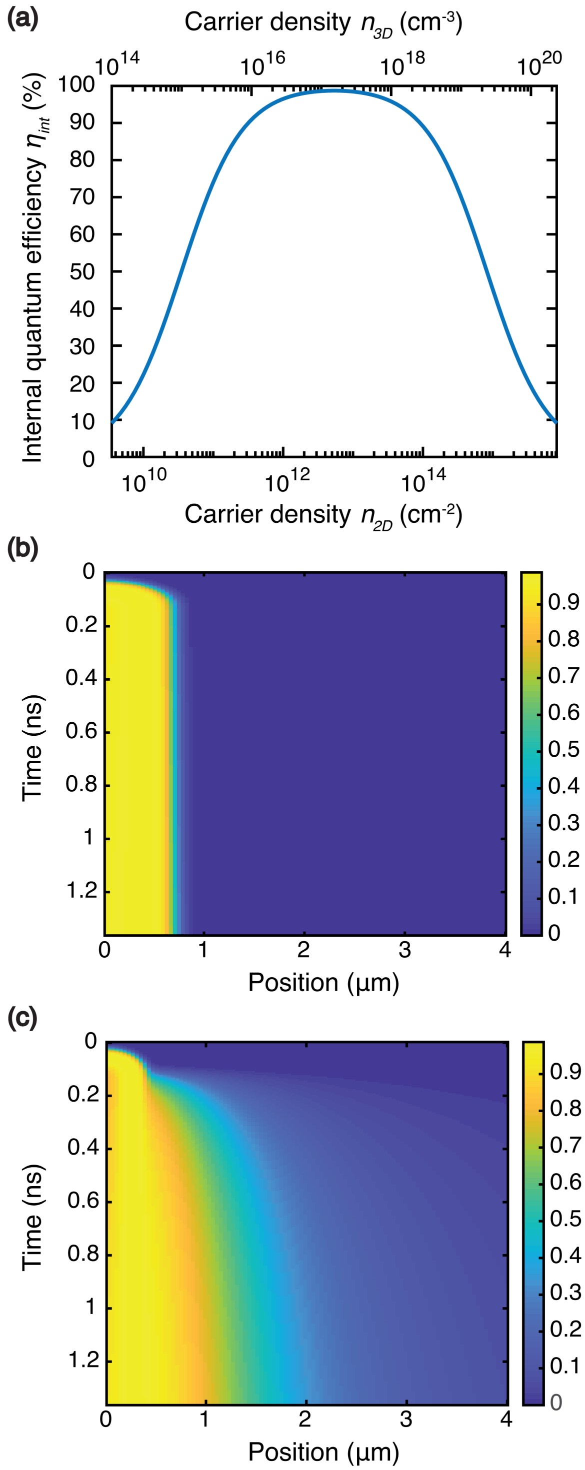

Figure 5.9 a) $PLQE$ or Internal quantum yield $\eta_{int}(r,t) = k_2^{int}n(r,t)/(k_1 + k_2^{int}n(r,t) + k_3n(r,t)^2)$ as a function of 2D and 3D carrier densities (roll-off graph). η_{int} versus space and time for b) without photon recycling and c) with photon recycling, calculated using data from panels a and b of Figure 5.8

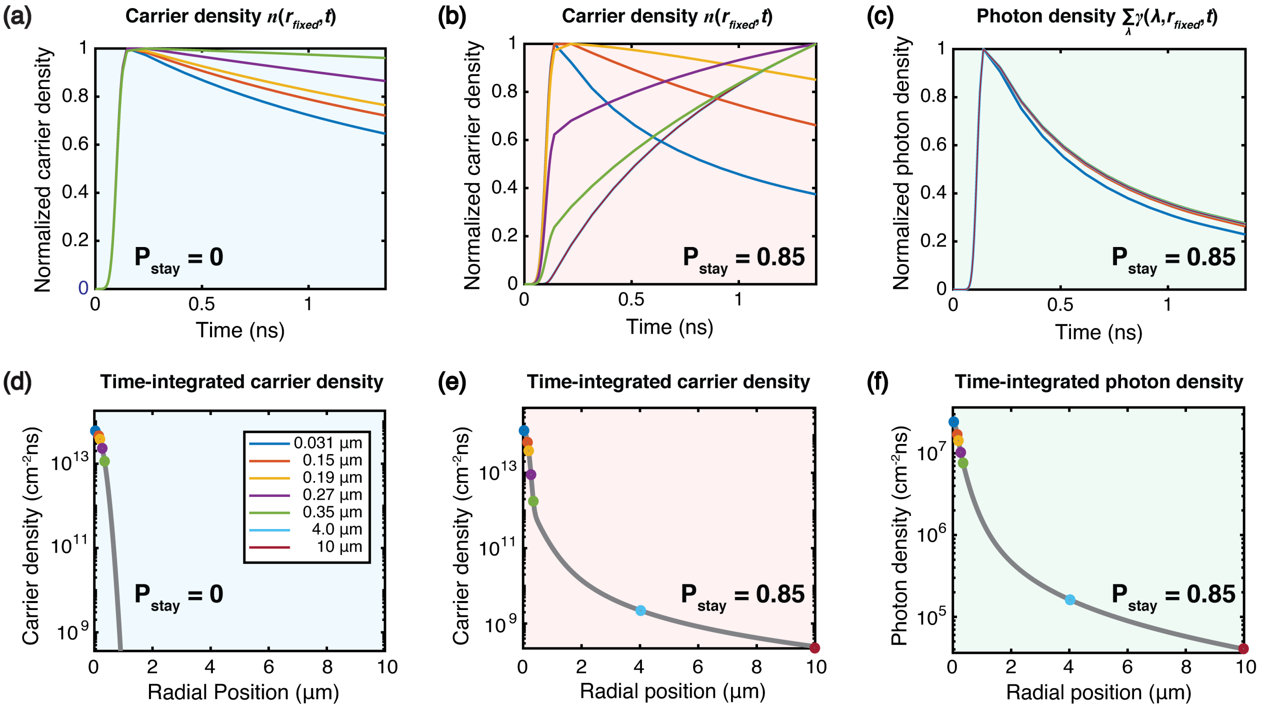

Figure 5.10 a-c) Time-dependent evolution of the simulated carrier and photon densities obtained at the selected positions identified in the inset of d). Time-integrated d-e) carrier and f) photon densities. The colored circles on the curves correspond to the locations where the traces of panels a-c) were taken.

To first examine the effect of photon recycling on carrier transport, spatiotemporal maps showing the calculated evolution of the carrier and photon densities in the absence ($P_{stay} = 0$) and presence ($P_{stay} = 0.85$) of photon recycling are shown in the panels of Figure 5.8. This simulation is performed at the experimental pulse fluence, which is high enough for photon recycling to play an important role and on a timescale corresponding to the observed spectral shifts. The value of the diffusion coefficient for the simulation is taken to be $D = 0$ cm^{2}s^{-1} to highlight the role of photon recycling. The effect of changing the initial carrier density and varying D will be studied in Subsection 5.3.3. Figure 5.8a shows the carrier evolution in the absence of photon recycling. In this case, there is a rapid apparent spreading at short times due to bimolecular recombination. This spreading is difficult to resolve in Figure 5.8a but corresponds to an increase of ~20 nm in the carrier distribution width. The effect of photon recycling on the carrier distribution is shown in Figure 5.8b. By comparing both panels, we immediately see that there are significantly more carriers far from the excitation spot when photon recycling is present. In regions more than 1 μm away from the pump, photon recycling leads to increases in carrier density by over 4 orders of magnitude as compared to the case in Figure 5.8a. Panels c-e show the evolution of the photon densities at various wavelengths when recycling is present. As expected, photons at longer wavelength spread out much faster due to the smaller absorption coefficient further out to the red (or equivalently higher D_λ). These longer wavelength photons are the main contributors to the carrier densities far away from the spot. The PL quantum yields at the carrier densities used for this calculation (corresponding to peak volume carrier densities near ~10^{18} cm^{-3}) are close to ~100% within 1 µm of the center and in the ~30–80% range 1–2 µm away from the pump (Figure 5.9). Far from the pump, re-emission is not possible due to the low quantum yield. Similarly, the impact of long wavelength photons on the central charge carrier distribution is minimal due to the small absorption coefficient.

Figure 5.10a-c shows the carrier and photon temporal evolution at various positions in space. Each time trace is normalized by the maximum value for the corresponding position. In Figure 5.10a, which is the case without photon recycling, the influence of bimolecular recombination is immediately apparent. Even within the excitation spot, the kinetics are very different as a function of position due to the Gaussian profile of the laser pump and the dependence of the radiative recombination rate on carrier density. In the situation without photon recycling, the densities are extremely small beyond $r \sim 1.2$ µm, reflecting the shape of the Gaussian pump. The photon recycling instance is shown in Figure 5.10b-c. Here, re-absorption generates carriers much further in space. The dynamics close to the pump spot also change qualitatively, showing a rise of the density with time due to re-absorption. This rise occurs on a sub-ns scale that is slightly faster than the expected radiative lifetime at densities near the center of the pump. The contribution of re-absorption can be observed until the end of our simulation window (36 µm) although the densities at this distance are very low. Given that most photons are initially emitted from the center of the pump and re-absorbed only once, the time-evolution of the integrated photon density in Figure 5.10c effectively maps out the carrier dynamics near $r = 0$ µm. 5.10d-f shows the time-integrated spatial distribution of charge carriers and photons in the presence and absence of photon recycling. The carrier density generated through photon recycling ($r > 2$ mm) is nearly 4 orders of magnitude lower than that in the center. On a linear scale, the effect of photon recycling on the PL spot shape is negligible.

5.3.2 Spectral Behaviour

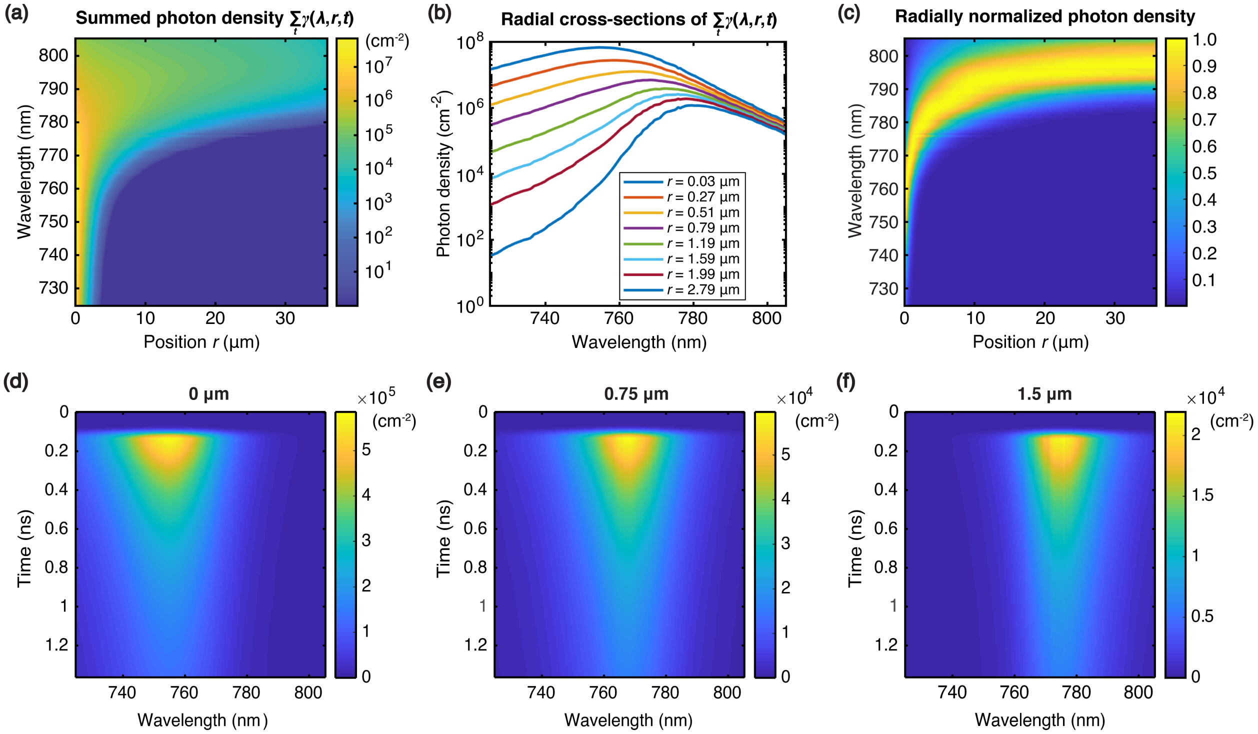

Figure 5.11 a) Simulated waveguided photon density as a function of position r and wavelength λ. b) Calculated spectral distribution of the photon density at different positions r away from the excitation spot, and in c) the normalized photon density to highlight the spectral shift as a function of space. d), e) and f) Time-dependent contour maps of the calculated spectra at positions $r = 0$, 0.75 and 1.5 µm.

The photon recycling simulations allow us to extract the spectra of waveguided photons. These are shown in Figure 5.11 at selected positions. The time-integrated spectra are shown in Figure 5.11a as a function of position. Individual spectra are also shown in Figure 5.11b for selected positions. Figure 5.11c shows a version Figure 5.11, which has been normalized to the spectral maximum at each position in order to better highlight the shift of the spectrum as a function of position. From the panels, we observe a clear red-shift of the spectrum when moving further away from the pump center. Figure 5.11b shows a shift in emission wavelength from ~755 nm to ~780 nm over 2.79 µm and from Figure 5.11c, this can be seen to extend up to ~795 nm over the 30 µm window. Note that at 2.79 µm, the peak photon density is already reduced by 2 orders of magnitude. Given that most photons are emitted near $r = 0$ µm, the shift is almost exclusively due to the spectrally dependent absorption tail of $MAPbI_3$. The size of this shift is consistent with previous experimental observations [180]. The time-dependent spectral behaviour is shown in Figure 5.11d-f for three values of r. In all of the cases, the spectral maximum is already shifted from that of the intrinsic $MAPbI_3$ PL near $t = 0$ and little to no further shift of the maximum is observed in time.

Given that most of these photons are waveguided, they are in principle not measurable from the outside for planar films. However, scattering due to surface roughness and grain boundaries in a realistic film can allow for partial out-coupling of these waveguided photons. Additionally, there is a very small region around the pump-spot defined by the critical angle where the effects of re-absorption (and potential re-emission) of photons within the light cone are observable. This corresponds to “absorption” in the context of Figure 5.1. Within this region, spectral shifts due to re-absorption can be measured. For these photons, the magnitude of the spectral shift is limited by the thickness of the film.

To probe whether such effects are relevant in PL measurements from a real film, we have performed spectrally-resolved streak camera measurements at several locations around a diffraction-limited excitation spot. To avoid any possible overlap in the spectra, we set the distance between adjacent measurement positions at a value larger than the fiber resolution (~0.6 µm). The results are shown in Figure 5.12 for the locations corresponding to the simulation of 5.11d-f (the fluence is identical). In Figure 5.12a, we see a clear red-shift, near $t = 0$, of the measured PL spectrum maximum when moving away from the pump, from 758 nm at $r = 0$ µm to 766 nm at $r = 1.5$ µm. The similarities, however, stop there. In contrast to the simulation results, all the spectra continue to red-shift in time for ~200-300 ps after $t = 0$. The magnitude of this shift in time is largest at the center of the pump, where the carrier density is highest. Such a time-dependent red-shift is inconsistent with the scattering of waveguided photons but agrees with the behavior anticipated from band filling.

Band-filling induces a carrier-dependent blue shift of the PL maximum due the Pauli exclusion principle. Hence, the most pronounced blue shift is expected at $r = 0$ µm and the smallest at $r = 1.5$ µm. Given that carrier cooling and thermalization occur at the ~1 ps scale [193], which is much faster than the measurement resolution, the measured spectra are representative of the quasi-equilibrium carrier concentration. By using Equation (5.6), the spectrum can be calculated as a function of carrier and compared to experiment. This can be done as a function of space and time. Figure 5.12b shows the photoluminescence lifetime, at 3 different locations, which can be mapped to carrier densities using the diffusion model in Equations (5.2) and (5.3). Figure 5.12c shows the theoretical peak PL wavelength as a function of carrier density. The data points correspond to the PL peaks measured at $t = 0$ and at $t = 0.9$ ns, at the indicated positions. The qualitative agreement between experimental data points (△,○) and calculated wavelength values (blue line) confirm that band filling is the

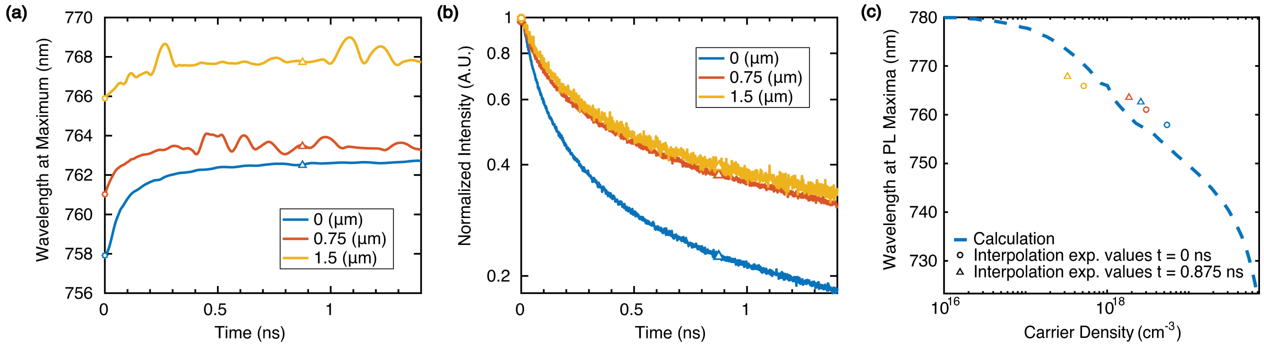

Figure 5.12 a) Experimentally measured peak PL position as a function of time at $r = 0$, 0.75 and 1.5 µm away from the excitation spot. b) Time-resolved PL measured at the same positions. c) Peak emission wavelength as a function of carrier density calculated from the absorption spectrum (dashed) and experimental points at selected carrier densities. The corresponding points in time, used to obtain the density are shown in panels a-b) as circles and triangles.

main source of the spectral shift. Note also that the model does not account for any possible local inhomogeneities in the perovskite bandgap (or PL). It only relies on the measured absorption spectrum. In addition, there is some experimental uncertainty in determining the exact carrier density due to an initial spreading of carrier density on a timescale shorter than the laser pulse width. Although this is beyond the scope of this thesis work, the importance of band filling also motivates inclusion of carrier dependence on P_λ within the photon recycling simulations.

5.3.3 Influence of The Initial Carrier Density and Diffusion Coefficient

The modelling in Figure 5.8 was performed for large pump fluences on a relatively short time scale, where band filling effects are prominent. We now consider a lower pump fluence of 0.42 µJ/cm^2 ($n_{0-3\mathrm{D}} = 1.5 \times 10^{16}$ cm^{-3}) and evolution over ~130 ns. Preliminary conclusions are rather similar, which is that photon recycling only contributes a tail to the excited carrier distribution, with a density ~4 orders of magnitude lower than the maximum. However, under these conditions, we can perform a detailed study to better understand the effects of fluence and diffusion coefficient on the involvement of photon recycling to the overall spreading. To study diffusion on a longer timescale (~120 ns), we compromise on wavelength resolution by reducing the number of points from 161 to 9. The input parameters for this low wavelength resolution simulation are shown in Figure 5.13. We use a lower fluence of 0.42 µJ/cm^2 ($n_{0-3\mathrm{D}} = 1.5 \times 10^{16}$ cm^{-3}) to study the spreading behaviour under conditions of reduced higher order recombination. The simulation results are shown in Figures 5.13–5.16.

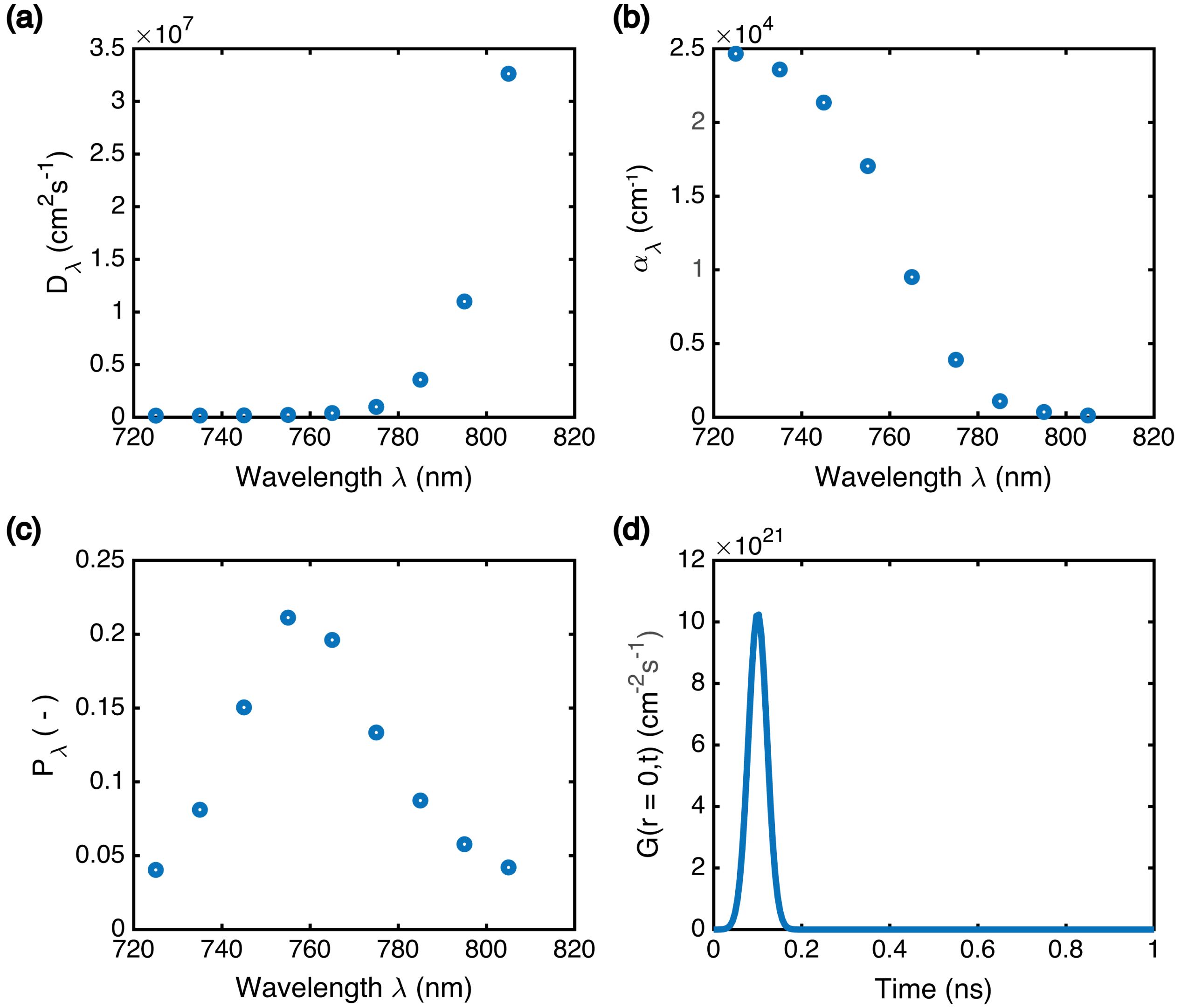

Figure 5.13 Input parameters for low wavelength resolution simulation (fluence of 0.42 µJ/cm^2 or $n_{0-3\mathrm{D}} = 1.54 \times 10^{16}$ cm^{-3}).

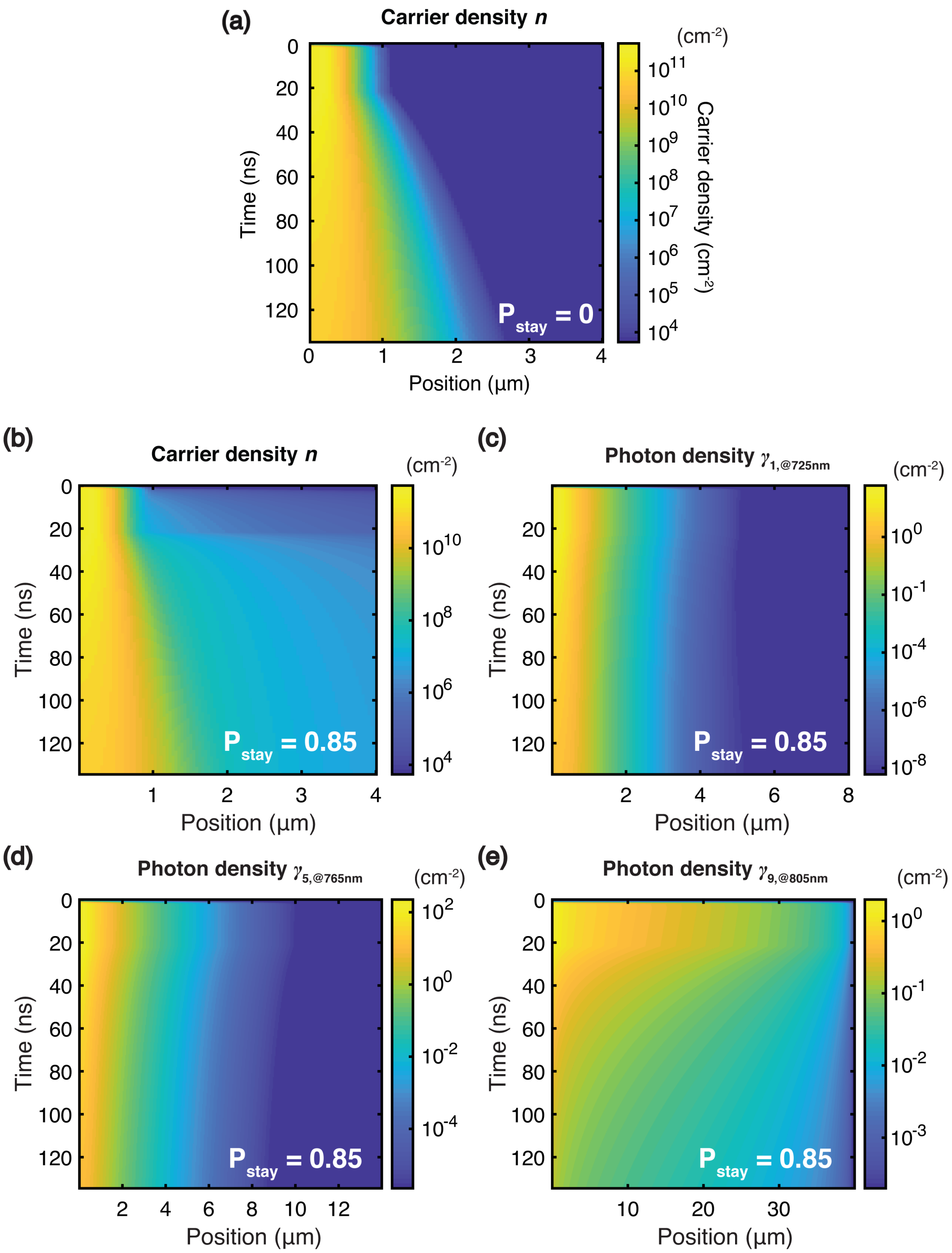

Figure 5.14 For $n_{0-\mathrm{3D}} = 1.5 \times 10^{16}$ cm^{-3} excitation, spreading in time and space when photon recycling is absent ($P_{stay} = 0$) shown in a) for carriers, and when photon recycling is present ($P_{stay} = 0.85$) in b) for carriers and in c-e) for photons of wavelengths 705, 765 and 805 nm.

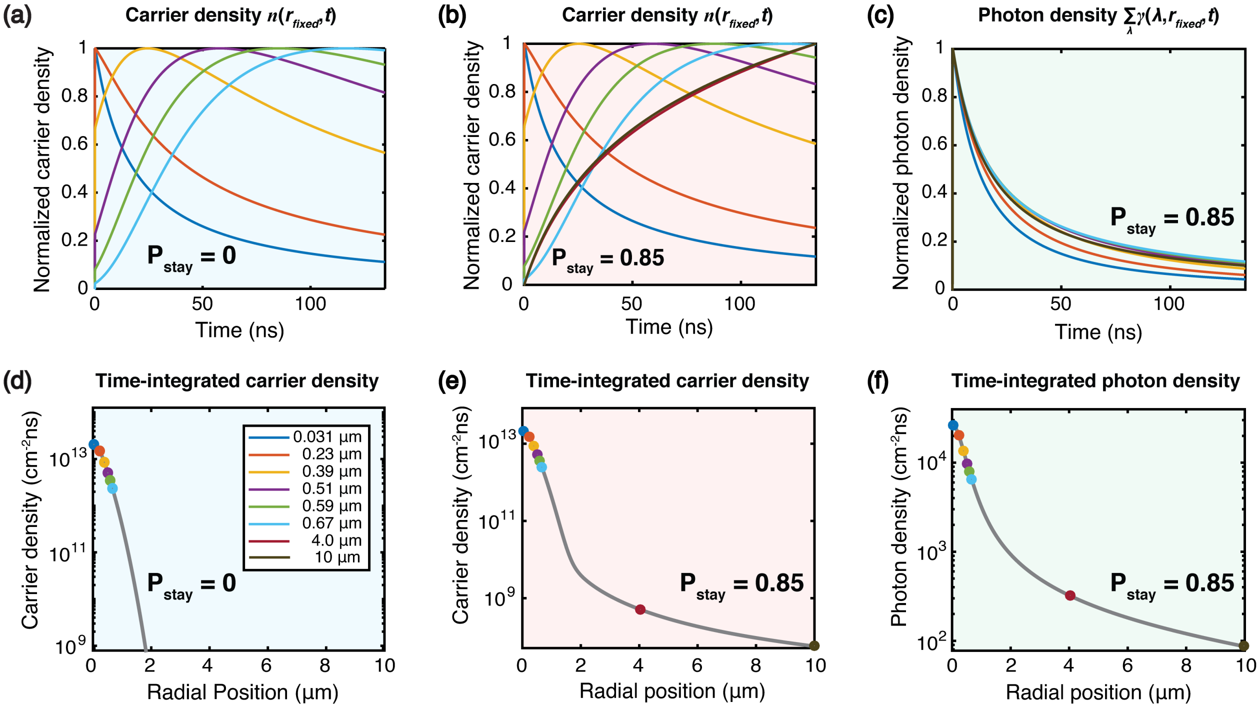

Figure 5.15 Lifetimes at different radial positions (slices from spatio-temporal data) as well time-integrated densities for both carriers and photons extracted from spreading shown in Figure 5.14.

In Figures 5.14−5.16, we use a value of $D = 6.9 \times 10^{-3}$ cm^{2}s^{-1}, based on a slow regime diffusion coefficient obtained in previous measurements for the MA-ACN sample (Chapter 4). In the longer time window, we can find the impact of the diffusion coefficient clearly. The spreading zone expands beyond the 1 μm region as we approach ~20 ns for both situations of with and without photon recycling. In panels a and b, the increased time window allows clear visualization of the carrier population changes due to diffusion. Panels d and e in Figure 5.14 show a wider spatial profile within 2 μm than what is seen for the case of $D = 0$ cm^{2}s^{-1} within the sub-ns window. Panels c and f for photons are quite similar for the two simulations and consequently the tail region, in the presence of photon recycling, is similar for both cases.

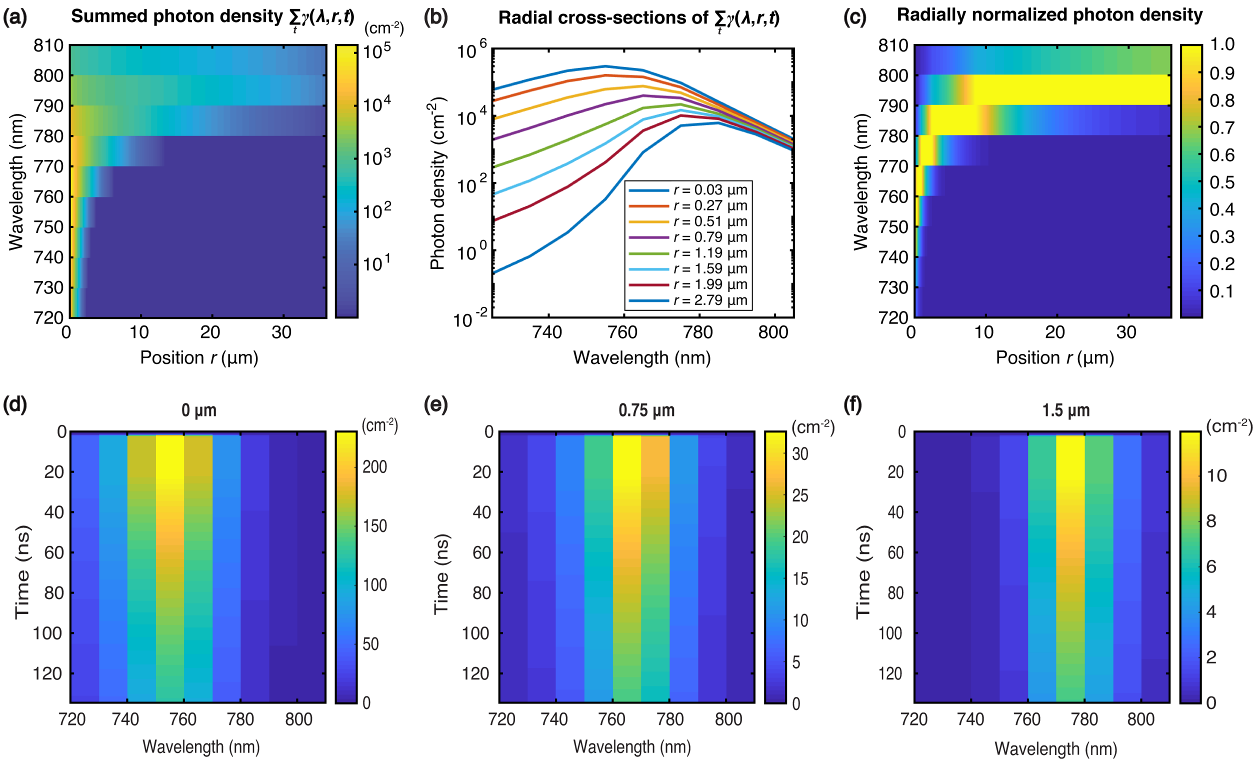

Figure 5.16 For fluence of 0.42 µJ/cm^2 ($n_{0-3\mathrm{D}} = 1.54 \times 10^{16}$ cm^{-3}), a) Emitted photon density as a function of position r and wavelength λ, b) Spectral distribution of carrier densities at different positions r, and c) the normalized carrier density (peak tracing) as a function of position r and wavelength λ. d), e) and f) Spectro-temporal cross-sections at positions $r = 0$, 0.75 and 1.5 µm.

The features of the spectral shift in the panels of Figure 5.16 are quite clear despite the low resolution. The spectral behaviour in this 120 ns time window replicates quite well the results from the high resolution simulation. Panels a to c appear identical to those in Figure 5.11. In panels d-f, the data are constant with time. This is an indication that the spectral red shift reaches maximum value and plateaus within the ~ns time frame. The relationships between fluence, peak carrier densities and spreading (standard deviation σ at $t = 0$) are shown for the study above in Figure 5.17. The relationship between peak density and fluence is quite stable for all diffusion coefficients. However, discrepencies between photon recycling and non photon recycling data points are more apparent with higher fluences, due to higher order recombination, as well as increasing diffusion coefficients.

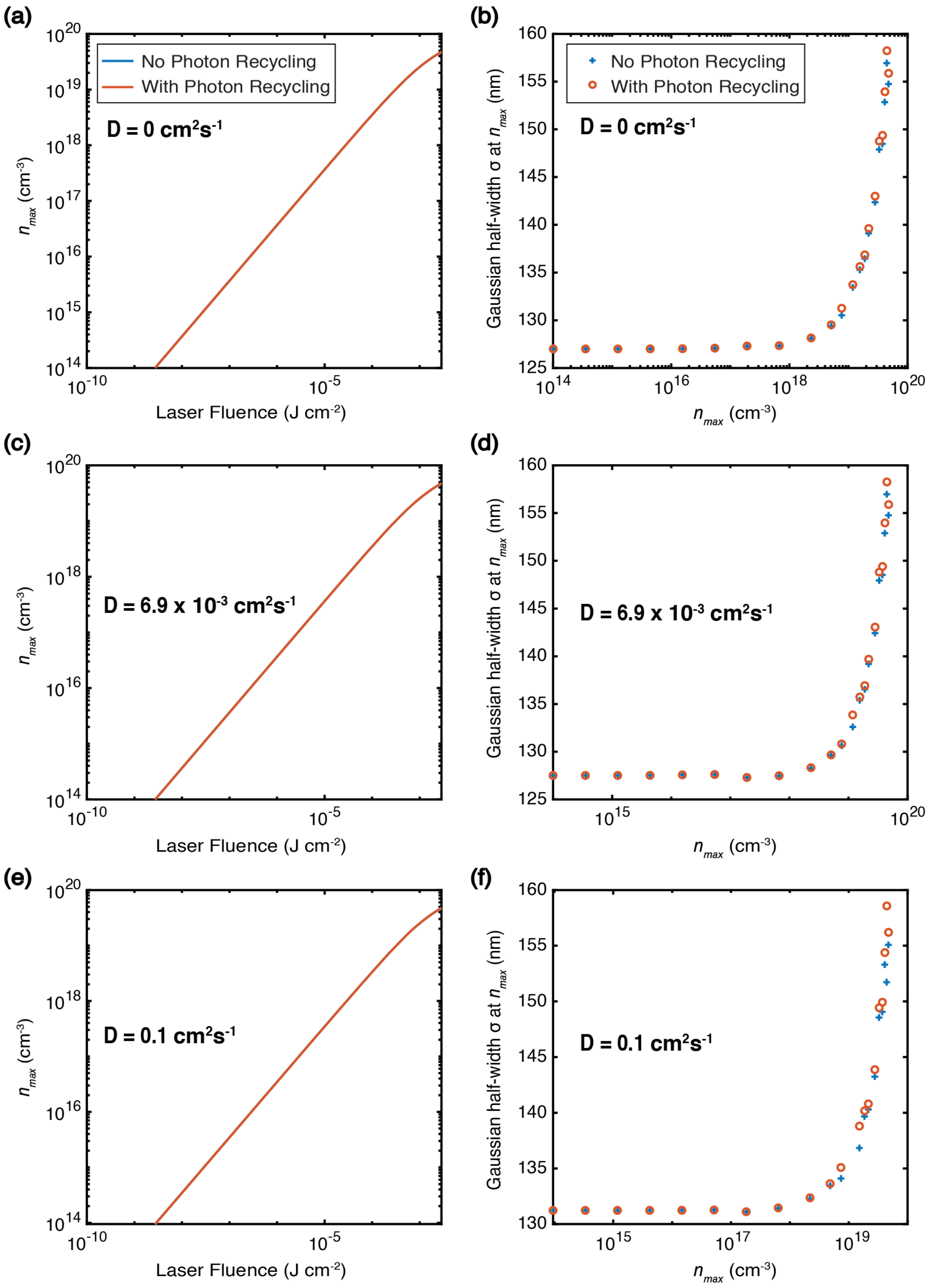

Figure 5.17 For varying D in presence as well as absence of photon recycling, we show in a), c) and e) the peak carrier density as function of fluence and in b), d) and f) the spreading as function of peak carrier density.

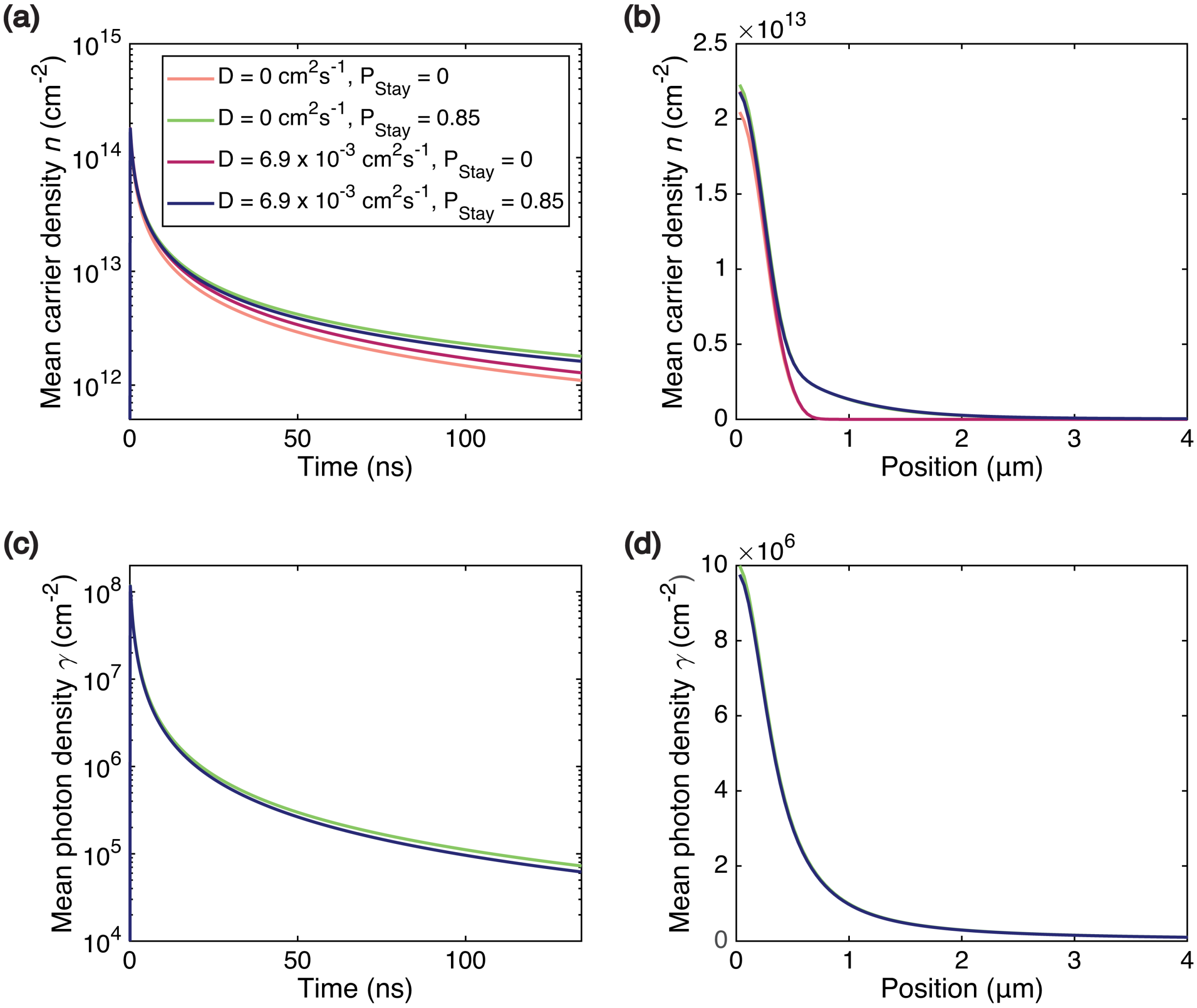

Figure 5.18 Average lifetimes and radial profiles of carriers, in a) and b), and recycled photons, in c) and d), simulated at a fluence of 0.42 µJ/cm^2 ($n_{0-3\mathrm{D}} = 1.5 \times 10^{16}$ cm^{-3}) for $D = 0$ and 6.9×10^{-3} cm^{2}s^{-1}.

Figure 5.18 depicts the integrated view of the spatial-temporal data over each coordinate. The mean lifetime, for example, is calculated as $(\sum_{j=0}^{J} n(r_j = j \cdot dr, t))/J$ whereas the mean radial profile is obtained using $(\sum_{i=0}^{T} n(r, t_i = i \cdot dt))/T$; where J and T correspond to the number of space and time points. Photon recycling contributes to longer lifetimes and to general increase in carrier densities. The tails of the radial profile, especially, increase relatively more. A higher diffusion coefficient, on the other hand, reduces densities, in the central region, as well as integrated lifetimes within the simulation window.

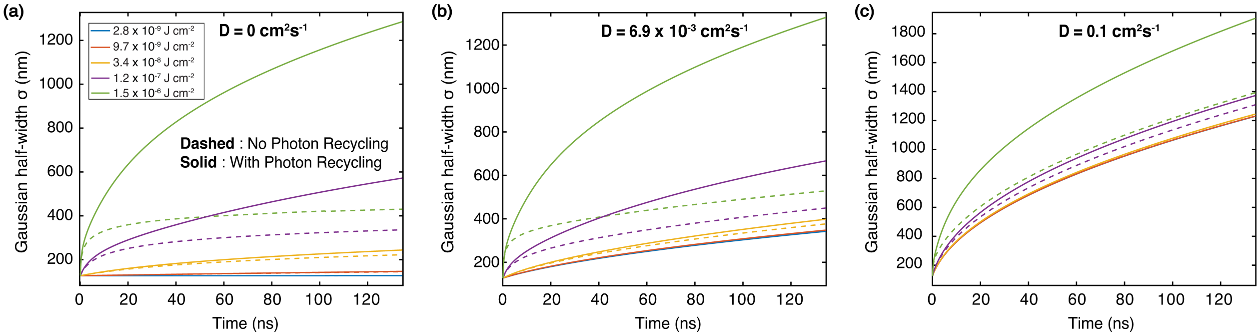

Figure 5.19 Calculated time-dependent spreading of the Gaussian half-width (standard deviation) of the PL as a function of the initial pulse fluence in the presence and absence of photon recycling for different diffusion coefficients a) $D = 0$ cm^{2}s^{-1}, b) $D = 6.9 \times 10^{-3}$ cm^{2}s^{-1} and c) $D = 0.1$ cm^{2}s^{-1}. The corresponding peak densities at $t = 0$ for the fluences in the legend are $n_{0-3\mathrm{D}} = 9.9 \times 10^{13}$, 1.5×10^{16}, 1.9×10^{17}, 2.3×10^{18}, 1.9×10^{19} cm^{-3}.

Figure 5.19 explicitly shows the influence of the diffusion coefficient and pump fluence on the Gaussian width of the PL. Spreading of the spot is important under all conditions including $D = 0$ cm^{2}s^{-1}, independent of whether photon recycling is present. In the absence of photon recycling, the spreading is a result of faster recombination at the center of the carrier distribution due to the presence of nonlinear terms in the diffusion equation (Chapter 4). As expected, larger diffusion coefficients increase the degree of time-dependent spreading, particularly at low fluence where it is the most important mechanism. Meanwhile, when photon recycling is present, the spreading is further increased. However, this increase is only important at large fluences or for small values of D. The reason for this is that the quantum yield plays a critical role in determining the relative importance of photon recycling. When the fluence is low, the quantum yield quickly becomes negligible a few mm away from the excitation spot. This makes the re-emission of absorbed photons impossible. Similar conclusions can be derived in Figure 5.20, where we varied spot sizes, fluences and diffusion coefficients. Panels a to c show that effects of photon recycling are more prominent at higher fluences. Panel d presents the case of $D = 0$ cm^{2}s^{-1} for the same fluence as in panel b. By comparing these two panels, we observe that diffusion overpowers the effects of higher order recombination independent of photon recycling presence. Although photon recycling always contributes to the wings of the carrier density, there is only a limited window of experimental conditions where photon recycling plays an important role in significantly changing the luminescence properties, such as its width (Figure 5.18). This only occurs for low values of D, where diffusion is less prominent, and for large values of the initial carrier density, where the PL quantum yield in the wings of the initial carrier distribution is high enough for multiple photon recycling events to occur. The first condition could play an

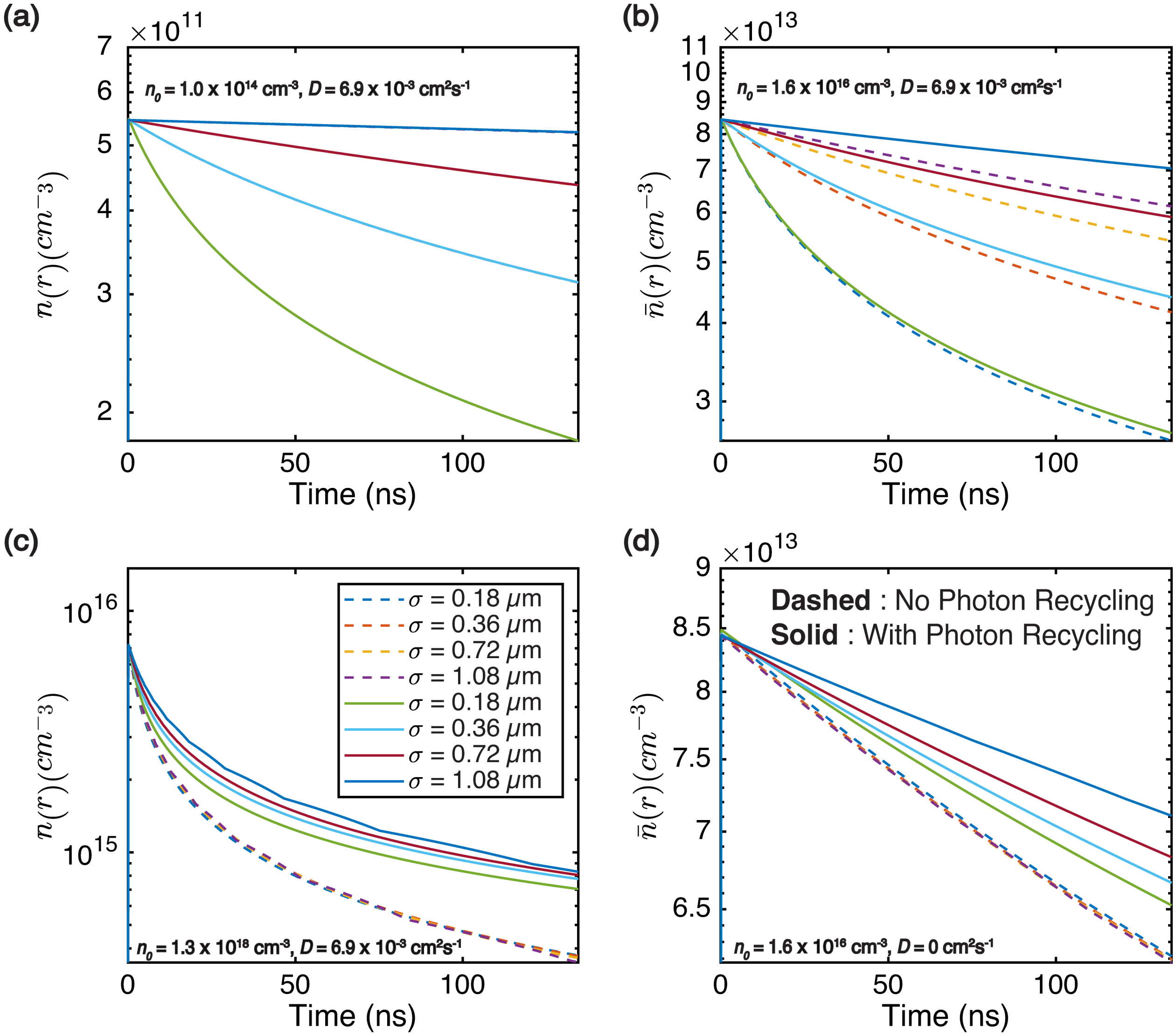

Figure 5.20 Effect of changing spot size for different fluence/peak densities in a), b) and c). In d), D is set to 0 cm^{2}s^{-1} for same density as b). In panel a, the dashed and solid sets of curves are overlapping.

important role in crossing grain boundaries where diffusion is suppressed.

5.4 Summary

We have numerically studied the effect of photon recycling on carrier transport within the plane of perovskite films, under focussed excitation conditions. Our results reveal that re-absorption leads to the generation of carriers at significant distances away from the excitation spot. However, the densities in these regions are negligible compared to those near the excitation region (>4 orders of magnitude lower after 1–2 mm). As a result, re-emission (recycling) is not possible for these carriers and one can understand their spatial behavior simply based on the tail of the absorption spectrum. The low carrier density and subsequent low PL quantum yields lead to a negligible contribution to the PL shape, when reported on a linear scale. We also compared the temporal and spatial dependence of the PL spectrum to simulation results. From the analysis, we find that band-filling leads to a space (and time)-dependent red-shift of the PL away from the excitation spot. This behavior can be quantitatively estimated from the Lasher-Stern-Würfel relation. Lastly, we studied the effect of varying the initial fluence (and hence the quantum yield) and diffusion coefficient on transport in the presence of photon recycling. We find that photon recycling can only meaningfully modify the carrier distribution in circumstances where the excitation fluence is high and D is small. In contrast to the situation of homogeneous excitation at densities typical of solar cell operating conditions, photon recycling can be safely neglected in microscopy measurements performed at peak densities ~10^{15} cm^{-3}.

CHAPTER 6 CONCLUSION AND OUTLOOK

6.1 Contributions to Scientific Progress

As stated in the outline, the objectives of this thesis are centered around two fundamental research questions. The first relates to elucidating the nature and effects of lateral diffusion in hybrid perovskite materials whereas the second seeks to clarify the contribution of photon recycling in enhancing lateral charge carrier diffusion under focussed conditions as those in typical microscopy measurements. The first question was initially explored at the end of Chapter 3, where we presented our new technique for imaging carrier diffusion in both space and time. This technique relies on a streak camera to image the photoluminescence coming from a picosecond laser excited perovskite thin film. We conducted preliminary measurements on toluene washed $MAPbI_3$ based mixed halide samples, of $PbCl_2$ and $PbAc_2$ precursors, as a base reference for future experiments. We identified that anti-solvent treatment using toluene visibly improved morphology and lead to higher spreading. This was validated for $PbAc_2$ sample where in the absence of toluene treatment, no spreading was observed. Microscope images showed the $PbAc_2$ sample to be more conducive for uninhibited diffusion on paper as it presented a superior morphology. The streak camera measurements also revealed longer lifetimes for this sample, i.e. ~100 ns measurement window versus ~10 ns for $PbCl_2$. This is indicative of lower trap-based recombination environment which should be beneficial for superior device performance. Our devices made from the $PbAc_2$ films presented indeed a higher device efficiency (~12.4 %) compared to those made from $PbCl_2$ (~3 %). This is a surprising result from a diffusion perspective considering how the $PbCl_2$ based film showed spreading beyond 1 µm in a much shorter time (< 10 ns) as opposed to $PbAc_2$ one (~100 ns). Further insight on the carrier physics beyond qualitative observations could only be obtained with knowledge of underlying parameters such as diffusion and recombination coefficients. To do this, fundamental necessities of the moment were high quality device grade samples, an improved experimental setup for better characterization and lastly, an appropriate mathematical treatment for the accurate interpretation of observed data.

In Chapter 4, we improved the streak camera setup with a sweeping unit for sub ns resolution and developed a new statistical model-based fitting procedure for extracting recombination and diffusion coefficients from raw data. This time, the measurement was performed on five device grade perovskite thin films provided by our collaborators from Princeton University: MA ($MAPbI_3$), FA ($FAPbI_3$), FAMA ($FA_{0.85}MA_{0.15}Pb(I_{0.85}Br_{0.15})_3$), MA-ACN (Acetonitrile processed $MAPbI_3$) and BR ($MAPbBr_3$). Among those presented here, the best reported devices in literature are made of FAMA and MA-ACN films. Our results, astonishingly, show the smallest diffusion coefficients for these samples. This is unexpected from a standard semiconductor theory perspective, where large diffusion coefficients automatically lead to higher short-circuit currents, and therefore higher efficiencies. Zooming into very small sub-ns timescales for the MA-ACN sample, we also discovered a higher diffusion regime. Overall, D appears to decrease with increasing timescale for all samples. The timescale dependence of diffusion is indicative of inhibited spreading over multi-grain distances due to trapping/de-trapping process at various recombination centers along the way. We also discovered significant discrepancy between the laser and initial PL($t = 0$) spot sizes that could not be temporally resolved even within the 1 ns measurement window. A simple calculation of spreading for a single photon recycling appears to explain this spreading difference, although further attention to photon recycling is necessary to confirm this hypothesis. The main takeaway from these results is that despite low diffusion coefficients, devices can achieve very high efficiencies. This also explains why our $PbAc_2$ samples produced better devices in the preliminary measurement despite lower spreading capacities with regards to the $PbCl_2$ film. We attribute our device success in large part to the high $PLQE$ values, rather than diffusion, as observed for the FAMA and MA-ACN samples.

In Chapter 5, we address the second research question concerning the interaction of photon recycling with charge carrier lateral diffusion. We approached this problem from both, experimental and theoretical angles. On the experimental side, we modified the streak camera setup to perform spectro-temporal measurements at different radial positions of the PL profile. On the theoretical side, we solved the coupled charge carrier/photon recycling equations numerically to study the spatio-spectro-temporal behaviour resulting from the interplay between these mechanisms. Although, we do observe significant spatial redistribution of charge carriers at larger distances due to photon recycling in our simulations, the direct comparison of experimental and theoretical spectral shifts appears to indicate that photon recycling alone does not explain the measured spectral behaviour. We found that the spectral shift is better explained by a phenomenon called band filling wherein the spectral emission is directly correlated to spatiotemporal carrier densities in the film. High/low densities lead to higher/lower energies (or low/high wavelength) emission due to an increasing/decreasing quasi-Fermi splitting $\Delta\mu$. Lastly, through our numerical fluence studies, we revealed that photon recycling under focussed conditions plays a significant role at high densities alone. Also, if the diffusion coefficient D is large enough, the spreading contribution of photon recycling relative to D becomes quickly negligible. Based on a small timescale observation of rapid spreading, for high densities and $D = 0$, we also believe that the previously observed early timescale discrepancy between the laser and initial PL profiles in Chapter 4 is due to apparent/intensity-dependent spreading rather than diffusion. Overall, the renewed understanding on the interplay between diffusion, photon recycling and band filling will be very helpful in future interpretation of micro-PL measurement results where the influence of photon recycling can often be overestimated, particularly at lower densities.

6.2 Limitations and Constraints

In our spatiotemporal diffusion measurements, there are significant limitations in terms of instrumentation and modelling assumptions. Currently, the most important significant experimental limitation is the minimum threshold for excitation requiring carrier densities to be above 10^{16} cm^{-3}. This means that a lack of experimental data at lower densities (~10^{15} cm^{-3}) is currently preventing us from fully understanding diffusive properties of real devices under 1 sun illumination intensities. As for the modelling, many of our assumptions are non-applicable for low injection scenarios. The most important one is ambipolar transport, i.e. we consider n and p type carriers to be non-distinguishable. Although the model is valid for our experimental data, generalization of results to lower densities does carry some level of uncertainty. There are several modelling restrictions, especially with regards to both diffusion-only and photon recycling simulations. Depending on the input parameters, our simulations require 15-120 mins/run. We therefore limit ourselves to isotropic conditions in an effort to minimize intensive computations. Similarly, batch simulations of 3D photon recycling/diffusion also remain a challenge.

We also face significant obstacles in elucidating the precise influence of morphology on transport properties. In our measurements, we do observe a decrease in spreading with larger timescales (or multi-grain distances) experimentally. Furthermore, our photon recycling fluence studies also reveal varying timescale dependent spreading regimes, particularly at high densities. Although, our results point towards apparent/intensity-dependent spreading as the main phenomenon responsible for the observed behaviour, we cannot safely discard the role of morphology due to the assumptions in our calculations. We have also neglected grain boundary modelling, which currently remains a challenge due to a lack of consensus in the scientific community as to their precise role in carrier dynamics. Some reports indicate that boundaries are recombination centers whereas other report shorter lifetimes within the grain as opposed to the edges. However, recent time-resolved photoelectron microscopy measurements (TR-PEEM) present stronger evidence for a dominant hole trapping mechanism resulting from interstitial iodine defect clusters, that are particularly concentrated at the boundaries [194]. Further advancement in this field could better direct our methodologies in the future as well.

6.3 Strategies and Outlook

Overall, we have focussed on elucidating fundamental carrier physics in hybrid perovskites based on optical streak camera techniques and simulations. Future research should first address the above listed limitations and constraints vis-à-vis our experimental and analytical methods.

Diffusion Measurements: With regards to the experimental setup, the next step should directly focus on morphology, particularly effects of grain boundaries in PL behaviour. The measurements presented here are biased in terms of measurement location as the excitation is always performed within a large grain with no surrounding impediments. However, in the future, one could use a microscope image to obtain a grid trace of the 2D grain boundary lines to simulate real anisotropic conditions that are observed in the experiment. An important hurdle though would be to design a robust and optimized simulation that is adapted for anisotropic conditions. Above all, the usage of radial coordinates and ideal symmetric conditions for mathematical simplicity would no longer be applicable. Therefore, innovation is necessary in the following three areas: mathematical modelling, coding/algorithms, and implementation. Although our results present a good picture of the underlying physics, we still don't have a way to directly correlate our results with a quantifiable change in actual device parameters. Future measurements should focus on bridging the divide between optical characterization measurements and device parameters. For example, we could potentially also incorporate localized J-V measurements alongside streak camera PL measurements akin to scanning photocurrent microscopy (SPCM) method. This will allow us to track changes in carrier densities through both optical and electrical methods simultaneously and therefore increase the accuracy of interpretation.

Photon Recycling: An interesting experimental strategy could be a temperature dependent measurement involving a cryostat. We have excluded excitons in our modelling due to the low room temperature exciton binding energies of our materials. However, both the band filling absorption/emission model as well as carrier dynamics/photon recycling equations allow for future accommodation of excitonic features. Carrying out temperature dependent studies could lead to a deeper understanding on how phase transitions and excitonic features could potentially alter diffusion and photon recycling in perovskites. Focussing on the photon recycling simulation alone, a plethora of enhancements are possible to further our understanding of the subject. For one, instead of simply using a probability coefficient (P_{stay}) to quantify light confinement, in future calculations, we could include the complete optical model (Beer-Lamber/Light Trapping/Layers) in the simulation to precisely track the spatial photon behaviour within the film. A significant add-on would be the inclusion of band filling effects directly in the calculation. Currently, we use a constant absorption/emission spectrum for photon recycling simulation at every spatio-temporal node. In the future, this could be transformed into spatio-temporal coordinate and density dependent spectra to account for band-filling induced changes in the material spectral properties. This will be a more accurate way to reconcile experiment and theoretical spectra.

Overall, we need to test many types of perovskite samples to establish higher measurement and fitting consistency for both objectives. Based on these recommendations, in the coming years, we hope to uncover more answers (and questions!) which could help the global research community in approaching the maximum PSC theoretical efficiency.

REFERENCES

[1] BP, “BP statistical review of world energy 2019,” p. 61, 2019. [Online]. Available: https://www.bp.com/content/dam/bp/business-sites/en/global/corporate/pdfs/energy-economics/statistical-review/bp-stats-review-2019-full-report.pdf

[2] IRENA, “Worldwide investment trends in renewable energy by source,” 2020. [Online]. Available: http://resourceirena.irena.org/gateway/dashboard/?topic=6{&}subTopic=11

[3] Solargis, “Solar resource map: Photovoltaic power potential,” 2021. [Online]. Available: https://api.globalsolaratlas.info/download/World/World_PVOUT_mid-size-map_160x95mm-300dpi_v20191015.png

[4] IEA, “World energy investment report 2019,” 2019. [Online]. Available: https://www.iea.org/reports/world-energy-investment-2019

[5] M. Riordan and L. Hoddeson, “Origins of the pn junction,” *IEEE Spectrum*, vol. 34, no. 6, pp. 46–51, 1997.

[6] H. Theurer, “Purification of silicon,” *Bell Laboratories Record*, vol. 33, pp. 327–330, 1955.

[7] J. Czochralski, “Ein neues verfahren zur messung der kristallisationsgeschwindigkeit der metalle,” *Zeitschrift für Physikalische Chemie*, vol. 92, p. 219, 1918.

[8] K. Yoshikawa, H. Kawasaki, W. Yoshida, T. Irie, K. Konishi, K. Nakano, T. Uto, D. Adachi, M. Kanematsu, H. Uzu, and K. Yamamoto, “Silicon heterojunction solar cell with interdigitated back contacts for a photoconversion efficiency over 26%,” *Nature Energy*, vol. 2, no. 5, 2017.

[9] M. Green, E. Dunlop, J. Hohl-Ebinger, M. Yoshita, N. Kopidakis, and X. Hao, “Solar cell efficiency tables (version 57),” *Progress in Photovoltaics: Research and Applications*, vol. 29, no. 1, pp. 3–15, 2021.

[10] J. Jean, P. R. Brown, R. L. Jaffe, T. Buonassisi, and V. Bulović, “Pathways for solar photovoltaics,” *Energy and Environmental Science*, vol. 8, no. 4, pp. 1200–1219, 2015.

[11] E. A. Alsema, “Energy pay-back time and CO_2 emissions of PV systems,” *Progress in Photovoltaics: Research and Applications*, vol. 8, no. 1, pp. 17–25, 2000.

[12] F. Cucchiella and I. Dadamo, "Estimation of the energetic and environmental impacts of a roof-mounted building-integrated photovoltaic systems," *Renewable and Sustainable Energy Reviews*, vol. 16, no. 7, pp. 5245–5259, 2012.

[13] A. K. Chilvery, A. K. Batra, B. Yang, K. Xiao, P. Guggilla, M. D. Aggarwal, R. Surabhi, R. B. Lal, J. R. Currie, and B. G. Penn, "Perovskites: Transforming photovoltaics, a mini-review," *Journal of Photonics for Energy*, vol. 5, no. 1, p. 057402, 2015.

[14] E. Yablonovitch, T. Gmitter, J. P. Harbison, and R. Bhat, "Extreme selectivity in the lift-off of epitaxial GaAs films," *Applied Physics Letters*, vol. 51, no. 26, pp. 2222–2224, 1987.

[15] National Renewable Energy Laboratory (NREL), "Photovoltaic efficiency chart," 2020. [Online]. Available: https://www.nrel.gov/pv/assets/images/efficiency-chart.png

[16] M. Jeong, I. W. Choi, E. M. Go, Y. Cho, M. Kim, B. Lee, S. Jeong, Y. Jo, H. W. Choi, J. Lee, J. H. Bae, S. K. Kwak, D. S. Kim, and C. Yang, "Stable perovskite solar cells with efficiency exceeding 24.8% and 0.3-V voltage loss," *Science*, vol. 369, no. 6511, pp. 1615–1620, 2020.

[17] Y. Deng, E. Peng, Y. Shao, Z. Xiao, Q. Dong, and J. Huang, "Scalable fabrication of efficient organolead trihalide perovskite solar cells with doctor-bladed active layers," *Energy and Environmental Science*, vol. 8, no. 5, pp. 1544–1550, 2015.

[18] M. Hambsch, Q. Lin, A. Armin, P. L. Burn, and P. Meredith, "Efficient, monolithic large area organohalide perovskite solar cells," *Journal of Materials Chemistry A*, vol. 4, no. 36, pp. 13 830–13 836, 2016.

[19] S. Razza, F. Di Giacomo, F. Matteocci, L. Cinà, A. L. Palma, S. Casaluci, P. Cameron, A. D'Epifanio, S. Licoccia, A. Reale, T. M. Brown, and A. Di Carlo, "Perovskite solar cells and large area modules (100 cm^2) based on an air flow-assisted PbI_2 blade coating deposition process," *Journal of Power Sources*, vol. 277, pp. 286–291, 2015.

[20] J. H. Kim, S. T. Williams, N. Cho, C. C. Chueh, and A. K. Jen, "Enhanced environmental stability of planar heterojunction perovskite solar cells based on blade-coating," *Advanced Energy Materials*, vol. 5, no. 4, pp. 2–7, 2015.

[21] A. T. Barrows, A. J. Pearson, C. K. Kwak, A. D. Dunbar, A. R. Buckley, and D. G. Lidzey, "Efficient planar heterojunction mixed-halide perovskite solar cells deposited via spray-deposition," *Energy and Environmental Science*, vol. 7, no. 9, pp. 2944–2950, 2014.

[22] J. Berry, T. Buonassisi, D. A. Egger, G. Hodes, L. Kronik, Y. L. Loo, I. Lubomirsky, S. R. Marder, Y. Mastai, J. S. Miller, D. B. Mitzi, Y. Paz, A. M. Rappe, I. Riess, B. Rybtchinski, O. Stafsudd, V. Stevanovic, M. F. Toney, D. Zitoun, A. Kahn, D. Ginley, and D. Cahen, "Hybrid organic-inorganic perovskites (HOIPs): Opportunities and challenges," *Advanced Materials*, vol. 27, no. 35, pp. 5102–5112, 2015.

[23] J. H. Noh, S. H. Im, J. H. Heo, T. N. Mandal, and S. I. Seok, "Chemical management for colorful, efficient, and stable inorganic-organic hybrid nanostructured solar cells," *Nano Letters*, vol. 13, no. 4, pp. 1764–1769, 2013.

[24] J. S. Blakemore, "Semiconducting and other major properties of gallium arsenide," *Journal of Applied Physics*, vol. 53, no. 10, 1982.

[25] A. R. Srimath Kandada and A. Petrozza, "Photophysics of hybrid lead halide perovskites: The role of microstructure," *Accounts of Chemical Research*, vol. 49, no. 3, pp. 536–544, 2016.

[26] Y. Yamada, T. Nakamura, M. Endo, A. Wakamiya, and Y. Kanemitsu, "Photocarrier recombination dynamics in perovskite $CH_3NH_3PbI_3$ for solar cell applications." *Journal of the American Chemical Society*, vol. 136, no. 33, pp. 11 610–3, 2014.

[27] K. T. Munson, C. Grieco, E. Kennehan, R. J. Stewart, and J. B. Asbury, "Time-resolved infrared spectroscopy directly probes free and trapped carriers in organo-halide perovskites," *ACS Energy Letters*, vol. 2, no. 3, pp. 651–658, 2017.

[28] M. Saba, F. Quochi, A. Mura, and G. Bongiovanni, "Excited state properties of hybrid perovskites," *Accounts of Chemical Research*, vol. 49, no. 1, pp. 166–173, Sep. 2016.

[29] T. C. Sum, S. Chen, G. Xing, X. Liu, and B. Wu, "Energetics and dynamics in organic-inorganic halide perovskite photovoltaics and light emitters," *Nanotechnology*, vol. 26, no. 34, 2015.

[30] L. M. Herz, "Charge-carrier dynamics in organic-inorganic metal halide perovskites," *Annual Review of Physical Chemistry*, vol. 67, no. 1, pp. 65–89, May 2016.

[31] S. D. Stranks, V. M. Burlakov, T. Leijtens, J. M. Ball, A. Goriely, and H. J. Snaith, "Recombination kinetics in organic-inorganic perovskites: Excitons, free charge, and subgap states," *Physical Review Applied*, vol. 2, no. 3, p. 034007, Sep. 2014.

[32] G. J. A. Wetzelaer, M. Scheepers, A. M. Sempere, C. Momblona, J. Ávila, and H. J. Bolink, "Trap-assisted non-radiative recombination in organic-inorganic perovskite solar cells," *Advanced Materials*, vol. 27, no. 11, pp. 1837–1841, 2015.

[33] A. Baumann, S. Väth, P. Rieder, M. C. Heiber, K. Tvingstedt, and V. Dyakonov, “Identification of trap states in perovskite solar cells,” *Journal of Physical Chemistry Letters*, vol. 6, no. 12, pp. 2350–2354, 2015.

[34] G. Giorgi, J.-I. I. Fujisawa, H. Segawa, and K. Yamashita, “Small photocarrier effective masses featuring ambipolar transport in methylammonium lead iodide perovskite: A density functional analysis,” *Journal of Physical Chemistry Letters*, vol. 4, no. 24, pp. 4213–4216, Dec. 2013.

[35] V. D’Innocenzo, G. Grancini, M. J. Alcocer, A. R. S. Kandada, S. D. Stranks, M. M. Lee, G. Lanzani, H. J. Snaith, and A. Petrozza, “Excitons versus free charges in organo-lead tri-halide perovskites,” *Nature Communications*, vol. 5, p. 3586, 2014.

[36] P. Piatkowski, B. Cohen, F. Javier Ramos, M. Di Nunzio, M. K. Nazeeruddin, M. Grätzel, S. Ahmad, and A. Douhal, “Direct monitoring of ultrafast electron and hole dynamics in perovskite solar cells,” *Physical Chemistry Chemical Physics*, vol. 17, no. 22, pp. 14 674–14 684, 2015.

[37] M. Saba, M. Cadelano, D. Marongiu, F. Chen, V. Sarritzu, N. Sestu, C. Figus, M. Aresti, R. Piras, A. Geddo Lehmann, C. Cannas, A. Musinu, F. Quochi, A. Mura, and G. Bongiovanni, “Correlated electron-hole plasma in organometal perovskites,” *Nature Communications*, vol. 5, no. 1, p. 5049, Dec. 2014.

[38] V. Sarritzu, N. Sestu, D. Marongiu, X. Chang, S. Masi, A. Rizzo, S. Colella, F. Quochi, M. Saba, A. Mura, and G. Bongiovanni, “Optical determination of Shockley-Read-Hall and interface recombination currents in hybrid perovskites,” *Scientific Reports*, vol. 7, no. January, p. 44629, 2017.

[39] E. Edri, S. Kirmayer, S. Mukhopadhyay, K. Gartsman, G. Hodes, and D. Cahen, “Elucidating the charge carrier separation and working mechanism of $\mathrm{CH_3NH_3PbI_{3-x}Cl_x}$ perovskite solar cells,” *Nature Communications*, vol. 5, pp. 1–8, 2014.

[40] C. Wehrenfennig, M. Liu, H. J. Snaith, M. B. Johnston, and L. M. Herz, “Charge-carrier dynamics in vapour-deposited films of the organolead halide perovskite $\mathrm{CH_3NH_3PbI_{3-x}Cl_x}$,” *Energy and Environmental Science*, vol. 7, no. 7, pp. 2269–2275, 2014.

[41] C. Wehrenfennig, M. Liu, H. J. Snaith, M. B. Johnston, and L. M. Herz, “Charge carrier recombination channels in the low-temperature phase of organic-inorganic lead halide perovskite thin films,” *APL Materials*, vol. 2, no. 8, 2014.

[42] G. Xing, N. Mathews, S. Sun, S. S. Lim, Y. M. Lam, M. Gratzel, S. Mhaisalkar, and T. C. Sum, “Long-range balanced electron- and hole-transport lengths in organic-inorganic $CH_3NH_3PbI_3$,” *Science*, vol. 342, no. 6156, pp. 344–347, Oct. 2013.

[43] S. D. Stranks, G. E. Eperon, G. Grancini, C. Menelaou, M. J. P. Alcocer, T. Leijtens, L. M. Herz, A. Petrozza, and H. J. Snaith, “Electron-hole diffusion lengths exceeding 1 micrometer in an organometal trihalide perovskite absorber,” *Science*, vol. 342, no. 6156, pp. 341–344, Oct. 2013.

[44] Q. Dong, Y. Fang, Y. Shao, P. Mulligan, J. Qiu, L. Cao, and J. Huang, “Electron-hole diffusion lengths > 175 μm in solution-grown $CH_3NH_3PbI_3$ single crystals,” *Science*, vol. 347, no. 6225, pp. 967–970, 2015.

[45] T. Kirchartz, F. Staub, and U. Rau, “Impact of photon recycling on the open-circuit voltage of metal halide perovskite solar cells,” *ACS Energy Letters*, vol. 1, no. 4, pp. 731–739, 2016.

[46] T. Tiedje, E. Yablonovitch, G. Cody, and B. Brooks, “Limiting efficiency of silicon solar cells,” *IEEE Transactions on Electron Devices*, vol. 31, no. 5, pp. 711–716, May 1984.

[47] B. E. A. Saleh and M. C. Teich, *Fundamentals of Photonics*, 3rd ed. Wiley, 2019.

[48] N. Peyghambarian, S. W. Koch, and A. Mysyrowicz, *Introduction to Semiconductor Optics.* Englewood Cliffs, N. J.: Prentice Hall, 1993, vol. 28, no. 6.

[49] S. L. Chuang, *Physics of Optoelectronic Devices.* New York: Wiley, 1995.

[50] W. Van Roosbroeck and W. Shockley, “Photon-radiative recombination of electrons and holes in germanium,” *Physical Review*, vol. 94, no. 6, pp. 1558–1560, 1954.

[51] S. M. Sze and K. K. Ng, *Physics of Semiconductor Devices*, 3rd ed., 2006.

[52] J. Bisquert, *The Physics of Solar Cells : Perovskites, Organics, and Photovoltaic Fundamentals*, 1st ed. CRC Press, 2017.

[53] P. Bhattacharya and L. Y. Pang, *Semiconductor Optoelectronic Devices.* Upper Saddle River, NJ, USA: Prentice-Hall, Inc., 1994, vol. 47, no. 12.

[54] M. S. Esfahani, “Device physics of organic and perovskite solar cells,” Doctoral Dissertation, Iowa State University, Ames, Iowa, 2015. [Online]. Available: https://search.proquest.com/docview/1765206031?accountid=40695

[55] K. F. Brennan, *The Physics of Semiconductors: With Applications to Optoelectronic Devices.* Cambridge, UK: Cambridge University Press, 1999.

[56] D. A. Neamen, *Semiconductor Physics and Devices*, 4th ed. New York: McGraw-Hill, 2012.

[57] A. Fick, "On liquid diffusion," *Journal of Membrane Science*, vol. 100, no. 1, pp. 33–38, Mar. 1995.

[58] M. A. Green, *Solar Cells: Operating Principles, Technology and System Applications.* Englewood Cliffs, N. J.: Prentice Hall, 1982.

[59] W. Shockley, "The theory of p-n junctions in semiconductors and p-n junction transistors," *Bell System Technical Journal*, vol. 28, no. 3, pp. 435–489, Jul. 1949.

[60] "NREL ASTM G-173 spectra." [Online]. Available: https://www.nrel.gov/grid/solar-resource/spectra-am1.5.html

[61] J. Nelson, *The Physics of Solar Cells.* London: Imperial College Press, 2003.

[62] J. C. Blakesley and D. Neher, "Relationship between energetic disorder and open-circuit voltage in bulk heterojunction organic solar cells," *Physical Review B - Condensed Matter and Materials Physics*, vol. 84, no. 7, 2011.

[63] D. Ompong and J. Singh, "High open-circuit voltage in perovskite solar cells: The role of hole transport layer," *Organic Electronics*, vol. 63, pp. 104–108, 2018.

[64] W. Yang, Y. Yao, and C. Q. Wu, "Origin of the high open circuit voltage in planar heterojunction perovskite solar cells: Role of the reduced bimolecular recombination," *Journal of Applied Physics*, vol. 117, no. 9, 2015.

[65] R. Brenes, M. Laitz, J. Jean, D. W. Dequilettes, and V. Bulović, "Benefit from photon recycling at the maximum-power point of state-of-the-art perovskite solar cells," *Physical Review Applied*, vol. 12, no. 1, p. 1, 2019.

[66] U. Rau, U. W. Paetzold, and T. Kirchartz, "Thermodynamics of light management in photovoltaic devices," *Physical Review B - Condensed Matter and Materials Physics*, vol. 90, no. 3, pp. 1–16, 2014.

[67] M. Ansari-rad and J. Bisquert, "Insight into photon recycling in perovskite semiconductors from the concept of photon diffusion," *Physical Review Applied*, vol. 10, no. 3, p. 1, 2018.

[68] G. Rose, “Beschreibung einiger neuen mineralien des urals,” *Annalen der Physik*, vol. 126, no. 8, pp. 652–656, 1840.

[69] V. M. Goldschmidt, “Die gesetze der krystallochemie,” *Naturwissenschaften*, vol. 14, no. 21, pp. 477–485, 1926.

[70] H. Topsoe, “Krystallographisch-chemische untersuchungen homologer verbindungen,” *Zeitschrift für Kristallographie*, vol. 8, pp. 246–296, 1884.

[71] D. Weber, “$CH_3NH_3PbX_3$, ein Pb(II)-system mit kubischer perowskitstruktur $CH_3NH_3PbX_3$, a Pb(II)-system with cubic perovskite structure,” *Z. Naturforsch*, vol. 33, no. August 1978, pp. 1443–1445, 1978.

[72] A. Kojima, K. Teshima, Y. Shirai, and T. Miyasaka, “Organometal halide perovskites as visible-light sensitizers for photovoltaic cells,” *Journal of the American Chemical Society*, vol. 131, no. 17, pp. 6050–6051, 2009.

[73] A. M. Glazer, “The classification of tilted octahedra in perovskites,” *Acta Crystallographica Section B Structural Crystallography and Crystal Chemistry*, vol. 28, no. 11, pp. 3384–3392, Nov. 1972.

[74] Z. Li, M. Yang, J.-S. Park, S.-H. Wei, J. J. Berry, and K. Zhu, “Stabilizing perovskite structures by tuning tolerance factor: Formation of formamidinium and cesium lead iodide solid-state alloys,” *Chemistry of Materials*, vol. 28, no. 1, pp. 284–292, Jan. 2016.

[75] Z. Fan, K. Sun, and J. Wang, “Perovskites for photovoltaics: A combined review of organic-inorganic halide perovskites and ferroelectric oxide perovskites,” *Journal of Materials Chemistry A*, vol. 3, no. 37, pp. 18 809–18 828, 2015.

[76] C. C. Stoumpos, C. D. Malliakas, and M. G. Kanatzidis, “Semiconducting tin and lead iodide perovskites with organic cations: Phase transitions, high mobilities, and near-infrared photoluminescent properties,” *Inorganic Chemistry*, vol. 52, no. 15, pp. 9019–9038, 2013.

[77] J. S. Manser, J. A. Christians, and P. V. Kamat, “Intriguing optoelectronic properties of metal halide perovskites,” *Chemical Reviews*, vol. 116, no. 21, pp. 12 956–13 008, 2016.

[78] T. Baikie, Y. Fang, J. M. Kadro, M. Schreyer, F. Wei, S. G. Mhaisalkar, M. Graetzel, and T. J. White, “Synthesis and crystal chemistry of the hybrid perovskite

$(CH_3NH_3)PbI_3$ for solid-state sensitised solar cell applications," *Journal of Materials Chemistry A*, vol. 1, no. 18, pp. 5628–5641, 2013.

[79] S. Tao, I. Schmidt, G. Brocks, J. Jiang, I. Tranca, K. Meerholz, and S. Olthof, "Absolute energy level positions in tin- and lead-based halide perovskites," *Nature Communications*, vol. 10, no. 1, pp. 1–10, 2019.

[80] N. Pellet, P. Gao, G. Gregori, T. Y. Yang, M. K. Nazeeruddin, J. Maier, and M. Grätzel, "Mixed-organic-cation perovskite photovoltaics for enhanced solar-light harvesting," *Angewandte Chemie - International Edition*, vol. 53, no. 12, pp. 3151–3157, 2014.

[81] N. J. Jeon, J. H. Noh, W. S. Yang, Y. C. Kim, S. Ryu, J. Seo, and S. I. Seok, "Compositional engineering of perovskite materials for high-performance solar cells," *Nature*, vol. 517, no. 7535, pp. 476–480, 2015.

[82] A. Binek, F. C. Hanusch, P. Docampo, and T. Bein, "Stabilization of the trigonal high-temperature phase of formamidinium lead iodide," *Journal of Physical Chemistry Letters*, vol. 6, no. 7, pp. 1249–1253, 2015.

[83] W. S. Yang, B. W. Park, E. H. Jung, N. J. Jeon, Y. C. Kim, D. U. Lee, S. S. Shin, J. Seo, E. K. Kim, J. H. Noh, and S. I. Seok, "Iodide management in formamidinium-lead-halide-based perovskite layers for efficient solar cells," *Science*, vol. 356, no. 6345, pp. 1376–1379, 2017.

[84] J. P. Correa-Baena, A. Abate, M. Saliba, W. Tress, T. Jesper Jacobsson, M. Grätzel, and A. Hagfeldt, "The rapid evolution of highly efficient perovskite solar cells," *Energy and Environmental Science*, vol. 10, no. 3, pp. 710–727, 2017.

[85] T. Leijtens, G. E. Eperon, N. K. Noel, S. N. Habisreutinger, A. Petrozza, and H. J. Snaith, "Stability of metal halide perovskite solar cells," *Advanced Energy Materials*, vol. 5, no. 20, pp. 1–23, 2015.

[86] S. Tombe, G. Adam, H. Heilbrunner, D. H. Apaydin, C. Ulbricht, N. S. Sariciftci, C. J. Arendse, E. Iwuoha, and M. C. Scharber, "Optical and electronic properties of mixed halide ($X = I, Cl, Br$) methylammonium lead perovskite solar cells," *Journal of Materials Chemistry C*, vol. 5, no. 7, pp. 1714–1723, 2017.

[87] J. Cui, H. Yuan, J. Li, X. Xu, Y. Shen, H. Lin, and M. Wang, "Recent progress in efficient hybrid lead halide perovskite solar cells," *Science and Technology of Advanced Materials*, vol. 16, no. 3, p. 036004, 2015.

[88] S. Colella, E. Mosconi, P. Fedeli, A. Listorti, F. Gazza, F. Orlandi, P. Ferro, T. Besagni, A. Rizzo, G. Calestani, G. Gigli, F. De Angelis, and R. Mosca, "$MAPbI_{3-x}Cl_x$ mixed halide perovskite for hybrid solar cells: The role of chloride as dopant on the transport and structural properties," *Chemistry of Materials*, vol. 25, no. 22, pp. 4613–4618, 2013.

[89] N. Yantara, F. Yanan, C. Shi, H. A. Dewi, P. P. Boix, S. G. Mhaisalkar, and N. Mathews, "Unravelling the effects of Cl addition in single step $CH_3NH_3PbI_3$ perovskite solar cells," *Chemistry of Materials*, vol. 27, no. 7, pp. 2309–2314, 2015.

[90] S. Luo and W. A. Daoud, "Crystal structure formation of $CH_3NH_3PbI_{3-x}Cl_x$ perovskite," *Materials*, vol. 9, no. 3, pp. 1–13, 2016.

[91] T. C. Sum, N. Mathews, G. Xing, S. S. Lim, W. K. Chong, D. Giovanni, and H. A. Dewi, "Spectral features and charge dynamics of lead halide perovskites: Origins and interpretations," *Accounts of Chemical Research*, vol. 49, no. 2, pp. 294–302, 2016.

[92] T. Jesper Jacobsson, J. P. Correa-Baena, M. Pazoki, M. Saliba, K. Schenk, M. Grätzel, and A. Hagfeldt, "Exploration of the compositional space for mixed lead halogen perovskites for high efficiency solar cells," *Energy and Environmental Science*, vol. 9, no. 5, pp. 1706–1724, 2016.

[93] F. Brivio, C. Caetano, and A. Walsh, "Thermodynamic origin of photoinstability in the $CH_3NH_3Pb(I_{1-x}Br_x)$ hybrid halide perovskite alloy," *The Journal of Physical Chemistry Letters*, vol. 7, no. 6, pp. 1083–1087, Mar. 2016.

[94] A. Babayigit, A. Ethirajan, M. Muller, and B. Conings, "Toxicity of organometal halide perovskite solar cells," *Nature Materials*, vol. 15, no. 3, pp. 247–251, Mar. 2016.

[95] X. Xu, C. C. Chueh, Z. Yang, A. Rajagopal, J. Xu, S. B. Jo, and A. K. Jen, "Ascorbic acid as an effective antioxidant additive to enhance the efficiency and stability of Pb/Sn-based binary perovskite solar cells," *Nano Energy*, vol. 34, no. January, pp. 392–398, 2017.

[96] Q. Tai, X. Guo, G. Tang, P. You, T. W. Ng, D. Shen, J. Cao, C. K. Liu, N. Wang, Y. Zhu, C. S. Lee, and F. Yan, "Antioxidant grain passivation for air-stable tin-based perovskite solar cells," *Angewandte Chemie - International Edition*, vol. 58, no. 3, pp. 806–810, 2019.

[97] M. E. Kayesh, T. H. Chowdhury, K. Matsuishi, R. Kaneko, S. Kazaoui, J. J. Lee, T. Noda, and A. Islam, "Enhanced photovoltaic performance of $FASnI_3$-based per-

ovskite solar cells with hydrazinium chloride coadditive," *ACS Energy Letters*, vol. 3, no. 7, pp. 1584–1589, 2018.

[98] X. Meng, T. Wu, X. Liu, X. He, T. Noda, Y. Wang, H. Segawa, and L. Han, "Highly reproducible and efficient $FASnI_3$ perovskite solar cells fabricated with volatilizable reducing solvent," *Journal of Physical Chemistry Letters*, vol. 11, no. 8, pp. 2965–2971, 2020.

[99] C. Wang, Z. Song, Y. Yu, D. Zhao, R. A. Awni, C. R. Grice, N. Shrestha, R. J. Ellingson, X. Zhao, and Y. Yan, "Synergistic effects of thiocyanate additive and cesium cations on improving the performance and initial illumination stability of efficient perovskite solar cells," *Sustainable Energy and Fuels*, vol. 2, no. 11, pp. 2435–2441, 2018.

[100] G. E. Eperon, T. Leijtens, K. A. Bush, R. Prasanna, T. Green, J. T. W. Wang, D. P. McMeekin, G. Volonakis, R. L. Milot, R. May, A. Palmstrom, D. J. Slotcavage, R. A. Belisle, J. B. Patel, E. S. Parrott, R. J. Sutton, W. Ma, F. Moghadam, B. Conings, A. Babayigit, H. G. Boyen, S. Bent, F. Giustino, L. M. Herz, M. B. Johnston, M. D. McGehee, and H. J. Snaith, "Perovskite-perovskite tandem photovoltaics with optimized band gaps," *Science*, vol. 354, no. 6314, pp. 861–865, 2016.

[101] W. Liao, D. Zhao, Y. Yu, N. Shrestha, K. Ghimire, C. R. Grice, C. Wang, Y. Xiao, A. J. Cimaroli, R. J. Ellingson, N. J. Podraza, K. Zhu, R. G. Xiong, and Y. Yan, "Fabrication of efficient low-bandgap perovskite solar cells by combining formamidinium tin iodide with methylammonium lead iodide," *Journal of the American Chemical Society*, vol. 138, no. 38, pp. 12 360–12 363, 2016.

[102] R. Lin, K. Xiao, Z. Qin, Q. Han, C. Zhang, M. Wei, M. I. Saidaminov, Y. Gao, J. Xu, M. Xiao, A. Li, J. Zhu, E. H. Sargent, and H. Tan, "Monolithic all-perovskite tandem solar cells with 24.8% efficiency exploiting comproportionation to suppress Sn(II) oxidation in precursor ink," *Nature Energy*, vol. 4, no. 10, pp. 864–873, 2019.

[103] N. Marinova, S. Valero, and J. L. Delgado, "Organic and perovskite solar cells: Working principles, materials and interfaces," *Journal of Colloid and Interface Science*, vol. 488, pp. 373–389, Feb. 2017.

[104] Z. Song, S. C. Watthage, A. B. Phillips, and M. J. Heben, "Pathways toward high-performance perovskite solar cells: Review of recent advances in organo-metal halide perovskites for photovoltaic applications," *Journal of Photonics for Energy*, vol. 6, no. 2, p. 022001, Apr. 2016.

[105] C.-C. Chueh, C.-Z. Li, and A. K.-Y. Jen, “Recent progress and perspective in solution-processed interfacial materials for efficient and stable polymer and organometal perovskite solar cells,” *Energy & Environmental Science*, vol. 8, no. 4, pp. 1160–1189, 2015.

[106] P. Liao, X. Zhao, G. Li, Y. Shen, and M. Wang, “A new method for fitting current–voltage curves of planar heterojunction perovskite solar cells,” *Nano-Micro Letters*, vol. 10, no. 1, pp. 1–8, 2018.

[107] N. K. Elumalai, M. A. Mahmud, D. Wang, and A. Uddin, “Perovskite solar cells: Progress and advancements,” *Energies*, vol. 9, no. 11, 2016.

[108] P. Roy, N. Kumar Sinha, S. Tiwari, and A. Khare, “A review on perovskite solar cells: Evolution of architecture, fabrication techniques, commercialization issues and status,” *Solar Energy*, vol. 198, no. December 2019, pp. 665–688, 2020.

[109] J. H. Im, C. R. Lee, J. W. Lee, S. W. Park, and N. G. Park, “6.5% efficient perovskite quantum-dot-sensitized solar cell,” *Nanoscale*, vol. 3, no. 10, pp. 4088–4093, 2011.

[110] H. S. Kim, C. R. Lee, J. H. Im, K. B. Lee, T. Moehl, A. Marchioro, S. J. Moon, R. Humphry-Baker, J. H. Yum, J. E. Moser, M. Grätzel, and N. G. Park, “Lead iodide perovskite sensitized all-solid-state submicron thin film mesoscopic solar cell with efficiency exceeding 9%,” *Scientific Reports*, vol. 2, pp. 1–7, 2012.

[111] M. M. Lee, J. Teuscher, T. Miyasaka, T. N. Murakami, and H. J. Snaith, “Efficient hybrid solar cells based on meso-superstructured organometal halide perovskites,” *Science*, vol. 338, no. 6107, pp. 643–647, Nov. 2012.

[112] J. Burschka, N. Pellet, S. J. Moon, R. Humphry-Baker, P. Gao, M. K. Nazeeruddin, and M. Grätzel, “Sequential deposition as a route to high-performance perovskite-sensitized solar cells,” *Nature*, vol. 499, no. 7458, pp. 316–319, 2013.

[113] J. M. Ball, M. M. Lee, A. Hey, and H. J. Snaith, “Low-temperature processed meso-superstructured to thin-film perovskite solar cells,” *Energy and Environmental Science*, vol. 6, no. 6, pp. 1739–1743, 2013.

[114] H. Zhou, T.-b. Song, Y. Liu, Z. Hong, J. You, S. Luo, G. Li, Q. Chen, Y. Yang, H.-S. Duan, G. Li, S. Luo, T.-b. Song, H.-S. Duan, Z. Hong, J. You, Y. Liu, and Y. Yang, “Interface engineering of highly efficient perovskite solar cells,” *Science*, vol. 345, no. 6196, pp. 542–546, Aug. 2014.

[115] D. Liu and T. L. Kelly, "Perovskite solar cells with a planar heterojunction structure prepared using room-temperature solution processing techniques," *Nature Photonics*, vol. 8, no. 2, pp. 133–138, 2014.

[116] J. H. Heo, H. J. Han, D. Kim, T. K. Ahn, and S. H. Im, "Hysteresis-less inverted $CH_3NH_3PbI_3$ planar perovskite hybrid solar cells with 18.1% power conversion efficiency," *Energy and Environmental Science*, vol. 8, no. 5, pp. 1602–1608, 2015.

[117] W. S. Yang, J. H. Noh, N. J. Jeon, Y. C. Kim, S. Ryu, J. Seo, and S. I. Seok, "High-performance photovoltaic perovskite layers fabricated through intramolecular exchange," *Science*, vol. 348, no. 6240, pp. 1234–1237, 2015.

[118] X. Li, D. Bi, C. Yi, J. D. Décoppet, J. Luo, S. M. Zakeeruddin, A. Hagfeldt, and M. Grätzel, "A vacuum flash-assisted solution process for high-efficiency large-area perovskite solar cells," *Science*, vol. 353, no. 6294, pp. 58–62, 2016.

[119] M. Saliba, T. Matsui, J. Y. Seo, K. Domanski, J. P. Correa-Baena, M. K. Nazeeruddin, S. M. Zakeeruddin, W. Tress, A. Abate, A. Hagfeldt, and M. Grätzel, "Cesium-containing triple cation perovskite solar cells: Improved stability, reproducibility and high efficiency," *Energy and Environmental Science*, vol. 9, no. 6, pp. 1989–1997, 2016.

[120] Q. Jiang, Z. Chu, P. Wang, X. Yang, H. Liu, Y. Wang, Z. Yin, J. Wu, X. Zhang, and J. You, "Planar-structure perovskite solar cells with efficiency beyond 21%," *Advanced Materials*, vol. 29, no. 46, pp. 1–7, 2017.

[121] N. J. Jeon, H. Na, E. H. Jung, T. Y. Yang, Y. G. Lee, G. Kim, H. W. Shin, S. Il Seok, J. Lee, and J. Seo, "A fluorene-terminated hole-transporting material for highly efficient and stable perovskite solar cells," *Nature Energy*, vol. 3, no. 8, pp. 682–689, 2018.

[122] Y. Wang, M. Ibrahim Dar, L. K. Ono, T. Zhang, M. Kan, Y. Li, L. Zhang, X. Wang, Y. Yang, X. Gao, Y. Qi, M. Grätzel, and Y. Zhao, "Thermodynamically stabilized b-$CsPbI_3$–based perovskite solar cells with efficiencies >18%," *Science*, vol. 365, no. 6453, pp. 591–595, 2019.

[123] M. Kim, G. H. Kim, T. K. Lee, I. W. Choi, H. W. Choi, Y. Jo, Y. J. Yoon, J. W. Kim, J. Lee, D. Huh, H. Lee, S. K. Kwak, J. Y. Kim, and D. S. Kim, "Methylammonium chloride induces intermediate phase stabilization for efficient perovskite solar cells," *Joule*, vol. 3, no. 9, pp. 2179–2192, 2019.

[124] Z. Song, S. C. Watthage, A. B. Phillips, B. L. Tompkins, R. J. Ellingson, and M. J. Heben, “Impact of processing temperature and composition on the formation of methylammonium lead iodide perovskites,” *Chemistry of Materials*, vol. 27, no. 13, pp. 4612–4619, 2015.

[125] Y. Tidhar, E. Edri, H. Weissman, D. Zohar, G. Hodes, D. Cahen, B. Rybtchinski, and S. Kirmayer, “Crystallization of methyl ammonium lead halide perovskites: Implications for photovoltaic applications,” *Journal of the American Chemical Society*, vol. 136, no. 38, pp. 13 249–13 256, 2014.

[126] S. T. Williams, F. Zuo, C. C. Chueh, C. Y. Liao, P. W. Liang, and A. K. Jen, “Role of chloride in the morphological evolution of organo-lead halide perovskite thin films,” *ACS Nano*, vol. 8, no. 10, pp. 10 640–10 654, 2014.

[127] A. Buin, P. Pietsch, J. Xu, O. Voznyy, A. H. Ip, R. Comin, and E. H. Sargent, “Materials processing routes to trap-free halide perovskites,” *Nano Letters*, vol. 14, no. 11, pp. 6281–6286, 2014.

[128] M. H. Du, “Efficient carrier transport in halide perovskites: Theoretical perspectives,” *Journal of Materials Chemistry A*, vol. 2, no. 24, pp. 9091–9098, 2014.

[129] N. K. Noel, S. N. Habisreutinger, B. Wenger, M. T. Klug, M. T. Hörantner, M. B. Johnston, R. J. Nicholas, D. T. Moore, and H. J. Snaith, “A low viscosity, low boiling point, clean solvent system for the rapid crystallisation of highly specular perovskite films,” *Energy and Environmental Science*, vol. 10, no. 1, pp. 145–152, 2017.

[130] A. J. Ramadan, N. K. Noel, S. Fearn, N. Young, M. Walker, L. A. Rochford, and H. J. Snaith, “Unravelling the improved electronic and structural properties of methylammonium lead iodide deposited from acetonitrile,” *Chemistry of Materials*, vol. 30, no. 21, pp. 7737–7743, Nov. 2018.

[131] W. Tress, N. Marinova, T. Moehl, S. M. Zakeeruddin, M. K. Nazeeruddin, and M. Grätzel, “Understanding the rate-dependent J-V hysteresis, slow time component, and aging in $CH_3NH_3PbI_3$ perovskite solar cells: the role of a compensated electric field,” *Energy and Environmental Science*, vol. 8, no. 3, pp. 995–1004, 2015.

[132] M. Hirasawa, T. Ishihara, T. Goto, K. Uchida, and N. Miura, “Magnetoabsorption of the lowest exciton in perovskite-type compound $(CH_3NH_3)PbI_3$,” *Physica B: Physics of Condensed Matter*, vol. 201, no. C, pp. 427–430, 1994.

[133] K. Tanaka, T. Takahashi, T. Ban, T. Kondo, K. Uchida, and N. Miura, "Comparative study on the excitons in lead-halide-based perovskite-type crystals $CH_3NH_3PbBr_3$ $CH_3NH_3PbI_3$," *Solid State Communications*, vol. 127, no. 9-10, pp. 619–623, 2003.

[134] A. Miyata, A. Mitioglu, P. Plochocka, O. Portugall, J. T. W. Wang, S. D. Stranks, H. J. Snaith, and R. J. Nicholas, "Direct measurement of the exciton binding energy and effective masses for charge carriers in organic-inorganic tri-halide perovskites," *Nature Physics*, vol. 11, no. 7, pp. 582–587, Jul. 2015.

[135] F. Ruf, M. F. Aygüler, N. Giesbrecht, B. Rendenbach, A. Magin, P. Docampo, H. Kalt, and M. Hetterich, "Temperature-dependent studies of exciton binding energy and phase-transition suppression in $(Cs,FA,MA)Pb(I,Br)_3$ perovskites," *APL Materials*, vol. 7, no. 3, 2019.

[136] K. Galkowski, A. Mitioglu, A. Miyata, P. Plochocka, O. Portugall, G. E. Eperon, J. T. W. Wang, T. Stergiopoulos, S. D. Stranks, H. J. Snaith, and R. J. Nicholas, "Determination of the exciton binding energy and effective masses for methylammonium and formamidinium lead tri-halide perovskite semiconductors," *Energy and Environmental Science*, vol. 9, no. 3, pp. 962–970, 2016.

[137] M. H. Du, "Density functional calculations of native defects in $CH_3NH_3PbI_3$: Effects of spin-orbit coupling and self-interaction error," *Journal of Physical Chemistry Letters*, vol. 6, no. 8, pp. 1461–1466, 2015.

[138] W. Li, J. Liu, F. Q. Bai, H. X. Zhang, and O. V. Prezhdo, "Hole trapping by iodine interstitial defects decreases free carrier losses in perovskite solar cells: A time-domain ab initio study," *ACS Energy Letters*, vol. 2, no. 6, pp. 1270–1278, 2017.

[139] H. Uratani and K. Yamashita, "Charge carrier trapping at surface defects of perovskite solar cell absorbers: A first-principles study," *Journal of Physical Chemistry Letters*, vol. 8, no. 4, pp. 742–746, 2017.

[140] E. Mosconi, D. Meggiolaro, H. J. Snaith, S. D. Stranks, and F. De Angelis, "Light-induced annihilation of frenkel defects in organo-lead halide perovskites," *Energy and Environmental Science*, vol. 9, no. 10, pp. 3180–3187, 2016.

[141] J. S. Park, S. Kim, Z. Xie, and A. Walsh, "Point defect engineering in thin-film solar cells," *Nature Reviews Materials*, vol. 3, no. 7, pp. 194–210, 2018.

[142] L. D. Whalley, R. Crespo-Otero, and A. Walsh, "H-Center and V-center defects in hybrid halide perovskites," *ACS Energy Letters*, vol. 2, no. 12, pp. 2713–2714, 2017.

[143] C. Qin, T. Matsushima, T. Fujihara, W. J. Potscavage, and C. Adachi, "Degradation mechanisms of solution-processed planar perovskite solar cells: Thermally stimulated current measurement for analysis of carrier traps," *Advanced Materials*, vol. 28, no. 3, pp. 466–471, 2016.

[144] D. Meggiolaro, S. G. Motti, E. Mosconi, A. J. Barker, J. Ball, C. Andrea Riccardo Perini, F. Deschler, A. Petrozza, and F. De Angelis, "Iodine chemistry determines the defect tolerance of lead-halide perovskites," *Energy and Environmental Science*, vol. 11, no. 3, pp. 702–713, 2018.

[145] W. Kong, T. Ding, G. Bi, and H. Wu, "Optical characterizations of the surface states in hybrid lead-halide perovskites," *Physical Chemistry Chemical Physics*, vol. 18, no. 18, pp. 12 626–12 632, 2016.

[146] L. Vinet and A. Zhedanov, "A 'missing' family of classical orthogonal polynomials," *Journal of Physics A: Mathematical and Theoretical*, vol. 44, no. 8, pp. 1–8, 2011.

[147] Y. Chen, H. T. Yi, X. Wu, R. Haroldson, Y. N. Gartstein, Y. I. Rodionov, K. S. Tikhonov, A. Zakhidov, X. Y. Zhu, and V. Podzorov, "Extended carrier lifetimes and diffusion in hybrid perovskites revealed by hall effect and photoconductivity measurements," *Nature Communications*, vol. 7, no. 1, p. 12253, Dec. 2016.

[148] C. Wehrenfennig, G. E. Eperon, M. B. Johnston, H. J. Snaith, and L. M. Herz, "High charge carrier mobilities and lifetimes in organolead trihalide perovskites," *Advanced Materials*, vol. 26, no. 10, pp. 1584–1589, 2014.

[149] C. S. Ponseca, Y. Tian, V. Sundström, and I. G. Scheblykin, "Excited state and charge-carrier dynamics in perovskite solar cell materials," *Nanotechnology*, vol. 27, no. 8, p. 082001, 2016.

[150] M. B. Johnston and L. M. Herz, "Hybrid perovskites for photovoltaics: Charge-carrier recombination, diffusion, and radiative efficiencies," *Accounts of Chemical Research*, vol. 49, no. 1, pp. 146–154, 2016.

[151] Y. Yang, Y. Yan, M. Yang, S. Choi, K. Zhu, J. M. Luther, and M. C. Beard, "Low surface recombination velocity in solution-grown $CH_3NH_3PbBr_3$ perovskite single crystal," *Nature Communications*, vol. 6, p. 7961, 2015.

[152] G. A. Elbaz, D. B. Straus, O. E. Semonin, T. D. Hull, D. W. Paley, P. Kim, J. S. Owen, C. R. Kagan, and X. Roy, "Unbalanced hole and electron diffusion in lead bromide perovskites," *Nano Letters*, vol. 17, no. 3, pp. 1727–1732, 2017.

[153] D. Webber, C. Clegg, A. W. Mason, S. A. March, I. G. Hill, and K. C. Hall, "Carrier diffusion in thin-film $CH_3NH_3PbI_3$ perovskite measured using four-wave mixing," *Applied Physics Letters*, vol. 111, no. 12, p. 121905, 2017.

[154] P. Ščajev, R. Aleksiejunas, S. Miasojedovas, S. Nargelas, M. Inoue, C. Qin, T. Matsushima, C. Adachi, and S. Juršenas, "Two regimes of carrier diffusion in vapor-deposited lead-halide perovskites," *Journal of Physical Chemistry C*, vol. 121, no. 39, pp. 21 600–21 609, 2017.

[155] Z. Guo, J. S. Manser, Y. Wan, P. V. Kamat, and L. Huang, "Spatial and temporal imaging of long-range charge transport in perovskite thin films by ultrafast microscopy," *Nature Communications*, vol. 6, no. May, p. 7471, 2015.

[156] R. Long, J. Liu, and O. V. Prezhdo, "Unravelling the effects of grain boundary and chemical doping on electron-hole recombination in $CH_3NH_3PbI_3$ perovskite by time-domain atomistic simulation," *Journal of the American Chemical Society*, vol. 138, no. 11, pp. 3884–3890, 2016.

[157] D. W. DeQuilettes, S. M. Vorpahl, S. D. Stranks, H. Nagaoka, G. E. Eperon, M. E. Ziffer, H. J. Snaith, and D. S. Ginger, "Impact of microstructure on local carrier lifetime in perovskite solar cells," *Science*, vol. 348, no. 6235, pp. 683–686, 2015.

[158] R. Ciesielski, F. Schäfer, N. F. Hartmann, N. Giesbrecht, T. Bein, P. Docampo, and A. Hartschuh, "Grain boundaries act as solid walls for charge carrier diffusion in large crystal MAPI thin films," *ACS Applied Materials and Interfaces*, vol. 10, no. 9, pp. 7974–7981, 2018.

[159] S. Wieghold, J. Tresback, J. P. Correa-Baena, N. T. P. Hartono, S. Sun, Z. Liu, M. Layurova, Z. A. Vanorman, A. S. Bieber, J. Thapa, B. Lai, Z. Cai, L. Nienhaus, and T. Buonassisi, "Halide heterogeneity affects local charge carrier dynamics in mixed-ion lead perovskite thin films," *Chemistry of Materials*, vol. 31, no. 10, pp. 3712–3721, 2019.

[160] T. W. Jones, A. Osherov, M. Alsari, M. Sponseller, B. C. Duck, Y. K. Jung, C. Settens, F. Niroui, R. Brenes, C. V. Stan, Y. Li, M. Abdi-Jalebi, N. Tamura, J. E. MacDonald, M. Burghammer, R. H. Friend, V. Bulović, A. Walsh, G. J. Wilson, S. Lilliu, and S. D. Stranks, "Lattice strain causes non-radiative losses in halide perovskites," *Energy and Environmental Science*, vol. 12, no. 2, pp. 596–606, 2019.

[161] M. Kulig, J. Zipfel, P. Nagler, S. Blanter, C. Schüller, T. Korn, N. Paradiso, M. M. Glazov, and A. Chernikov, “Exciton diffusion and halo effects in monolayer semiconductors,” *Physical Review Letters*, vol. 120, no. 20, pp. 1–6, 2018.

[162] G. M. Akselrod, P. B. Deotare, N. J. Thompson, J. Lee, W. A. Tisdale, M. A. Baldo, V. M. Menon, V. Bulovic, and V. Bulović, “Visualization of exciton transport in ordered and disordered molecular solids,” *Nature Communications*, vol. 5, pp. 1–16, 2014.

[163] T. W. Crothers, R. L. Milot, J. B. Patel, E. S. Parrott, J. Schlipf, P. Müller-Buschbaum, M. B. Johnston, L. M. Herz, M. Peter, M. B. Johnston, P. Müller-Buschbaum, M. B. Johnston, and L. M. Herz, “Photon reabsorption masks intrinsic bimolecular charge-carrier recombination in $CH_3NH_3PbI_3$ perovskite,” *Nano Letters*, vol. 17, no. 9, pp. 5782–5789, Sep. 2017.

[164] F. Staub, H. Hempel, J. C. Hebig, J. Mock, U. W. Paetzold, U. Rau, T. Unold, and T. Kirchartz, “Beyond bulk lifetimes: Insights into lead halide perovskite films from time-resolved photoluminescence,” *Physical Review Applied*, vol. 6, no. 4, pp. 1–13, 2016.

[165] C. M. Sutter-Fella, Y. Li, M. Amani, J. W. Ager, F. M. Toma, E. Yablonovitch, I. D. Sharp, and A. Javey, “High photoluminescence quantum yield in band gap tunable bromide containing mixed halide perovskites,” *Nano Letters*, vol. 16, no. 1, pp. 800–806, 2016.

[166] D. W. DeQuilettes, S. Jariwala, S. Burke, M. E. Ziffer, J. T. Wang, H. J. Snaith, and D. S. Ginger, “Tracking photoexcited carriers in hybrid perovskite semiconductors: Trap-dominated spatial heterogeneity and diffusion,” *ACS Nano*, vol. 11, no. 11, pp. 11 488–11 496, 2017.

[167] P. Ščajev, C. Qin, R. Aleksiejunas, P. Baronas, S. Miasojedovas, T. Fujihara, T. Matsushima, C. Adachi, and S. Juršėnas, “Diffusion enhancement in highly excited $MAPbI_3$ perovskite layers with additives,” *Journal of Physical Chemistry Letters*, vol. 9, no. 12, pp. 3167–3172, 2018.

[168] J. R. Salcedo, A. E. Siegman, D. D. Dlott, and M. D. Fayer, “Dynamics of energy transport in molecular crystals: the picosecond transient-grating method,” *Physical Review Letters*, vol. 41, no. 2, pp. 131–134, 1978.

[169] R. J. Stoddard, F. T. Eickemeyer, J. K. Katahara, and H. W. Hillhouse, “Correlation between photoluminescence and carrier transport and a simple in situ passivation

method for high-bandgap hybrid perovskites," *Journal of Physical Chemistry Letters*, vol. 8, no. 14, pp. 3289–3298, 2017.

[170] J. M. Richter, M. Abdi-Jalebi, A. Sadhanala, M. Tabachnyk, J. P. Rivett, L. M. Pazos-Outón, K. C. Gödel, M. Price, F. Deschler, and R. H. Friend, "Enhancing photoluminescence yields in lead halide perovskites by photon recycling and light out-coupling," *Nature Communications*, vol. 7, pp. 506–514, 2016.

[171] R. T. Ross, "Some thermodynamics of photochemical systems," *The Journal of Chemical Physics*, vol. 46, no. 12, pp. 4590–4593, 1967.

[172] I. L. Braly, R. J. Stoddard, A. Rajagopal, A. K. Jen, and H. W. Hillhouse, "Photoluminescence and photoconductivity to assess maximum open-circuit voltage and carrier transport in hybrid perovskites and other photovoltaic materials," *Journal of Physical Chemistry Letters*, vol. 9, no. 13, pp. 3779–3792, 2018.

[173] R. R. Chance, A. Prock, and R. Silbey, *Advances in Chemical Physics*, ser. Advances in Chemical Physics, I. Prigogine and S. A. Rice, Eds. Hoboken, NJ, USA: John Wiley & Sons, Inc., Jan. 1978, vol. 37, no. 1-2.

[174] D. W. Dequilettes, K. Frohna, D. Emin, T. Kirchartz, V. Bulovic, D. S. Ginger, and S. D. Stranks, "Charge-carrier recombination in halide perovskites," *Chemical Reviews*, vol. 119, no. 20, pp. 11 007–11 019, 2019.

[175] T. Kirchartz, B. E. Pieters, K. Taretto, and U. Rau, "Mobility dependent efficiencies of organic bulk heterojunction solar cells: Surface recombination and charge transfer state distribution," *Physical Review B - Condensed Matter and Materials Physics*, vol. 80, no. 3, pp. 1–6, 2009.

[176] J. Wang, W. Fu, S. Jariwala, I. Sinha, A. K. Jen, and D. S. Ginger, "Reducing surface recombination velocities at the electrical contacts will improve perovskite photovoltaics," *ACS Energy Letters*, vol. 4, no. 1, pp. 222–227, 2019.

[177] Y. Yang, M. Yang, D. T. Moore, Y. Yan, E. M. Miller, K. Zhu, and M. C. Beard, "Top and bottom surfaces limit carrier lifetime in lead iodide perovskite films," *Nature Energy*, vol. 2, no. 2, pp. 1–7, 2017.

[178] T. Kirchartz, "High open-circuit voltages in lead-halide perovskite solar cells: Experiment, theory and open questions," *Philosophical Transactions of the Royal Society A: Mathematical, Physical and Engineering Sciences*, vol. 377, no. 2152, p. 20180286, Aug. 2019.

[179] R. L. Milot, G. E. Eperon, H. J. Snaith, M. B. Johnston, and L. M. Herz, "Temperature-dependent charge-carrier dynamics in $CH_3NH_3PbI_3$ perovskite thin films," *Advanced Functional Materials*, vol. 25, no. 39, pp. 6218–6227, 2015.

[180] L. M. Pazos-Outón, M. Szumilo, R. Lamboll, J. M. Richter, M. Crespo-Quesada, M. Abdi-Jalebi, H. J. Beeson, M. Vrućinić, M. Alsari, H. J. Snaith, B. Ehrler, R. H. Friend, and F. Deschler, "Photon recycling in lead iodide perovskite solar cells," *Science*, vol. 351, no. 6280, pp. 1430–1433, 2016.

[181] A. Sridharan, N. K. Noel, H. Hwang, S. Hafezian, B. P. Rand, and S. Kéna-Cohen, "Time-resolved imaging of carrier transport in halide perovskite thin films and evidence for nondiffusive transport," *Physical Review Materials*, vol. 3, no. 12, pp. 1–10, 2019.

[182] D. W. DeQuilettes, R. Brenes, M. Laitz, B. T. Motes, M. M. Glazov, and V. Bulovic, "Accurate determination of semiconductor diffusion coefficient using optical microscopy," *arXiv*, Mar. 2021.

[183] A. Martí, J. L. Balenzategui, and R. F. Reyna, "Photon recycling and Shockley's diode equation," *Journal of Applied Physics*, vol. 82, no. 8, pp. 4067–4075, 1997.

[184] R. Bhattacharya, B. Pal, and B. Bansal, "On conversion of luminescence into absorption and the van Roosbroeck-Shockley relation," *Applied Physics Letters*, vol. 100, no. 22, pp. 2012–2015, 2012.

[185] M. Furno, R. Meerheim, S. Hofmann, B. Lüssem, and K. Leo, "Efficiency and rate of spontaneous emission in organic electroluminescent devices," *Physical Review B - Condensed Matter and Materials Physics*, vol. 85, no. 11, pp. 1–21, 2012.

[186] T. D. Schmidt, T. Lampe, M. R. Daniel Sylvinson, P. I. Djurovich, M. E. Thompson, and W. Brütting, "Emitter orientation as a key parameter in organic light-emitting diodes," *Physical Review Applied*, vol. 8, no. 3, pp. 1–28, 2017.

[187] L. M. Pazos-Outón, T. P. Xiao, and E. Yablonovitch, "Fundamental efficiency limit of lead iodide perovskite solar cells," *Journal of Physical Chemistry Letters*, vol. 9, no. 7, pp. 1703–1711, 2018.

[188] R. J. Elliott, "Intensity of optical absorption by excitons," *Physical Review*, vol. 108, no. 6, pp. 1384–1389, 1957.

[189] J. K. Katahara and H. W. Hillhouse, "Quasi-Fermi level splitting and sub-bandgap absorptivity from semiconductor photoluminescence," *Journal of Applied Physics*, vol. 116, no. 17, 2014.

[190] G. Lasher and F. Stern, “Spontaneous and stimulated recombination radiation in semiconductors,” *Physical Review*, vol. 133, no. 2A, pp. A553–A563, Jan. 1964.

[191] P. Würfel and W. Ruppel, “The chemical potential of luminescent radiation,” *Journal of Luminescence*, vol. 24-25, pp. 925–928, 1981.

[192] J. K. Katahara and H. W. Hillhouse, “Erratum: Quasi-Fermi level splitting and sub-bandgap absorptivity from semiconductor photoluminescence (journal of applied physics (2014) 116 (173504)),” *Journal of Applied Physics*, vol. 119, no. 23, 2016.

[193] M. B. Price, J. Butkus, T. C. Jellicoe, A. Sadhanala, A. Briane, J. E. Halpert, K. Broch, J. M. Hodgkiss, R. H. Friend, and F. Deschler, “Hot-carrier cooling and photoinduced refractive index changes in organic-inorganic lead halide perovskites,” *Nature Communications*, vol. 6, no. May, pp. 1–8, 2015.

[194] T. A. Doherty, A. J. Winchester, S. Macpherson, D. N. Johnstone, V. Pareek, E. M. Tennyson, S. Kosar, F. U. Kosasih, M. Anaya, M. Abdi-Jalebi, Z. Andaji-Garmaroudi, E. L. Wong, J. Madéo, Y. H. Chiang, J. S. Park, Y. K. Jung, C. E. Petoukhoff, G. Divitini, M. K. L. Man, C. Ducati, A. Walsh, P. A. Midgley, K. M. Dani, and S. D. Stranks, “Performance-limiting nanoscale trap clusters at grain junctions in halide perovskites,” *Nature*, vol. 580, no. 7803, pp. 360–366, 2020.

APPENDIX A CARRIER GENERATION FOR A LASER PULSE

Here, the pulse energy P_E is known experimentally from a power measurement and the laser repetition rate. The symmetry in x and y makes the problem well suited for a coordinate transformation towards r and θ, where dependence on θ is non-existent and therefore ignored. We can express the photogeneration term $G(r,t)$ using the laser pulse energy P_E (measured laser power/repetition rate) by employing Gaussian distributions for the time and space profiles.

$$G(r,t) = \ G_0 \cdot f(r) \cdot g(t) = G_0 \cdot e^{-\frac{r^2}{2\sigma_L^2}} \cdot e^{-\frac{(t-t_0)^2}{2\sigma_\tau^2}} \tag{A.1}$$

G_0 is the generated carrier density at $(r,t) = (0,t_0)$ for a non-homogeneous (along r) normalized spatial profile $f(r)$ of Gaussian half-width σ_L and σ_τ is the temporal Gaussian half-width of the pump laser. For a given pulse energy, we can calculate G_0 by equating the integral $G(r,t)$ to the incoming photon flux $\phi_{inc}(r,t)$ assuming every photon is converted to electron-hole pair. The photon flux is related to the pulse energy P_E as follows:

$$\frac{P_E}{E_{ph}} = \int_{-\infty}^{\infty} \int_0^{2\pi} \int_0^{\infty} \phi_{inc}\left(r,t\right) \cdot r dr \partial\theta dt = \int_{-\infty}^{\infty} \int_0^{2\pi} \int_0^{\infty} G_0 \cdot e^{-\frac{r^2}{2\sigma_L^2}} \cdot e^{-\frac{t^2}{2\sigma_\tau^2}} \cdot r \partial r \partial\theta dt \tag{A.2}$$

Solving for G_0, we obtain:

$$G_0 = \frac{P_E}{E_{ph}(2\pi)^{3/2}\sigma_L^2\sigma_\tau} \tag{A.3}$$

Hence, substituting into Equation (A.1) we obtain the complete expression for $G(r,t)$:

$$G(r,t) = \frac{P_E}{E_{ph}(2\pi)^{3/2}\sigma_L^2\sigma_\tau} e^{-\frac{r^2}{2\sigma_L^2}} \cdot e^{-\frac{(t-t_0)^2}{2\sigma_\tau^2}} \tag{A.4}$$

Although, Beer-Lambert absorption is ignored here, we can include it by adding an extra z dependent term to Equation (A.1) as shown below:

$$G(r,t) = G_0 \cdot f(r) \cdot g(t) \cdot h(z) = G_0 \cdot e^{-\frac{r^2}{2\sigma_L^2}} \cdot e^{-\frac{(t-t_0)^2}{2\sigma_\tau^2}} \cdot e^{-\alpha z} \tag{A.5}$$

And doing so, we get the following result:

$$G(r,t) = \frac{\alpha P_E}{E_{ph}(2\pi)^{3/2}\sigma_L^2\sigma_\tau} \cdot e^{-\frac{r^2}{2\sigma_L^2}} \cdot e^{-\frac{(t-t_0)^2}{2\sigma_\tau^2}} \cdot e^{-\alpha z} \tag{A.6}$$

The above equation is useful for modelling carrier dynamics in the 2D plane in conjunction with photoluminescence measurements.

APPENDIX B DIFFUSION GAUSSIAN SOLUTION DERIVATION

B.1 Gaussian Solution Derivation for 1D Diffusion Equation

In this section, we present a gaussian Fourier transform based solution to the one-dimensional diffusion equation, i.e. Equation (2.91) presented in Section 2.7 of Chapter 2:

$$\frac{\partial W}{dt} = D\frac{\partial^2 W}{\partial x^2} \tag{B.1}$$

We first define the spatial Fourier transform of $W(x,t)$ and its inverse as follows:

$$\mathcal{F}\left\{W(x,t)\right\} = \hat{W}(k,t) = \int_{-\infty}^{\infty} W(x,t)e^{-2\pi ixk}\partial x \tag{B.2}$$

$$\mathcal{F}^{-1}\left\{\hat{W}(k,t)\right\} = W(x,t) = \int_{-\infty}^{\infty} \hat{W}(k,t)e^{2\pi ixk}dk \tag{B.3}$$

As per derivative properties of the Fourier Transform, we now have the following:

$$\mathcal{F}\left\{\frac{\partial^n W}{\partial x^n}\right\} = (2\pi ik)^n\hat{W} \tag{B.4}$$

Therefore, we can rewrite the Fourier transform of Equation B.1 as follows:

$$\frac{\partial\hat{W}}{\partial t} = D(2\pi ik)^2\hat{W} \tag{B.5}$$

The solution to this differential equation is:

$$\hat{W} = Ae^{-(2\pi k)^2Dt} \tag{B.6}$$

Lastly, we perform the inverse Fourier transform and through algebraic manipulation for the integral, we obtain the following solution:

$$W\left(x,t\right) = \int_{-\infty}^{\infty} Ae^{-(2\pi k)^2Dt}e^{2\pi ixk}dk = \frac{A}{\sqrt{4\pi Dt}}e^{-\frac{x^2}{4Dt}} = \frac{M}{\sqrt{t}}e^{-\frac{x^2}{4Dt}} \tag{B.7}$$

B.2 Gaussian Solution Derivation for 2D Diffusion Equation

In the previous section, we saw a gaussian Fourier transform based solution to the one-dimensional diffusion equation. A similar development can be done also in two-dimensions. Let us first start with the 2D diffusion equation in polar coordinates taken from Equation (2.102) in Chapter 2, Section 2.7:

$$\frac{\partial W}{\partial t} = D\left(\frac{\partial^2 W}{\partial r^2} + \frac{1}{r}\frac{\partial W}{\partial r}\right) \tag{B.8}$$

The Fourier transform in 2D polar coordinates becomes a Hankel transform. For a function $W(r,\theta)$, the Hankel transform, and its inverse are defined as:

$$\mathcal{H}_v\left\{W\left(r,\theta\right)\right\} = \widetilde{W_v}(\rho,\phi) = \int_0^{2\pi}\int_0^{\infty} W(r,\theta)e^{-i\rho r cos(\phi-\theta)} r\partial r\partial\theta \tag{B.9}$$

$$\mathcal{H}_v^{-1}\left\{\widetilde{W}(\rho,\phi)\right\} = W\left(r,\theta\right) = \int_0^{2\pi}\int_0^{\infty} \widetilde{W_v}(\rho,\phi)e^{-i\rho r cos(\phi-\theta)}\rho d\rho d\phi \tag{B.10}$$

The differential operator on which the Hankel transform operates is shown below:

$$\mathcal{L} = \left(\frac{d^2}{\partial r^2} + \frac{1}{r}\frac{d}{\partial r}\right) + \frac{v^2}{r}\frac{d}{\partial r} \tag{B.11}$$

$\upsilon = 0$ as our order produces the Laplacian operator in Equation B.8. The zeroth order Hankel transform for isotropic diffusion, i.e. in the absence of any angular dependence, simplifies to:

$$\mathcal{H}_0\left\{W(r)\right\} = \widetilde{W}_0(\rho) = \int_0^{\infty} rW(r)J_0(\rho r)\partial r \tag{B.12}$$

$$\mathcal{H}_0^{-1}\left\{\widetilde{W}_0(\rho)\right\} = W(r) = \int_0^{\infty} \rho\widetilde{W}_0 J_0(\rho r)d\rho \tag{B.13}$$

Based on the above, we can find the Hankel transform of the Laplacian operator to be:

$$\mathcal{H}_0\left\{\ \mathcal{L}W(r)\right\} = -\rho^2\widetilde{W}_0(\rho) \tag{B.14}$$

Applying the Hankel transform on Equation B.8, we can rewrite it as:

$$\frac{\partial\widetilde{W}_0}{\partial t} = -\rho^2 D\widetilde{W}_0 \tag{B.15}$$

The solution to differential equation above is given by:

$$\widetilde{W}_0(\rho) = Ae^{-Dt\rho^2} \tag{B.16}$$

Through a final inverse Hankel transform, we obtain the solution for the 2D diffusion equation:

$$W(r) = \mathcal{H}_0^{-1}\left\{\widetilde{W}_0(\rho)\right\} = A\int_0^\infty \rho e^{-\rho^2 Dt} J_0(\rho r) d\rho = \frac{A}{2Dt}e^{-\frac{r^2}{4Dt}} \tag{B.17}$$

APPENDIX C PHOTON RECYCLING MODELLING

To match the experimental powers to our modelling, we can express the photogeneration term $G(r,t)$ using the laser pulse energy P_E (measured laser power/repetition rate) by employing the expression we have derived in Equation (A.6). We need to model these equations using a central difference discretization scheme in Matlab. However, solving both equations simultaneously this way is computationally expensive. We can speed up the computation significantly if we can obtain an analytical solution of Equation (5.3) for $\gamma_\lambda(r,t)$ within every step time step dt. We can do this by fixing $n(r,t)$ as a constant; a valid assumption considering $dn(r,t)/n(r,t) \ll d\gamma_\lambda(r,t)/\gamma_\lambda(r,t)$ over the course of a time step dt. The step-by-step method for the analytical solution is presented in the next section alongside the details of the implemented algorithm. We now derive an analytical expression for $\gamma_\lambda(r,t)$ in a 2D scenario, i.e. with only r and t variable. $\gamma_\lambda(r,t)$ is computed in the frequency domain at the end of a time step dt using initial conditions from the previous time step. Hence, we use δt instead of t for clarity, i.e. $\delta t = 0$ at the beginning of the step and $\delta t = dt$ at the end of the step. We start with Equation (5.3) from the main article in polar coordinates:

$$\frac{d\gamma_\lambda(r,\delta t)}{d(\delta t)} = D_\lambda \nabla^2 \gamma_\lambda(r,\delta t) - \frac{c}{n_s}\alpha_\lambda \gamma_\lambda(r,\delta t) + (k_2 n(r,\delta t)^2 P_{stay})P_\lambda \tag{C.1}$$

This equation can be re-written as follows:

$$\frac{d\gamma_\lambda(r,\delta t)}{d(\delta t)} - D_\lambda \nabla^2 \gamma_\lambda(r,\delta t) + \frac{c}{n_s}\alpha_\lambda \gamma_\lambda(r,\delta t) = (k_2 n(r,\delta t)^2 P_{stay})P_\lambda \tag{C.2}$$

We will define the following:

$$A(r,\delta t) = (k_2 n(r,\delta t)^2 P_{stay})P_\lambda \tag{C.3}$$

$$B = \frac{c}{n_s}\alpha_\lambda \tag{C.4}$$

Re-writing Equation C.1 with above definitions, we obtain:

$$\frac{d\gamma_\lambda(r,\delta t)}{d(\delta t)} - D_\lambda \nabla^2 \gamma_\lambda(r,\delta t) + B\gamma_\lambda(r,\delta t) = A(r,0) \tag{C.5}$$

We use $A(r,0)$ here instead of $A(r,t)$ as $n(r,0)$ is assumed to be a constant over the course of the time step $d(\delta t)$. Since we wish to solve for $\gamma_\lambda(r, \delta t)$, a simple approach would be to treat the above equation in the Hankel domain (Refer to Appendix B). Applying the Hankel operator and its properties on Equation C.5, we obtain:

$$\frac{d\widetilde{\gamma}_\lambda(r, \delta t)}{d(\delta t)} + D_\lambda \rho^2 \widetilde{\gamma}_\lambda(\rho, \delta t) + \ B\widetilde{\gamma}_\lambda(\rho, \delta t) = \widetilde{A}(\rho, 0) = \widetilde{A}_0 \tag{C.6}$$

We first solve the above differential equation for the homogeneous case $\widetilde{\gamma}_{\lambda,H}$, where $\widetilde{A}_0 = 0$.

$$\frac{d\widetilde{\gamma}_{\lambda,H}(r, \delta t)}{d(\delta t)} + D_\lambda \rho^2 \widetilde{\gamma}_{\lambda,H}(\rho, \delta t) + \ B\widetilde{\gamma}_{\lambda,H}(\rho, \delta t) = 0 \tag{C.7}$$

$$\frac{d\widetilde{\gamma}_{\lambda,H}(r, \delta t)}{\widetilde{\gamma}_{\lambda,H}(\rho, \delta t)} = -(D_\lambda \rho^2 + \ B) d(\delta t) \tag{C.8}$$

$$\widetilde{\gamma}_{\lambda,H}(\rho, \delta t) = Ce^{-(D_\lambda \rho^2 + \ B)\delta t} \tag{C.9}$$

Now we solve for particular solution $\widetilde{\gamma}_{\lambda,P}(\rho, \delta t) = H$, where H is a constant. Substituting into Equation C.6, we obtain:

$$0 + D_\lambda \rho^2 H + BH = \widetilde{A}_0 \tag{C.10}$$

$$\widetilde{\gamma}_{\lambda,P}(\rho, \delta t) = H = \frac{\widetilde{A}_0}{(D_\lambda \rho^2 + B)} \tag{C.11}$$

The solution for $\widetilde{\gamma}_\lambda(\rho, \delta t)$ is given by the superposition of the homogeneous and particular solutions $\widetilde{\gamma}_{\lambda,H}(\rho, \delta t)$ and $\widetilde{\gamma}_{\lambda,P}(\rho, \delta t)$.

$$\widetilde{\gamma}_\lambda(\rho, \delta t) = \widetilde{\gamma}_{\lambda,H}(\rho, \delta t) + \widetilde{\gamma}_{\lambda,P}(\rho, \delta t) \tag{C.12}$$

Hence, the solution for $\widetilde{\gamma}_\lambda(\rho, \delta t)$ is given by:

$$\widetilde{\gamma}_\lambda(\rho, \delta t) = Ce^{-(D_\lambda \rho^2 + B)\delta t} + \frac{\widetilde{A}_0}{(D_\lambda \rho^2 + B)} \tag{C.13}$$

Applying the initial condition $\widetilde{\gamma}_\lambda(\rho, \delta t = 0) = \widetilde{\gamma}_{\lambda,0}$, at $\delta t = 0$, we can find the constant C:

$$C = \widetilde{\gamma}_\lambda \left(\rho, 0\right) - \frac{\widetilde{A}_0}{(D_\lambda \rho^2 + B)} \tag{C.14}$$

And thus, the analytical expression for $\widetilde{\gamma}_\lambda(\rho, t)$ is given by:

$$\widetilde{\gamma}_\lambda(\rho, \delta t) = \left(\widetilde{\gamma}_{\lambda,0} - \frac{\widetilde{A}_0}{D_\lambda \rho^2 + B}\right) e^{-(D_\lambda \rho^2 + B)\delta t} + \left(\frac{\widetilde{A}_0}{D_\lambda \rho^2 + B}\right) \tag{C.15}$$

The algorithm is implemented as follows:

1. At the start of a time step, we first evaluate use $\widetilde{\gamma}_\lambda(\rho, t)$ and $\widetilde{A}(\rho, t)$ (from previous time step). In discretizated notation we use $t = i \cdot dt$ and $r \;= j \cdot \partial r$ for representing the time and space coordinates. This translates to $\widetilde{\gamma}_{\lambda,0} = \widetilde{\gamma}_\lambda\big|_j^{i-1}$. And $\widetilde{A}_0 = \widetilde{A}\big|_j^{i-1} = DHT\left\{(k_2 n\big|_j^{i-1} P_{stay}) P_\lambda\right\}$ for a previous time step $t = (i-1) \cdot dt$, i.e. $DHT\{\quad\}$ is the Discrete Hankel Transform operator representing the discretized version of the Hankel Transform operator $\mathcal{H}\{\quad\}$.
2. Then, we evaluate $\widetilde{\gamma}_\lambda(\rho, t = i \cdot dt)$ at current time step i using the analytical expression derived in Equation (2.11):

$$\widetilde{\gamma}_\lambda\big|_j^i = \left(\widetilde{\gamma}_\lambda\big|_j^{i-1} - \frac{\widetilde{A}\big|_j^{i-1}}{D_\lambda \rho^2 + \; B}\right) e^{-(D_\lambda \rho^2 + B)dt} + \left(\frac{\widetilde{A}\big|_j^{i-1}}{D_\lambda \rho^2 + B}\right) \tag{C.16}$$

3. We the recalculate $\gamma_\lambda(r, t = i \cdot dt)$ using the inverse operator, i.e. $\gamma_\lambda\big|_j^i = DHT^{-1}\left\{\, \widetilde{\gamma}_\lambda\big|_j^i\right\}$.
4. We can then evaluate $n(r, t = i \cdot dt)$, i.e. $n\big|_j^i$, in the new time step using Equation (5.2) from the main article using a finite difference scheme containing the new values of $\gamma_\lambda\big|_j^i$.